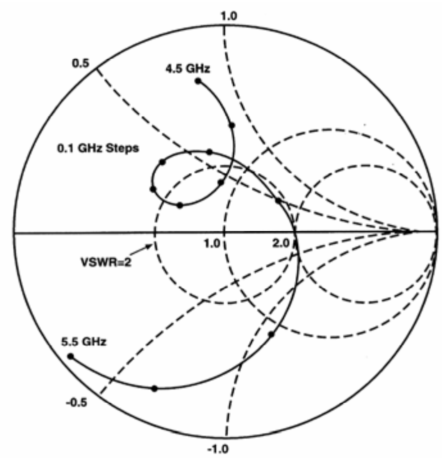

Applied Computational Electromagnetics Society Journal

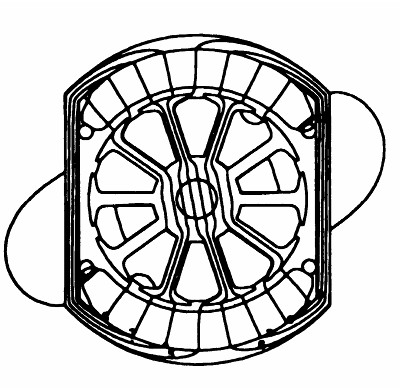

Special Issue on
ACES 2009 Conference Part I

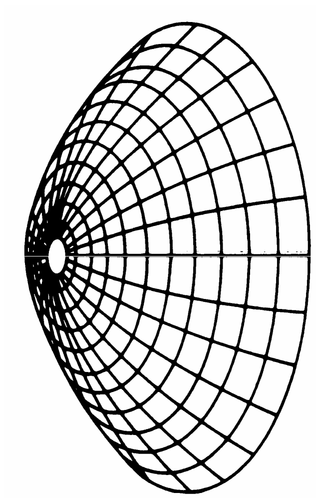

Guest Editor
Sami Barmada

December 2009
Vol. 24 No. 6
ISSN 1054-4887

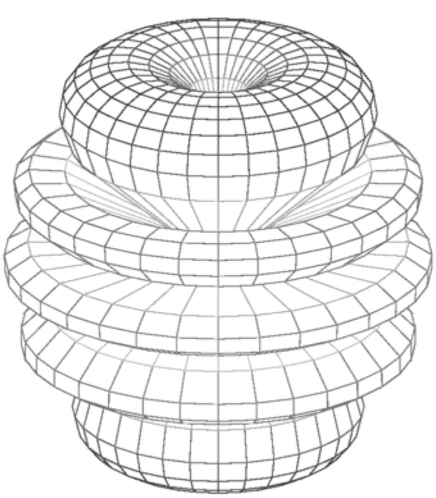

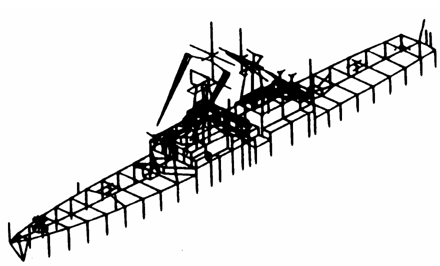

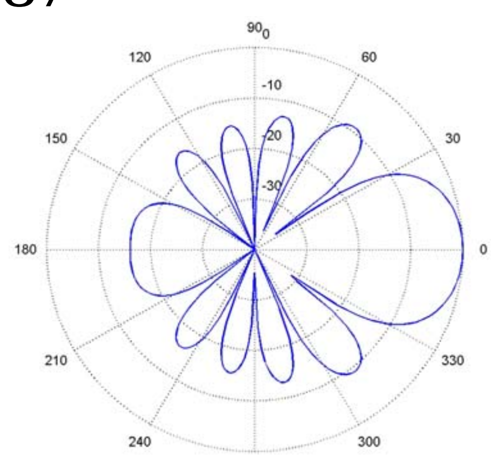

GENERAL PURPOSE AND SCOPE: The Applied Computational Electromagnetics Society ***(ACES)*** Journal hereinafter known as the ***ACES Journal*** is devoted to the exchange of information in computational electromagnetics, to the advancement of the state-of-the art, and the promotion of related technical activities. A primary objective of the information exchange is the elimination of the need to "re-invent the wheel" to solve a previously-solved computational problem in electrical engineering, physics, or related fields of study. The technical activities promoted by this publication include code validation, performance analysis, and input/output standardization; code or technique optimization and error minimization; innovations in solution technique or in data input/output; identification of new applications for electromagnetics modeling codes and techniques; integration of computational electromagnetics techniques with new computer architectures; and correlation of computational parameters with physical mechanisms.

SUBMISSIONS: The ***ACES Journal*** welcomes original, previously unpublished papers, relating to applied computational electromagnetics. Typical papers will represent the computational electromagnetics aspects of research in electrical engineering, physics, or related disciplines. However, papers which represent research in applied computational electromagnetics itself are equally acceptable.

Manuscripts are to be submitted through the upload system of ***ACES*** web site http://aces.ee.olemiss.edu See "Information for Authors" on inside of back cover and at ***ACES*** web site. For additional information contact the Editor-in-Chief:

Dr. Atef Elsherbeni
Department of Electrical Engineering
The University of Mississippi
University, MS 386377 USA
Phone: 662-915-5382 Fax: 662-915-7231
Email: atef@olemis.edu

SUBSCRIPTIONS: All members of the Applied Computational Electromagnetics Society who have paid their subscription fees are entitled to receive the ***ACES Journal*** with a minimum of three issues per calendar year and are entitled to download any published journal article available at http://aces.ee.olemiss.edu.

Back issues, when available, are $15 each. Subscriptions to ***ACES*** is through the web site. Orders for back issues of the ***ACES Journal*** and changes of addresses should be sent directly to ***ACES***:

Dr. Allen W. Glisson
302 Anderson Hall
Dept. of Electrical Engineering
Fax: 662-915-7231
Email: aglisson@olemiss.edu

Allow four week's advance notice for change of address. Claims for missing issues will not be honored because of insufficient notice or address change or loss in mail unless the Executive Officer is notified within 60 days for USA and Canadian subscribers or 90 days for subscribers in other countries, from the last day of the month of publication. For information regarding reprints of individual papers or other materials, see "Information for Authors".

LIABILITY. Neither ***ACES***, nor the ***ACES Journal*** editors, are responsible for any consequence of misinformation or claims, express or implied, in any published material in an ***ACES Journal*** issue. This also applies to advertising, for which only camera-ready copies are accepted. Authors are responsible for information contained in their papers. If any material submitted for publication includes material which has already been published elsewhere, it is the author's responsibility to obtain written permission to reproduce such material.

APPLIED COMPUTATIONAL ELECTROMAGNETICS SOCIETY JOURNAL

Guest Editor
Sami Barmada

December 2009
Vol. 24 No. 6
ISSN 1054-4887

The ACES Journal is abstracted in INSPEC, in Engineering Index, DTIC, Science Citation Index Expanded, the Research Alert, and to Current Contents/Engineering, Computing & Technology.

The first, fourth, and sixth illustrations on the front cover have been obtained from the Department of Electrical Engineering at the University of Mississippi.

The third and fifth illustrations on the front cover have been obtained from Lawrence Livermore National Laboratory.

The second illustration on the front cover has been obtained from FLUX2D software, CEDRAT S.S. France, MAGSOFT Corporation, New York.

THE APPLIED COMPUTATIONAL ELECTROMAGNETICS SOCIETY

JOURNAL

Vol. 24 No. 6 December 2009

TABLE OF CONTENTS

Computational Electromagnetics and Model-Based Inversion: A Modern Paradigm for Eddy-Current Nondestructive Evaluation

Harold A. Sabbagh[1], R. Kim Murphy[1], Elias H. Sabbagh[1], John C. Aldrin[2], Jeremy Knopp[3], and Mark Blodgett[3]

[1] Victor Technologies LLC, Bloomington, IN 47401, USA
has@sabbagh.com, kimmurphy1@aristotle.net, ehs@sabbagh.com,

[2] Computational Tools, Gurnee, IL 60031, USA
aldrin@computationaltools.com,

[3] Air Force Research Laboratory (AFRL/MLLP), Wright-Patterson AFB, OH 45433, USA
jeremy.knopp@wpafb.af.mil, mark.blodgett@wpafb.af.mil

(Invited Paper)

Abstract **─** This is the first of a planned series of papers in which we demonstrate the application of computational electromagnetics, especially the volume-integral method, to problems in eddy-current nondestructive evaluation (NDE). In particular, we will apply the volume-integral code, VIC-3D, to solve forward and inverse problems in NDE. The range of problems that will be considered spans industries from nuclear power to aerospace to materials characterization. In this paper we will introduce the notion of model-based inversion, emphasizing the role of `estimation-theoretic metrics' to the practical application of inverse theory.

Index Terms **─** volume-integral equations, electromagnetic nondestructive evaluation, model-based inversion, model-based standards, estimation-theoretic metrics.

I. INTRODUCTION

Nondestructive evaluation (NDE) is to materials and structures what CAT scanning is to the human body–an attempt to look inside without opening up the body. As in CAT scanning, modern NDE requires sophisticated mathematical software to perform its function. This is especially true with regard to quantitative NDE, wherein we attempt to quantify defects, that is, determine their size, location, even shape, rather than just to detect their presence. Low-frequency electromagnetic methods using eddy-currents are a traditional mode of doing NDE (approximately 35% of NDE uses eddy-currents, depending upon the specific application), but the technology still suffers from a lack of algorithms and software to allow its full potential to be realized.

In its essence, electromagnetic (eddy-current) nondestructive evaluation (NDE) is a scattering problem in which the anomaly (the flaw) in Figure 1 produces a current whose associated magnetic field is coupled into the probe coil. The change in driving-point impedance seen at the terminals of the coil is the measurable that indicates the presence of the anomaly. The 'anomalous current' associated with the flaw, then, is the principle electromagnetic quantity that is to be computed in order to determine the change in impedance, and to this end we have introduced VIC-3D© [1], a volume-integral code [2] [3].

The anomalous current is defined to be

$$\begin{aligned}\mathbf{J}_a(\mathbf{r}) &= (\sigma_f(\mathbf{r}) - \sigma_h)\mathbf{E}(\mathbf{r}) \\ &= \sigma_a(\mathbf{r})\mathbf{E}(\mathbf{r})\end{aligned} \tag{1}$$

where σ is the conductivity of the flaw region, σ_h is the (uniform) conductivity of the host, and $\mathbf{E}(\mathbf{r})$ is the total electric field, which is the sum of the incident field due to the probe coil and the secondary field due to $\mathbf{J}_a(\mathbf{r})$. Clearly, because the anomalous current is identically zero away from the flaw (or anomalous region), only this region needs to be gridded in order to transform the volume-integral equation into its discrete form via the Galerkin variant of the method of moments. Furthermore, if the grid is uniform in all three directions, the resulting discretized equations have matrix elements that are either Töplitz or Hankel. The *ij*th element of a Töplitz matrix is a function of $(i-j)$ and is a function of $(i+j)$ for a Hankel matrix. This allows one to compute matrix-vector products very quickly using the FFT when solving large problems with an iterative scheme, such as the conjugate-gradient method. Indeed, we solve problems with 100,000 unknowns quite routinely in a matter of minutes on personal computers using the volume-integral method. See [2] and [3] for the technical details.

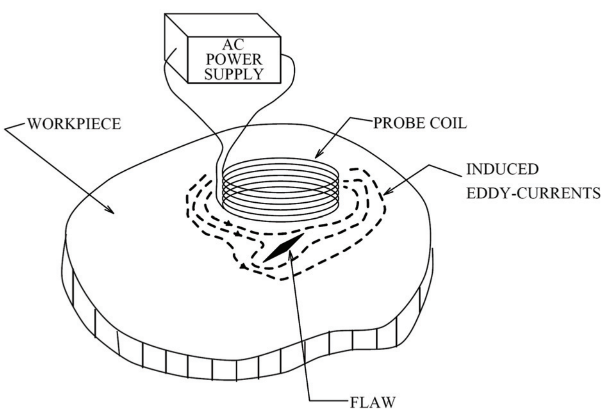

Fig. 1. Illustrating eddy-current nondestructive evaluation as a scattering problem.

II. MODEL-BASED INVERSION

In solving problems in eddy-current NDE, one often models the anomaly as a region that can be defined in terms of a few parameters. For example, we can model corrosion pitting in aerospace structures or heat-exchanger tubes in nuclear power plants by truncated right-circular cylinders–'pillboxes'–for which the parameters would be height and diameter (and perhaps the coordinates of the center of the pillbox). The inverse-scattering problem in which these parameters are to be determined from measurements of the driving-point impedance of the probe coil is what we call 'model-based inversion.'

Figure 2 illustrates a system representation for three important problems: (a) a direct problem, in which the input and system are known, and the output is to be determined; (b) a signal-detection (communication) problem, in which the system (a communication channel) and output are known, and the problem is to determine the input signal; and (c) the inverse problem, in which the input and outputs are known, and we must determine the system.

For the most part, the problems solved in [2]-[6] are direct problems; we assume knowledge of the probe and flaw, and determine the response of the probe, namely the driving-point or transfer impedances. The second problem of Figure 2 is dealt with in communication and information theory texts, and has a close relation to inverse problems.

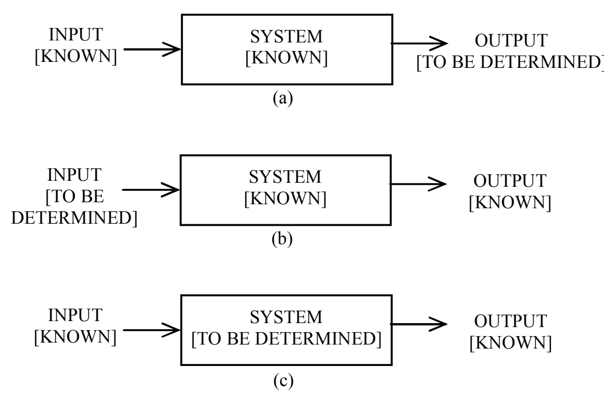

Fig. 2. System representation of direct and inverse problems: (a) The direct problem; (b) The signal-detection (communication) problem; (c) The inverse problem.

Nonlinear Least-Squares Parameter Estimation

Let

$$Z = g(p_1, \ldots, p_N, f), \tag{2}$$

where $p_1, \ldots, p_N$ are the N parameters of interest, and f is a control parameter at which the impedance, Z is measured. The parameter f can be frequency, scan-position, lift-off, etc. It is, of course, known; it is not one of the parameters to be determined. To be explicit during our initial discussion of the theory, we will call f 'frequency.'

In order to determine $p_1, \ldots, p_N$, we measure Z at M frequencies, $f_1, \ldots, f_M$, where $M > N$:

$$\begin{aligned} Z_1 &= g(p_1,\ldots,p_N,f_1) \\ &\vdots \\ Z_M &= g(p_1,\ldots,p_N,f_M). \end{aligned} \tag{3}$$

The right-hand side of (3) is computed by applying the volume-integral code to a model of the problem, usually at a discrete number of values of the vector, **p**, forming a multidimensional interpolation grid.

Because the problem is nonlinear, we use a Gauss-Newton iteration scheme to perform the inversion. First, we decompose (3) into its real and imaginary parts, thereby doubling the number of equations (we assume the $p_1,\ldots,p_N$ are real). Then we use the linear approximation to the resistance, R_i, and reactance, X_i, at the ith frequency:

$$\begin{bmatrix} R_1 \\ X_1 \\ \vdots \\ R_M \\ X_M \end{bmatrix} \approx \begin{bmatrix} R_1(p_1^{(q)},\ldots,p_N^{(q)}) \\ X_1(p_1^{(q)},\ldots,p_N^{(q)}) \\ \vdots \\ R_M(p_1^{(q)},\ldots,p_N^{(q)}) \\ X_M(p_1^{(q)},\ldots,p_N^{(q)}) \end{bmatrix} + \begin{bmatrix} \frac{\partial R_1}{\partial p_1}\cdots\frac{\partial R_1}{\partial p_N} \\ \frac{\partial X_1}{\partial p_1}\cdots\frac{\partial X_1}{\partial p_N} \\ \vdots \\ \frac{\partial R_M}{\partial p_1}\cdots\frac{\partial R_M}{\partial p_N} \\ \frac{\partial X_M}{\partial p_1}\cdots\frac{\partial X_M}{\partial p_N} \end{bmatrix}_{p_1^{(q)},\ldots,p_N^{(q)}} \begin{bmatrix} p_1 - p_1^{(q)} \\ \vdots \\ p_N - p_N^{(q)} \end{bmatrix}, \tag{4}$$

where the superscript (q) denotes the qth iteration, and the partial derivatives are computed numerically by the software. The left side of (4) is taken to be the measured values of resistance and reactance. We rewrite (4) as

$$0 \approx r + Jp, \tag{5}$$

where r is the $2M$-vector of residuals, J is the $2M \times N$ Jacobian matrix of derivatives, and p is the N-dimensional correction vector. Equation (5) is solved in a least-squares manner starting with an initial value, $(x_1^{(0)},\ldots,x_N^{(0)})$, for the vector of unknowns, and then continuing by replacing the initial vector with the updated vector $(x_1^{(q)},\ldots,x_N^{(q)})$ that is obtained from (4), until convergence occurs [7].

III. ESTIMATION-THEORETIC METRICS

We are interested in determining a bound for the sensitivity of the residual norm to changes in some linear combination of the parameters. Given an $\varepsilon > 0$ and a unit vector, v, the problem is to determine a sensitivity (upper) bound, σ, such that

$$\left\| r(x^* + \sigma v) \right\| \le (1+\varepsilon)\left\| r(x^*) \right\|. \tag{6}$$

A first-order estimate of σ is given by

$$\sigma_v = \left(\frac{\left\| r(x^*) \right\|}{\left\| J(x^*)\cdot v \right\|} \right). \tag{7}$$

Note that if $\left\| J(x^*)\cdot v \right\|$ is small compared to $\left\| r(x^*) \right\|$, then σ is large and the residual norm is insensitive to changes in the linear combination of the parameters specified by v. If $v = e_i$, the ith column of the N x N identity matrix, then (7) produces σ_i, the sensitivity bound for the ith parameter. Since σ_i will vary in size with the magnitude of x_i^*, it is better to compare the ratios σ_i / x_i^*, for $i = 1,\ldots,N$ before drawing conclusions about the fitness of a solution.

The importance of these results is that we now have metrics for the inversion process: $\Phi = \left\| r(x^*) \right\|$, the norm of the residual vector at the solution, tells us how good the fit is between the model data and measured data. The smaller this number the better, of course, but the ‘smallness’ depends upon the experimental setup and the accuracy of the model to fit the experiment. Heuristic judgment based on experience will help in determining the quality of the solution for a given Φ.

The sensitivity coefficient, σ, is more subtle, but just as important. It, too, should be small, but, again, the quality of the ‘smallness’ will be determined by heuristics based upon the problem. If σ is large in some sense, it suggests that the solution is relatively independent of that parameter, so that we cannot reasonably accept the value assigned to that parameter as being meaningful, as suggested in Figure 3, which shows a system, *S*, for which the system is sensitive to variable, x_i, at the solution point, x_i^*, and another system, *I*, for which the system is insensitive to x_i.

An example occurs when one uses a high-frequency excitation, with its attendant small skin depth, to interrogate a deep-seated flaw. The flaw will be relatively invisible to the probe at this frequency, and whatever value is given for its parameters will be highly suspect. When this occurs we will either choose a new parameter to characterize the flaw, or acquire data at a lower frequency.

These metrics are not available to us in the current inspection method, in which analog instruments acquire data that are then interpreted by humans using hardware standards. The opportunity to use these metrics is a significant advantage to the model-based inversion paradigm that we propose in this paper.

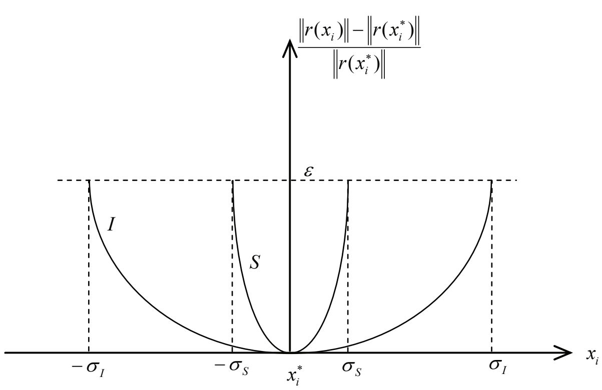

Fig. 3. Showing sensitivity parameters for two system responses to x_i. Response *S* is sensitive to x_i at $\boldsymbol{x_i^*}$, whereas response *I* is not.

IV. INVERSE METHOD QUALITY METRICS

Given the potential of inverse methods, it is important to develop a rigorous method for quantifying the performance and reliability of inversion schemes [8]. Although empirical studies provide the means for evaluating the quality of NDE techniques incorporating inverse methods, opportunities also exist with inverse methods to use the model calculations with quantitative measures to evaluate key estimation performance metrics without considerable experimental burden.

In estimation theory, the Cramer-Rao Lower Bound (CRLB) provides the minimum variance that can be expected for an unbiased estimator of a set of unknown parameters. In other words, the CRLB provides a way of quantifying the inversion algorithm performance. For Gaussian noise, there is a simple inverse relationship between the CRLB and the Fisher information [9]:

$$\mathrm{var}\left(\hat{\theta}_i\right) = \left[C_{\hat{\theta}}\right]_{ii} \geq \left[I^{-1}(\theta)\right]_{ii}, \tag{8}$$

where $\boldsymbol{C}$ is the covariance matrix, the Fisher information is defined as

$$I(\theta)_{ij} = -E\left[\frac{\partial^2 \ln f(Z;\theta)}{\partial\theta_i \partial\theta_j}\right]. \tag{9}$$

θ is the parameter being estimated, and Z is the measurement vector. Fisher information represents the amount of information contained in a measurement and depends on the derivatives of the likelihood function which is based on the forward model and the noise parameters. The variance in a measurement is inversely related to the amount of information contained in the measurement, so it is not a surprise that (8) shows that the variance in the measurement is greater than or equal to the inverse of the Fisher information matrix. In eddy current NDE, the measurement is often the real and imaginary component of the impedance, $Z=[R,X]$, and the Fisher information becomes a square matrix with dimensions equal to the number of parameters being estimated.

The covariance matrix can be evaluated as a performance metric for inverse methods. First, the diagonal terms of the covariance matrix (the CRLB variances) provide a metric of sensitivity of a parameter estimated using inverse methods to measurement variation. Second, the off-diagonal terms represent the interdependence between select parameters being estimated to measurement variation. The corresponding metric is the correlation coefficient given by

$$\rho_{i,j} = \frac{C_{ij}}{\sqrt{C_{ii}C_{jj}}}. \tag{10}$$

These metrics can be used with parametric studies involving frequency or other probe parameters to optimize the NDE system design. As a general design rule for inverse methods, it is desirable to minimize the sensitivity to variation (the CRLB variances) and to have the correlation coefficient between the parameters being estimated approach zero.

Another tool used in numerical linear algebra for sensitivity analysis is singular value decomposition (SVD). SVD essentially provides a measure of sensitivity of measurements to perturbations in the unknown parameters [10]. To evaluate the sensitivity of an inverse problem for a set of measurements to changes in fit parameters, SVD can be applied to the Jacobian matrix such that

$$\mathrm{J} = U \Sigma V', \tag{11}$$

where U is an orthogonal matrix that contains the left singular vectors of J, V is an orthogonal matrix that contains the right singular vectors, and Σ is a diagonal matrix that contains the singular values of J.

The condition number (CN) of the matrix is defined as the ratio of the largest and smallest singular values resulting from SVD. For inversion, CN has been used to quantify the well-posedness of the inverse problem for select parameters [11]. The ability to estimate parameters independently increases as the condition number approaches 1. It should be noted that SVD does not incorporate noise; it depends only on the noiseless relationship between the measurement output and the parameter changes.

V. OPTIMIZING LAYER ESTIMATION USING METRICS

An inversion experiment is revisited [12] for the purpose of demonstrating estimation theory metrics. In this experiment, the thickness of an AISI-304 stainless steel plate and probe liftoff were estimated. The estimation procedure is represented in (12), which is a specialization of (4) to this problem with two unknown parameters. The left side is the measured impedance, the Jacobian is simply the derivative information from the forward model, and the thickness and liftoff parameters are updated until this equation converges,

$$\begin{bmatrix} R(f,t,l) \\ X(f,t,l) \end{bmatrix} \approx \begin{bmatrix} R(f,t_0,l_0) \\ X(f,t_0,l_0) \end{bmatrix} + \begin{bmatrix} \frac{\partial R}{\partial t} & \frac{\partial R}{\partial l} \\ \frac{\partial X}{\partial t} & \frac{\partial X}{\partial l} \end{bmatrix}_{t_0,l_0} \begin{bmatrix} t-t_0 \\ l-l_0 \end{bmatrix}. \tag{12}$$

Four scenarios in particular are investigated. Impedance values were generated for combinations of lift-off values of 0.75 and 1.5 mm and a plate thickness values of 1.0 mm and 2.0 mm with Gaussian noise of 1% of the impedance value added as shown in Figure 4(a). For each of these "measurements", the NLSE algorithm is applied to estimate the thickness and liftoff simultaneously. Figure 4(b) shows the inversion results in the parameter space. Note that for high liftoff, visual inspection indicates the variance in the estimation is much greater for liftoff and likewise for the thicker plate, the variance of the estimation of thickness is greater.

The calculations required for the CRLB involve taking numerical derivatives of the impedance changes with respect to the parameter changes from the forward model. These calculations thus require far less computational expense with respect to Monte-Carlo simulation. Following (9), the Fisher information for this particular case is given by:

$$I = \begin{bmatrix} J_{11}^2 + J_{21}^2 & J_{12}J_{11} + J_{22}J_{21} \\ J_{11}J_{12} + J_{21}J_{22} & J_{12}^2 + J_{22}^2 \end{bmatrix}. \tag{13}$$

The covariance matrix is then calculated from the Fisher information by (8):

$$C = \sigma^2 I^{-1}. \tag{14}$$

The Jacobian is also decomposed into its singular values and singular vectors in the form of the right hand side of (11). The ratio of the smallest to largest singular values provides the condition number.

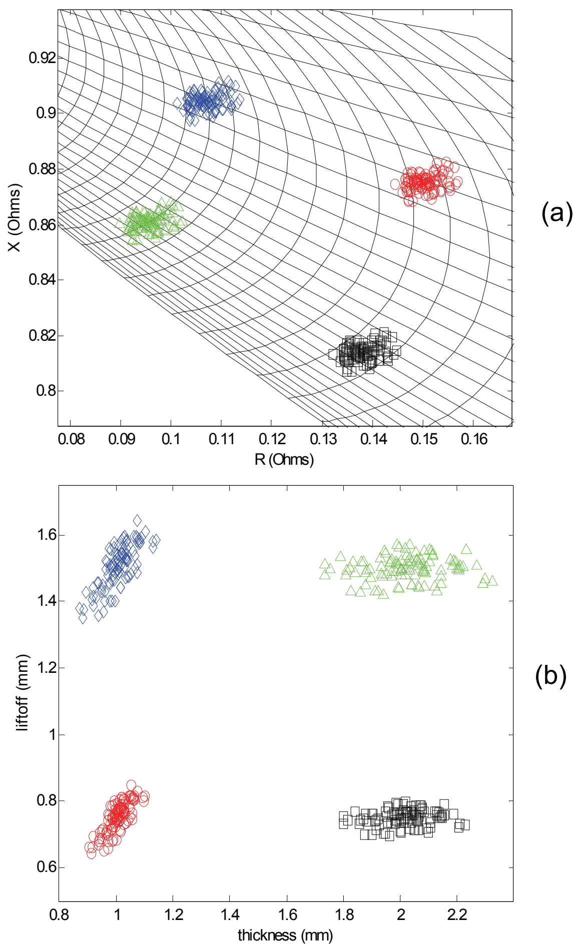

Fig. 4. (a) Distribution of source data in impedance plane and (b) corresponding estimated values in liftoff-thickness parameter space.

Figure 5 shows the CRLB of the estimation of the thickness and liftoff of a 1 mm thick plate and 1 mm lift-off for multiple frequencies. The agreement between the CRLB and the Monte-Carlo approach is quite good. This analysis demonstrates that there is an optimal frequency to achieve highest accuracy in the estimation of thickness. Estimating conductivity and thickness simultaneously is typically more ill-conditioned than estimating thickness and liftoff simultaneously. The CRLB for conductivity and thickness estimation along with the condition number and correlation number as a function of frequency are all displayed in Figure 6. The behavior of the CRLB as a function of frequency for estimating conductivity and thickness simultaneously follows a similar trend and this is expected since the impedance changes due to conductivity and thickness are similar. The condition number reaches a maximum around 95 kHz which implies that selectivity is good and the correlation is zero at this frequency which further confirms that point.

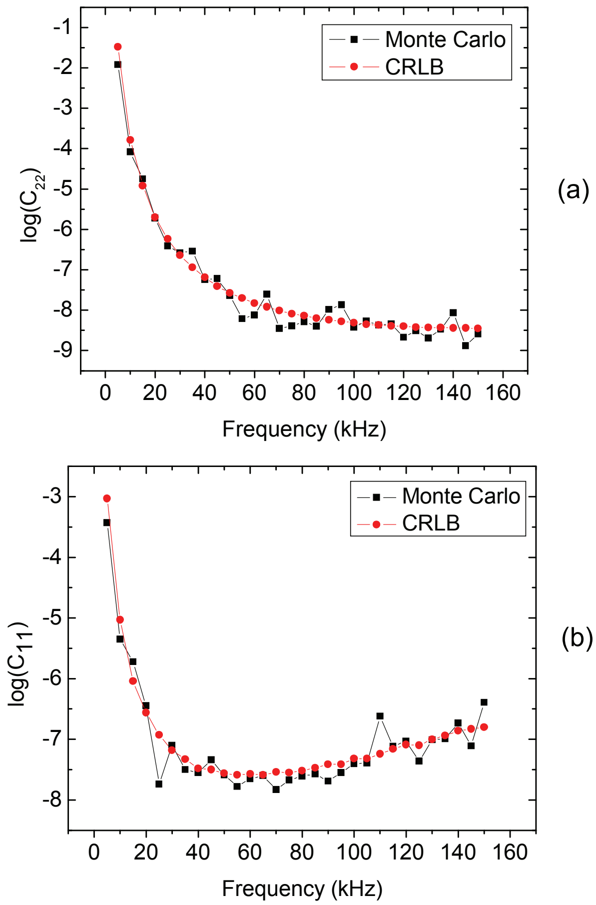

Fig. 5. Comparison of variance for varying frequency using CRLB and Monte Carlo methods for estimating (a) liftoff and (b) thickness respectively.

VI. CONCLUSION

The electromagnetics volume-integral code, VIC-3D(c), was developed to address the forward problem in eddy current NDE and provide the foundation for flaw characterization using inverse methods. The numerical method addresses a range of problems spanning industries from nuclear power to aerospace to materials characterization. The notion of model-based inversion was introduced, emphasizing the role of estimation-theoretic metrics to the practical application of inversion theory. Several metrics from estimation theory were proposed to evaluate the quality of inversion schemes. These metrics can be used in the design and validation of NDE inspection systems. Here, the CRLB has been evaluated for two parameter estimation problems. The CRLB was found to converge to the variance from Monte-Carlo simulations for Gaussian noise. The condition number derived from SVD and the correlation terms were also presented for two parameter estimation often with similar trends corresponding to parameter selectivity. It is interesting to note that if the CRLB and the condition number are used to determine the optimal frequency for inversion, they may not be in agreement. Further work will be conducted to understand the proper way to compromise between these estimation metrics. Furthermore, studies addressing more challenging estimation problems including more than two parameters and multiple frequencies will be pursued. Lastly, estimation metrics will be extended to non-Gaussian noise cases.

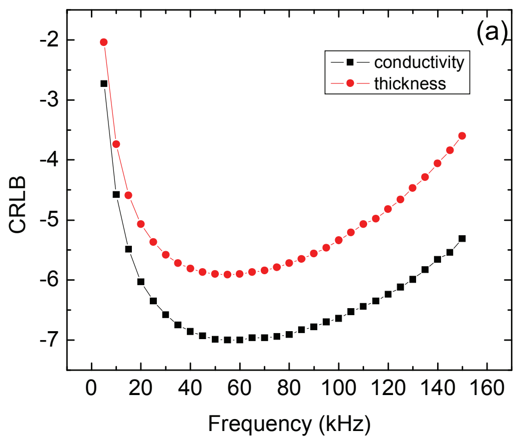

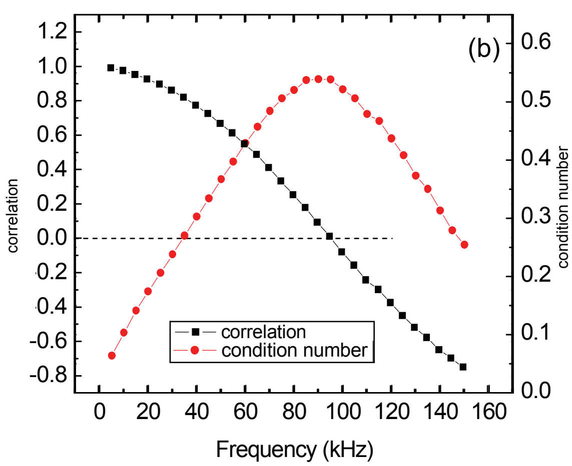

Fig. 6. Comparison of inversion metrics for varying frequency: (a) CRLB variance for thickness and conductivity estimation and (b) correlation and condition number.

ACKNOWLEDGEMENT

Partial funding was provided by the Air Force Research Laboratory – NDE Branch and Air Force Office of Scientific Research.

REFERENCES

[1] http://www.kiva.net/~sabbagh.

[2] R. K. Murphy, H. A. Sabbagh, J. C. Treece and L. W. Woo, 'A Volume-Integral Code for Electromagnetic Nondestructive Evaluation,' Conference Proceedings: 11th Annual Review of Progress in Applied Computational Electromagnetics, Monterey, CA, March 20-25, pp. 109-116, 1995.

[3] R. Murphy, H. Sabbagh, A. Chan, and E. Sabbagh, "A volume integral code for electromagnetic nondestructive evaluation", *Proceedings of the 13th Annual Review of Progress in Applied Computational Electromagnetics*, Monterey, CA, March 1997.

[4] J. S. Knopp, H. A. Sabbagh, J. C. Aldrin, R. K. Murphy, E. H. Sabbagh, J. Hoffmann and G. J. Steffes, 'Efficient Solution of Electromagnetic Scattering Problems using Spatial Decomposition Algorithms,' Conference Proceedings: Review of Progress in Quantitative Nondestructive Evaluation, Volume 25A, D. O. Thompson and D. E. Chimenti, eds., American Institute of Physics, pp. 299-306, 2006.

[5] J. R. Bowler, L. D. Sabbagh, and H. A. Sabbagh, "A Theoretical and Computational Model of Eddy-Current Probes Incorporating Volume Integral and Conjugate Gradient Methods," IEEE Trans. Magnetics, vol. 25, no. 3, pp. 2650-2664, 1989.

[6] J. S. Knopp, J. C. Aldrin, and P. Misra, "Considerations in the Validation and Application of Models for Eddy Current Inspection of Cracks Around Fastener Holes", Journal of Nondestructive Evaluation, vol. 25, no. 3, pp. 123-138, 2006.

[7] J. J. More, B. S. Garbow, and K. E. Hillstrom, *USER GUIDE FOR MINPACK-1*,

ANL-80-74, Argonne National Laboratory, August 1980.

[8] J. S. Knopp, J. C. Aldrin, H. A. Sabbagh, K. V. Jata, "Estimation Theory Metrics in Electromagnetic NDE", Electromagnetic Nondestructive Evaluation Workshop Proceedings, Soeul, Korea, June 10-12, 2008.

[9] S. M. Kay, *Fundamentals of Statistical Processing, Volume I: Estimation Theory*, Prentice Hall PTR, 1993.

[10] L. N. Trefethen and D. Bau, *Numerical Linear Algebra*, SIAM, 1997.

[11] N. J. Goldfine, "Magnetometers for Improved Materials Characterization in Aerospace Applications", *Mat. Eval*. vol. 51, pp. 396-405, 1993.

[12] O. Baltzersen, "Model-Based Inversion of Plate Thickness and Liftoff from Eddy Current Probe Coil Measurements", *Mat. Eval.*, vol. 51, pp. 72-76, 1993.

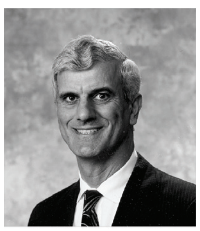

Harold A. Sabbagh received his BSEE and MSEE from Purdue University in 1958, and his PhD from Purdue in 1964. In 1980 he formed Sabbagh Associates, Inc., and did research in the application of computational electromagnetics to nondestructive evaluation (NDE). This research evolved into the commercial volume-integral code, VIC-3D. In 1998 he formed Victor Technologies, LLC, in order to continue this research and further development of VIC-3D. His past professional activities have included a stint as president of ACES.

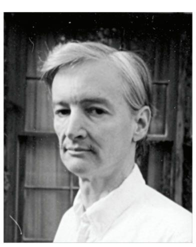

R. Kim Murphy received his B.A. in physics from Rice University in 1978 and his Ph.D. in physics from Duke University in 1984. Since 1989, he has worked as a Senior Physicist for Sabbagh Associates Inc., and Victor Technologies, LLC. Dr. Murphy has been active in formulating models and coding in VIC-3D®, performing validation numerical experiments, and solving one-dimensional and three-dimensional inverse problems.

Elias H. Sabbagh received the B.Sc. in Electrical Engineering and the B.Sc. in Economics from Purdue University in 1990 and 1991. He has worked as system administrator, software engineer, and researcher for Victor Technologies since its inception. His interests include object-oriented programming, database administration, system architecture, scientific programming, and distributed programming.

John C. Aldrin received B. Sc. and M.Sc. degrees in mechanical engineering from Purdue University, West Lafayette, IN, USA, in 1994 and 1996 and the Ph. D. degree in theoretical and applied mechanics from Northwestern University, Evanston, IL, USA in 2001. Since 2001, he has worked as the principal of Computational Tools. His research interests include computational methods: modeling, data analysis and inverse methods, in ultrasonic and eddy current nondestructive evaluation.

Jeremy Knopp received the B. Sc. degree in engineering physics and the M.Sc. degree in electrical engineering from Wright State University, Dayton, OH, USA, in 2001 and 2005, respectively. Since 2002, he has worked as a researcher at the nondestructive evaluation (NDE) branch of the Air Force Research Laboratory (AFRL). His research interests include eddy current NDE, computational electromagnetics, inverse problems, and model-assisted probability of detection. In 2009, he won the Charles J. Cleary award for basic research at AFRL.

Mark Blodgett received the B. Sc. in metallurgical engineering from Iowa State University, Ames, Iowa, USA in 1985 and M.Sc. and Ph.D. degrees in materials engineering from University of Dayton, Dayton Ohio, USA in 1992 and 2000, respectively. Since 1986, he has worked as materials research engineer in the Nondestructive Evaluation Branch at the Air Force Research Laboratory. His research interests include developing electromagnetic and multi-modal NDE approaches for materials characterization.

Adaptive Arrays

Randy L. Haupt

Applied Research Laboratory, Pennsylvania State University, State College, PA 16804-0030
rlh45@psu.edu

(Invited Paper)

Abstract– This paper presents some types of adaptive antennas and the historical development of adaptive antennas. It explains some of the common algorithms associated with digital beamforming then presents techniques for adaptation using conventional arrays with corporate feeds, including the use of reconfigurable antenna elements.

Index terms– adaptive antenna, adaptive nulling, genetic algorithms reconfigurable antenna.

I. TYPES OF ADAPTIVE ANTENNAS

An adaptive antenna is an antenna that modifies its receive or transmit characteristics in order to enhance the antenna's performance. The antenna alters its performance in order to respond to environmental or operational changes. Adaptive antennas rely upon signal processing and/or artificial intelligence algorithms to make changes or adapt. "Smart" and "Adaptive" are often used interchangeably.

Some types of adaptive antennas and how they work include:

1. Beam switching selects the beam that best receives the desired signal. Fig. **1** shows an array with a Rotman lens [1] feed. Only beams pointing in the directions of sources receive a signal. The beams can be switched as the signal environment changes.

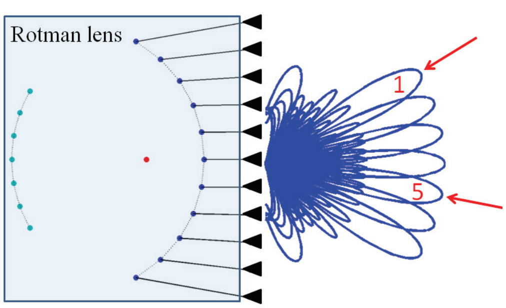

Fig. 1. Rotman lens with multiple beams.

2. Direction finding automatically detects signals and places nulls in the directions of those signals. An algorithm determines where those nulls are and hence the location of the signals. An Adcock array [2] was developed about 100 years ago. It finds the signal direction by calculating the ratio of the difference to sum patterns. Fig. **2** shows the sum and difference patterns associated with a four element Adcock array.

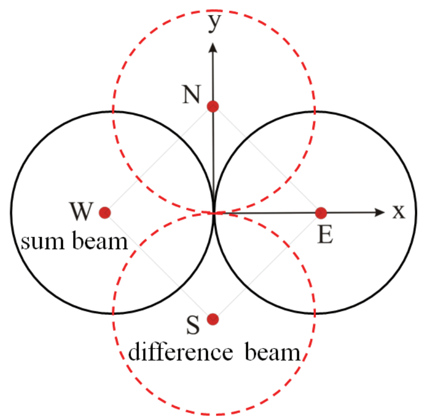

Fig. 2. Diagram of an Adcock array.

3. Retrodirective arrays retransmit a received signal in a desired direction, usually the direction of the incident signal. The retrodirective array in Fig. **3** receives a signal, takes the complex conjugate (and possibly amplifies it), then retransmits it.
4. MIMO (multiple input multiple output) has arrays at the transmit and receive ends of a communications system (Fig. **4**). The signals at each element are weighted such that the desired signal is received in a high multipath environment. The channel path is characterized between each element (h_{mn}) and placed in a channel matrix. The transmitted data is found by inverting the channel matrix

1054-4887 © 2009 ACES

and multiplying the received data. The arrays must be continuously calibrated in order to have accurate values of h_{mn}.

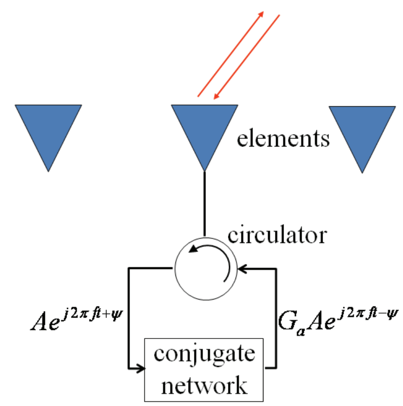

Fig. 3. Diagram of a retrodirective array.

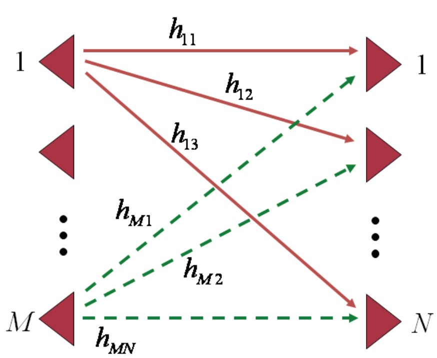

Fig. 4. MIMO concept.

5. Reconfigurable antennas alter their physical properties (usually through some type of switch) in order to change their resonant frequency or polarization. The main patch in Fig. **5** is resonant at f_0. Closing the switches increases the size of the patch and makes it resonant at a new frequency that is lower than f_0.

Fig. 5. Reconfigurable patch antenna.

6. Adaptive nulling places a null in the direction of interfering signals while maintaining sufficient gain in the direction of the desired signal to receive it. If an interference signal enters a sidelobe (dashed line in Fig. **6**), then the adaptive algorithm finds array weights that place a null in the direction of the interference (solid line in Fig. **6**).

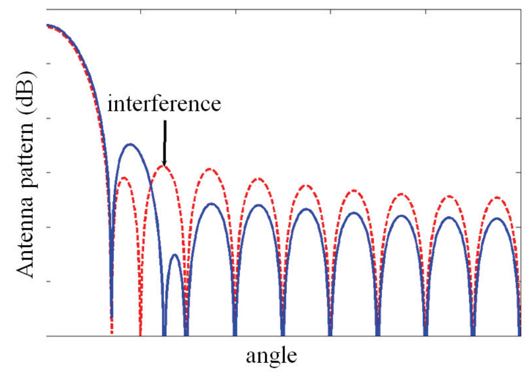

Fig. 6. Adaptive nulling places a null in the sidelobe where interference is present.

The next section describes the historical development of adaptive antennas along with a brief summary of some of the popular algorithms. The antenna architecture of choice is the digital beamforming array. An alternative is to use a more conventional corporate fed array with hardware signal weights at the elements. Some hardware and software developments for this approach are also presented. This paper is based upon the plenary talk given at the 2009 ACES Conference [1].

II. HISTORICAL DEVELOPMENT

Antenna arrays are necessary for implementation of almost all adaptive antenna ideas. Direction finding had a giant leap forward when Adcock used four monopole antennas placed on the edges of a square, and Watson-Watt [3] developed the simple trigonometric formula for finding the elevation and azimuth of a source incident on an Adcock array.

Scanning an array by changing the phase of the signals to the elements in the array was first tried by Braun [4]. Other antenna array developments centered upon developing low sidelobe amplitude tapers for linear arrays. Starting with the impractical binomial taper [5] then progressing to the more practical Dolph-

Chebychev [6] and further to the useful Taylor amplitude taper [7]. Along the way, Schelkunoff [8] outlined the use of the z-transform for general synthesis of antenna patterns.

Ideas for actual "adaptive" antennas did not originate until the 1950's. The Van Atta array reflects an incident wave in a predetermined direction with respect to the incident angle [9]. Usually, this type of retrodirective array amplifies and phase shifts the receive signal such that it retransmits in the direction of the incident field.

Beam switching is based upon the idea that multiple beams are formed by the array and the beam that best receives the desired signal is selected. Multiple beams are possible through feed networks like the Butler matrix and the Rotman lens . Both approaches have orthogonal beams that can cover a wide area. Beam switching steers a high gain beam in the direction of the desired signal but does nothing to mitigate interference entering the sidelobes.

An antenna array has many signals incident on it as shown in Fig. 7. The goal of a direction finding array is to place nulls in the directions of all signals by adjusting the weighting at each element then calculate the location of the nulls from the resultant weights. Adaptive nulling is similar, except it does not want to place a null in the direction of the desired received signal. The signal processing algorithms used for direction finding and adaptive nulling are similar and based upon knowing the amplitude and phase of the signals received at each element in the array.

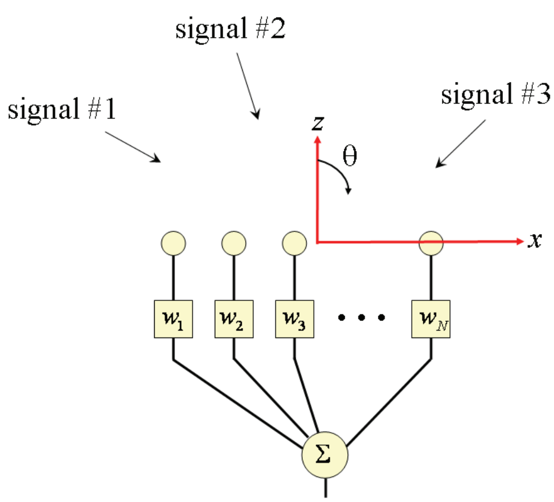

Fig. 7. Diagram of an antenna array with weights at each element.

The first adaptive nulling array was sidelobe canceller developed in the late 1950’s by Howells and Applebaum [11]. A sidelobe canceller has a high gain antenna for receiving the desired signal accompanied by one or more small low gain, broad beam antennas for sidelobe cancellation (Fig. **8**). The low gain antenna amplifies the jamming and desired signals the same, since it is omnidirectional. Appropriately weighting and subtracting the low gain antenna signal from the high gain antenna signal cancels the interference. Applying this concept to every element in an array resulted in a fully adaptive array [12].

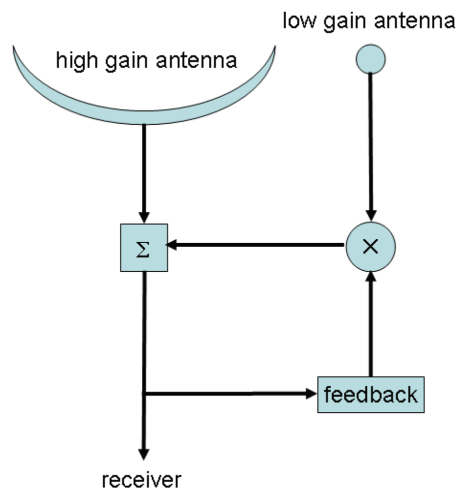

Fig. 8. Single Howells-Applebaum loop for a sidelobe canceller.

Almost all adaptive nulling algorithms are based upon the Wiener-Hopf solution [13] which gives the optimum weights at the elements in the array.

$$\mathbf{w}_{opt}(\kappa) = \mathbf{R}^{-1}(\kappa) E\left[\mathbf{d}(\kappa)\mathbf{s}(\kappa)\right] \qquad (1)$$

where

$\mathbf{R}$ = signal covariance matrix
$\mathbf{d}$ = desired signal
$\mathbf{s}$ = signal vector
κ = time step
$E[\ ]$ = expected value operator

In the 1960's the least mean square (LMS) algorithm was developed [14] and became the standard. Most adaptive algorithms started with hardware implementations, because computer resources were limited. A variety of algorithms have been developed over the past 40 years, many based upon the LMS algorithm given by

$$\mathbf{w}(\kappa+1)=\mathbf{w}(\kappa)+\mu\mathbf{s}(\kappa)\left[\mathbf{d}(\kappa)-\mathbf{w}^{\dagger}\mathbf{s}(\kappa)\right] \tag{2}$$

where μ is the step size. Other well-known algorithms, such as recursive least squares and constant modulus, use various techniques for approximating the inverse signal covariance matrix in (1).

III. DIGITAL BEAMFORMING

The signal covariance matrix is easily formed when every element in the array has a receiver. Ideally, placing an analog-to-digital (AD) converter at each element in the array feeds a digital signal to the computer where all the beamforming and beam steering is done. Adaptively switching beams as well as placing nulls in sidelobe becomes relatively easy with a digital beamformer. Unfortunately, calibrating the hardware and developing the hardware necessary to do the processing is difficult and expensive. AD converters are limited to frequencies in the low GHz range. The next two sections describe some DF and adaptive nulling algorithms that use a digital beamformer.

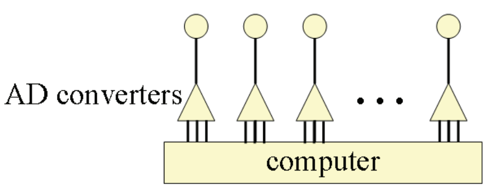

Fig. 9. Digital beamforming array.

IV. DIRECTION FINDING

Direction finding is accomplished by either pointing the main beam or pointing nulls at N_s sources. The relative array output power as a function of angle can be found by

$$P(\theta)=A^{\dagger}(\theta)R_T A(\theta) \tag{3}$$

where the uniform array steering vector is given by

$$A(\theta)=e^{jkx_n\cos\theta}, \theta_{\min}\le\theta\le\theta_{\max}. \tag{4}$$

A plot of the output power vs. angle is known as a periodogram. This spectrum is basically the output from steering the main beam between $\theta_{\min}$ and $\theta_{\max}$. Resolving closely spaced signals is limited by the array beamwidth.

The signal-to-interference ratio at the array output is maximized by the following array weights:

$$w=\frac{R_T^{-1}A}{A^{\dagger}R_T^{-1}A} \tag{5}$$

The resulting Capon spectrum [15] is given by

$$P(\theta)=\frac{1}{A^{\dagger}(\theta)R_T^{-1}A(\theta)}. \tag{6}$$

The (MUSIC) [16] *MU*ltiple *SI*gnal *C*lassification spectrum is given by

$$P(\theta)=\frac{A^{\dagger}(\theta)A(\theta)}{A^{\dagger}(\theta)V_{\lambda}V_{\lambda}^{\dagger}A(\theta)} \tag{7}$$

where V_{λ} is a matrix whose columns contain the eigenvectors of the noise subspace. The eigenvectors of the noise subspace correspond to the $N-N_s$ smallest eigenvalues of the correlation matrix. The denominator of (7) can be written as

$$A^{\dagger}(\theta)V_{\lambda}V_{\lambda}^{\dagger}A(\theta)=\sum_{n=M+1}^{M-1}c_n z^n \tag{8}$$

where

$z=e^{jknd\sin\theta}$

$c_n=\sum_{r-c=n}V_{\lambda}V_{\lambda}^{\dagger}$ =sum of nth diagonal of $V_{\lambda}V_{\lambda}^{\dagger}$

Solving for the angle of the phase of the roots of the polynomial in (8) produces

$$\theta_m=\sin^{-1}\left(\frac{\arg(z_m)}{kd}\right). \tag{9}$$

The maximum entropy method (MEM) spectrum is given by [18]

$$P(\theta)=\frac{1}{A^{\dagger}(\theta)R_T^{-1}[:,n]R_T^{\dagger-1}[:,n]A(\theta)} \tag{10}$$

where n is the n$^{\text{th}}$ column of the inverse correlation matrix.

To demonstrate the capabilities of these algorithms, consider an 8 element array of isotropic point sources spaced $\lambda/2$ apart and lying along the x-axis. Sources are incident on the array at -60^o, 0^o, and 10^o with relative powers of 0, 4, and 12 dB, respectively. The periodogram has broad peaks and cannot distinguish the sources at 0^o and 10^o. Capon, MUSIC, and MEM spectra have very sharp spikes in the directions of the sources and can distinguish closely spaced sources.

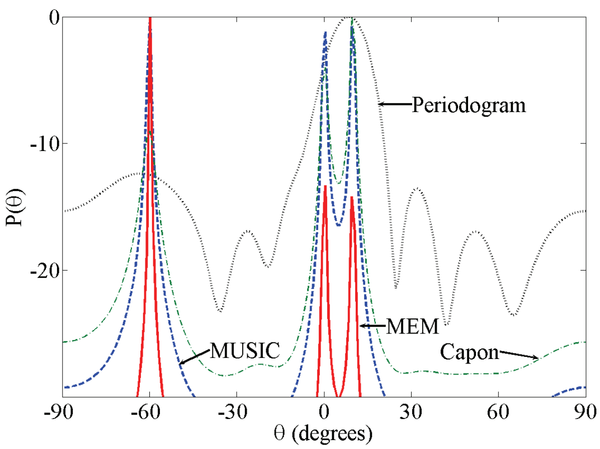

Fig. 10. Plot of the direction finding spectra for an 8 element array.

V. ADAPTIVE NULLING

In practice, the correlation matrix is estimated by a sample matrix, $\hat{R}_T$. This estimate can be formed using K samples of the received element signals

$$R_T = \frac{1}{K}\sum_{\kappa=1}^{K} x(\kappa)x^{\dagger}(\kappa) \tag{11}$$

and the correlation vector is

$$\mathbf{q}(\kappa) = \frac{1}{K}\sum_{\kappa=1}^{K} d^{\dagger}(\kappa)\mathbf{s}(\kappa). \tag{12}$$

This approach is known as sample matrix inversion (SMI) [18]. At the kth time sample, the SMI weights are given by

$$w(\kappa) = R_T^{-1}(\kappa)q(\kappa). \tag{13}$$

The recursive least squares (RLS) algorithm [19] recursively updates the correlation matrix such that more recent time samples receive a higher weighting than past samples. A straight-forward implementation of the algorithm is written as

$$R_T(\kappa) = x(\kappa)x^{\dagger}(\kappa) + \alpha R_T(\kappa-1) \tag{14}$$

and the correlation vector is

$$\mathbf{q}(\kappa) = d^{\dagger}(\kappa)\mathbf{s}(\kappa) + \alpha q(\kappa-1) \tag{15}$$

where the forgetting factor, α, is limited by $0 \le \alpha \le 1$.

To demonstrate the capabilities of these algorithms, consider an 8 element array of isotropic point sources spaced $\lambda/2$ apart and lying along the x-axis. The desired source is incident on the main beam at 0^o, and the undesired sources are at -60^o and 10^o. Both algorithms nicely place nulls in the desired directions while costing only a small amount of main beam gain.

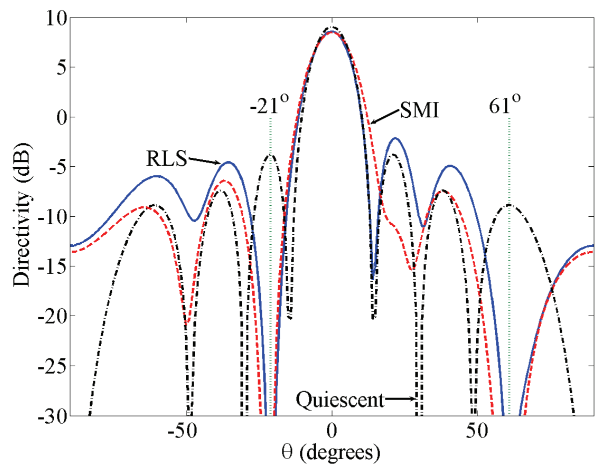

Fig. 11. Adapted patterns using RLS and SMI.

VI. ADAPTIVE NULLING VIA POWER MINIMIZATION

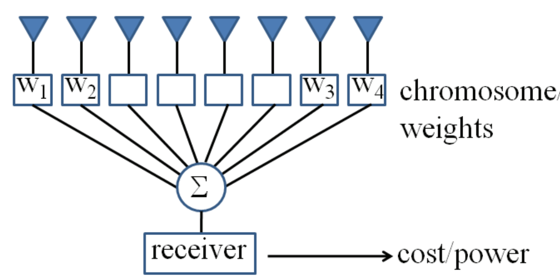

Fig. 12. Diagram of an adaptive array that minimized total output power.

Adaptive nulling described in the previous section has a receiver or AD converter at every element in the array. This approach is a very expensive proposition and requires a method that maintains calibration of all the channels. A much simpler approach makes use of conventional phased array architecture and varies the phase shifters and/or attenuators to minimize the total output power of the array (Fig. **12**). Phase only adaptive nulling has the least amount of hardware requirements of any adaptive nulling approach [20]. A genetic algorithm (GA) [21] has been useful in these types of applications. [22].

If only a few of the elements in the array are adaptive, then nulls can be placed in the sidelobes with little perturbation to the main beam [23]. The weight settings are placed in a vector called a chromosome, and each chromosome has an associated power measurement. A population is a matrix with several chromosomes as rows (Figure 13). The population matrix undergoes natural selection where chromosomes with high output power are discarded. The remaining chromosomes mate and mutate to form new members for the population that replace the members discarded during the natural selection process. The GA iterates until a satisfactory weight setting is found (Fig. **14**). This adaptive nulling approach has been experimentally validated using digital phase shifters and attenuators as the weights [24].

$$\begin{array}{c} w_1 \quad w_2 \quad w_3 \quad w_4 \\ \begin{bmatrix} .12 & .54 & .62 & .98 \\ .44 & .23 & .71 & .38 \\ & \vdots & & \\ .85 & .15 & .22 & .59 \end{bmatrix} \\ \text{population} \end{array} \Rightarrow \begin{array}{c} \text{dBm} \\ \begin{bmatrix} -50 \\ -59 \\ \vdots \\ -63 \end{bmatrix} \\ \text{cost} \end{array}$$

Figure 13. The weights are placed in a population matrix and the cost is the power received.

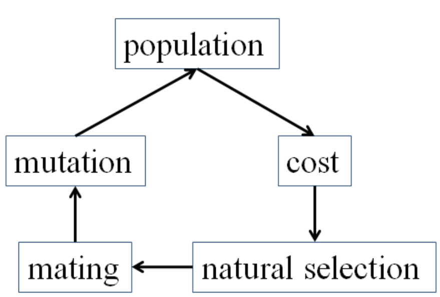

Fig. 14. Flow chart of GA for adaptive nulling.

The 8 element array of $\lambda/2$ dipoles spaced $\lambda/2$ apart in Fig. **15** is modeled using the method of moments [25]. A 0 dB desired source is incident at $\phi = 90^o$, and a 15 dB interference signal is incident at $\phi = 68^o$. After 20 generations, the GA having a population of 8 and 15% mutation rate finds the adapted pattern in Fig. **16**. The algorithm placed a 20 dB null in the sidelobe while only losing 1 dB from the main beam.

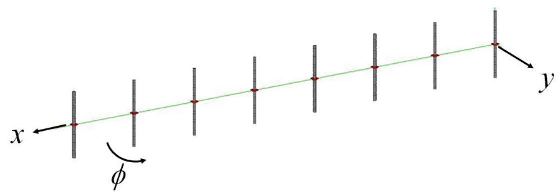

Fig. 15. Adaptive dipole array.

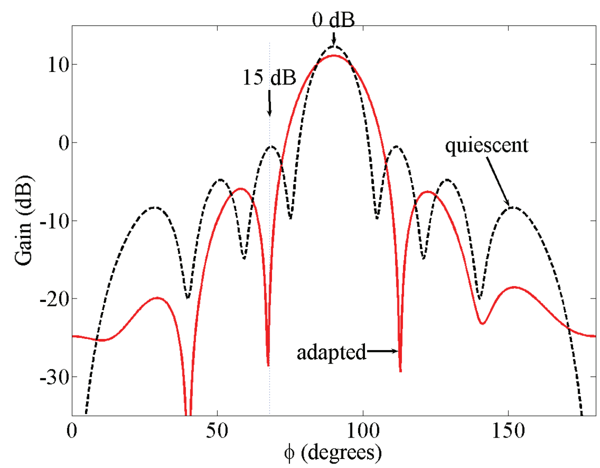

Fig. 16. Adapted and quiescent patterns.

VII. ADAPTIVE ARRAYS WITH RECONFIGURABLE ELEMENTS

Reconfigurable elements come in many forms. One type changes the conductivity of silicon on part of an antenna in order to control its radiation properties [26][27]. An array can be made adaptive using reconfigurable elements (rather than attenuators and phase shifters) and the power minimization approach [28]. Fig. **17** is a model of a patch antenna with a thin strip of silicon between the main patch and a thin metal extension. The conductivity of the silicon is dependent upon the infrared illumination provided from an infrared source at the bottom. Changing the conductivity of that small strip of silicon alters the radiation and impedance of the patch. A graph of the amplitude of the return loss is shown in Fig. **18** for conductivities between 0 and 1000 S/m. The patch is resonant at 2 GHz when the illumination is off.

Increasing conductivity to 1000 S/m causes the patch to resonate at 1.78 GHz. Changing the conductivity from 0 to 1000 S/m, causes the s_{11} at 2 GHz to increase from 0 to 0.9. As a result, the photoconductive silicon acts as an amplitude control for that element. Placing these elements together in an array, as shown in Fig. **19** permits control of the array pattern by changing the illumination of the silicon. The spacing between elements is 75 mm or 0.5λ .

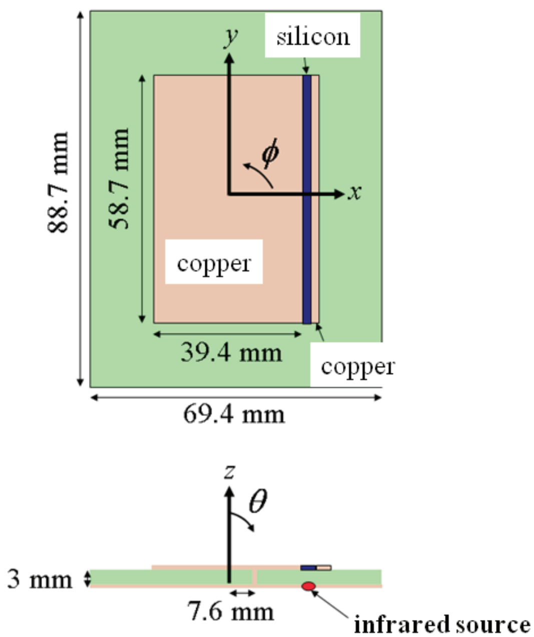

Fig. 17. Reconfigurable patch.

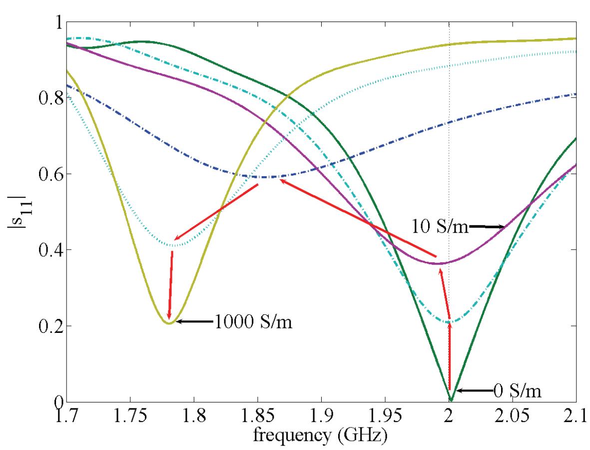

Fig. 18. Reflection coefficient as a function of frequency for several different silicon conductivities.

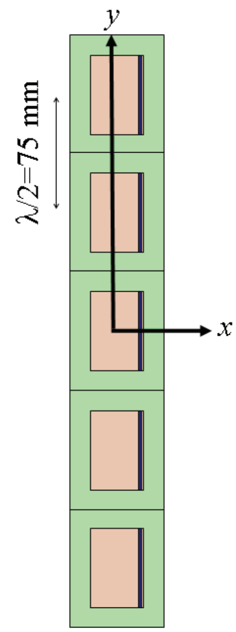

Fig. 19. Linear array of reconfigurable elements.

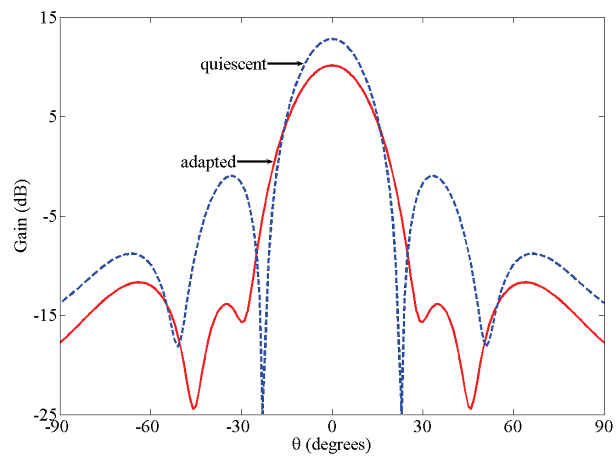

Fig. 20. Quiescent and adapted patterns for reconfigurable array.

If the silicon insets all have a conductivity of zero (illumination off), then the array is uniform with a far field pattern shown in Fig. **20**. The calculations for this example used CST Microwave Studio [29]. This quiescent pattern has a gain of 12.8 dB and a relative peak sidelobe level of 13.8 dB. Illuminating the silicon at each element with a different optical intensity produces a conductivity, hence amplitude, taper across the array. An equal sidelobes array pattern results when the conductivity has values of [16 5 0 5 16] S/m. The corresponding antenna pattern is shown in Fig. **20**. It has a gain of 10.4 dB and a peak relative sidelobe level 23.6 dB below the main beam. Thus, the array can switch from a higher gain, high sidelobe pattern to a lower gain, low sidelobe pattern whenever there is interference entering the sidelobes.

VIII. CONCLUSIONS

Adaptive arrays come in many forms. Many signal processing algorithms exist to automatically place nulls in the sidelobes while keeping the main beam intact. They all rely upon the use of an array with a receiver or AD converter at each element. The costs and calibration requirements limit the use of these arrays. Another approach that minimizes the total output power using a GA limits the main beam reduction by limiting the number of adaptive elements in the array. This type of algorithm works on commonly existing array architectures. Using reconfigurable elements rather than phase shifters and attenuators is a novel approach that needs further testing in an adaptive nulling situation.

ACKNOWLEDGMENT

Part of this work was sponsored by Army CECOM under contract N00024-02-D-6604 DO-295.

REFERENCES

[1] R. L. Haupt, "Adaptive antennas," ACES Conference, Monterey, CA, pp. 660-664, Mar 2009.

[2] F. Adcock, "Improvement in Means for Determining the Direction of a Distant Source of Electromagnetic Radiation," British Patent 1304901919, 1917.

[3] E. J. Baghdady, "New Developments in Direction-of-Arrival Measurement Based on Adcock Antenna Clusters," Proc. of the IEEE Aerospace and Electronics Conference, Dayton, OH, May 22-26, pp. 1873 – 1879, 1989.

[4] F. Braun, "Directed wireless telegraphy," The Electrician, vol. 57, pp. 222, May 1925.

[5] J. S. Stone, US Patent 1,643,323, 27 Sep 1927.

[6] C. L. Dolph, "A current distribution for broadside arrays which optimizes the relationship between beam width and sidel-lobe level," Proceedings of the IRE, vol. 34, no. 6, pp. 335- 348, Jun 1946.

[7] T. T. Taylor, "Design of line source antennas for narrow beamwidth and low side lobes," IRE AP Trans., vol. 3, pp. 16-28, 1955.

[8] S. A. Schelkunoff, "A mathematical theory of linear arrays," Bell System Technical Journal, vol. 22, pp. 80-107, 1943.

[9] L. C. Van Atta, "Electromagnetic Reflection," U.S. Patent 2908002, October 6, 1959.

[10] W. Rotman and R. F. Turner, "Wide angle microwave lens for line source applications", *IEEE AP-S Trans.*, vol. 11, pp. 464-472, 1963.

[11] P.W. Howells, "Explorations in fixed and adaptive resolution at GE and SURC," IEEE AP-S Trans., vol. 24, no. 5, pp. 575-584, Sep 1976.

[12] S. P. Applebaum, "Adaptive arrays," IEEE AP-S Trans., vol. 24, no. 5, pp. 585-598, Sep 1976.

[13] R.T. Compton, Jr., *Adaptive Antennas Concepts and Performance*, Englewood Cliffs, NJ: Prentice Hall, 1988.

[14] B. Widrow, P.E. Mantey, L.J. Griffiths, and B.B. Goode, "Adaptive antenna systems," Proceedings of the IEEE, vol. 55, no. 12, pp. 21-43, Dec 1967.

[15] J. Capon, "High-resolution frequency-wavenumber spectrum analysis," *Proceedings of the IEEE,* vol. 57, no. 8, pp. 1408-1418, 1969.

[16] R. Schmidt, "Multiple emitter location and signal parameter estimation," *Antennas and Propagation, IEEE Transactions on,* vol. 34, no. 3, pp. 276-280, 1986.

[17] J. P. Burg, "The relationship between maximum entropy spectra and maximum likelihood spectra," *Geophysics,* vol. 37, no. 2, pp. 375-376, 1972.

[18] I. Gupta, "SMI adaptive antenna arrays for weak interfering signals," *Antennas and Propagation, IEEE Transactions on,* vol. 34, no. 10, pp. 1237-1242, 1986.

[19] F. B. Gross, *Smart antennas for wireless communications : with MATLAB*, New York: McGraw-Hill, 2005.

[20] C. A. Baird and G. G. Rassweiler, "Adaptive nulling using digitally controlled phase-shifters," IEEE AP-S Trans., vol. 24, no. 5, pp. 638-649, Sep 1976.

[21] R. L. Haupt and S.E. Haupt, *Practical Genetic Algorithms*, 2nd edition, New York: John Wiley & Sons, 2004.
[22] R. L. Haupt, "Phase-only adaptive nulling with a genetic algorithm," *IEEE AP-S Trans.*, vol. 45, pp. 1009-1015, Jun 1997.
[23] D. Morgan, "Partially adaptive array techniques," *Antennas and Propagation, IEEE Transactions on,* vol. 26, no. 6, pp. 823-833, 1978.
[24] R. L. Haupt and H. L. Southall, "Experimental adaptive nulling with a genetic algorithm," Microwave Journal, vol. 42, no. 1, pp. 78-89, Jan 99.
[25] FEKO Suite 5.4, EM Software and Systems (www.feko.info), 2008.
[26] R. L. Haupt, "Reconfigurable patch with switchable conductive edges," Microwave and Optical Technology Letters, vol. 51, no. 7, pp. 1757-1760, Jul 2009.
[27] J. R. Flemish, H. W. Kwan, R. L. Haupt and M. Lanagan, "A new silicon-based photoconductive microwave switch," vol. 51, no. 1, Microwave and Optical Technology Letters, Jan 2009.
[28] R. L. Haupt, "An adaptive rectangular microstrip patch antenna array element using photonic controls," IEEE Aerospace Conference, Big Sky, MT, pp. 1-6, Mar 2008.
[29] CST Microwave Studio, Version 2008.06, May 26, 2008.

Randy L. Haupt is an IEEE and an ACES Fellow and is Dept. Head of Computational Electromagnetics and Senior Scientist at the Penn State Applied Research Lab. He has a Ph.D. in Electrical Engineering from the University of Michigan, MS in Electrical Engineering from Northeastern University, MS in Engineering Management from Western New England College, and BS in Electrical Engineering from the USAF Academy. He was Professor and Department Head of Electrical and Computer Engineering at Utah State University from 1999-2003. He was a Professor of Electrical Engineering at the USAF Academy and Professor and Chair of Electrical Engineering at the University of Nevada Reno. In 1997, he retired as a Lt. Col. in the USAF. Dr. Haupt was a project engineer for the OTH-B radar and a research antenna engineer for Rome Air Development Center.

Study of Exact and High-Frequency Code Solvers for Applications to a Conformal Dipole Array

S. D. Walker and D. Chatterjee

Department of Computer Science and Electrical Engineering
University of Missouri-Kansas City (UMKC), Kansas City, MO 64110, USA
chatd@umkc.edu

(Invited Paper)

Abstract **–** The embedded element pattern of a conformal dipole array of seven elements is calculated using integral equation algorithms in exact solvers such as FEKO and WIPL-D, with the central element excited and other elements match-terminated in a 50Ω load. A technique is developed that uses the FEKO subdomain basis function current weights to derive the equivalent current weight for a single entire domain basis function for use in the high-frequency code NECBSC. This process includes effects of mutual coupling in the NECBSC calculations. The results for the embedded element pattern for cylinders with $ka = 10, 20, 30, 40, 60$ and 80, computed via FEKO, WIPL-D, and NECBSC, reveal discrepancies in the deep shadow (or creeping wave) regions. Parametric simulation studies for dipole currents, by varying the cylinder radius or radial distance of the array arc from the cylinder curved surface, are also included.

I. Introduction

Conformal arrays, flush -mounted on electrically large convex bodies, often cannot be analyzed by *exact* numerical techniques due to increased demands for computational resources [1]. The integral equation (EFIE) methods [2], [3] require a discretization size of $\lambda/10$ for such electrically large structures, where λ is the wavelength. This presents a practical difficulty in using exact solvers such as WIPL-D [4] and FEKO [5] that solve the radiation/scattering problem by discretization of the EFIE. In contrast, the *Uniform Theory of Diffraction* (UTD) [3], [6] is particularly suitable for electrically large problems because it does not require structural discretization at any frequency. The subject of this investigation is the calculation of element patterns of a single ring, sectoral dipole array in presence of an electrically large PEC cylinder shown in Fig. 1.

The UTD formulations in the NECBSC code require antennas to be 0.25λ off the cylinder curved surface [7]. With reference to Fig. 1, a cylindrical dipole array was studied in [8] which serves as a motivation for the work reported here. The high-frequency radiation from such an array in the shadow ($\phi \rightarrow 180°$ in Fig. 1) regions can be described in terms of "*creeping waves*". Past investigations on creeping wave radiation have shown discrepancies between exact and UTD results [9]-[11] for isolated single sources located off the cylinder curved surface. However, these studies did not consider conformal array [8] radiation, and hence are distinct from the present investigation. A methodology to accomplish this comparative analysis for conformal arrays, by combining appropriate solutions from both exact [5] and high-frequency code [7] solvers, is the purpose of this investigation.

The results in this paper are restricted to a 7-element dipole array because such a model retains all the canonical features without unnecessarily complicating the problem. Validation studies of the exact code solvers available in [12]-[14] lent confidence in their application to conformal array problems. Finally, this paper is an extension of but is mostly distinct from [15].

The conformal array problem and its NECBSC solution is described in the next section. This is followed by extensive results and their discussion. The conclusions are summarized with a list of relevant references.

II. Problem Description and Solution Methodology

For an array with large number of elements the total array element pattern in the radiation zone is generically written as:

$$\mathrm{F}(r,\theta,\phi) = \frac{e^{-jkr}}{r} g_{elm}(\theta,\phi) \sum_{n=1}^{\mathrm{N}} \mathrm{C}_n e^{j\psi_n} \quad (1)$$

The summation in (1) indicates the (complex) array factor of N elements with complex (current or voltage) excitations C_n; ψ_n is the phase at n^{th} element. The $g_{elm}(\theta,\phi)$ is the embedded element pattern of a single element while all other elements are terminated in a matched load. The $g_{elm}(\theta,\phi)$ varies across a finite array because the elements close to the array edges "see" a different environment than the ones at the center. It is implicit that $g_{elm}(\theta,\phi)$ contains the effects of the mutual coupling from nearby elements. The exact solvers in [4], [5] can directly calculate the array mutual coupling unlike [7]. Thus, a method by which array mutual coupling can be included in NECBSC output is the main contribution of this paper.

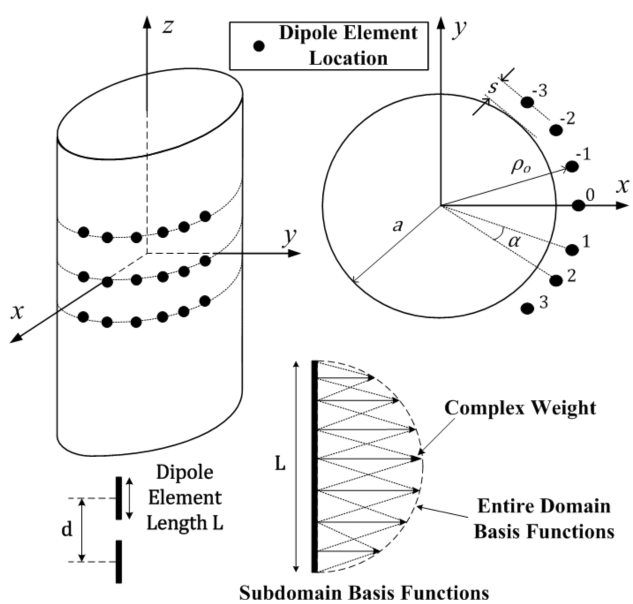

Fig. 1. Geometry of a conformal cylindrical dipole array of $\lambda/2$ dipole; the cylinder radius is ka and the dipoles have an inter-arc spacing of b/λ, and are off the PEC curved surface of the cylinder by a distance s/λ. In the present problem, only a single arc-ring, 7-element, azimuthally located dipole array is considered. Here $\mathrm{b} = \alpha\rho_o$ with $\rho_o = a + s$. The numbering scheme for the 7-element array is also shown.

To that end, the analysis developed gainfully utilizes FEKO output currents which include mutual coupling effects *in-situ*. The FEKO uses overlapping triangular basis function on the individual dipole elements. If the current on the dipole element is $i(z)$, it can be expressed in the two forms as,

$$i(z) = \begin{cases} \displaystyle\sum_{p=1}^{\mathrm{P}} \Psi_\Delta(z)\mathrm{I}_\Delta^p, & \text{for FEKO} \\ \mathrm{I_o}\cos\left(\dfrac{\pi z}{\mathrm{L}}\right), & \text{for NECBSC} \end{cases} \quad (2)$$

The dipole of length L is discretized into P segments in FEKO and over each segment the overlapping triangular basis functions with weights I_Δ^p are used. In the NECBSC a purely entire domain basis function can be used [7]. For the NECBSC, $-\mathrm{L}/2 \leq z \leq \mathrm{L}/2$; in the FEKO code, the triangular basis function in (2) is given as:

$$\Psi_\Delta(z) = \begin{cases} \dfrac{z - z_{p-1}}{z_p - z_{p-1}}, & \text{for } z_{p-1} \leq z \leq z_p \\ \dfrac{z_{p+1} - z}{z_{p+1} - z_p}, & \text{for } z_p \leq z \leq z_{p+1} \end{cases} \quad (3)$$

The I_Δ^p are the *complex* current weights associated with the triangular basis functions in FEKO. These can be directly obtained in the output file of FEKO through use of appropriate input commands to store these segment currents, when developing the input geometry file. Our objective is to express $\mathrm{I_o}$ in terms of the FEKO segment currents I_Δ^p. From (2) and (3) it readily follows that

$$\mathrm{I_o} \int_{-\mathrm{L}/2}^{\mathrm{L}/2} \cos^2\left(\frac{\pi z}{\mathrm{L}}\right) dz = \sum_{p=1}^{\mathrm{P}} \mathrm{I}_\Delta^p \int_{-\mathrm{L}/2}^{\mathrm{L}/2} \Psi_\Delta(z)\cos\left(\frac{\pi z}{\mathrm{L}}\right) dz \quad (4)$$

Further reduction of (4) then produces the desired result,

$$\mathrm{I_o} = \frac{4}{\pi}\left[\frac{\sin^2\left(\frac{\pi\Delta\mathrm{L}}{4\mathrm{L}}\right)}{\frac{\pi\Delta\mathrm{L}}{4\mathrm{L}}}\right] \sum_{p=1}^{\mathrm{P}} \mathrm{I}_\Delta^p \sin\left(\frac{\pi z_p}{\mathrm{L}}\right) \quad (5)$$

In (5) $\Delta \mathrm{L} = z_{p+1} - z_{p-1}$. The node at z_p falls midway between the $(p+1)^{th}$ and $(p-1)^{th}$ nodes. The complex current weight I_Δ^p is associated with the location of the p^{th} node. It is reiterated that I_o in (5) is a complex current weight. To summarize, (5) allows a very convenient way of incorporating the mutual coupling information in the NECBSC code from a-priori information of the same from the FEKO code.

III. Results and Discussion

The results are shown in Figs. 2 to 15. The numerical data are shown in the figure captions therein. For the FEKO calculations, dipoles of length $\mathrm{L} = \lambda/2$ were discretized into $\mathrm{P} = 51$ to 101 segments, which yields the node location $z_p = p(\mathrm{L}/\mathrm{P})$, with $p = 1, 2, 3, \cdots, \mathrm{P}$. For either 51 or 101 segments on the dipole, the corresponding equivalent complex current weight I_o from (5) was found not to be significantly different. The results are discussed briefly below. In Figs. 2 and 3 magnitude and phase comparisons between I_o obtained via (5), and the I_Δ^p on the central segment of the excited (#0) dipole is shown for increasing s/λ. The comparison reveals the two features:

(a) I_Δ^p on the central segment of the dipole, as available from the FEKO output file, is a very good approximation to I_o obtained via (5). This is expected because I_o is the maxima at the center of the support region of the cosinusoidal entire domain basis function.

(b) The decaying oscillatory nature of the magnitude and phase with s/λ. This is due to the standing wave interactions between the dipole and the cylinder curved surface. As the dipole array moves away from the cylinder curved surface, the degree of this interaction decreases and is evidenced by the decrease in the peaks and nulls in the variations.

Figures 4 and 5 show the effects of the scattering structure, which is the electrical radius ka of the cylinder, on the current I_o using (5). The I_o data in these figures were computed for each of the individual seven elements in the dipole array from the corresponding FEKO output file.

The dominant effect of the cylinder radius ka on the current magnitudes is noticeable on the central (excited) element as in Fig. 4. The current magnitude I_o on the farthest elements (#2, -2, 3 & -3) in Fig. 4 is apparently insensitive to increase in ka. However the same figure shows that the noticeable influence of the cylinder curvature on the excited (or central #0) element for $ka = 10 \rightarrow 50$. Beyond $ka \geq 50$, the curvature effects are imperceptible.

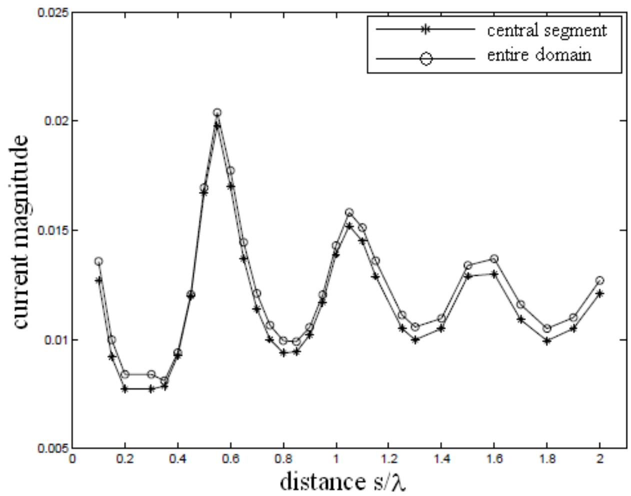

Fig. 2. Current amplitude variation on the excited dipole (#0) element located at the array center; $ka = 30$, $\mathrm{b}/\lambda = 0.5$, $\mathrm{L}/\lambda = 0.5$ and the cylinder height is $\mathrm{H}/\lambda = 10$. All other dipoles are terminated in a 50Ω load. The entire domain result refers to (5).

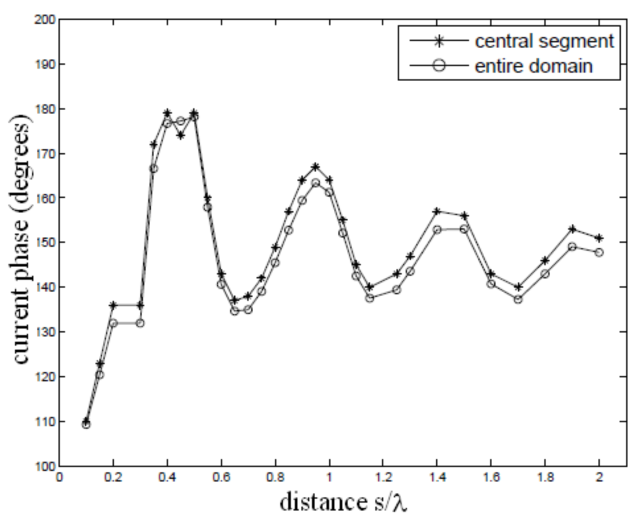

Fig. 3. Current phase variation on the excited dipole (#0) element located at the array center; $ka = 30$, $\mathrm{b}/\lambda = 0.5$, $\mathrm{L}/\lambda = 0.5$ and the cylinder height is $\mathrm{H}/\lambda = 10$. All other dipoles are terminated in a 50Ω load. The entire domain result refers to (5).

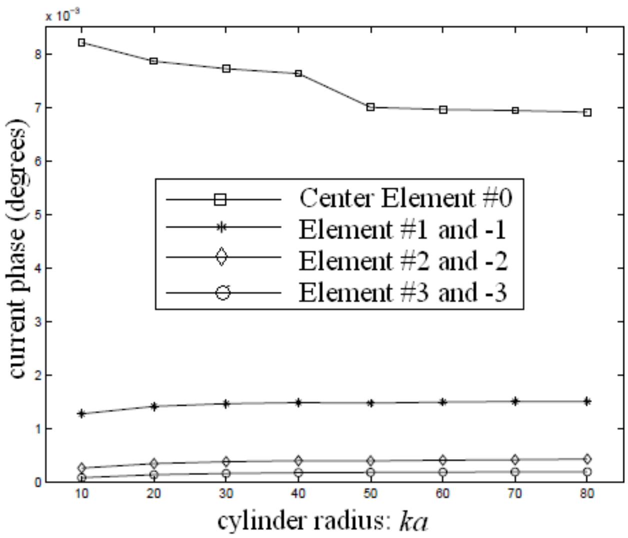

Fig. 4. Current magnitude variation on all the dipole elements; $b/\lambda = 0.5$, $L/\lambda = 0.5$, $s/\lambda = 0.25$ and the cylinder height is $H/\lambda = 10$. The central dipole element (#0) is excited, with all others terminated in a 50Ω load. The entire domain result refers to (5).

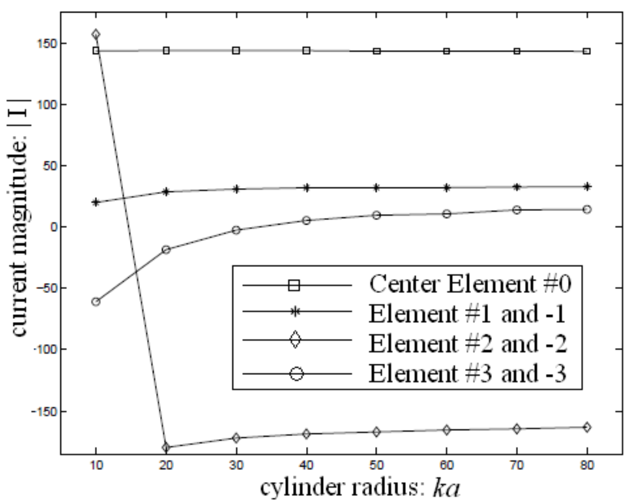

Fig. 5. Current phase variation on all the dipole elements; $b/\lambda = 0.5$, $L/\lambda = 0.5$, $s/\lambda = 0.25$ and the cylinder height is $H/\lambda = 10$. The central dipole element (#0) is excited, with all others terminated in a 50Ω load. The entire domain result refers to (5).

A similar conclusion can be arrived by examining the sensitivity of the phase of the currents on the individual dipole elements in Fig. 5. (The single point at $ka = 10$ for element #2 and -2, appears to be an exception, and is apparently intractable at this stage.) While there is a marked difference in the levels, the increase of cylinder radius apparently causes little change in the element phases.

The results in Figs. 4 and 5 present some interesting and useful insights into computation involving electrically large conformal arrays. The information gleaned suggests that because the current I_o is relatively insensitive to increase in cylinder radius ka, it may be reasonable to obtain these currents for an electrically small cylinder using exact code solvers (FEKO or WIPL-D) and then subsequently use them to calculate scattering by an electrically large cylinder using high-frequency solvers like the NECBSC code. This process would result in substantial savings in computational resources. Based on the results presented here, it appears that the embedded element pattern, $g_{elm}(\theta, \phi)$, would not be substantially different obtained by this proposed approach.

Figures 6 to 15 show the azimuth ($\theta = 90°$) plane embedded element pattern for the central dipole (#0) with others terminated in a matched load, and, for a wide range of cylinder radius ($ka = 10$ to 80). All other data is included in the figures and is omitted here. For the NECBSC results, the excitation currents for every individual element in the dipole array were computed via equation (5). This implies that the NECBSC results include mutual coupling effects when the center dipole is excited.

The results in Figs. 6 to 9 generally exhibit similar nature. For $ka = 10$ and 20 the differences between FEKO, WIPL-D and NECBSC in the shadow (creeping wave) region is not significant. However the same is not generally true for the results in Figs. 10 to 12.

The results in Figs. 8 and 9 are explained in some detail here. The NECBSC result in Fig. 9 was obtained by using the FEKO current weight on the central segment of each dipole element in the array. In contrast in Fig. 8, the currents for NECBSC data was obtained via (5). The comparison of the NECBSC embedded element pattern, $g_{elm}(\theta, \phi)$, suggests that there is only minimal variation in the embedded element pattern and it is noticeable in the deep shadow regions only.

The comparative analysis of the embedded element patterns for electrically large cylinders is shown in Figs. 10 to12. The results indicate good agreement in the 'lit' region – where the geometric optics ray fields exist – for cylinders of electrical radius $ka = 40$ (Fig. 10). All the three cases show marked disagreements in the creeping wave or deep shadow regions. Interestingly, in Figs. 11 ($ka = 60$) and 12 ($ka = 80$), the differences in the results from the exact and high-frequency code solvers are also noticeable in the lit regions.

The effects of varying s/λ on the embedded element pattern is shown in Figs. 13 to 15. Including the result in Fig. 8, imparts a broader overview. The results indicate that the increase of s/λ is somewhat unpredictable. For example, the result in Fig. 13 shows the worst agreement between the three codes. However this trend is not predictive as the distance s/λ is increased to 0.75 (Fig. 14) and 1.0 (Fig. 15). In the latter two figures the level of disagreement is less pronounced in the deep-shadow or creeping wave regions as compared to the corresponding one in Fig. 13. Note that in Fig. 8 the disagreement is less compared to Fig. 13.

The results indicate that NECBSC scattering formulations in the creeping wave region of PEC convex surfaces need more theoretical investigations. This was also observed in earlier investigations [9] and [10]. In both these cases the high-frequency fields in the creeping wave region of a PEC elliptic and circular cylinders were found to disagree with the exact analysis for the same problem. The numerical results for the embedded element pattern for investigation presented here appears to confirm the earlier conclusions in [9] and [10] for a similar (but not identical) problem.

Finally, our results are at variance with the earlier investigations in [11]. The analysis in [11] was specifically for a line source. In particular, this present study did not investigate in detail the effects decreasing s/λ height as was done in [11]. The minimum height chosen was $s/\lambda = 0.25$ for the results in this paper, while in [11] the UTD curved surface scattering formulations were studied for very small heights $s/\lambda = 0.05$. The choice of the minimum height in this paper specifically focused on examining the limits of applicability of the NECBSC code, and not necessarily the general UTD formulations.

To that end, it appears instructive following the results and conclusions in [11] to examine the effects of the height factor in view of the more recent work in [6]. The various high-frequency formulations and their regions of validity has been studied there, and its application to conformal dipole arrays such as in [8] needs to be more carefully investigated.

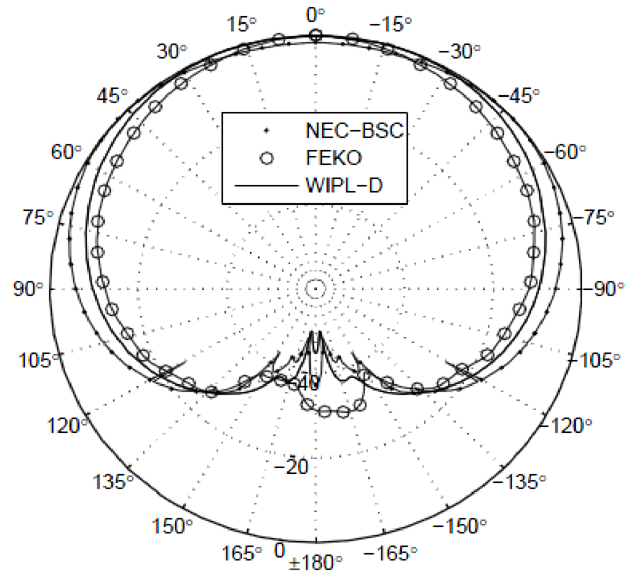

Fig. 6. Comparison of radiation patterns vs. azimuth angle ϕ, in the $\theta = 90°$ plane for a 7-element $\lambda/2$ dipole array with central element excited and all others terminated in a 50Ω load $ka = 10$, $s/\lambda = 0.25$, $b/\lambda = 0.5$, $L/\lambda = 0.5$, $\alpha = 18.013°$, and cylinder height is $H/\lambda = 10$.

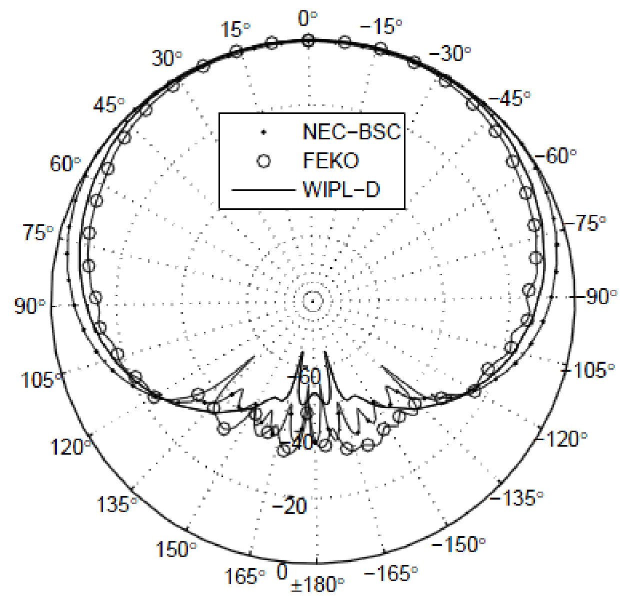

Fig. 7. Comparison of radiation patterns vs. azimuth angle ϕ, in the $\theta = 90°$ plane for a 7-element $\lambda/2$ dipole array with central element excited and all others terminated in a 50Ω load $ka = 20$, $s/\lambda = 0.25$, $b/\lambda = 0.5$, $L/\lambda = 0.5$, $\alpha = 9.006°$, and cylinder height is $H/\lambda = 10$.

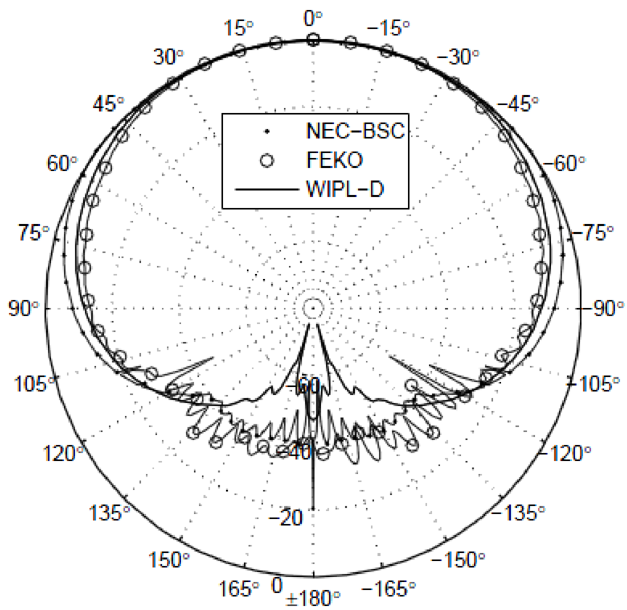

Fig. 8. Comparison of radiation patterns vs. azimuth angle ϕ, in the $\theta = 90°$ plane for a 7-element λ/2 dipole array with central element excited and all others terminated in a 50Ω load $ka = 30$, $s/\lambda = 0.25$, $b/\lambda = 0.5$, $L/\lambda = 0.5$, $\alpha = 6.005°$, and cylinder height is $H/\lambda = 10$.

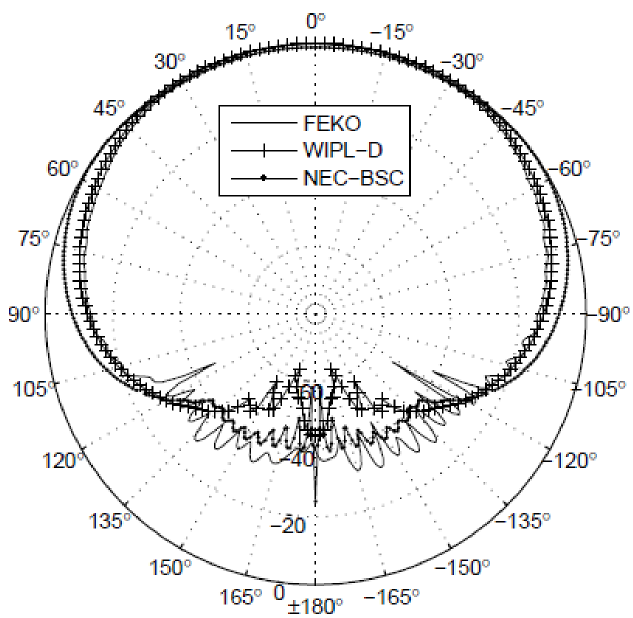

Fig. 9. All of the data is the same as in Fig. 8 above. For NECBSC results, the currents on the dipoles were approximated as that on the central segment of each dipole. The data here is taken from [15].

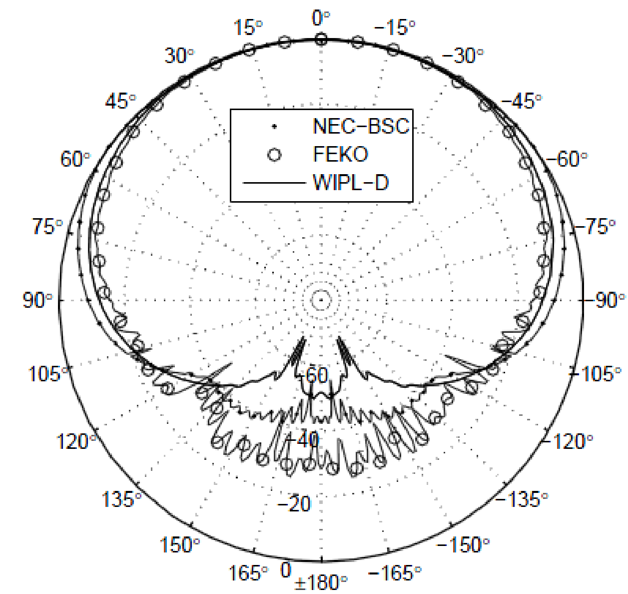

Fig. 10. Comparison of radiation patterns vs. azimuth angle ϕ, in the $\theta = 90°$ plane for a 7-element λ/2 dipole array with central element excited and all others terminated in a 50Ω load $ka = 40$, $s/\lambda = 0.25$, $b/\lambda = 0.5$, $L/\lambda = 0.5$, $\alpha = 4.497°$, and cylinder height is $H/\lambda = 10$.

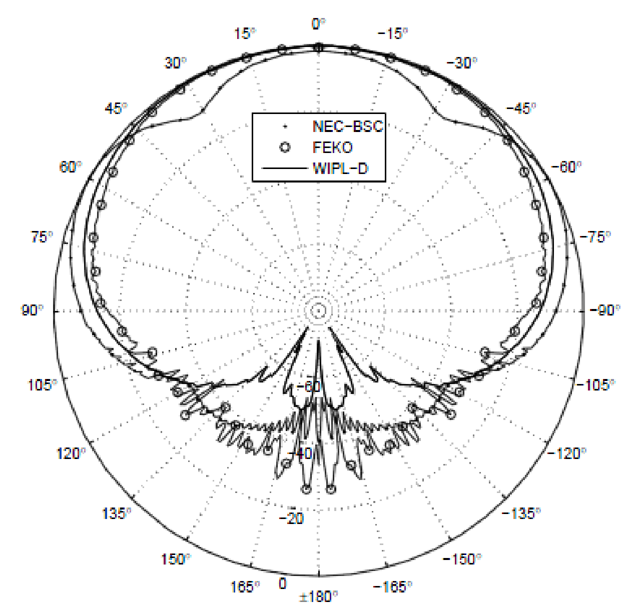

Fig. 11. Comparison of radiation patterns vs. azimuth angle ϕ, in the $\theta = 90°$ plane for a 7-element λ/2 dipole array with central element excited and all others terminated in a 50Ω load $ka = 60$, $s/\lambda = 0.25$, $b/\lambda = 0.5$, $L/\lambda = 0.5$, $\alpha = 2.923°$, and cylinder height is $H/\lambda = 10$.

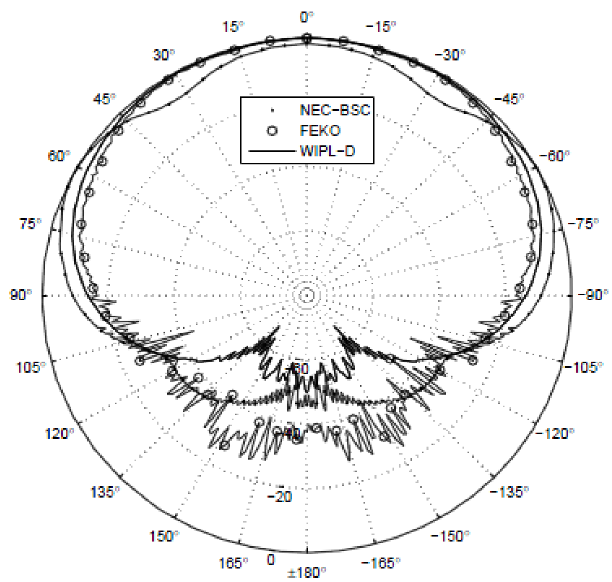

Fig. 12. Comparison of radiation patterns vs. azimuth angle ϕ, in the $\theta = 90°$ plane for a 7-element $\lambda/2$ dipole array with central element excited and all others terminated in a 50Ω load $ka = 80$, $s/\lambda = 0.25$, $b/\lambda = 0.5$, $L/\lambda = 0.5$, $\alpha = 2.207°$, and cylinder height is $H/\lambda = 10$.

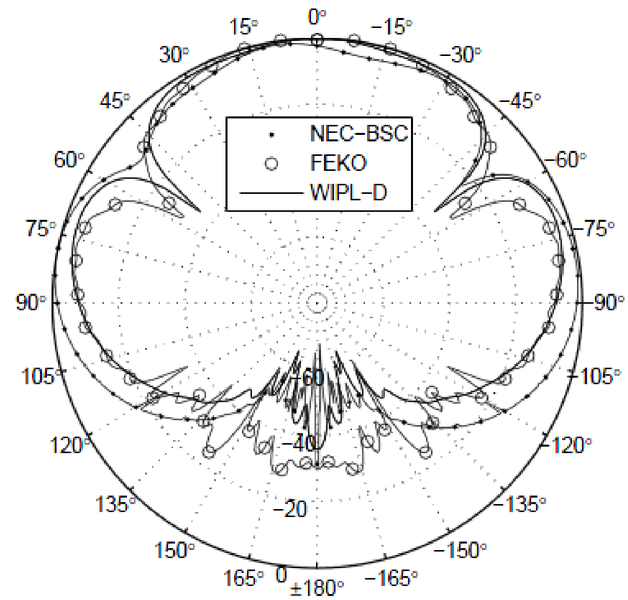

Fig. 14. Comparison of radiation patterns vs. azimuth angle ϕ, in the $\theta = 90°$ plane for a 7-element $\lambda/2$ dipole array with central element excited and all others terminated in a 50Ω load $ka = 30$, $s/\lambda = 0.75$, $b/\lambda = 0.5$, $L/\lambda = 0.5$ and cylinder height is $H/\lambda = 10$.

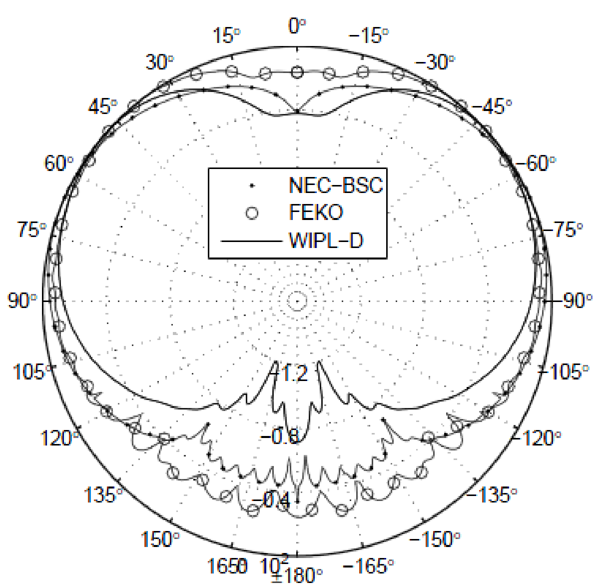

Fig. 13. Comparison of radiation patterns vs. azimuth angle ϕ, in the $\theta = 90°$ plane for a 7-element $\lambda/2$ dipole array with central element excited and all others terminated in a 50Ω load $ka = 30$, $s/\lambda = 0.5$, $b/\lambda = 0.5$, $L/\lambda = 0.5$, and cylinder height is $H/\lambda = 10$.

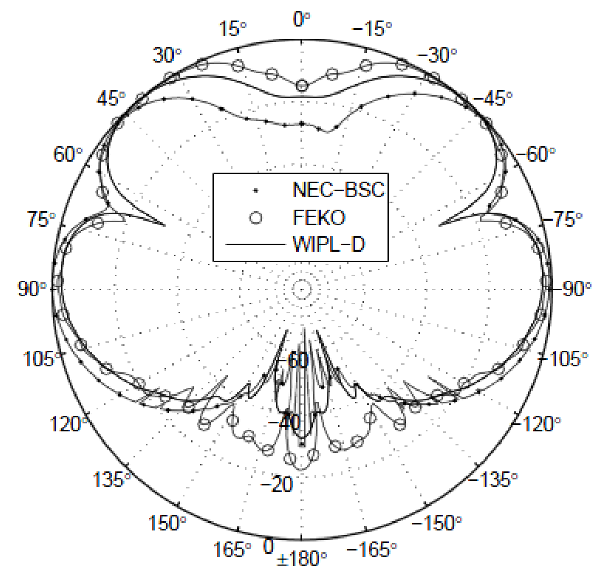

Fig. 15. Comparison of radiation patterns vs. azimuth angle ϕ, in the $\theta = 90°$ plane for a 7-element $\lambda/2$ dipole array with central element excited and all others terminated in a 50Ω load $ka = 30$, $s/\lambda = 1.0$, $b/\lambda = 0.5$, $L/\lambda = 0.5$ and cylinder height is $H/\lambda = 10$.

IV. Summary and Conclusion

In this investigation a technique by which mutual coupling effects can be included while modeling a conformal dipole array via the high-frequency NECBSC code, has been developed by utilizing the output from the exact integral equation solver as contained in the commercially available FEKO code. The embedded element patterns for a seven element array were compared via FEKO, WIPL-D and NECBSC codes. The results showed that in the deep shadow region the disagreements were more pronounced for cylinders with electrically large radius of curvature. This is an interesting observation because NECBSC is expected to be more accurate as the cylinder size increased. Furthermore, it was found that the effect of the curvature on the element currents in the dipole array was insignificant beyond $ka \geq 50$. Thus, it was concluded that for electrically large conformal dipole arrays the solution to the dipole currents can be obtained to a reasonable degree of accuracy by solving an electrically smaller problem via the exact solvers such as FEKO or WIPL-D. The results of this investigation thus provide a computationally efficient strategy for determining radiation behavior of electrically large conformal arrays.

V. Acknowledgement

The authors remain grateful to Prof. Tapan K. Sarkar, EECS department, Syracuse University for the version of WIPL-D code used to generate the results, and, to Dr. C. J. Reddy EMS Software, Hampton, Virginia for technical support and use of FEKO software. The authors acknowledge the support from Dr. Kevin Z. Truman, Dean School of Computing and Engineering, UMKC, during the course of writing this paper. Finally, many useful technical discussions with Richard D. Swanson, Principal Engineer, Honeywell Federal Manufacturing and Technologies (FM & T), Kansas City, over the period of investigation of this project, helped improve the quality of the paper.

REFERENCES

[1] L. Josefsson and P. Persson, *Conformal Array Antenna Theory and Design*. IEEE Wiley-Interscience, NY, USA, pp.101, 2006.

[2] C. A. Balanis, *Antenna Theory: Analysis and Design* (3rd edition). John-Wiley & Sons, Inc., NY, 2005.

[3] D. B. Davidson, *Computational Electromagnetics for RF and Microwave Engineering*. Cambridge University Press, NY, 2008 (digital reprint).

[4] FEKO User’s Manual (Suite # 5.3). EM Software and Systems, Norfolk, VA, USA, July 2007.

[5] T. K. Sarkar, *WIPL-D User’s Manual*, OHRN Enterprises, NY, USA; (private communication).

[6] H. T. Chou, P. H. Pathak and M. Hsu, “Extended Uniform Geometrical Theory of Diffraction Solution for the Radiation by Antennas Located Close to an Arbitrary, Smooth, Perfectly Conducting, Convex Surface,” *Radio Science*, vol. 32, no. 4, pp. 1297-1317, July-August 1997.

[7] R. J. Marhefka and J. W. Silvestro, “Near Zone -Basic Scattering Code (User’s Manual with Space Station Application),” technical report #716199-13, NASA, Hampton, VA, by the ElectroScience Laboratory, Ohio State University, Columbus, OH, USA, March 1989.

[8] J. C. Herper, A. Hessel and B. Tomasic, “Element Pattern of an Axial Dipole in a Cylindrical Phased Array, Part II: Element Design and Experiments,” *IEEE Trans. Antennas Propagat.*, vol. AP-33, pp. 273-278, March 1985.

[9] F. G. Leppington, “Creeping Waves in the Shadow of an Elliptic Cylinder,” *Jour. Inst. Math. Applics.* vol. 3, pp. 388402, 1967.

[10] P. Hussar and R. Albus, “On the Asymptotic Behavior of Uniform GTD in the Shadow of a Smooth, Convex Surface,” *IEEE Trans. Antennas. Propag.*, vol. 39, no. 12, pp. 1672-1680, December 1991.

[11] R. Paknys, “On the Accuracy of the UTD for Scattering by a Cylinder,” *IEEE Trans. Antennas. Propag.*, vol. 42, no. 5, pp. 757-760, May 1994.

[12] S. D. Walker, “Surface Curvature Effects on the Scan Element Pattern of a Sector Electric-Dipole Array above a Cylindrical PEC Surface,” FEKO International Student Competition, September 2008.

[13] S. D. Walker and D. Chatterjee, “ Studies on Development of Conformal Antennas and

Arrays," final technical report #ECE-UMKC08HNYWL-TR01, Honeywell Federal Manufacturing and Technologies (FM & T), contract #224256, CSEE Dept., School of Computing and Engineering, UMKC, KC, MO, USA, September 2008.
[14] S. D. Walker and D. Chatterjee, "Surface Curvature Effects on Element Characteristics on Large, Finite, Conformal Cylindrical Dipole Arrays," *Proc. IEEE Intl. Symp. Antennas and Propagat.*, (4 pages), San Diego, USA, July 5-11, 2008.
[15] S. D. Walker and D. Chatterjee, "Study of Exact and High-Frequency Code Solvers for Applications to a Conformal Cylindrical Dipole Array," *Proceedings of the Annual Review of Progress in Applied Computational Electromagnetics*, (6 pages), Monterey, California. March 08-12, 2009.

Shaun D. Walker obtained bachelor's degrees in Electrical and Computer Engineering (BSECE) and Computer Science (BSCS) from the Computer Science and Electrical Engineering Department at the University of Missouri-Kansas City (UMKC) in 2006, and is currently finishing his MSEE with the same department. His research interests are in analytical and numerical methods in electromagnetics for electrically large problems, conformal arrays and propagation in layered media. Shaun participated in the FEKO International Student Competition in 2008 and his report on conformal arrays received a special mention. In 2009 (June to August), Shaun worked as a ASEE-ONR student researcher at the US Naval Research Laboratory, Washington, DC on problems related to radiation from antennas embedded inside layered media. Shaun is simultaneously dual enrolled in the doctoral (PhD) degree program at UMKC.

Deb Chatterjee received BSETE, M.Tech, M.A.Sc and PhD degrees in 1981,'83,'92 and '98, respcetively. From 1983-1986 he worked with the Antenna Group at Hindustan Aeronautics Limited (HAL), Hyderabad, India. Since August 1999 he is with the Computer Science and Electrical Engineering (CSEE) department, University of Missouri Kansas City (UMKC), where he is now an associate professor. His research interests are in analytical and numerical techniques in electromagnetics, with an emphasis on high-frequency (asymptotic) applications, phased arrays and electromagnetic effects in biological systems. In 2009 (June to August) he was ASEE-ONR summer faculty fellow at the US Naval Research Laboratory, Washington, DC working on electromagnetic propagation problems in layered media. Dr. Chatterjee is a member of the IEEE Antennas and Propagation and Applied Computational Electromagnetics Societies, and reviewer for the *IEEE Transactions on Antennas and Propagation*, *IEEE Antennas and Wireless Propagation Letters*, *IEEE Antennas and Propagation Magazine*, *Applied Computational Electromagnetics Society* Journal, and *Radio Science*. He currently serves as an associate editor for the *International Journal on Antennas and Propagation* (Hindawi publications).

Design and Fabrication of an Axial Mode Helical Antenna

William Coburn, Canh Ly, Timothy Burcham, Russell Harris and Amid Bamba
U.S. Army Research Laboratory
Adelphi, MD 20783
wcoburn@arl.army.mil, ly@arl.army.mil, burcham@arl.army.mil, rharris@arl.army.mil, amid.bamba@arl.army.mil

Abstract – Given generalized requirements for a medium gain circularly polarized (CP) antenna we design and fabricate an axial mode helical antenna. This well known antenna has a relatively wide (1.7:1) bandwidth with gain proportional to the overall length. The antenna and ground plane diameters are determined by the chosen center frequency of operation. We evaluate the antenna design using FEKO electromagnetic simulation software for a center frequency of 700 MHz. We then fabricate one prototype with center metal rod support and foam core as in the conventional construction. We also desire a hollow core variant and use fiberglass to support the helical antenna. We present the measured results for these two types of construction compared to model results. Although the helical antenna embedded in fiberglass is a very rugged design it also involves sufficient dielectric loading to shift the antenna bandwidth to lower frequencies.

Index Terms– Helical antenna, circular polarization, fiberglass, Method of Moments, FEKO

I. INTRODUCTION

When circular polarization (CP) is required, the antenna designer has many choices, but for broadband applications a spiral or helical antenna structure often provides the best performance. A spiral antenna can be ultra-wideband whereas a helical antenna is typically limited to less than an octave bandwidth (1.7:1) [1]. We quantify the antenna impedance bandwidth (BW) in terms of the input reflection coefficient where the return loss is better than 10 dB while the realized gain BW depends on the application. Our objectives were for a 500 – 900 MHz right-handed CP (RHCP) antenna with 9 dBic average gain realized in the most compact size. To approach the gain requirement with a single antenna element we select a helix with axial length, $L = 2$ ft. We use the well known helix design procedure with a shaped metal ground plane although this does not address the effects of dielectric loading [1]. We model the helix using the FEKO electromagnetic simulation software[8]. We have modeled the dielectric structures using both the Method of Moments (MoM) surface equivalence principle (SEP), the thin dielectric sheet (TDS) and coated wire approximations in FEKO. We find only minor differences in results with these methods and use the hybrid finite element method (FEM) for uniform dielectrics without conductors. We summarize our findings using the coated wire approximation to represent the helix embedded in fiberglass and show results compared to measurements. The antenna is fed using a linear tapered 50 to 100 Ω microstrip transition 3-inch in length which is included in our refined model.

Once the basic design is complete we considered different fabrication options including foam, PVC pipe and a fiberglass tube on which to wind the helix. The conventional approach uses a foam core or dielectric rods to support the helical wire element. An axial mode helix is not very sensitive to metallic structures along the helical axis so that a metal support rod can be used. But this feature of the helical antenna may also allow other metal structures to be coaxially incorporated into the helical antenna. So we desire a hollow core helix that is still very rugged and use fiberglass sheets with polyester resin to encase the helical conductor. We describe the classical helix design and fabrication of the foam core and two fiberglass variants. The fiberglass thickness is non-uniform owing to the overlapping glass mat but is estimated at 1/16 – 1/6-inch when using 2 or

5 woven fiberglass mats to encase the ¼-inch diameter hollow copper tubing. We present measured results for these three prototype antennas compared to FEKO model predictions. By making assumptions about dielectric parameters we arrive at a model that can be validated with measurements to sufficient accuracy for engineering purposes.

II. ANTENNA DESIGN AND SIMULATION

The helical antenna design begins with the circumference, C, of the helical coils being chosen near the wavelength, λ_c, at the desired center frequency of operation. The coil diameter would be $D = \lambda_c/\pi$ = 5.37-inch for a center frequency of operation, f_c = 700 MHz. We chose a slightly larger diameter D = 5.56-inch, based on the outer diameter of a standard 5-inch PVC pipe as a convenient way to support the ¼-inch outside diameter copper tubing. The helix then has an impedance BW for wavelengths in the range $4/3C$ to $3/4C$ or 507 – 902 MHz. The classical helical antenna and design equations are well summarized in [1] where the example presented is very close to our desired frequency range. One important aspect for roughly uniform performance over the BW is the pitch angle $\alpha = \tan^{-1}(L/N\pi D)$ for N turns in the helical coil. Although the optimum α may be controversial [2], and tapered windings can be used, the typical choice is a constant pitch angle in the range, 12° – 15° [3]. Maintaining a constant or tapered pitch angle over the antenna length is one of the most difficult aspects of prototype fabrication.

Krauss provides an estimate for the helical antenna directivity $G \approx K_g \left(\frac{C}{\lambda}\right)^2 \frac{L}{\lambda}$, which includes a scale factor, K_g ~ 15, determined from empirical studies [3]. The half-power beamwidth (HPBW) of the radiation pattern is estimated according to $G(\mathrm{HPBW})^2 < 41250$ or HPBW ~ 43°. At the center frequency this provides an upper bound on the directivity G ~ 13.6 dBic but the data used were for $\alpha < 15°$. Based on the FEKO model results we chose a 5-turn helix with $\alpha = 15.4°$ having an axial length of 2 feet. We use a shaped ground plane where the minimum diameter is often chosen as $d_g = 0.8\lambda_c$ = 13.5-inch [1]. With FEKO we find only a small gain reduction using $d_g = 0.76\lambda_c$ = 12.75-inch which corresponds to the outer diameter of a 12-inch PVC pipe. Even though we choose to use thin fiberglass for this outer protective radome, we consider this a minimum diameter ground plane. The optimum height of the edge has been reported as $\lambda_c/4$ = 4.22-inch [1] and our FEKO model results support this choice. The ground plane size is chosen to be as small as possible without reducing the gain or pattern purity over the desired BW, although the front-to-back (F/B) ratio decreases with a smaller ground plane size. The model with the helix wound on 5-inch PVC pipe and an outer 12-inch PVC pipe to protect the antenna along with the thin fiberglass variant are shown in Fig. 1. We use hollow copper tubing with outer diameter ¼-inch to wind the helix since very thin wire can limit the antenna BW. The shaped (or cupped) ground plane improves the gain ~1 dB over the BW, which is about the same improvement that can be obtained by significantly increasing the ground plane diameter.

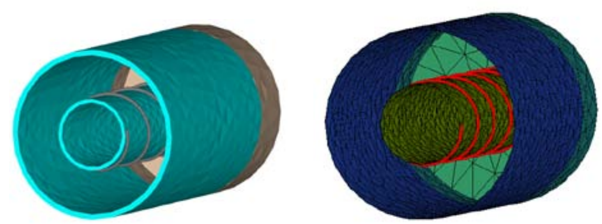

(a) (b)

Fig. 1. The FEKO model for a helical antenna with shaped ground plane wound on (a) PVC pipe and (b) thin fiberglass forms.

The metal rod with foam core to support the helix has been previously described and is approximated in FEKO by including only the helical conductor and ground plane. We also modeled various materials to construct a hollow core structure including PVC pipe and thin fiberglass laminates, although the dielectric parameters used in the model are approximate. For a standard 5-inch PVC pipe thickness (0.26-inch) we used the SEP in FEKO compared to the TDS approximation with negligible differences. The large PVC thickness has an impact on performance (not shown) so we focus on fiberglass construction where the helical element is embedded during the lay-up process. With this construction the helical conductor is larger than the fiberglass thickness which would be difficult to model exactly. Comparing measurements for the helix wound on a foam core and embedded in fiberglass we observe a shift in the return loss and boresight gain to lower frequencies associated with the dielectric loading effects on the antenna, in addition to a high frequency gain reduction. We perform a parameter study of the fiberglass thickness and loss tangent because these parameters are not known exactly. They depend on the dielectric properties of the resin and the resin content in the cured structure. Based on this study we use a large dielectric loss tangent, tanδ = 0.1 and a thickness of 1/8-inch or 1/6-inch for which the results provide an upper and lower bound to the measurements. The actual loss tangent and thickness could be variable over the various cured fiberglass structures so that some approximations and assumptions are required to develop a practical model.

The coated wire approximation provides similar results as the TDS but is much more efficient taking about half the time for these simulations. So we use a coated wire to model the helix embedded in thin fiberglass having $\varepsilon_r = 4.5$ with loss tangent, tanδ = 0.1. The construction includes a nylon base as part of the cured fiberglass structure which is then bolted to the ground plane. The effect of the nylon base is less than that for the fiberglass since the dielectric loading effect of the nylon is only in the antenna feed region. We use the coated wire approximation to represent the helix embedded in thin fiberglass providing the most efficient simulation with the expected frequency dependence. This model includes the nylon base as a uniform dielectric volume having $\varepsilon_r = 3.2$ and tanδ = 0.1 solved by the hybrid finite element method (FEM) in FEKO. It includes the impedance transformer which is located in the approximate position of the prototype antennas and its substrate is also solved with the FEM. Model results are compared to measurements in terms of return loss, realized gain and axial ratio (AR) versus frequency. In all cases the helical element is wound for RHCP.

III. PROTOTYPE FABRICATION

We use a 50 to 100Ω microstrip transition to match the antenna to a 5Ω input. The des ign was developed using FEKO and artwork for fabrication was produced with LPKF CircuitCAM[9]. The 3-inch long linear tapered transition with a 1.25-inch wide bottom ground plane was fabricated with two layers of Rogers RT/Duroid 5870 using an LPKF 93s circuit board milling machine. The material for each layer is 125 mil thickness with single sided ½ ounce copper and has a relative dielectric constant, ε_r = 2.33 and loss tangent, tanδ = 0.0012. The two unclad sides were bonded together with 3M adhesive film [10]. The transmission line width tapers linearly from 669 mil (17 mm) to 158 mil (4 mm) with wire connection at one end and the helical element directly soldered to the opposite end. The FEKO model, with current at 700 MHz, and installed part are shown in Fig. 2.

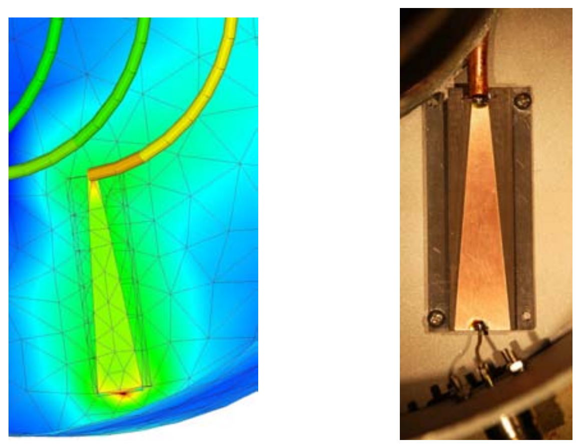

(a) (b)

Fig. 2. Linear tapered microstrip impedance transformer (a) model and (b) as installed part.

We fabricated both the foam core and hollow core fiberglass structures in order to make measurements on both approaches for model validation. The ground plane is fabricated from cold-rolled Al with a welded lip. The foam core was supported by a 1.2-inch diameter metal rod on the centerline bolted to the cupped ground plane as shown in Fig. 3(a) during the antenna measurements. The helical element is simply glued to the foam support and soldered to the microstrip impedance transformer. This approach is low-cost and lightweight but the helical conductor is exposed and possibly prone to damage or changes in position which would reduce performance. The 2nd prototype used the same cupped ground plane but now the helical element is embedded in fiberglass as shown in Fig. 3(b). The cured structure includes a notched cylindrical nylon base 3-inch in height which is then bolted to the ground plane. The antenna element extends from the fiberglass to allow attachment to the microstrip transformer. Using 5-layers of fiberglass was very rugged but thicker than desired for minimal performance impact so we used only 2-layers for the thinnest structure that would still be reasonably rigid. The 2-layers of fiberglass have thickness about half the conductor diameter. The basic helical antenna design is straightforward and normally becomes an exercise in impedance matching to obtain wide band performance. In our case the dielectric loading complicates the design and the development of accurate models because the dielectric losses are difficult to estimate as a function of frequency.

(a) (b)

Fig. 3. Helical antenna element (a) on foam core and (b) embedded in fiberglass.

IV. ANTENNA MEASUREMENTS

The various prototype antennas were measured in the ARL tapered anechoic chamber [4, 5]. We used two Satimo SH400 [11] wide band dual-ridged horns as reference antennas. These horns have an impedance BW of 0.4 – 6 GHz with highly accurate performance data to provide a reference antenna with known gain as specified by the manufacture. With careful installation and laser alignment we obtain an accurate calibration over the entire frequency band of interest, 0.4 – 1 GHz. With the correct alignment of transmit and receive antenna boresight directions we can obtain a typical measurement error of ±0.25 dB for gain measurements. This assumes that the reference antennas are aligned and the reference gain is known accurately such that this source of error is negligible. We carefully calibrate every day and since the Satimo antenna gain has been well validated this is not a bad assumption. Positioning error of the antenna under test is the largest source of uncertainty and the large diameter of the helix antenna make this alignment more difficult. Based on repeat measurements we estimate a worst-case error of ±0.5 dB or 11% error. We measure the gain on the helix axis (or boresight) versus frequency so that relative to the reference measurement we can normalize our radiation pattern data to the measured gain at each frequency. Using a linearly polarized transmit antenna requires rotating the CP antenna under test about the helix axis to obtain a maximum in order to align the antenna polarization ellipse to the transmit antenna polarization. Then, we can rotate the test antenna $90^{o} \pm 0.1^{o}$ to obtain the orthogonal component. We collect azimuthal pattern data every 100 MHz in 1^{o} angular steps for both the major and minor axis of the circularly polarized antenna. The data can then be combined to obtain the RHCP gain and AR as a function of frequency and the RHCP radiation patterns. Since we combine two gain measurements which can have error in the boresight alignment we must accept a larger error of 15% in the RHCP gain and AR measurements. Thus we consider comparisons to model results to within this error of ±0.7 dB to be excellent agreement.

V. RESULTS

We compare model results and measurements for three different prototype antennas. The first is the foam core with metal rod support (H0). The others are fiberglass encasing the helical conductor with minimum thickness of approximately 1/8-inch (H1) or 1/16-inch (H2). The measured S_{11} for these three prototypes are compared in Fig. 4(a) with the FEKO model results shown in Fig. 4(b). Notice that the shift to lower frequencies with increasing fiberglass thickness is evident in the model results. But for input impedance the model is only approximate because the feed region connections are not modeled exactly. The input impedance is quite sensitive to the physical configuration of the 1st half turn of the helix and how the connector is attached. We attempt to transition the helical conductor smoothly from where it is attached directly to the microstrip transformer to following the desired pitch angle. The model results are better than 10 dB return loss over the entire 500 – 900 MHz BW whereas the prototype antennas have somewhat larger reflection co-efficient at some frequencies. The prototypes also have resonant peaks near 900 MHz that exceed the objective. The majority of these differences are due to the wire connection for the coaxial connector (see Fig. 2(b)). Although not shown, the results for the connector pin soldered directly to the microstrip transformer are much closer to predicted.

The RHCP gain on boresight versus frequency is shown in Fig. 5 for the thinnest fiberglass antenna compared to coated wire models with different thickness. The FEKO results are for the helix having 1/16 or 1/8-inch thick fiberglass coating where the maximum thickness for this electrically thin layer approximation is 1/6-inch. The model result for a 1/8-inch thickness is most similar to the measurement so the actual fiberglass construction is probably thicker than assumed but could also vary over the antenna length. None of our models predict the extended performance below about 450 MHz because the input impedance is not well predicted at these frequencies. However, the predicted frequency shift in the impedance bandwidth with increasing fiberglass thickness is consistent with measurements as can be seen in Fig. 4(a) but is less obvious in the realized gain versus frequency.

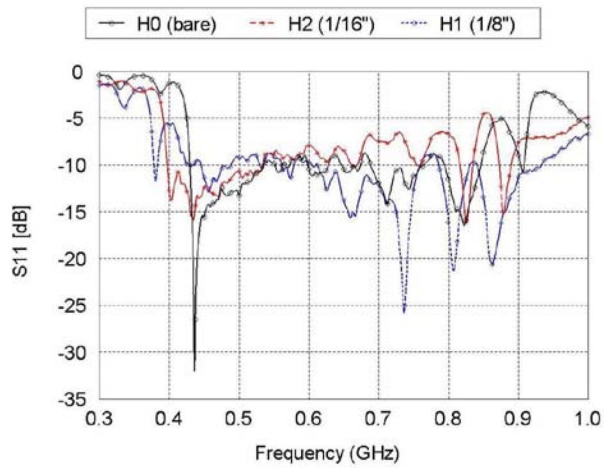

(a)

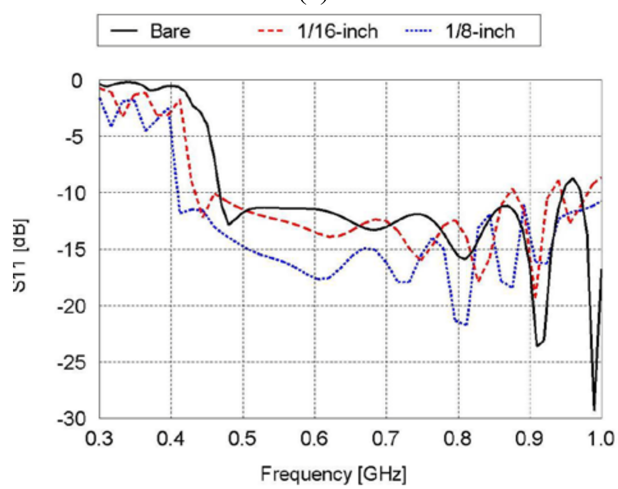

(b)

Fig. 4. (a) Measured S_{11} for three prototype helical antennas and (b) model results.

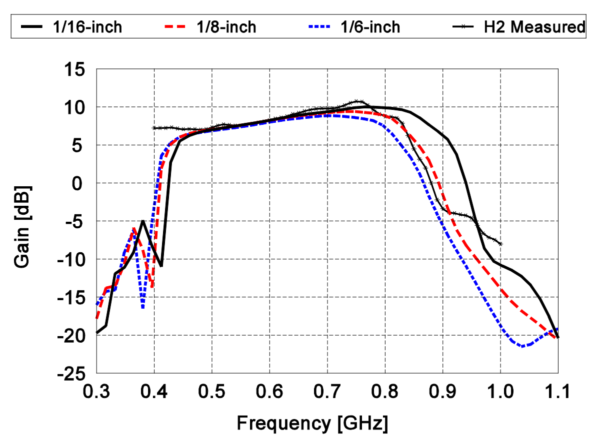

Fig. 5. The calculated versus measured RHCP realized gain on boresight for H2.

The boresight AR comparison (in linear space) is shown in Fig. 6 where in FEKO negative values represent left-handed CP (LHCP) whereas in our measurements LHCP is indicated by values larger than unity. As can be seen the antennas have excellent AR ~ 1 which would correspond to 0 dB. Our fiberglass model is either 1/16 or 1/6-inch thickness using the coated wire approximation which is valid at the frequencies of interest. The relative permittivity of fiberglass is typically ε_r = 4.5 but that for the resin or the cured combination (20 – 30% resin by volume) is uncertain. The loss tangent is more difficult to obtain for the polyester resin, but other researchers have found resin systems to have an imaginary part of the permittivity to be roughly flat with frequency at ε_r'' ~ 0.5 [6], so we use tanδ = 0.1.

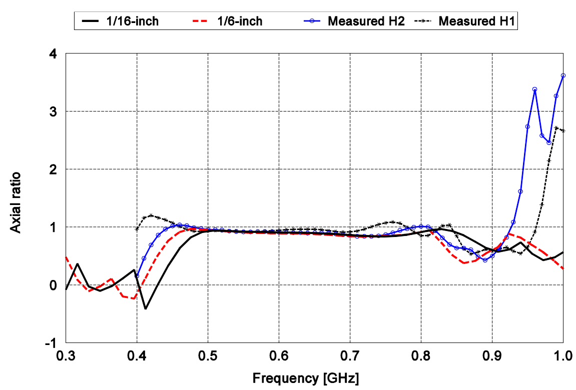

Fig. 6. The calculated versus measured AR on boresight for two prototype antennas.

Selected pattern measurements are compared to the model results for the helix with 1/8-inch thick fiberglass coating. The comparisons at 500 and 600 MHz are shown in Fig. 7 (a) and (b), respectively. The model agreement over the pattern beamwidth is excellent but the back lobes are not well predicted as is often the case in pattern comparisons [7]. Obviously there are more asymmetries in the as-fabricated prototypes than in the model which is typical since there is always some physical modeling error.

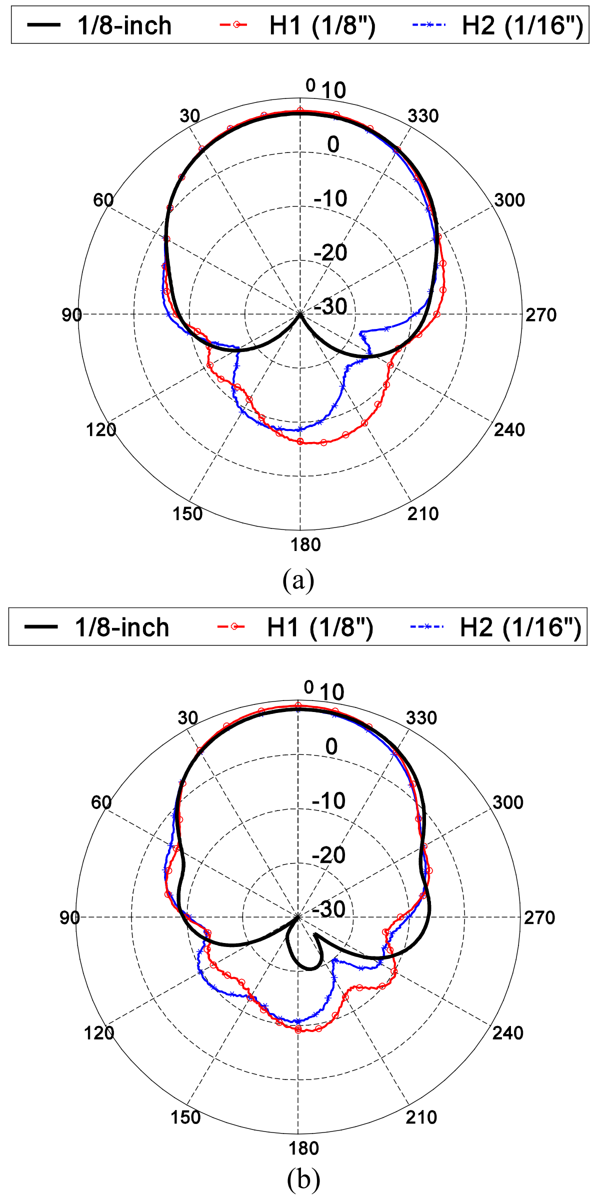

Fig. 7. Measured RHCP radiation patterns compared to model results at (a) 500 MHz and (b) 600 MHz.

The comparisons at 700 and 800 MHz are shown in Fig. 8 (a) and (b), respectively. The patterns at the band edges have off-boresight peak gain. At higher frequencies the helix radiation mode changes with a conical pattern [1]. In all cases the pattern comparison near boresight is excellent with differences on the order of the experimental error. At other angles the agreement is reasonable except in the back lobes. The FEKO model indicates that this choice of ground plane size is sufficient to obtain a good F/B ratio > 20 dB but this is not supported by the measurements.

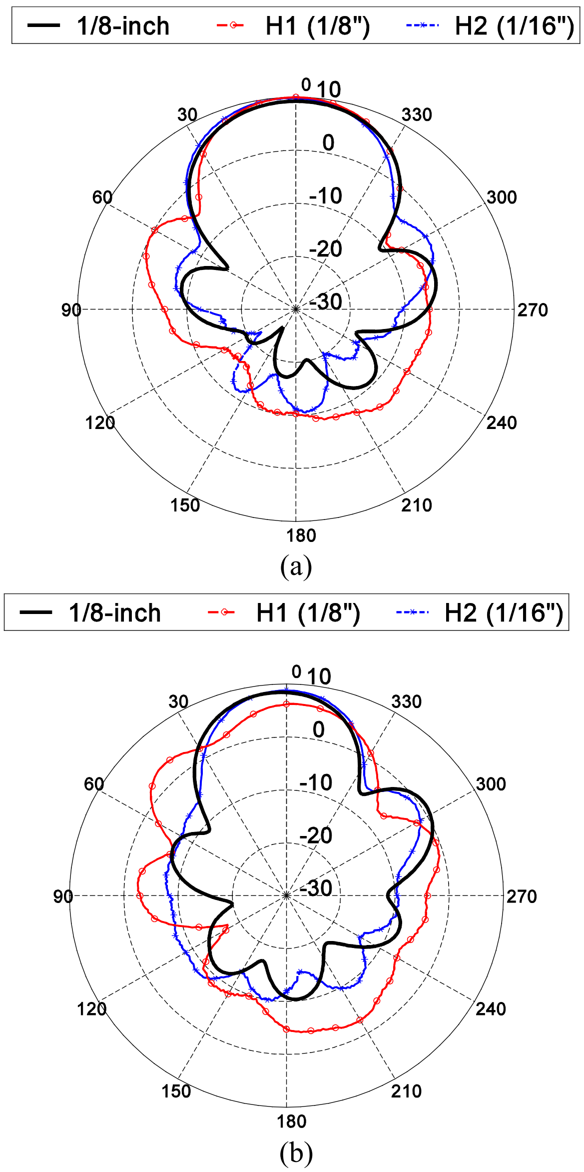

Fig. 8. Measured RHCP radiation patterns compared to model results at (a) 700 MHz and (b) 800 MHz.

VI. CONCLUSIONS

The fiberglass prototype measurements have approximately the predicted shift in impedance bandwidth to lower frequencies with increasing fiberglass thickness. However, the data indicates a larger shift in the gain BW to lower frequencies than predicted although we did not make measurements below 400 MHz. The thicker fiberglass produces a larger shift in the gain and impedance BW with reduced gain at higher frequency. Our fiberglass model with $\varepsilon_r = 4.5$ and $\tan\delta = 0.1$ has this same trend but not to the same extent as measured. By increasing the thickness we obtain better agreement which implies that the fiberglass thickness can be used as a design parameter. That is, the basic helix can be designed to operate at a higher frequency than desired expecting the dielectric loading to shift the antenna frequency response. In the range where the gain remains roughly constant versus frequency, the radiation patterns are stable and have excellent AR. The measured forward patterns for the fiberglass prototypes compared to the model results are in good agreement in this frequency range. Although a larger error is possible when measuring the antenna backlobes, the discrepancies in this part of the pattern comparisons are larger than expected so that the model results can be misleading if the F/B ratio is a concern. For the fiberglass construction the patterns become corrupt around 800 MHz with reduced gain and AR. The as-fabricated helical antennas cannot be modeled exactly but the numerical model provides the correct frequency trends. In order to meet our BW objectives the helix would have to be redesigned accounting for the dielectric loading effects. Thus a smaller diameter helix would be used to shift the antenna performance to higher frequencies and the relatively larger ground plane size may improve the F/B ratio. Although the modeling uncertainties reduce the model accuracy, the model is sufficient for engineering analysis and provides a baseline for model refinement and optimization.

REFERENCES

[1] H. E. King, J. L. Wong, and E.H. Newman, “Helical Antennas,” *Antenna Engineering Handbook*, 4th Ed., J. L. Volakis (ed.), Chap. 12, New York: McGraw-Hill, 2007.

[2] A. R. Djordjevic, A. G. Zajic, M. M. Ilic and G. L. Stuber, “Optimization of Helical Antennas,” *IEEE Antennas and Propagation Magazine*, vol. 48, no. 6, pp. 107 – 115, Dec. 2006.

[3] J. D. Kraus, "The Helical Antenna," *Antennas*, Chap. 7 (New York: McGraw-Hill, 1950).

[4] S. Weiss and A. Leshchyshyn, "Anechoic Chamber Upgrade," Army Armament Research, Development and Engineering Center, ARAED-TR-95009, May 1995.

[5] "Free Space VSWR Test for Tapered Anechoic Chamber," Advanced Testing Services, 13116-TR-VSWR, January 2009.

[6] R. B. Bossoli, "The Microwave Permittivity of Two Sprayable Resin Systems," U.S. Army Research Laboratory, ARL-TR-3907, September 2006.

[7] W. O. Coburn and C. Fazi, A Lumped Circuit Model for a Tri-Band Trapped Dipole Array– Part 2: Stacked Arrays, *IEEE Antennas Wireless Propag. Lett.*, vol. 7, pp. 648 – 651, 2008.

[8] EM Software and Systems, "FEKO", *www.feko.info*.

[9] LPKF Laser and Electronics, "LPKF CircuitCAM", *www.lpkfusa.com*.

[10] 3M, "3M adhesive film", *www.3m.com*.

[11] Satimo, "Satimo SH400", *www.satimo.com*.

William O'Keefe Coburn received his BS in Physics from Virginia Polytechnic Institute in 1984. He received an MSEE in Electro physics in 1991 and Doctor of Science in Electromagnetic Engineering from George Washington University (GWU) in 2005. He has 28 years experience as an electronics engineer at the Army Research Laboratory (formerly the Harry Diamond Laboratories) primarily in the area of CEM for EMP coupling/hardening, HPM and target signatures. He currently is in the RF Electronics Division of the Sensors and Electron Devices Directorate applying CEM tools for antenna design and analysis.

Canh Ly received the Bachelor of Science degree in Electrical Engineering from the University of Maryland, College Park, MD, the Master of Science degree in Electrical Engineering from the Johns Hopkins University, and the Ph.D. degree in Information Technology from the George Mason University. Dr. Ly has been Member of Technical Staff at U.S. Army Research Laboratory (ARL). He has submitted three patents related to frequency estimation technique, patch array antennas, and published papers in IEEE Radar Conference Proceedings, Asilomar Conference, and SPIE Conference. His research interests include antenna design, advanced HEMP techniques, superresolution algorithms for millimeter wave (MMW) radars, statistical signal processing, and radar array processing.

Timothy A. Burcham has been a member of the US Army research and testing community for over twenty years providing engineering design and technical expertise to many military programs. He has been involved in many novel experiments for agencies such as DARPA and Army weather command.

Russel Harris worked for the past 27 years at the US Army Research Laboratory doing digital design, programming and printed circuit board design. Received a B.S. in Microbiology from the University of Maryland in 1973 and worked as a support scientist for the USDA in plant pathology until 1982.

Amid M. Bamba is an undergraduate student of Electrical Engineering at Morgan State University. His research interests include investigating and testing the electromagnetic behavior of antennas.

Rotman Lens Amplitude, Phase, and Pattern Evaluations by Measurements and Full Wave Simulations

Junwei Dong [1], Amir I. Zaghloul [1, 3], Rensheng Sun [2], C. J. Reddy [2], Steven J. Weiss[3]

[1] Department of Electrical & Computer Engineering
Virginia Polytechnic Institute and State University, VA 22043, USA
djwei@vt.edu , amirz@vt.edu

[2] EM Software & Systems (USA)
144 Research Dr, Hampton, VA 23666, USA
ray@emssusa.com, cjreddy@emssusa.com

[3] U.S. Army Research Laboratory, Adelphi, MD 20783, USA
amir.zaghloul@us.army.mil , steven.weiss@us.army.mil

Abstract **─** Microwave lens' performance is depicted by several parameters such as phase error, amplitude taper, and array scan pattern etc. For decades, these parameters have been estimated by the geometry optics method that does not capture the mutual couplings within the lens geometry. Full wave simulation toolkits to conduct EM prediction are now available. However, using them to synthesize and optimize the electrical performance of Rotman lens is still relatively new. Several microwave lens full wave simulations have been attempted using different methods, such as FDTD, FEM, and FIT. They were reported from the perspectives of either phase or amplitude predictions at a single port or single frequency. However, the lens properties at multiple frequencies and for multiple beam ports using MoM have not been investigated. In this paper, we address such simulations using the planar Green's function in FEKO. The phase, amplitude and array factor across the frequency band for multiple beam ports are compared with the measured results, and their errors are evaluated. Prominent agreement between FEKO and measurement is demonstrated. The performance of a prototype lens is presented, followed by discussing few future aspects of lens optimization using full wave simulations.

Index Terms **─** Microstrip Lens, Rotman Lens, MoM, FEKO, Mutual Coupling.

I. INTRODUCTION

In radar and communications array systems, the Beam Forming Network (BFN) is a critical device that produces feeding phases and amplitudes for the antenna elements to perform electrical scanning. Two popular passive BFNs are the Butler Matrix and Bootlace/Rotman lens [1]. The Rotman Lens has superior performance to the Butler Matrix because of its intrinsic True Time Delay (TTD), wide band and wide scan angle characteristics. To design a microwave lens, one follows geometrical optics models [1, 2, 3] to formulate initial phase centers of the input and output ports. Then physical implementations are applied by using waveguide, stripline or microstrip mechanisms. The mutual couplings between the adjacent ports as well as the multiple reflections are not predicted using the initial direct ray formulation. Consequently, to draw reasonable predictions of the phase and amplitude information, accurate analysis tools such as full wave solvers are desired. In recent years, researchers have analyzed Rotman Lens using different numerical techniques, including with finite different time domain (FDTD) in XFDTD [4], with finite element method (FEM) in HFSS [5], and with finite integration technique (FIT) in CST Microwave Studio [6]. However, to conduct lens optimization, more efficient and accurate methods are still in demand. In this paper, we analyze one printed microstrip lens. Given the nature of the printed structure of this lens, method of moments (MoM) with planar Green's Function is very suitable in terms of both accuracy and computation efficiency.

The Rotman Lens under consideration is 8x8 microstrip lens (8 scanning beams, 8 fed array elements). To capture its general performance, we evaluate the phase and amplitude coupling between each beam port and receiving port across the frequency band, as well as the single port to aperture phase and amplitude couplings. Pattern performance is achieved by calculating the array factor using the simulated and measured amplitude and phase information. The errors occurred in the phases, amplitudes and radiation pattern are emphasized through post processing by assuming a linear phase shift, uniform amplitude distribution and true time delay design. Simulation results are compared with the measurement across the frequency band of 4-5 GHz throughout the evaluation.

II. ROTMAN LENS MODEL

Electrically steerable array system uses Beam Forming Networks (BFN) to form different phase fronts across the aperture for different input excitations. In doing so, it achieves planar waves traveled to separate spatial directions by simply switching the inputs, as shown in Fig. 1(a). Microwave lens, connecting each input to a beam port, utilizes a lens cavity and transmission lines to guide the wave propagation. By properly controlling the beam port positions, receiving port positions and transmission line lengths, the lens is able to achieve the linear phase front across the array output, as indicated in Fig. 1(b). These parameters can be determined by theories of the traditional trifocal lens [1], the quadrufocal lens [2], or the non-focal lens [3]. Upon achieving this information, the port and cavity can be implemented in waveguide, microstrip or stripline media, while the transmission lines can be realized by either the same medium or separate cables.

The Rotman lens presented in this paper is built on the microstrip laminate Rogers 5870. Lens layout is shown in Fig. 2, whose beam ports 1 through 8 are marked as 1, receiving ports 9 through 16 are marked as 2, and dummy ports are marked as 0. Note that the dummy ports in lens design are sometimes necessary in order to reduce the side wall reflections as well as to increase the adjacent beam port isolations. In the current lens, all ports are implemented by physical triangular tapered mictorstrip horns, and the transmission lines are built on the same layer using traditional 50-Ω microstrip lines. Port numbers are included in Figure 2 as well to facilitate the analysis in forthcoming sections.

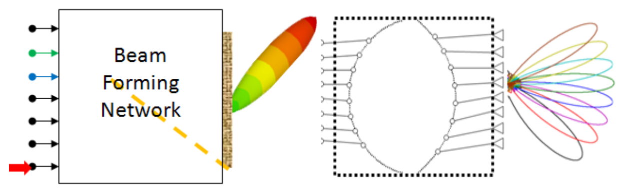

(a) (b)

Fig. 1. Microwave lens as beam forming network.

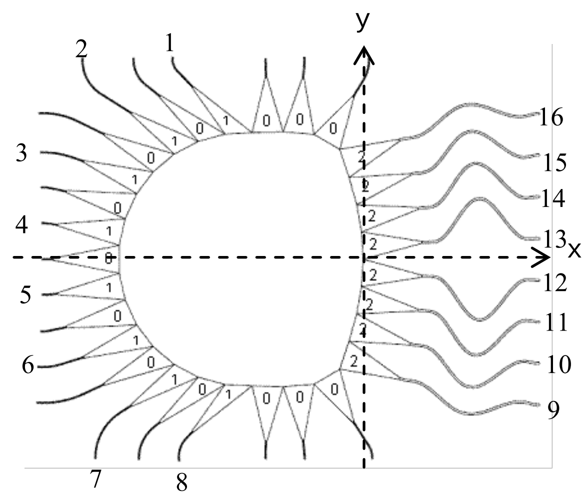

Fig. 2. Rotman lens layout.

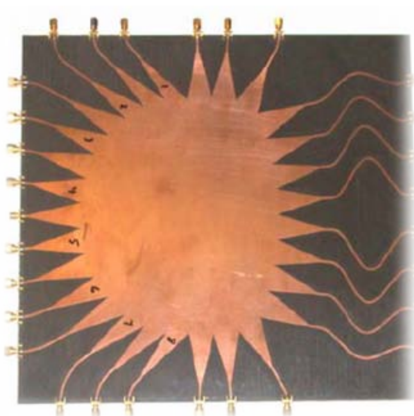

Fig. 3. Fabricated Rotman lens prototype.

Fig. 3 is the Rotman lens prototype that was fabricated by the Army Research Lab in Adelphi, MD. This lens was designed at center frequency 4.6 GHz, and extensive S-parameter measurements were taken [7]. This printed circuit lens is the product of a series of Rotman lens developments that have been going on at ARL for a number of years [8]. The results in [7] are used in this paper for validating the FEKO model as well as evaluating the lens performance. Some technical parameters used to construct the lens are listed in Table 1.

Table 1. Rotman lens Parameters.

Symbol	Quantity	Value
f_0	Center Frequency	4.6 GHz
B	Testing Band	4-5 GHz
N_b	Beam Port #	8
N_r	Receive Port #	8
ε_r	Relative Permittivity	2.3
tanδ	Loss tangent	0.0012
σ	Conductivity	5.7 e+7
d	Array Spacing	31.9mm
h	Substrate Thickness	0.508 mm
t	Copper thickness	0.07 mm

*Terminal impedance is 50Ω, so the width of the transmission line is designed approximately 1.526 mm.

III. SIMULATION AND MEASUREMENT RESULTS

In this section, we focus on the full wave simulation in FEKO and its validation versus measurement data. We shall keep in mind that Rotman lens is a multiple-port-network structure. While conducting comparisons, both beam-port to receiving-port coupling, or transmission factor, across frequency and coupling from a beam-port to all receiving aperture ports at single frequency, in both amplitude and phase, are important.

The simulation was based on the Planar Green's Function solver in FEKO by assuming an infinite ground plane. Each input/output is modeled as microstrip port. Each port is assigned 50-Ohm load so that when any beam port is excited, all others are terminated. The S-parameters between the beam ports and the receiving ports are registered. Eleven discrete frequency steps from 4 to 5 GHz were simulated. The entire simulation took 8.965 hours in a 64-bit workstation, using 4-core Intel(R) Xeon(R) 3.0GHz CPUs. The peak memory consumption of all processes was 2.136 GByte.

For performance across the receiving aperture, the amplitude and phase couplings are studied when single ports are excited at a single frequency. For performance across the frequency band, we can study the beam-port to receiving-port couplings in amplitude and phase. Due to the symmetric structure of a Rotman lens, it is not necessary to compare the results for all ports. Typical ports and comparison strategies are listed in Table 2. In this section, we present a comprehensive comparison between FEKO and measurements. Next section focuses on the performance analysis based on the beam-port to receiving-port coupling discussed in this section.

Table 2. Comparison objects between FEKO simulations and measurements.

Uppercase	1. Couplings across aperture at 4.6 GHz				2. Couplings Across 4-5 GHz			
Feed Port	1	2	3	4	5	6	7	8
Receiving Port	9–16	9–16	9–16	9–16	13	14	15	16
Amplitude	√	√	√	√	√	√	√	√
Phase	√	√	√	√	√	√	√	√
Figures	Fig. 5, Fig. 6				Fig. 7, Fig. 8			

1. Couplings Across Aperture at 4.6 GHz

In both simulation and measurements, the data achieved is more or less the single port-to-port S-parameters with amplitude and phase information. For lens design, a primary objective is for the single port excitation to produce the right amplitude taper and linear phase information across the receiving array aperture at the desired frequency, as indicated in Fig. 4.

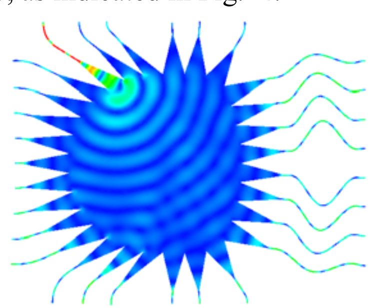

Fig. 4. Surface current for single port excitations.

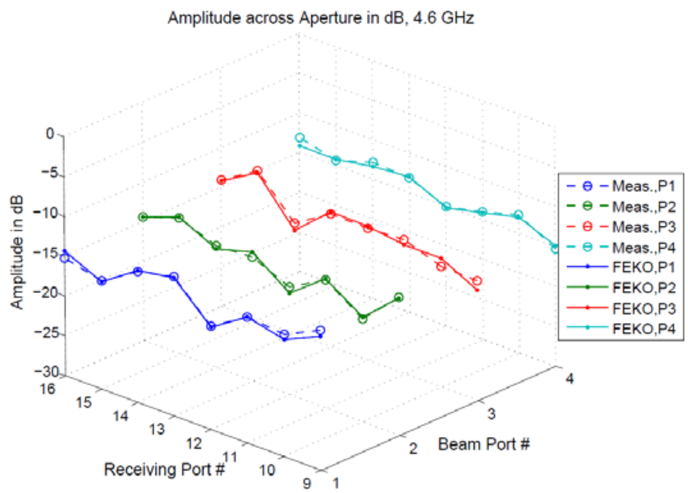

Fig. 5. Comparison between FEKO and measurements for amplitude taper across the aperture at 4.6 GHz.

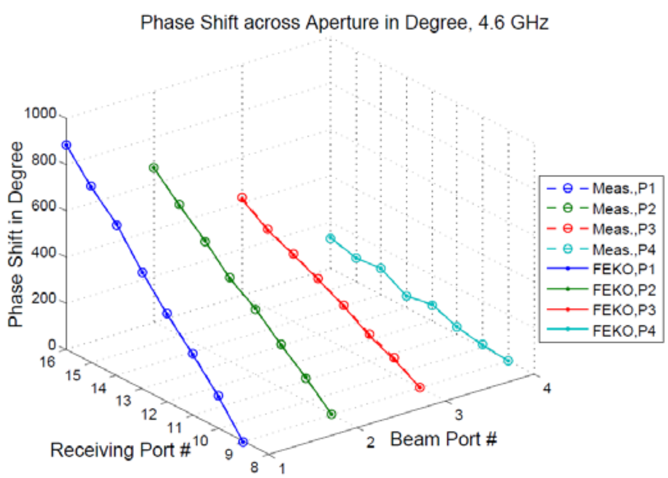

Fig. 6. Comparison between FEKO and measurements, for phase shift across the aperture at 4.6 GHz.

In Fig. 5 and Fig. 6 we arrange the amplitude coupling and phase shift between beam ports (1-4) and all receiving ports (9-16) in 3-D plots. It is observed that the amplitude varies along -15dB for all four port excitations. However, as the beam port moves into the center (from 1 to 4), there is a trend that the amplitude fluctuations saturate. From the phase shift perspective, both simulation and measurements show good agreements and the lens achieves a linear phase shift across the aperture. The phase shift for the large angle beam port (e.g. port 1) has a higher slope than the center port (e.g. port 4). Ideally, the lens is desired to have uniform amplitude taper for highest gain or other amplitude tapers for low sidelobes, and perfect linear phase shift for beam scanning. The errors occurred over the ideal case are considered in the error analysis, which will be explained in the next section.

2. Couplings Across Aperture Across 4-5 GHz

The insertion loss across frequency for single beam-port to receiving-port is another important factor from the communications system design point of view. This reflects how much of gain variation tolerance over the frequency the device possesses. Besides, the phase variations across the frequencies may be significant if the medium is dispersive.

To illustrate the comparison results between FEKO and measurements across 4-5GHz, according to Table 2, we plot the amplitude and phase couplings between the chosen beam ports (5, 6, 7, 8) and chosen receiving ports (13, 14, 15, 16) in Fig. 7 and Fig. 8. It is observable that the simulation agrees well with the measurements. However, it is also noticed that the amplitudes encounter higher attenuation at certain frequencies for different port couplings. This is probably due to two factors: the reflection within the cavity and the different beam port frequency responses.

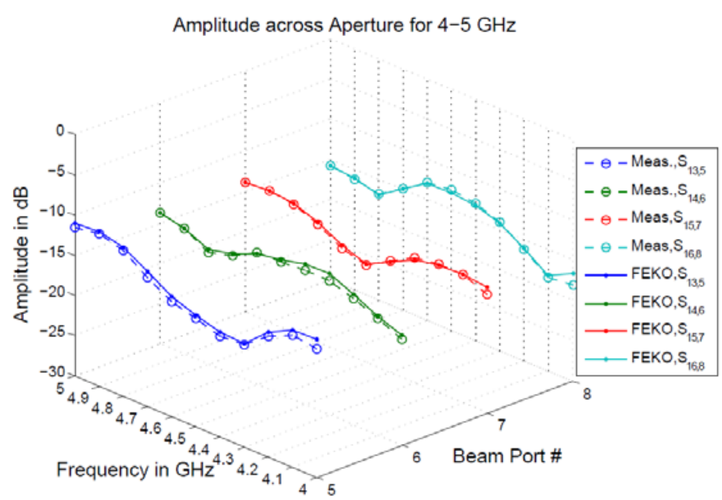

Fig. 7. Port to port amplitude coupling comparison between FEKO and measurements for 4-5 GHz.

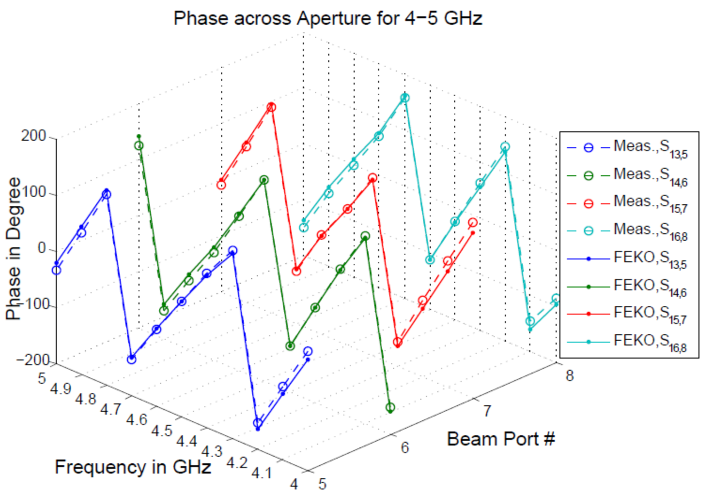

Fig. 8. Port to port phase coupling comparison between FEKO and measurements for 4-5 GHz.

IV. PERFORMANCE ANALYSIS

So far we have been able to do accurate comparison between FEKO and measurement, but we have not interpreted the results in a way to assist the lens optimizations. To conduct lens optimization, it is necessary to know how much the results deviate from the objectives. Although the goal of this section is not to conduct lens optimization, it helps to focus on the error analysis for general lens designs from the perspectives of phase, amplitude and pattern, which are essential components of lens optimization. In the next section, we discuss some of the full wave lens optimization strategies.

The general objective of the lens design assumes to achieve uniform amplitude tapering so as to yield maximum gain, and perfect linear phase shift across the aperture so as to produce stable beams. Resulting from both factors, the true time delay is also a key objective of lens design, meaning, the scanning pointing direction should not change as the frequency varies. In this section, we analyze the amplitude, phase and the scanning direction errors.

1. Amplitude error analysis

In Fig. 5 we showed the amplitude taper across the aperture for different beam port excitations. For each beam port, there are corresponding amplitude errors. Fig. 9 shows the amplitude errors across the aperture for beam port 4 at 4.6 GHz. The standard deviation among all ports can also be used to assess the variation of the amplitude errors. Fig. 10 illustrates standard deviations across the receiving ports for all beam ports at 4.6GHz. It is noted that the deviation from uniform amplitudes is higher at edge beam ports relative to the center beam ports. This may be due to the more symmetric view of the receiving ports for the center beam ports.

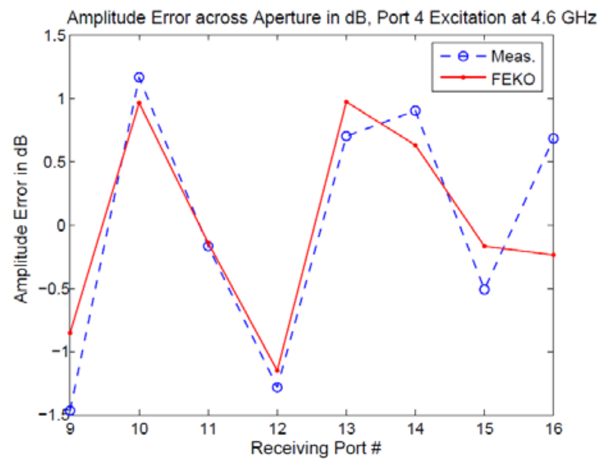

Fig. 9. Amplitude errors across the output ports for port 4 excitations at 4.6GHz.

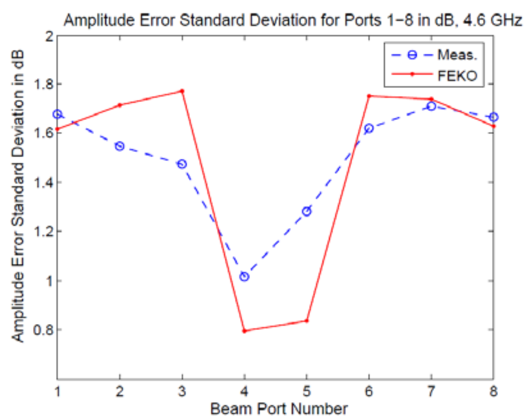

Fig. 10. Amplitude error standard deviation for all beam ports across aperture at 4.6GHz.

Fig. 11 plots the amplitude deviations for all beam ports at various frequencies. It is found that the lens under test maintains average amplitude error of about 1.5dB for all beam ports across the entire frequency band of interest. As the frequency increases, both measurement and FEKO indicate that the amplitude variation increases.

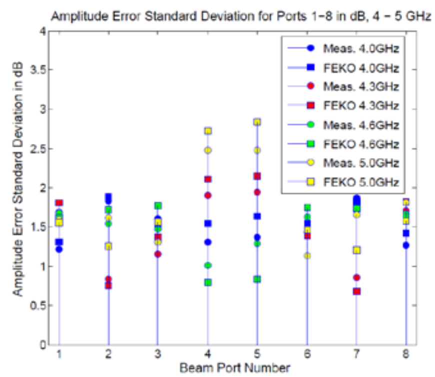

Fig. 11. Amplitude error standard deviation for all beam ports across aperture at 4-5GHz.

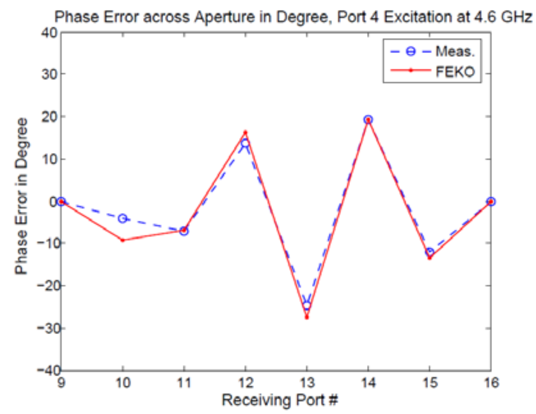

Fig. 12. Phase errors across the output ports for port 4 excitations at 4.6GHz.

2. Phase Error Analysis

The phase shift representation at single frequency was shown in Fig. 6. The phase error occurs when phase shift is not linear with the receive element location. Similar to amplitude errors, phase errors across aperture are different for different beam ports. Example for port 4 excitation at 4.6 GHz is shown in Fig. 12. The phase error standard deviations for all beam ports at 4.6 GHz are shown in Fig. 13. Note that the center beam ports 4 and 5 have exhibited high phase errors up to 15 degrees for the given lens. This may be due to the fact that the lens design and the transmission line length were optimized to produce two perfect focal points off axis in the tri-focal lens design.

Fig. 14 plots the phase error deviations for all beam ports at 4-5 GHz. It is found that the lens under test has average phase error of about 12 degrees for all beam ports across the entire frequency band of interest. As the frequency increases, the variations in phases increase as well, indicating that more attention should be paid to the high frequency operation during the initial formulation.

3. Array Factor Analysis

Whether the amplitude variations in Fig 11 and the phase variations in Fig. 14 are acceptable or not depends on the resulting array performance. Typically, amplitudes and phases affect side lobe levels, and the scanning directions. These parameters can be estimated by calculating the array factors, in other words, solving the pattern for isotropic radiation elements.

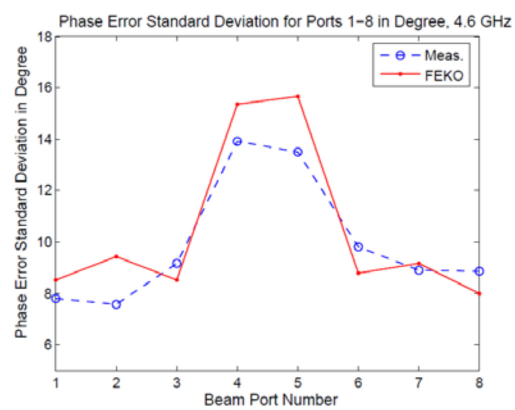

Fig. 13. Phase error standard deviation for all beam ports across aperture at 4.6GHz.

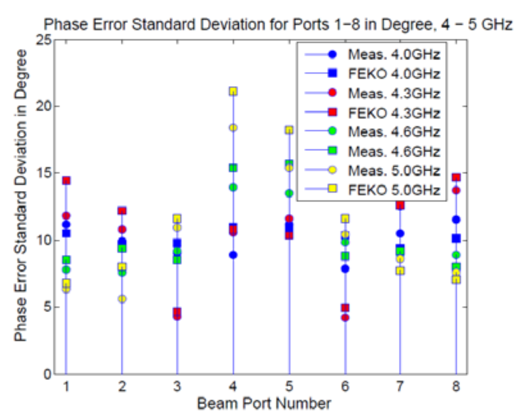

Fig. 14. Phase error standard deviation for all beam ports across aperture at 4.6GHz.

We investigate the pattern performance by calculating the array factor at the lowest frequency, 4GHz, and the highest frequency, 5GHz. The following plots assume a linear array with uniform spacing of 31.9mm. Both measurement and simulation data are used in Fig.

15 and Fig. 16 for 4 GHz and 5 GHz, respectively. For single frequency operation, the lens scans up to ±45^o in eight discrete steps, which result from the eight beam port excitations. In general, as the scanning angle increases, gain decreases and the beam width increases. Comparison between Fig. 15 and Fig. 16 indicates that the beam width decreases and highest gain increases as the frequency increases. Besides, as implied by the high variations in both phase and amplitude tapering at higher frequency, patterns at 5GHz reflect higher gain variations than that at 4GHz.

We also investigate the true time delay behavior for the given Rotman lens. As it shows in Fig. 17, the scanning angle variations between 4GHz and 5GHz change between 0.54^o and 1.45^o. The beam pointing directions have slightly higher errors at the high scan angles. Note that both measurement and FEKO have predicted asymmetric patterns between 1-4 port excitations and 5-8 port excitations due to possible implementation errors.

In the error analysis presented in this, we processed the phase errors in terms of linear phase shift, calculated amplitude errors based on uniform tapering objectives and estimated the pattern performance based on true time delay property. FEKO simulation and measurements have demonstrated consistent results. The fabricated lens can be characterized by average amplitude errors of 1.5 dB, phase errors of 12 degrees, true time delay with tolerance of less than 1.5 degrees across 4-5 GHz.

There are several strategies for improving the microwave lens design using the full wave analysis. The next section will address some of these strategies.

IV. DISCUSSION ON PERFORMANCE IMPROVEMENTS

In previous sections, we have shown that the amplitude and phase errors can be accurately estimated by measurements and full wave simulations. The former is considered a sure validation, while the latter is a fast way to conduct lens optimizations. The amplitude errors may be caused by the unbalanced propagation directions as well as the reflections within the cavity. The phase errors are caused by the phase center shift as well as the reflections within the cavity. We list several possibilities of improvement below.

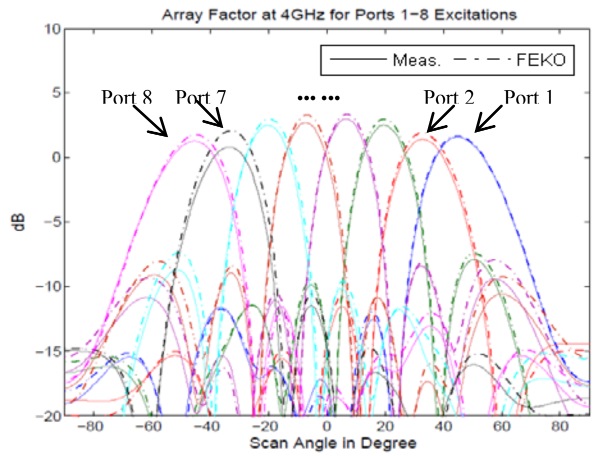

Fig. 15. Array factor for all beam port excitations at 4GHz based on measurement and simulation.

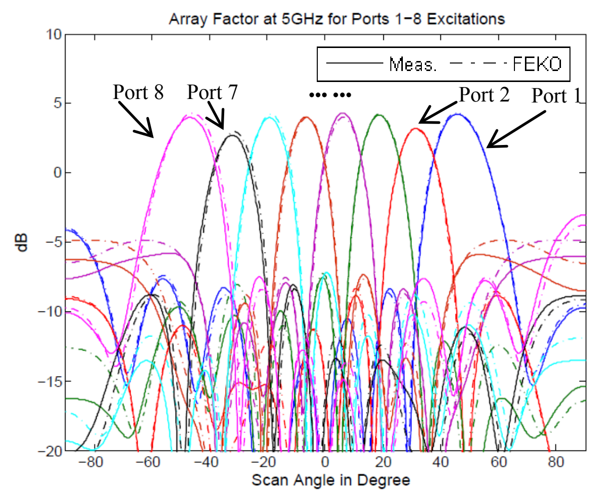

Fig. 16. Array factor for all beam port excitations at 5GHz based on measurement and simulation.

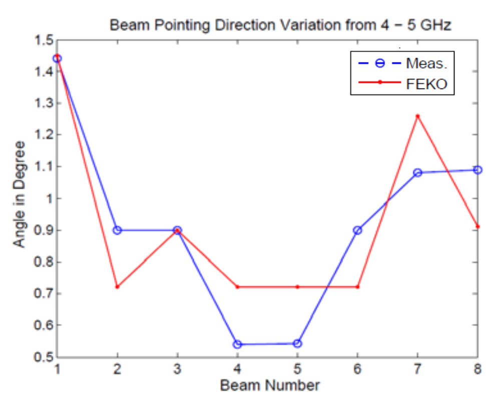

Fig. 17. Scanning angle variation between 4GHz and 5GHz.

1. Beam Port Pointing Direction

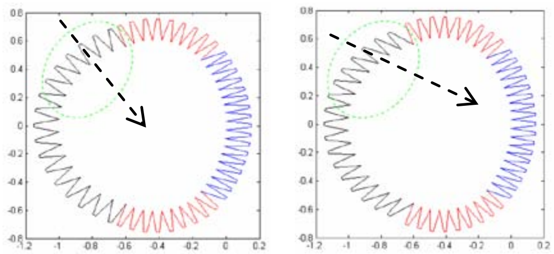

Fig. 18. Beam Port Porting Direction Layout.

The beam port pointing direction, shown in Fig. 18, affects the gain pattern of each port excitation. Typical lenses are designed with the beam ports pointing to the origin of the structure or the center of the receiving ports. However, different subtended angles caused by different pointing angles may yield the desired amplitude distributions along the aperture.

2. Sidewall Freedom of Designs

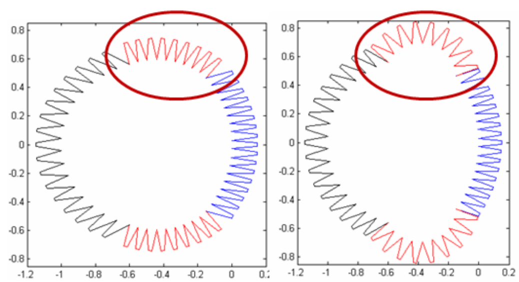

Fig. 19. Lens layout with different sidewalls.

As it shows in [9], the sidewall dummy port terminations play important rule in reducing the reflections in the cavities. To maximize the absorbing ratio or minimize the reflection in certain directions, the sidewall curvature (Fig. 19), as well as the port sizes are essential parameters. The parametric studies of sidewall optimization have not been reported by full wave analysis so far.

3. Tapered Horn Optimization

When a single beam port is excited, all dummy ports and other beam ports are loaded in matched terminations. The geometry of the tapered printed feed elements greatly affects their reflection coefficients. It also affects the operational bandwidth of the lens. So far, most printed Rotman lenses have adopted triangular shape taper horn due to its simplicity. However, it has been found that such tapered line is not optimized, hence has high return loss. Several alternative tapered horns as it indicates in Figure 20 are worth investigating for the optimal frequency response.

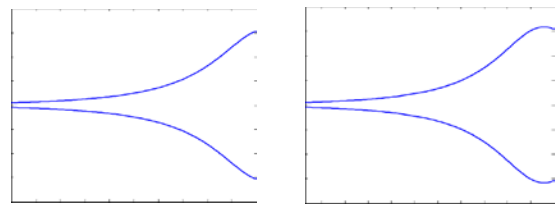

Fig. 20. Tapered horn with different geometries.

Using full wave simulation to optimize lens design has not been extensively addressed. There are more design freedoms than the ones listed above to improve its performance, such as phase center variations versus frequency and mismatch between the cavity and the tapered port junctions, etc. The evolving efficient full wave simulators will soon lead to designs of low amplitude errors, low phase errors, and wideband microwave lenses.

V. CONCLUSION

In this paper we investigated Rotman lens' amplitude, phase and pattern performance by using measurements and full wave simulations. We demonstrated that FEKO is accurate to estimate such parameters based on measurement validations of a given prototype lens. Analysis results show that this lens has average amplitude error of 1.5dB, phase error of 12 degrees, and true time delay tolerance angle of 1.5 degrees across a frequency band 4-5GHz. The presented lens is not optimized, but a few improvement strategies by using full wave simulations are proposed.

REFERENCES

[1] W. Rotman and R. Turner, "Wide-angle Microwave Lens for Line Source Applications," *IEEE Transactions on Antennas and Propagation*, vol. 11, pp. 623-632, 1963.

[2] C. Rappaport and A.I. Zaghloul, "Optimized Three-dimensional Lenses for Wide-angle Scanning," *IEEE Transactions on Antennas*

and Propagation, vol. 33, pp. 1227-1236, 1985.
[3] J. Dong, A. I. Zaghloul, and R. Rotman, "Non-Focal Minimum-Phase-Error Planar Rotman Lens," in URSI National Radio Science Meeting, Colorado, 2008.
[4] C. W. Penney, R. J. Luebbers, and E. Lenzing, "Broad Band Rotman Lens Simulations in FDTD," in IEEE Antennas and Propagation Society International Symposium, 2005.
[5] J. Silvestro, M. Longtin, S. Din-Kow, and Z. Cendes, "Rotman Lens Simulation using the Finite Element Domain Decomposition Method," in IEEE Antennas and Propagation Society International Symposium, 2005.
[6] J. Dong, A.I. Zaghloul, and R. Rotman, "A Fast Ray Tracing Method for Microstrip Rotman Lens Analysis," in XXIXth URSI General Assembly Chicago, 2008.
[7] S. Weiss, S. Keller, and C. Ly, "Development of Simple Affordable Beamformers for Army Platforms," in Proceedings of GOMACTech-07 Conference Lake Buena Vista, FL, 2006.
[8] O. Kilic and R. Dahlstrom, "Rotman Lens Beam Formers for Army Multifunction RF Antenna Applications," in IEEE Antennas and Propagation Society International Symposium, 2005.
[9] J. Dong, Hsu-Cheng Ou, A. I. Zaghloul, "Measurement Investigation of Microstrip Lens Sidewall's Termination", USNC/URSI National Radio Science Meeting, South Carolina, June 2009.

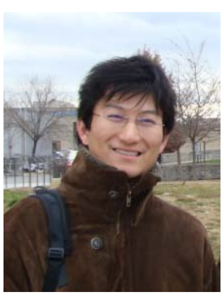

Junwei Dong was born in Hebei, China, in 1983. He received B.S. degree in Measurement & Control and Instrumentation (Signal Processing) from Jilin University, Jilin, China, in 2006. He received his M.S. and Ph.D. in Electrical Engineering at Virginia Polytechnic Institute and State University (Virginia Tech), Virginia, USA, in 2009.

He joined the Virginia Tech Antenna Group (VTAG) as a graduate student in 2006, where he conducted research on antennas, microwave lens designs and electromagnetic simulations. After graduation, he joined Microwave Engineering Corporation (MEC), North Andover, MA as a research scientist. He currently conducts research on microwave component optimization and fabrication techniques.

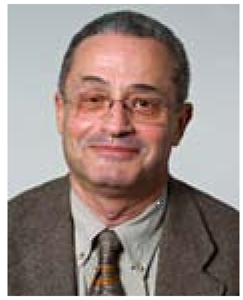

Amir I. Zaghloul is with the US Army Research Lab (ARL) on an IPA (Inter-Governmental Personnel Act) agreement with Virginia Polytechnic Institute and State University (Virginia Tech), which he had joined in 2001 as Professor in the Bradley Department of Electrical and Computer Engineering. Prior to Virginia Tech, he was at COMSAT Laboratories for 24 years performing and directing R&D efforts on satellite communications and antennas. He is a Fellow of the IEEE, an Associate Fellow of The American Institute of Aeronautics and Astronautics (AIAA), a Member of Commissions A, B & C of the International Union of Radio Science (URSI), and a member of the Board of the Applied Computational Electromagnetics Society (ACES). He was the general chair of the 2005 "IEEE International Symposium on Antennas and Propagation and USNC/URSI Meeting," held in Washington, D.C.

Dr. Zaghloul received the Ph.D. and M.A.Sc. degrees from the University of Waterloo, Canada in 1973 and 1970, respectively, and the B.Sc. degree (Honors) from Cairo University, Egypt in 1965, all in electrical engineering.

Rensheng Sun was born in Heilongjiang, China, in 1975. He received the B.E. degree from Tsinghua University, Beijing, China, in 1999, the M.S. degree from Villanova University, Villanova, PA, in 2002, and Ph.D. degree from Michigan State University, East Lansing, MI, in 2005, all in electrical engineering.

He served as a Visiting Assistant Professor in the Department of Electrical and Computer Engineering at Michigan State University during Fall Semester, 2005. Since January 2006, he has been working as a Senior Application Engineer at

EM Software & Systems (USA) Inc., Hampton, VA. His research interests include computational electromagnetics, antenna design, and multiphysics modeling. He is a member of IEEE, AMTA, Eta Kappa Nu, and Tau Beta Pi.

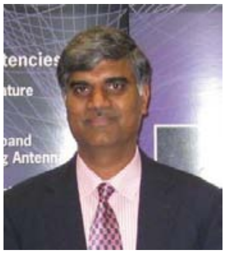

C. J. Reddy received B.Tech. degree in Electronics and Communications Engineering from Regional Engineering College (now National Institute of Technology), Warangal, India in 1983. He received his M.Tech. degree in Microwave and Optical Communication Engineering and Ph.D. degree in Electrical Engineering, both from Indian Institute of Technology, Kharagpur, India, in 1986 and 1988 respectively. From 1987 to 1991, he worked as a Scientific Officer at SAMEER (India) and participated in radar system design and development. In 1991, he was awarded NSERC Visiting Fellowship to conduct research at Communications Research Center, Ottawa, Canada. Later in 1993, he was awarded a National Research Council (USA)'s Research Associateship to conduct research in computational electromagnetics at NASA Langley Research Center, Hampton, Virginia. Dr. Reddy worked as a Research Professor at Hampton University from 1995 to 2000, while conducting research at NASA Langley Research Center. During this time, he developed various FEM codes for electromagnetics. He also worked on design and simulation of antennas for automobiles and aircraft structures. Particularly development of his hybrid Finite Element Method/Method of Moments/Geometrical Theory of Diffraction code for cavity backed aperture antenna analysis received Certificate of Recognition from NASA.

Currently, Dr. Reddy is the President and Chief Technical Officer of Applied EM Inc, a small company specializing in computational electromagnetics, antenna design and development. At Applied EM, Dr. Reddy successfully led many Small Business Innovative Research (SBIR) projects from the US Department of Defense (DoD). Some of the technologies developed under these projects are being considered for transition to the DoD. Dr. Reddy also serves as the President of EM Software & Systems (USA) Inc. At EMSS (USA), he is leading the marketing and support of commercial 3D electromagnetic software, FEKO in the US, Canada, Mexico and Central America.

Dr. Reddy is a Senior Member of the IEEE. He is also a member of Applied Computational Electromagetic Society (ACES) and serves as a member of Board of Directors. He has published more than 60 referred journal articles and conference papers.

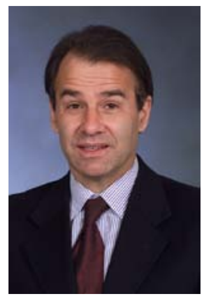

Steven J. Weiss was born in Utica, NY in 1955. He graduated from The George Washington University in 1995 with a doctoral degree in Electrical Engineering. He is presently with the Army Research Lab working with antenna systems. His research areas include specialized antennas for military applications. He is a Senior Member of the IEEE Antennas and Propagation Society.

FEKO Simulation of a Wedge Mounted Four Element Array Antenna

Steven Weiss[1], Keefe Coburn[1], and Ozlem Kilic[2]

[1]U.S. Army Research Laboratory
2800 Powder Mill Road
Adelphi, MD 20783
sweiss@arl.army.mil,

[2]Department of Electrical Engineering and Computer Science
The Catholic University of America, Washington, DC 20064, USA
kilic@cua.edu

Abstract–A four element patch array with main beam locations approaching endfire has been developed. The initial design was accomplished using EMAG's EMPicasso software. The array is intended to be used in a monopulse configuration on the sides of a wedge-like structure. As such, accurate estimations of the patterns need to be obtained when the antenna is mounted on the geometry of the wedge. These simulations were not possible with 2.5 dimensional software, such as EMPicasso (www.emagware.com). We present measured data as compared to simulations using FEKO (www.feko.info) software for the array on a wedge.

Index Terms: FEKO, EMPicasso, patch array, monopulse array, conformal antenna

I. OVERVIEW OF THE ANTENNA ARRAY

Designing antennas that conform to a particular structure has potential use for military applications, [1]-[3]. One such design under consideration is a 1x4 linear patch array that has been developed at 9.35 GHz. The application required the antenna to be mounted on a wedge shaped structure with its main beam locations approaching endfire. An aperture fed patch antenna as shown in Figure 1 was designed to meet these specifications. The spacing between the elements is 0.877 wavelengths, resulting in an overall size (including the patch length) of 10.4 cm. The substrate is Rogers RT/Duroid 5880 for which we use ε_r = 2.33 and tanδ = 0.0002 in these simulations. The initial development was accomplished using EMAG's EMPicasso software. This Method of Moments (MoM) simulation uses the 2.5-D Mixed Potential Integral Equation (MPIE) formulation of planar structures [4, 5]. The FEKO MoM software also has this formulation for planar structures but in addition can simulate 3-D objects combined with planar geometries [6]. FEKO uses the Fast Multipole Method (FMM) to save memory for electrically large problems and has advanced features such as hybrid techniques with the Finite Element Method (FEM) and with approximate high frequency methods [7, 8]. For example, in FEKO the antenna substrate can be infinite in extent while the ground plane is a finite size, or vice versa. Thus EMPicasso provides approximate results for actual microstrip antennas where the largest differences are observed in the calculated pattern compared to measurements.

We note some unusual aspects of the array at the onset of this discussion:

(1) The resonant length is such that one wavelength (within the dielectric) is traversed along the length of the element as opposed to a half wavelength, which is the typical size for patch antennas. As a consequence, the electric fields at the radiating edges of the patch are 180 degrees out of phase, [8] causing a null on broadside and main beams approaching endfire as shown in Figure 2.

(2) In an effort to keep the sidelobe levels down, the array was excited with amplitude weights of: 1: 2: 2: 1 through the use of current dividers at the junction of the power splitters as shown in the right-hand side of Figure 3.

(3) For a half wavelength patch, the aperture is typically placed at the center where the magnetic field peaks. The patch length in this example is one wavelength. Therefore, the magnetic field has two peaks located ¼ wavelength from each radiating edge instead of the center of the patch, [10]. Consequently, there are two optimal placements of the aperture. For the first element in the array, the patch is fed ¼ wavelength form its left edge. In order to have the radiation from the second patch contribute in phase, we have opted to feed the second patch ¼ wavelength from its right edge with a feed in the opposite direction to the first feed. The opposite locations of the aperture and the opposite orientation of the feed directions both introduce a 180 degree phase shift and allow for in-phase excitation of the two elements. The same feeding structure is repeated in the next pair of patches, so all patches radiate in phase.

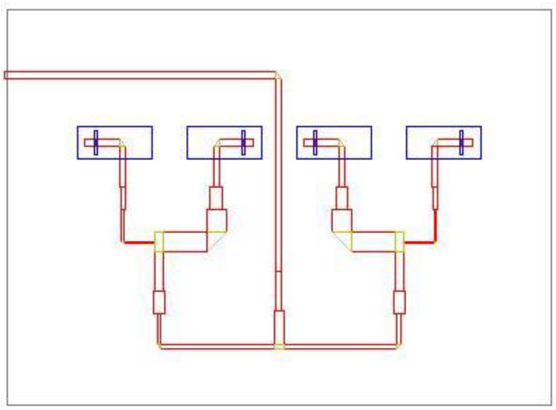

Figure 1. Outline of four element array developed using EMAG Picasso.

II. SIMULATIONS OF THE ANTENNA ARRAY

Some preliminary simulations have been run using FEKO to account for the finite ground plane of the array. First the single patch element was modeled using FEKO with a multilayer Green's function model for the substrates but finite size ground plane. We note that special attention had to be given to the meshing about the perimeter of both the patch and the aperture and in FEKO this is user defined. Some of these refinements are evident in Figure 4 where the ground plane mesh size increases with distance from the slot aperture. More difficult to see is that the ground plane beneath the microstrip is meshed more finely also in the same manner as the strip conductors. This is a key step in obtaining a reasonable estimation of the impedance match.

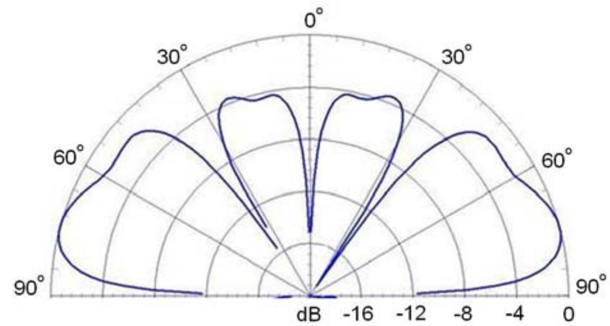

Figure 2. Radiation pattern of the array using EMAG Picasso.

The microstrip line was excited via a probe. The simulated return loss for the patch antenna is presented in Figure 5, which shows a better than 25 dB return loss at 9.35 GHz using FEKO. The simulated E-plane antenna pattern for this single element is shown in Figure 6. Note the symmetric and idealized nature of the EMPiCASSO backplane pattern compared to the finite ground plane result where the back lobes are not symmetric since the slot is not symmetric with respect to the patch. This patch will be used in the array estimation of the problem and then applied to the wedge geometry.

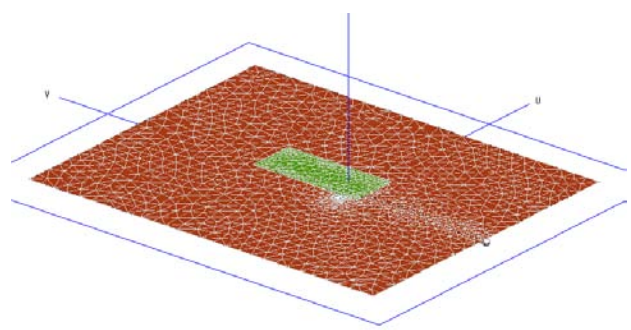

Figure 3. Mesh refinements for simulation of a single patch on a ground plane.

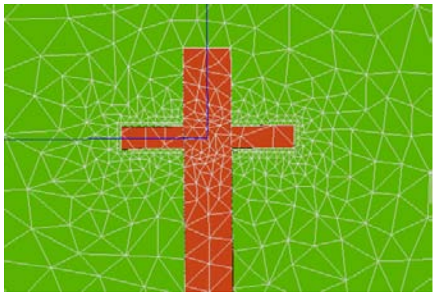

Figure 4. Mesh refinements about the feed line and the aperture beneath the patch.

Figure 5. Computed return loss using Picasso (infinite ground plane - top) and FEKO (finite ground plane - bottom.)

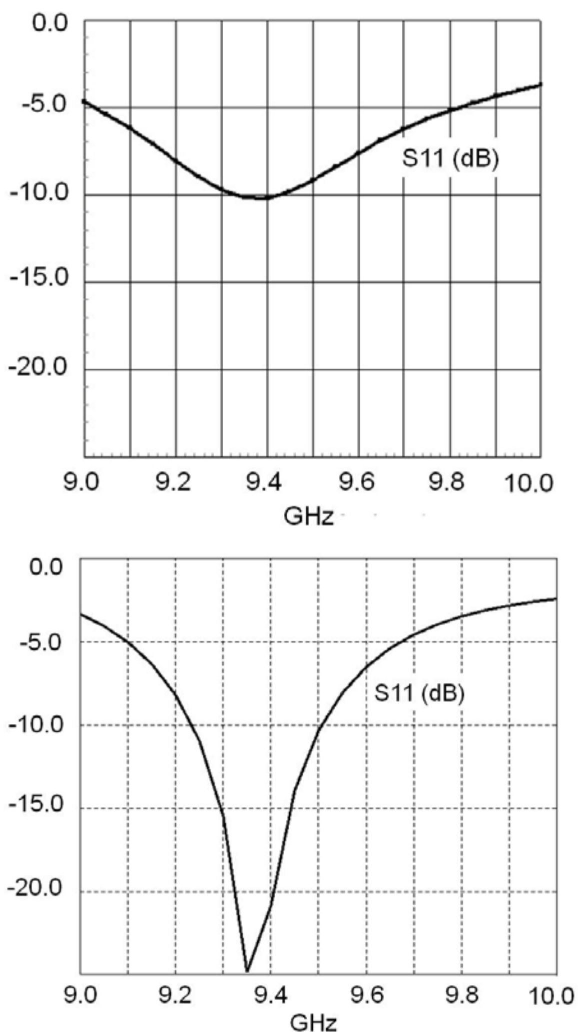

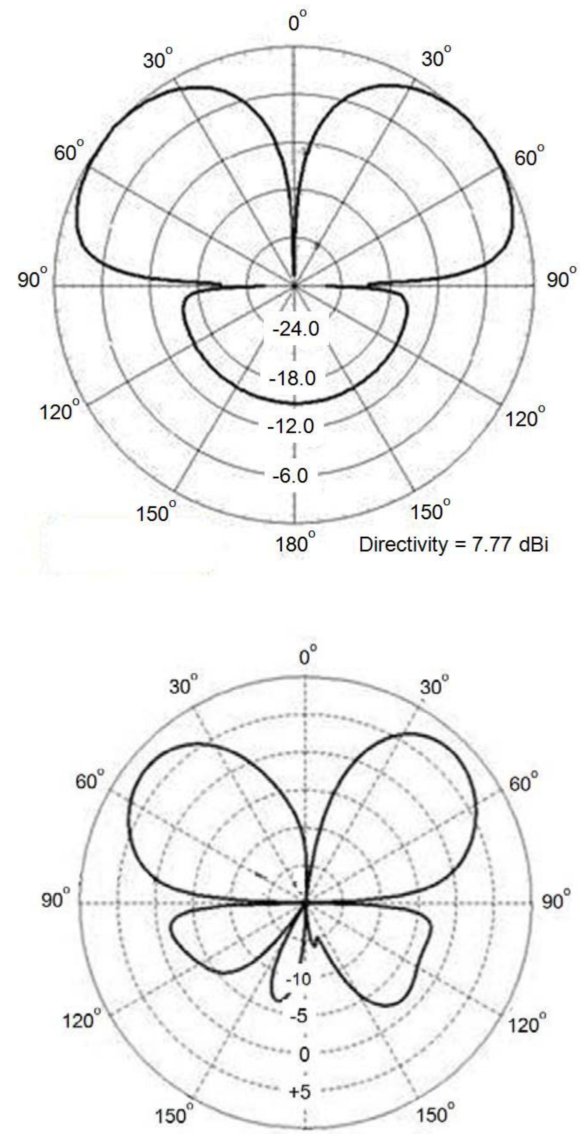

Figure 6. Computed radiation patterns using Picasso (infinite ground plane) and FEKO (finite ground plane)

III. OPERATIONAL DETAILS OF THE ANTENNA

This antenna was developed to operate on the sides of a wedge in a monopulse configuration and would require at least two arrays on either side of the conducting wedge as shown in Figure 7. This is the actual structure from which our measurements were taken. Notice that the metal ground plane extends around all sides of the antenna arrays. Figure 8 gives the monopulse pattern of the two antenna arrays mounted on the wedge and fed in phase. It shows the characteristic forward null of the monopulse configuration. Measurements of the pattern are presented to demonstrate the potential of this technique to determine the direction of a target.

Figure 7. Actual array(s) placed on a slanted (wedge) ground plane.

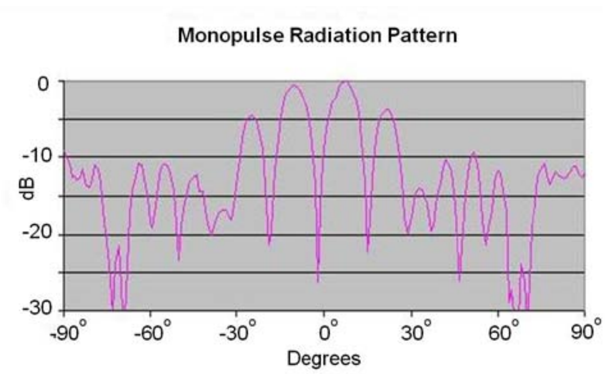

Figure 8. Measured monopulse normalized radiation pattern.

IV. SIMULATIONS OF THE WEDGE CONFIGURATION

All simulations for this section used a dual core XEON 5150, 2.66 GHz machine with 16 GB DDR2 RAM and a 533 MHz bus. The operating system was Red Hat LINUX 64-bit and CAD FEKO Version 2.0.5 (FEKO Suite 5.2) was used. The multilevel fast multipole method (MLFMM) was used which save memory and run-time compared to standard MoM [6]. A convergence study confirmed that the mesh refinement was adequate and that the ground plane mesh size can increase away from the microstrip line. The coarser mesh provided a more efficient simulation without reducing accuracy and required about 5 hrs per frequency.

Actual simulations (FEKO) of the wedge proved time consuming because of the size of the problem. In Figure 9 we detail the geometry of a FEKO simulation using a planar geometry. Such a simulation lends itself to a 2.5 dimensional Green's function solution so the dielectric lateral dimensions can be unbounded in the x-y plane (seen as the region about the finite ground plane of the patch.) This solution ran reasonably fast – on the order of 1 hr per frequency depending on the requested output. For this smaller problem the FMM does not provided a significant memory reduction. The patterns for this simulation are not shown.

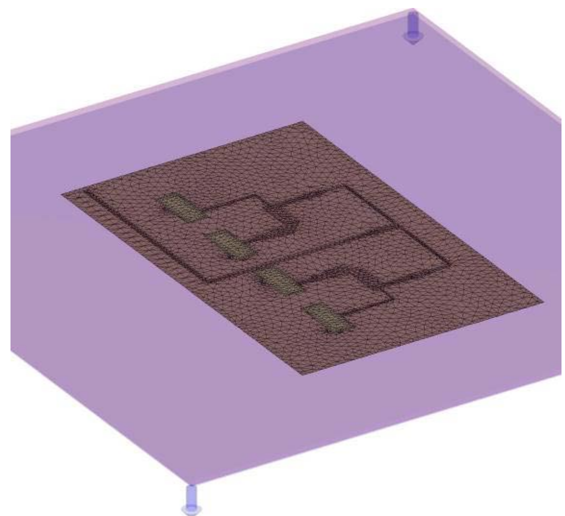

Figure 9. FEKO simulation using a Green's function model for the substrate.

Simulations of the wedge were more challenging because the Green's function approach only lends itself to problems residing on planar geometries. In Figure 10, we show our configuration for two 4-element array antennas mounted on a wedge. For this simulation, the ground plane extends the length of either side, but the dielectric is terminated and does not extend to the actual tip of the wedge using the Surface Equivalence Principle (SEP) to represent the dielectric surfaces rather than a volume mesh. Now the problem size is significantly larger and the FMM provides substantial memory reduction from ~60 GB to less than 2 GB. Termination of the dielectric region was necessary to match the demonstration wedge array configurations although the ground plane on the sides of the arrays was not simulated (see Figure 7). The actual tip of the wedge, Figure 11, was simulated as a flat surface, ensuring a symmetrical mesh on either side of the wedge.

Figure 10. Two 4-element array antennas mounted on a wedge.

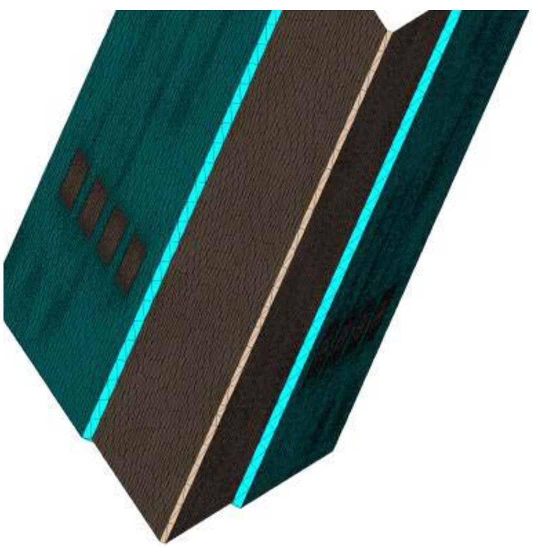

Figure 11. FEKO implementation of the wedge tip.

In Figure 12, we present a simulation model that closely approximated the fabricated wedge that was measured. Note the inclusion of a flat metallic disc suppressing radiation to the back direction. This was consistent with the metal base plate of the anechoic chamber mast as used in the measurement.

In Figure 13, we present the simulated radiation patterns (FEKO) for both the wedge and the wedge with the back plate at a frequency of 9.45 GHz. The simulation results should be compared to the measured data of Figure 8.

Figure 12. FEKO wedge model with a metallic back plate.

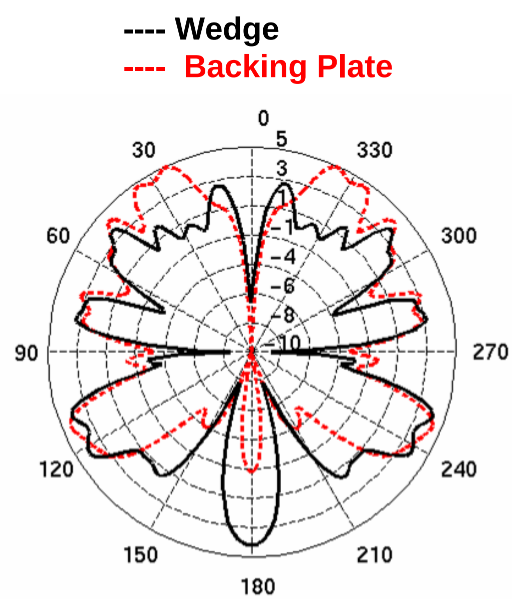

Figure 13. Simulated patterns for the two wedge configurations.

The measured peak locations and the simulation *without* the backplane closely track at about 10 Degrees from the plane containing the wedge's tip. However, the simulation predicts a broad side lobe only 3 dB below the main lobe whereas the data indicates a distinctive first side lobe with back lobes 10 dB below peak. The lack of a back plane predicts a major lobe at 180° in contrast to measured data. The inclusion of a back plane suppresses the back radiation in the computer simulation, but widens the two peak locations to about 25°. The pattern has large side lobes possibly owing to smaller and more asymmetric ground plane surfaces transverse to the arrays.

An even larger mesh would be required to adequately simulate the ground plane used in the measurements. The problem quickly requires more memory than available on most desktop workstations and parallel computing or approximate methods may be required [7]. To conserve computational resources a coarse mesh could be used on the back plate and ground plane sections removed from the antennas with a corresponding reduction in accuracy. Other approximate methods such as Physical Optics are not appropriate for this array [8]. The MoM is typically more efficient than finite difference methods for such large arrays over narrow bandwidths. The finite element method is an alternative that can be efficient since the matrix is sparse and can take advantage of fast solvers. Regardless of the chosen method, compromises are often required to obtain an adequate mesh resolution of the array within the available computational resources.

V. CONCLUSIONS

This paper discusses a unique patch array designed for use on a wedge in a monopulse configuration. The original design was accomplished with 2.5 dimensional MoM software (EMPicasso). FEKO was used to investigate the effect of a finite size ground plane showing that the 2.5 dimensional model was adequate for the forward radiation pattern but results in an idealized backplane pattern. The antenna arrays were placed on a wedge structure for measurements. FEKO was used to simulate the wedge ground plane; however, the inclusion of a conducting back plane needs further investigation. It is needed (and was present in the measurements) for suppression of back radiation, but in our limited size model it degrades the position of the forward beam. A larger ground plane is required in the simulation but results in a problem nearing the limits of our available RAM. Improved accuracy can often be obtained in FEKO by using the MoM/FEM hybrid technique which uses an FEM volume mesh in the dielectric substrate. A microstrip edge source in FEKO can also improve accuracy compared to a thin-wire probe feed. A refined model will be developed to investigate such alternatives and include the as-tested ground plane size. Based on the available computational resources, some tradeoffs in accuracy are often necessary in order to develop a practical yet realistic simulation.

REFERENCES

[1] O. Kilic and S. J. Weiss, "Conformal Antenna Design for Military Vehicle Armor," *Proc. IEEE AP-S and USNC/URSI*, Albuquerque, NM, 2006.

[2] O. Kilic, A. Zaghloul, E. Kohls, R. Gupta, and D. Jimenez, "Flat Antenna Design Considerations for SOTM and SOTP Applications," Invited, *MILCOM*, vol. 2, pp. 790 – 794, 2001.

[3] O. Kilic and A. Zaghloul, "Integrated Antenna System for Blockage and Interference Mitigation for Satellite-on-the-Move (SOTM) Communications," *Proc. 23rd Army Science Conference,* Orlando, FL, Dec 2-5, 2002.

[4] K. F. Sabet, *Novel Efficient Integral Equation Based Techniques for Characterization of Planar Microwave Structures*, Ph.D. dissertation, University of Michigan, April 1995.

[5] K. F. Sabet, J. Cheng, K. Sarabandi, and L. Katehi, "An Advanced Electromagnetics Tool for Design of Multilayer Printed Antenna Arrays," at www.emagtechnologies.com.

[6] J. van Tonder and U. Jakobus, "Fast Multipole Solution of Metallic and Dielectric Scattering Problems in FEKO," *Applied Computational Electromagnetics Society (ACES) Conference*, 2005.

[7] U. Jakobus, "Application of Integral Equation and Hybrid Techniques to Parallel Computation of Electromagnetic Fields in a Distributed Memory Environment," *Applied Computational Electromagnetics Society (ACES) Journal*, Special Issue vol. 13, no. 2, 1998.

[8] U. Jakobus, "*Extension of MoM/PO Hybrid Technique to Homogeneous Dielectric Bodies*," *Applied Computational Electromagnetics Society (ACES) Conference*, *Wash. D.C., 1998.*

[9] J. R. James and P. S. Hall, *Handbook of Microstrip Antennas*, Chapter 2, Peter Peregrinus Ltd., London, UK. 1989.

[10] F. Croq and D. Pozar, "Millimeter-Wave Design of Wide-Band Aperture-Coupled Stacked Microstrip Antennas," *IEEE Transactions on Antennas and Propagation*, vol. 49, no 12, pp. 1770-1776, Dec. 1991.

Steven Weiss was born in Utica, NY in 1955. He graduated from The George Washington University in 1995 with a doctoral degree in Electrical Engineering. He is presently with the Army Research Lab working on antenna systems. His research areas include specialized antennas for military applications.

William O'Keefe Coburn graduated from The George Washington University in 2005 with a doctoral degree in Electrical Engineering. Dr. Keefe Coburn has been with Army Research Laboratory (formerly Harry Diamond Labs) since 1981. His recent experience has been in CEM code development, verification and application in the areas of radar scattering and antennas for Army applications.

Ozlem Kilic graduated from The George Washington University in 1996 with a doctoral degree in Electrical Engineering. She is presently a professor with the Catholic University of America. Her research areas include computational electromagnetics, hardware accelerated programming for scientific computing and radiation and scattering problems from random media.

Infinite Periodic Boundary Conditions in FEKO

Johann van Tonder and Ulrich Jakobus
EM Software and Systems – S.A. (Pty) Ltd
Stellenbosch, South Africa
jvtonder@emss.co.za , jakobus@emss.co.za

Abstract **—** Infinite periodic boundary conditions (PBC's) implemented in FEKO are presented. To enable the analysis of a wide variety of problems, the PBC includes dielectric objects, metallic surfaces, metallic wires and connection points between wires and surfaces. In addition, the geometry is allowed to touch the periodic boundaries (i.e. continuous current flow onto the neighboring cell which requires special basis function treatment).

Index Terms **—** FEKO, Periodic Structures, Antenna Arrays, Frequency Selective Surfaces.

I. INTRODUCTION

FEKO [1] is a commercial and comprehensive 3-D electromagnetic field solver which can be applied to a variety of problems. This paper focuses on periodic structures, for example antenna arrays and frequency selective surfaces. In particular, infinite periodic structures will be analyzed by considering only the unit cell element. Although FEKO can model large finite arrays with the Multilevel Fast Multipole Method (MLFMM), the computational resources of the PBC are much cheaper since we only consider one single unit cell element.

The paper is outlined as follows: Implementation details are given in Section II, verification examples in Sections III-IV, and finally the conclusions in Section V.

II. PERIODIC BOUNDARY CONDITION

The PBC feature enables the analysis of infinite periodic structures by simulating only a single unit cell element. Both 1-D and 2-D (including skewed) lattices are allowed as shown in Figs. 1 and 2, respectively. The phase shift along the lattice vectors can be determined automatically if a plane wave is used as excitation, or it can be specified by the user (say antenna array). Large but finite sized arrays can be approximated as an infinite array. This allows the use of the PBC to minimize the total number of unknowns (and therefore memory) as well as the computation time.

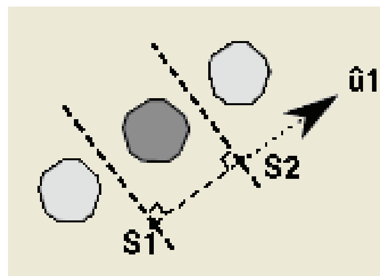

Fig. 1. 1-D periodic boundary.

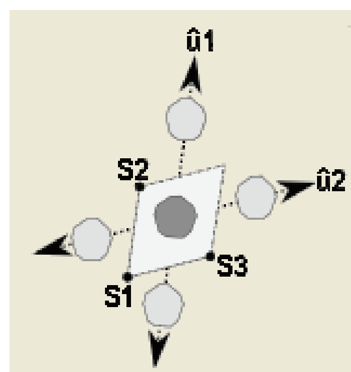

Fig. 2. 2-D periodic boundary with skewed lattice.

A. Geometry Across Boundary

FEKO allows the geometry to touch the periodic boundary (i.e. one part in one cell will then be connected to another geometry part in the neighboring cell). The two unit cells in Fig. 3 are equivalent (different split of a patch array) and will produce the same results.

Modified Rao-Wilton-Glisson (RWG) [2] basis functions on the boundary in Fig. 4 ensure continuous current flow across the unit cell boundary into the neighboring periodic element.

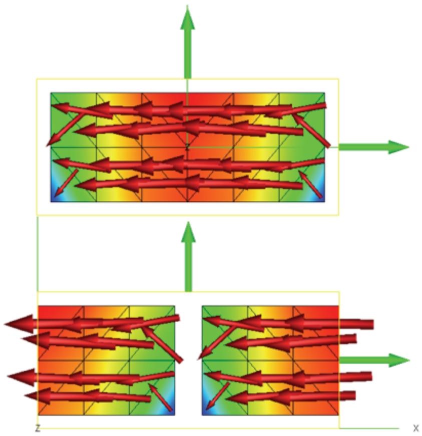

Fig. 3. Current on equivalent unit cells.

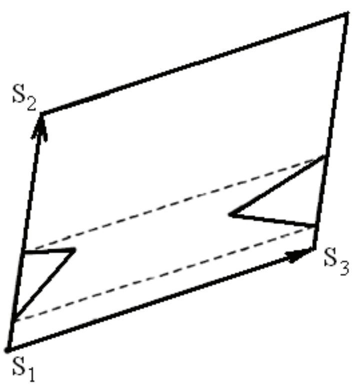

Fig. 4. Special basis function on boundaries.

B. Ewald Transformation

The free space 2-D periodic Green's function in the spectral domain has the form [3]

$$G_p(r,r_s) = \sum_{m=-\infty}^{\infty}\sum_{n=-\infty}^{\infty}\frac{e^{-jk_{tmn}\cdot(\rho-\rho_s)}}{2jAk_{zmn}}\cdot \cdot\left[\, e^{-jk_{zmn}|z-z_s|}\right] \tag{1}$$

and in the spatial domain [3]

$$G_p(r,r_s) = \sum_{m=-\infty}^{\infty}\sum_{n=-\infty}^{\infty} e^{-jk_{t00}\cdot\rho_{mn}}\frac{e^{-jk_0R_{mn}}}{4\pi R_{mn}}. \tag{2}$$

For high accuracy, the PBC implementation uses the Ewald transformation in order to get fast convergence for these infinite sums. In this formulation, the periodic Green's function is written as the sum of a modified spectral portion and a modified spatial portion [3]

$$\boldsymbol{G_p(r,r_s) = G_{p1}(r,r_s) + G_{p2}(r,r_s)}. \tag{3}$$

The modified spectral portion contains the complex error function, and is given by [3]

$$\boldsymbol{G_{p1}(r,r_s)} = \sum_{\boldsymbol{m=-\infty}}^{\infty}\sum_{\boldsymbol{n=-\infty}}^{\infty}\frac{\boldsymbol{e^{-jk_{tmn}\cdot(\rho-\rho_s)}}}{\boldsymbol{4jAk_{zmn}}}\cdot\Big[\sum_{\pm}\boldsymbol{e^{\pm jk_{zmn}|z-z_s|}}\ \mathbf{erfc}\left(\frac{\boldsymbol{jk_{zmn}}}{\boldsymbol{2E}}\pm|\,\boldsymbol{z-z_s}\,|\,\boldsymbol{E}\right)\Big]. \tag{4}$$

Similarly, the modified spatial portion is [3]

$$G_{p2}(r,r_s) = \sum_{m=-\infty}^{\infty}\sum_{n=-\infty}^{\infty}\frac{e^{-jk_{t00}\cdot\rho_{mn}}}{8\pi R_{mn}}\cdot\Big[\sum_{\pm}e^{\pm jk_0R_{mn}}\ \mathrm{erfc}\left(R_{mn}E \pm \frac{jk}{2E}\right)\Big]. \tag{5}$$

The number of terms in the infinite sums is determined automatically by adding more terms until convergence (within 0.01%) is reached. It includes the required Floquet modes (both propagating and evanescent) to achieve high accuracy.

The Ewald transform is also used for the 1-D PBC implementation. The modified spatial portion is the same as for the 2-D case, but the modified spectral portion now contains the exponential integral [4]

$$\frac{1}{4\pi d}\sum_{q=-\infty}^{\infty}e^{-jk_{zq}z}\sum_{p=0}^{\infty}\frac{(-1)^p}{p!}(\rho\mathcal{E})^{2p}E_{p+1}\left(\frac{-k_{\rho q}^2}{4\mathcal{E}^2}\right). \tag{6}$$

C. Dielectrics

In the Method of Moments (MoM), metallic and dielectric triangles allow the use of the surface equivalence principle (SEP) to model any dielectrics within the unit cell. Since we allow the geometry to extend across the unit cell (by using special basis functions), infinite dielectric regions can also be modeled. This makes FEKO a powerful tool to analyze printed antennas with inhomogeneous media. The SEP has a clear advantage over both the finite-element/boundary-integral (FE/BI) method [3], and the hybrid MoM/Green's function method [5] where the volume equivalence principle (VEP) is used. The SEP only meshes the surface of the dielectric, whereas the FE/BI and VEP methods use volume elements to mesh the dielectric.

Another advantage of using the SEP is that we can ignore all dielectric surfaces which are located on the unit cell boundaries. This is valid since identical dielectrics are touching the boundary surface on both the inside and outside (from the neighboring unit cell). In contrast, for the FE/BI method the boundary conditions must also be imposed on the FE mesh located on these side walls.

Multiple dielectric regions are allowed to touch the same boundary to enable the analyses of, for example, a dielectric substrate with periodic holes. The advantages of the SEP will become clear in the microstrip example in the next section.

III. EXAMPLES

A. Pin-fed Microstrip Patch Array

Consider the pin fed microstrip patch antenna in Fig. 5, with side lengths L = W = 30 mm and vertical feed probe at (x,y) = (-7.5,0) mm. The unit cell is square with dimensions a = b = 50 mm, substrate permittivity ε_r = 2.55 and substrate thickness d = 2 mm. A close-up of the pin-fed excitation is shown in Fig. 6, consisting of two wire segments connecting the ground plane and the patch.

The SEP is used to model the dielectric, with the vertical side walls excluded from the mesh below. The ground plane and patch are modeled with metallic triangles, and dielectric triangles are used to model the top dielectric interface. There are special basis functions on the periodic boundaries for both the metallic and dielectric triangles to ensure current continuity.

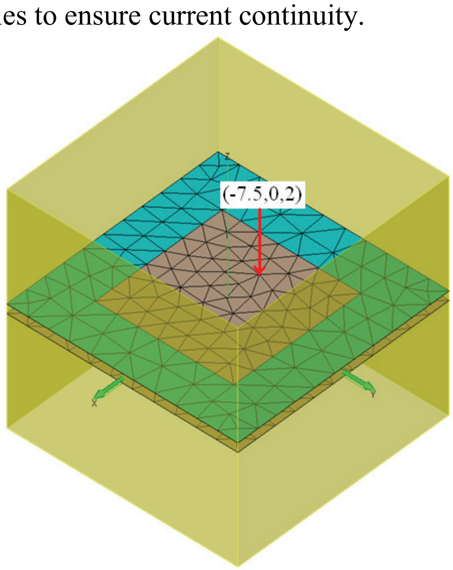

Fig. 5. Pin-fed microstrip patch array.

The active input impedance is defined as the input impedance in the active array environment when all elements are excited. We will compute the active input impedance when all elements are fed in phase to produce a main beam at broadside. The calculated broadside scanning input resistance and reactance are shown in Figs. 7 and 8, respectively. Good agreement to the published FE/BI results [6] can be seen.

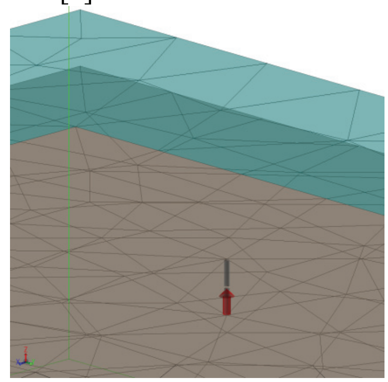

Fig. 6. Close-up of pin-fed excitation.

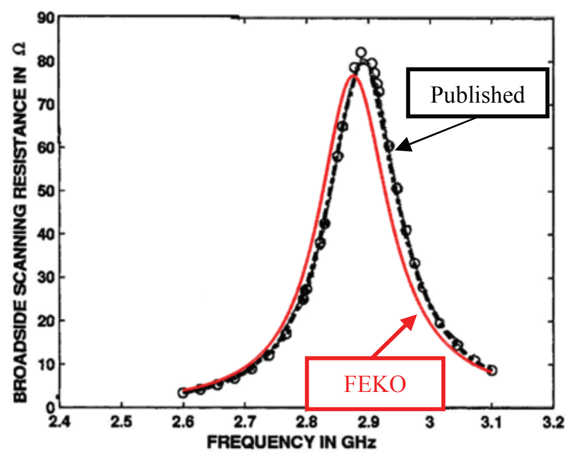

Fig. 7. Active input resistance.

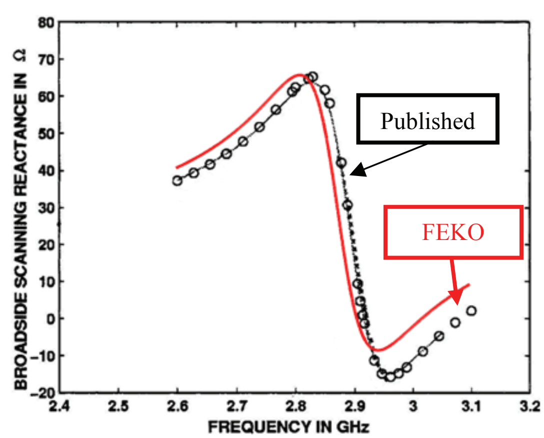

Fig. 8. Active input reactance.

B. Printed Dipole Array

Scan blindness will be demonstrated for the infinite array of printed dipoles [5] in Fig. 9. Parameters: Dipole length L = 0.39 λ, width W = 0.01 λ, square unit cell a = b = 0.5 λ, substrate thickness d = 0.19 λ and permittivity ε_r = 2.55. The centre of the dipole is excited by an edge voltage source.

The active reflection coefficient is defined when all dipoles are excited with the correct phase to produce a main beam in the direction ϑ (ϑ=0° is broadside):

$$R(\vartheta) = \frac{Z_{in}(\vartheta) - Z_{in}(\vartheta = 0°)}{Z_{in}(\vartheta) + Z_{in}^{*}(\vartheta = 0°)}. \tag{7}$$

The feed network is matched for broadside scanning to the internal source impedance of Z_{in} (ϑ = 0°).

The computed active reflection coefficient versus scan angle compares very well to the published results [5], for both magnitude and phase as shown in Figs. 10 and 11, respectively. Note the unity reflection coefficient at the scan blindness angle of 45°.

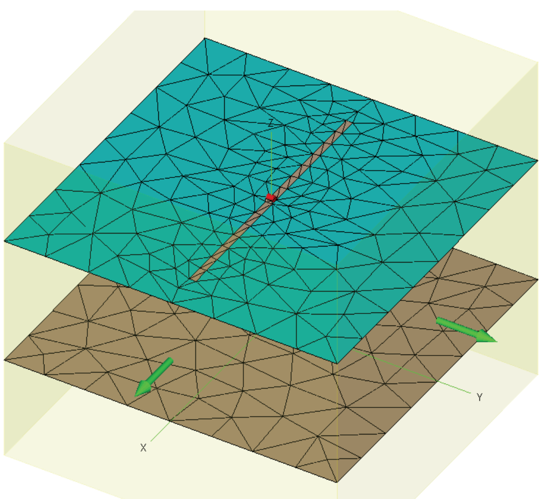

Fig. 9. Printed dipole array.

C. Frequency Selective Surfaces

The Jerusalem-cross frequency selective surface (FSS) in Fig. 12 was analyzed. Fig. 13 shows the unit cell and plane wave excitation.

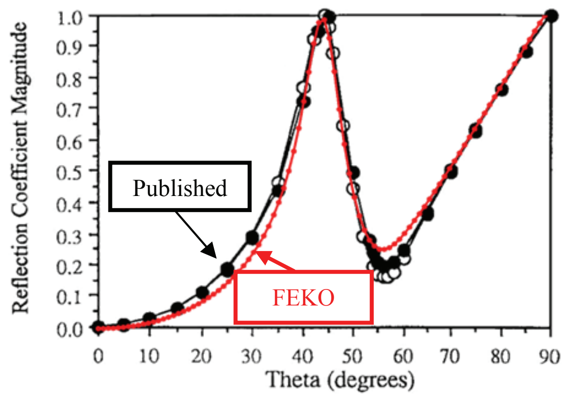

Fig. 10. Magnitude of active reflection coefficient.

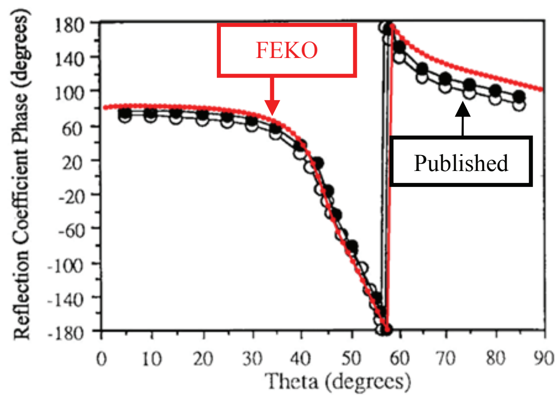

Fig. 11. Phase of active reflection coefficient.

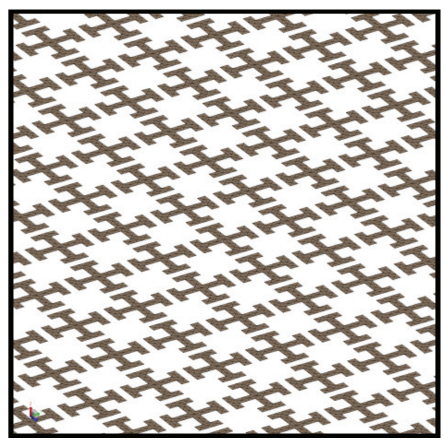

Fig. 12. Jerusalem-cross FSS.

To verify the PBC results the MLFMM was used to analyze a large finite 51x51 FSS. Excellent agreement in the current distribution at 7 GHz can be seen in Figs. 14 and 15.

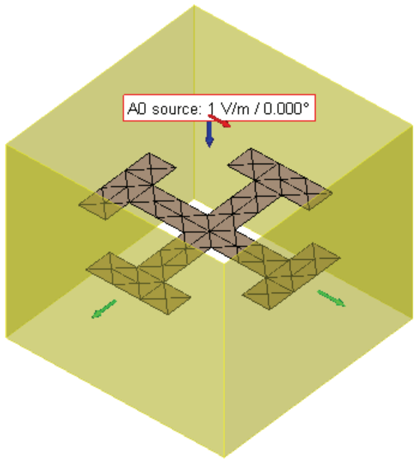

Fig. 13. FSS unit cell and plane wave excitation.

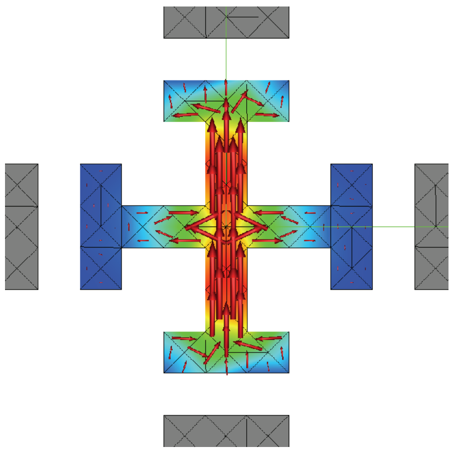

Fig. 14. Finite 51x51 FSS solved with MLFMM.

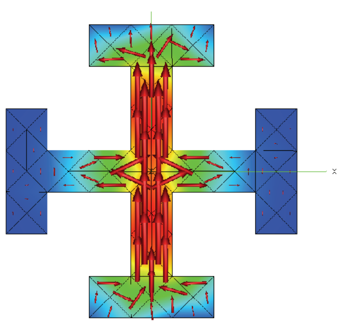

Fig. 15. Single element solved with infinite PBC.

The magnitude and phase of the reflection coefficient (versus frequency) are plotted in Figs. 16 and 17, respectively. This is for a normal incident plane wave on the FSS. Excellent agreement to the published results [7] can be seen, for both magnitude and phase.

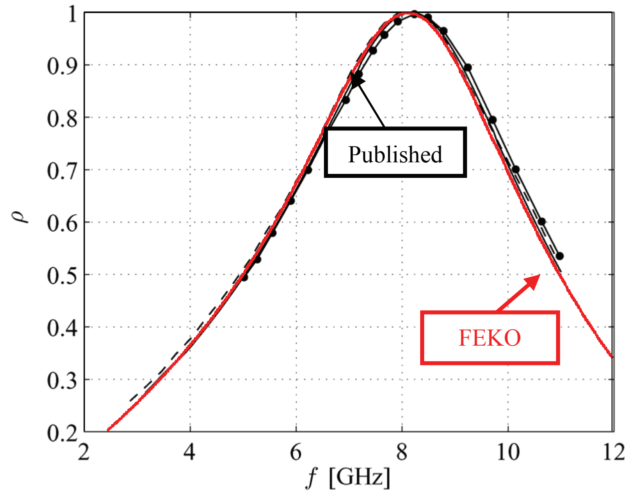

Fig. 16. Magnitude of the reflection coefficient.

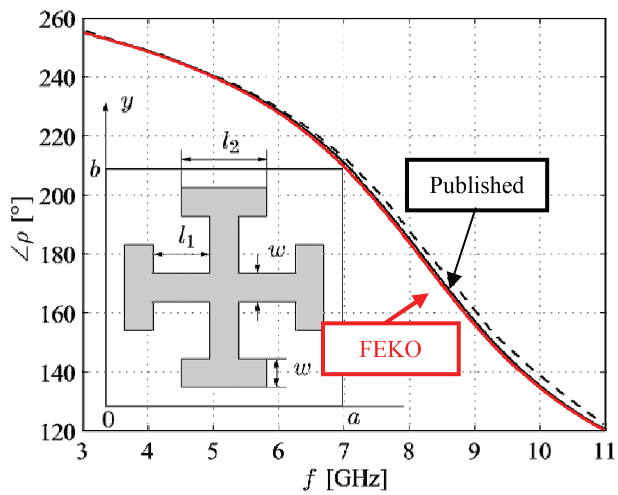

Fig. 17. Phase of the reflection coefficient.

D. Infinite Cylinder

An infinite cylinder shown in Fig. 18 is modeled as a finite cylinder with 1-D PBC at both ends. FEKO can handle arbitrary incidence, but the published results for this example used a z-directed normal incident plane wave. The diameter of the cylinder is varied and the scattered electric field is computed versus the observation angle, in order to get the scattering width (SW) defined as

$$\sigma_{2-D} = \lim_{\rho\to\infty} \left(2\pi\rho \frac{| E_z^s |^2}{| E_z^i |^2} \right). \tag{8}$$

In Fig. 19 the computed SW is in very good agreement to the published results [8].

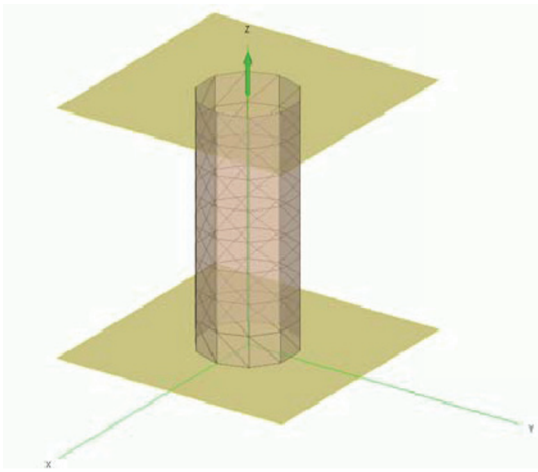

Fig. 18. Unit cell of infinite cylinder.

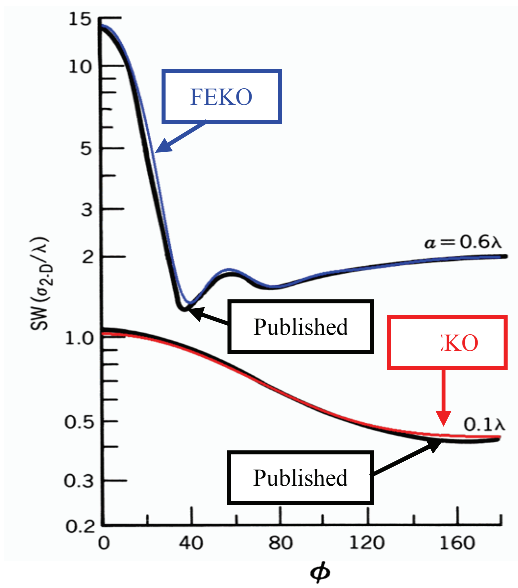

Fig. 19. Scattering width of infinite cylinder.

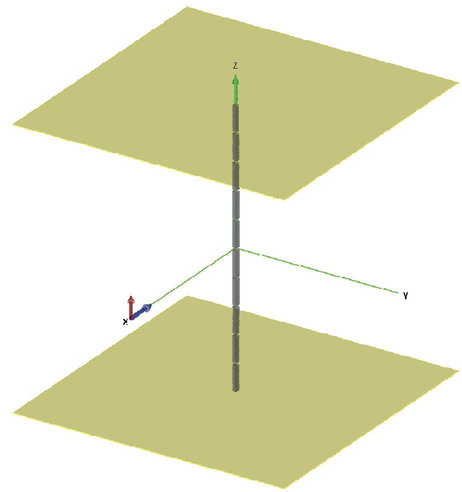

Fig. 20. Unit cell of infinite wire.

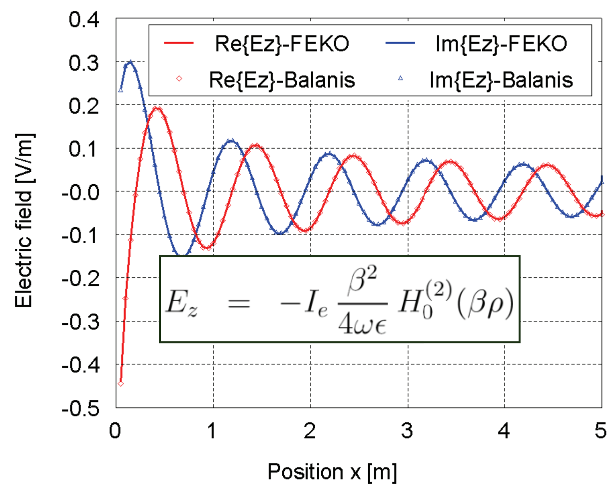

Fig. 21. Near electric field of infinite wire.

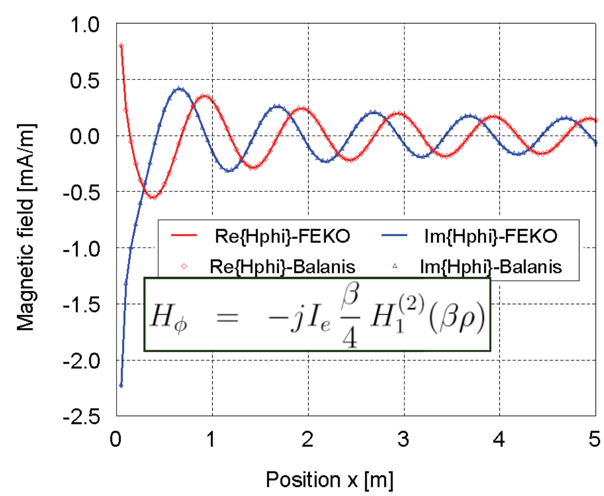

Fig. 22. Near magnetic field of infinite wire.

E. Infinite Wire

To verify the implementation of the special basis functions for wires at 1-D periodic boundaries consider the infinite z-directed wire, with the unit cell shown in Fig. 20. A z-directed plane wave is incident along the x-axis. The near-field for the infinite wire is known analytically [8]. The computed near electric and magnetic fields are shown in Figs. 21 and 22, respectively. Excellent agreement to the analytical values can be seen. This verifies the special basis function implementation for wires at the boundaries, as well as the near-field computation for both electric and magnetic fields together with the PBC.

IV. FAR-FIELD

In this section the far-field of a finite *M*x*N* array will be computed using the infinite array approximation to obtain the current distribution on the elements. Consider the example of a 2-D antenna array of strip dipoles, with the unit cell in Fig. 23. Parameters: Dipole length L = 0.45 λ, width W = 0.02 λ, unit cell length a = 0.50 λ and width b = 0.30 λ. The elements are fed with the correct phase increment to obtain a main beam pointing in the direction ϑ=20°, requiring a phase increment of $(2\pi a/\lambda)\sin\vartheta =$ 61.564°.

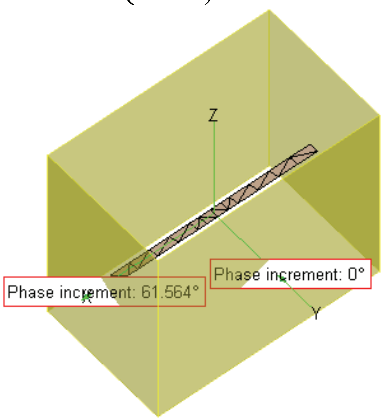

Fig. 23. Unit cell of strip dipole array.

The PBC analysis will give the correct current distribution on the unit cell dipole in an infinite array environment (including all mutual coupling). With this current distribution, the single unit cell dipole on its own radiates a doughnut shaped far-field pattern as shown in Fig. 24.

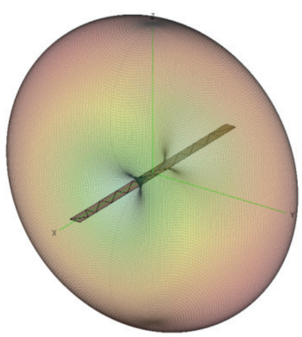

Fig. 24. Far-field of single unit cell element.

To compute the far-field of a finite *M*x*N* array as shown in Fig. 25, we sum the far-field pattern of the unit cell with the correct phase and position of each element in the array. Computing the far-field using the PBC ignores edge effects, since it assumes that the current distribution is identical on all array elements (except for the phase shift). The far-field computed with the PBC approximation was validated using the MLFMM, which analyzes the complete finite array. The MLFMM computes the correct currents on all elements and includes edge effects. Results for two array sizes are shown in Figs. 26 and 27. As expected, the main beam points in the direction ϑ=20°. Good agreement between the PBC approximation and the MLFMM can be seen.

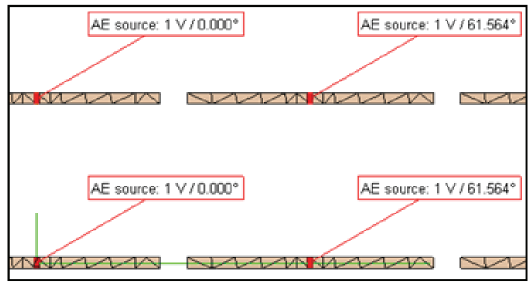

Fig. 25. Finite *M*x*N* array.

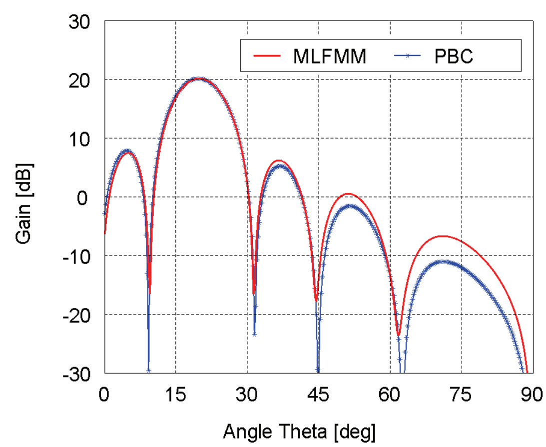

Fig. 26. Far-field of 11 x 11 array.

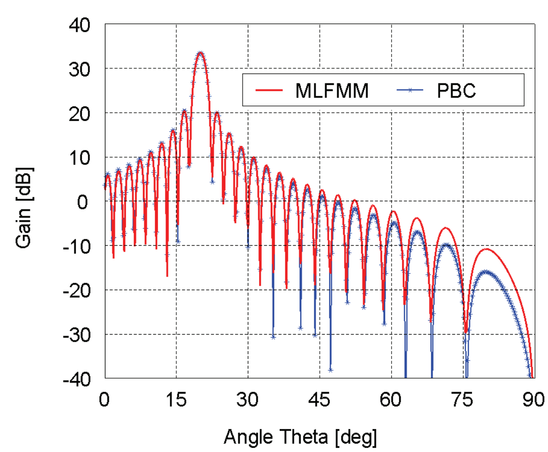

Fig. 27. Far-field of 51 x 51 array.

V. CONCLUSIONS

Infinite periodic boundary conditions were implemented in FEKO using the efficient Ewald transform to obtain fast convergence for the infinite sums. Both 1-D and 2-D (including skewed) lattices are supported. The geometry is allowed to extend into the neighboring cell with the use of special basis functions on the boundary. The phase shift along the periodic lattice can be determined automatically from plane wave excitations, or it can be specified by the user. The PBC includes metallic and dielectric triangles, wires, connection points. This makes FEKO a powerful tool to analyze printed antenna arrays with inhomogeneous media and also frequency selective surfaces. By ignoring edge effects, the PBC enables efficient far-field calculations of finite *M*x*N* arrays.

REFERENCES

[1] EM Software and Systems – S.A. (Pty) Ltd, Stellenbosch, South Africa: *FEKO – Field Computations Involving Bodies of Arbitrary Shape*, http://www.feko.info.

[2] S. M. Rao, D. R. Wilton and A. W. Glisson, "Electromagnetic Scattering by Surfaces of Arbitrary Shape", *IEEE Trans. Antennas Propagat*., vol. 30, no. 3, pp. 409-418, May 1982.

[3] T. F. Eibert, J. L. Volakis, D. R. Wilton and D. R. Jackson, "Hybrid FE/BI Modeling of 3-D Doubly Periodic Structures Utilizing Triangular Prismatic Elements and an MPIE Formulation Accelerated by the Ewald Transformation", *IEEE Trans. Antennas Propagat*., vol. 47, no. 5, pp. 843-849, May 1999.

[4] F. Capolino, D. R. Wilton and W. A. Johnson, "Efficient computation of the 3D Green's function for the Helmholtz operator for a linear array of point sources using the Ewald method", *Journal of Computational Physics*, vol. 223, pp. 250-261, 2007.

[5] W. J. Tsay and D. M. Pozar, "Radiation and Scattering from Infinite Periodic Printed Antennas with Inhomogeneous Media", *IEEE Trans. Antennas Propagat*., vol. 46, no. 11, pp. 1641-1650, 1998.

[6] D. S. Filipovic, L. S. Anderson and J. L. Volakis, "A Multiresolution Method for Simulating Infinite Periodic Arrays", *IEEE Trans. Antennas Propagat*., vol. 48, no. 11, pp. 1784-1786, November 2000.

[7] I. Stevanovic, P. Crespo-Valero, K. Blagovic, F. Bongard and J. R. Mosig, "Integral-Equation Analysis of 3-D Metallic Objects Arranged in 2-D Lattices Using the Ewald Transformation", *IEEE Trans. Microwave Theory and Techniques*, vol. 54, no. 10, pp. 3688-3697, October 2006.

[8] C. A. Balanis, Advanced Engineering Electromagnetics, Wiley, pp. 607, 1989.

Johann van Tonder received the Ph.D. degree in electronic engineering from the University of Stellenbosch, South Africa, in 1995. Since 1996, he has been a FEKO research and development engineer.

Ulrich Jakobus received the diploma, doctoral, and Habilitation degrees in Electrical Engineering from the University of Stuttgart, Germany in 1991, 1994, and 1999, respectively. The focus of his research was numerical algorithms for high frequency electromagnetic simulations and the development of the computer code FEKO. In October 2000 he joined EM Software & Systems, Stellenbosch, South Africa, where he is a Director, the FEKO Product Manager, and heading the FEKO kernel team.

A Mode Selecting Eigensolver for 2D FIT Models of Waveguides

Bastian Bandlow, and Rolf Schuhmann
FG Theoretische Elektrotechnik, EIM-E
University of Paderborn, D-33098 Paderborn, Germany
bandlow@tet.upb.de, schuhmann@tet.upb.de

Abstract **─** For the computation of eigenmodes in multimodal waveguide structures, the Jacobi-Davidson eigenvalue solver is extended by a vector-based weighting function. It allows to generate only modes with a desired field distribution. The performance of this solver is studied by means of an eigenmode computation in a photonic crystal fiber which is discretized by the finite integration technique. The new algorithm is able to separate the modes in the fiber core from a number of non-physical modes which originate from a transversal PML-type boundary condition.

Index Terms **─** Jacobi-Davidson, Eigenvalues, Mode Calculation, Photonic Crystal Fiber.

I. INTRODUCTION

The computation of eigenvalues in two- and three-dimensional electromagnetic structures is a challenging task in engineering. Since dielectric waveguides for optical applications (fibers) can be highly multi-modal, the corresponding 2D-eigenvalue problem may include a high number of guided modes, with only little differences in their propagation constants.

For such modes, the power is confined within the core of the fiber, and the field strength in the cross section decays exponentially with increasing radius. With this a-priori knowledge, one may wish to apply an adequate transversal boundary condition, which allows to truncate the mesh close to the core of the fiber. Such an 'open boundary' can be modeled by a perfectly matched layer (PML), which absorbs the evanescent wave parts by real-coordinate stretching [1]. However, the application of the PML changes the discrete eigenvalue problem, and the staggered material layers of the PML themselves can act as a waveguiding structure. This leads to a spoiled spectrum, which consists not only of the desired guided modes within the core, but we observe a lot of additional non-physical modes, which are guided inside the PML.

In order to get rid off of these spurious modes, we use an extended Jacobi-Davidson eigenvalue solver [2] [3] which allows to distinguish between the two classes of eigenvectors *within the solution process* and to produce only the desired core-modes in an efficient way.

Preliminary work has been done by [4], [5] and [6] for microstrip lines and lasing structures. They rely on smart chosen, limited areas of the spectrum in order not to calculate too many of the undesired eigenmodes. However it is unavoidable that some of them occur in their approach since not the eigenvector is analyzed during iteration but only the eigenvalue. Therefore, they identify the desired eigenmodes in an a-posteriori processing step.

II. FORMULATION

The eigenvalue problem for waveguide cross-section is formulated using the finite integration technique (FIT) [7], [7].

The FIT is based on a spatial segmentation of the computational domain by a computational grid pair, the normal grid G and the dual grid $\widetilde{G}$. The degrees of freedom of the method are the so-called integral state variables, defined as integrals of the electric and magnetic field vectors over edges $L_i, \widetilde{L}_i$ and facets $A_j, \widetilde{A}_j$ of the normal grid G and the dual grid $\widetilde{G}$, respectively:

$$\widehat{e}_i = \int_{L_i} \vec{E} \cdot d\vec{s} \qquad \widehat{\widehat{d}}_i = \int_{\widetilde{A}_i} \vec{D} \cdot d\vec{A} \tag{1}$$

$$\widehat{\widehat{j}}_i = \int_{\widetilde{A}_i} \vec{J} \cdot d\vec{A} \tag{2}$$

$$\widehat{h}_j = \int_{\widetilde{L}_j} \vec{H} \cdot d\vec{s} \qquad \widehat{\widehat{b}}_j = \int_{A_{ji}} \vec{B} \cdot d\vec{A} \tag{3}$$

Using this discrete formulation the fundamental physical properties of Maxwell's equations like energy and charge conservation and also the orthogonality of eigenmodes are maintained. The Maxwell grid equations can be written down as

$$\mathbf{C}\widehat{\mathbf{e}} = -\frac{d}{dt}\widehat{\widehat{\mathbf{b}}} \qquad \tilde{\mathbf{C}}\widehat{\mathbf{h}} = \frac{d}{dt}\widehat{\widehat{\mathbf{d}}} + \widehat{\widehat{\mathbf{j}}} \tag{4}$$

with the material relations $\widehat{\widehat{\mathbf{d}}} = \mathbf{M}_\varepsilon \widehat{\mathbf{e}}$, $\widehat{\widehat{\mathbf{j}}} = \mathbf{M}_\kappa \widehat{\mathbf{e}}$ and $\widehat{\widehat{\mathbf{b}}} = \mathbf{M}_\mu \widehat{\mathbf{h}}$. $\mathbf{C}$ and $\tilde{\mathbf{C}}$ are the topological curl-operators containing entries with {-1;0;1}. All the FIT matrices of topological operators are sparse and have band structure which allows an efficient processing on computer systems.

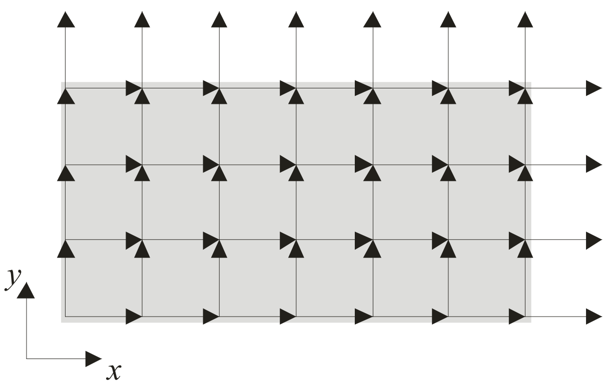

Fig. 1. FIT discretization scheme of the 2D light grey shape. nx components in x-direction and ny components in y-direction: Some components do not exist.

The FIT discretization of a waveguide cross-section is shown in Fig. 1 for the tangential electric grid voltages $\widehat{\mathbf{e}}_t$. It has been shown in former work [9] that the eigenvalue problem

$$(\mathbf{A}_1 - k_z^2 \mathbf{A}_2 - \omega^2 \mathbf{I})\widehat{\mathbf{e}}_t = 0 \tag{5}$$

can be formulated for unknown k_z or unknown ω. $\mathbf{A}_1$ contains the 2D curl-curl-operator and the inverse permeability. $\mathbf{A}_2$ contains again some material properties cf. [9]. The longitudinal components $\widehat{\mathbf{e}}_z$ can be obtained through continuous calculus considerations. The 2D eigenvalue problem for the tangential electric grid voltage $\widehat{\mathbf{e}}_t$ (5) leads in the case of a given frequency ω and a PML for evanescent tangential waves to a system matrix $\mathbf{A}_{cc} = \mathbf{A}_2^{-1}(\mathbf{A}_1 - \omega^2\mathbf{I})$, which is in the specific case real and non-symmetric. A symmetrization is in some cases theoretically possible, as long as no complex modes occur. The number of degrees of freedom is $2n_x n_y - (n_x + n_y)$ for n_x, n_y being the number of discretization steps in the particular direction, when no special boundary treatment is applied (cf. Fig. 1).

III. JACOBI-DAVIDSON ALGORITHM

The Jacobi-Davidson algorithm [2], [3] is feasible for the computation of a few interior or exterior eigenvalues of the spectrum. Within the algorithm, the original eigenvalue problem is projected and solved on a low-dimensional subspace $\mathbf{V}$, which is gradually refined by solving a correction equation. We use a Matlab implementation of the JD-algorithm from its original authors which is available from [3]. As so-called target value, an end of the spectrum or an arbitrary value within the spectrum can be specified. According to this target value, the approximate eigenvalues are sorted in different sophisticated ways during the solution process. Moreover, the JD algorithm computes the eigenpairs one after another and not a block of eigenvalues simultaneously.

The solution of the low-dimensional, projected eigenvalue problem, however, does not only yield approximations of the eigenvalues, but of course we also obtain approximations of the corresponding eigenvectors. If we expand them again to full dimension, we can interpret these vectors as approximations of field solutions of the discrete formulation.

To establish a new criterion for the choice of the desired modes, we test these field distributions against a weighting vector $\mathbf{f}$, which describes a scalar spatial distribution for each field component with its maximum at the core and a decay towards the boundaries. The components of these vectors are depicted in Fig. 2. We choose a Gaussian profile, since it is easy to define and it fulfills the requirements of a strong decay toward the boundaries. Moreover, the Gaussian shape is not equal to a solution of the problem and therefore we do not plug in a pre-known solution into the process.

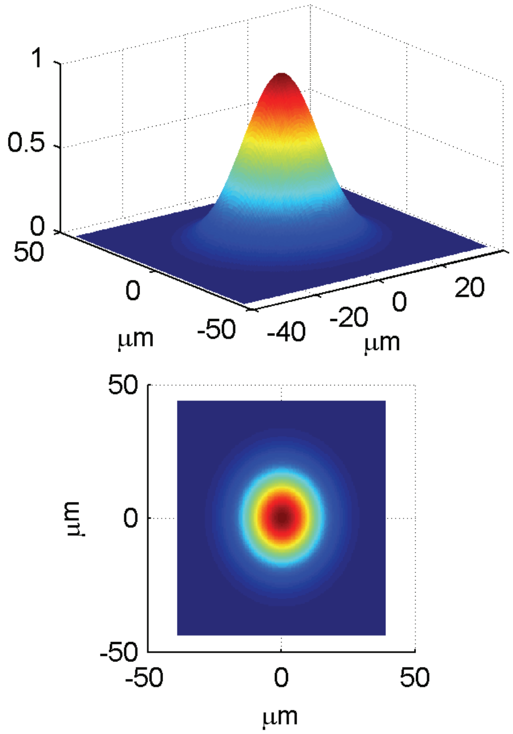

Fig. 2. Weighting vector $\mathbf{f}$ with Gaussian profile for x - and y - components.

Now, we can measure the quality of our approximate eigenvectors u_i within the JD-algorithm very easily. The product

$$\psi = \langle \mathbf{f}; |\mathbf{u}_i| \rangle \tag{6}$$

with $\|\mathbf{u}_i\|_2 = 1$ and $\|\mathbf{f}\|_\infty = 1$ can be used to decide, whether the field strength is concentrated around the core ($\psi > 1$) or whether it is concentrated inside the boundary ($0 < \psi < 1$). Taking the absolute value of the eigenvector's components $|\mathbf{u}_i|$ ensures that also core guided modes with a null in the center are found. The weighting function does not have to provide necessarily the profile shape of the modal field to be computed. The weighting function only provides information about the spatial distribution of the field to be computed.

Within the original Jacobi-Davidson algorithm the eigenvalue approximations are sorted according to their distance to the target value. In our modification of the algorithm we select only those of the sorted eigenvalue approximations, which fulfill the weighting criterion (6).

IV. NUMERICAL EXAMPLE

We choose a photonic crystal fiber (PCF) [10] as an example, which is operated at $2\mu\text{m}$ wavelength (Fig. 3). It consists of a glass core ($n_G = 1.45$) with a surrounding hexagonal lattice of air holes. Each hole has a radius of $2.9\mu\text{m}$ and the lattice constant is $9.4\mu\text{m}$. The discrete model is truncated by a PML boundary condition and has the dimensions $74\mu\text{m} \times 84\mu\text{m}$.

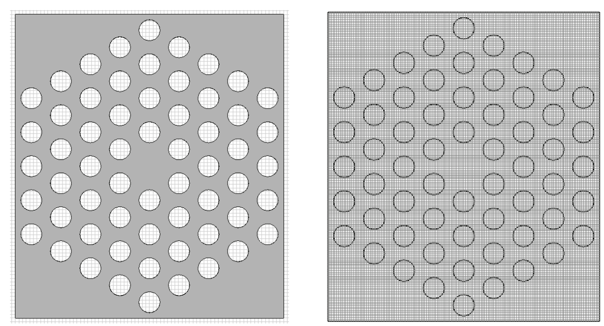

Fig. 3. PCF consisting of glass and air holes ($74\mu\text{m} \times 84\mu\text{m}$). Mesh settings ($155 \times 193$ lines).

The cross section of the fiber is discretized by the finite integration technique, using CST MICROWAVE STUDIO [11] for all preprocessing steps. The resulting two-dimensional model has 155×193 grid points, and we add 4 grid lines in each transversal direction for the PML. The eigenvalue problem [9] for the squared propagation constants β^2 is linear, of the type

$$\mathbf{A}_{cc}\mathbf{x} = \lambda\mathbf{x}, \tag{7}$$

and has 64438 degrees of freedom. We are interested in the first two guided modes of the PCF whose distribution of its electrical field strength is depicted in Fig. 4.

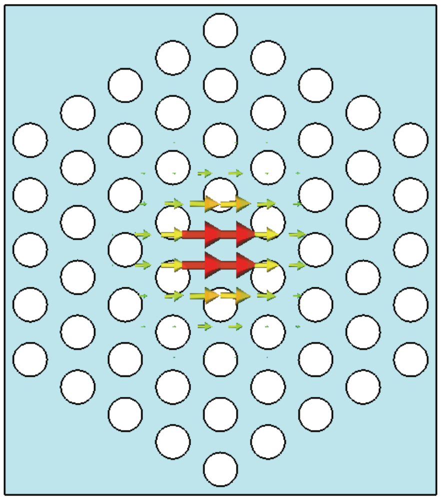

Fig. 4. Electrical field of the first desired mode.

Fig. 6 shows the part of the spectrum with the smallest real part, since the propagation constants β_i are calculated from the eigenvalues λ_i by $\beta_i = \sqrt{-\lambda_i}$. The first 36 modes (marked by diamonds) are guided within the PML according to Fig. 5. Modes 37 and 38 are the ones we are looking for and which fulfill our weighting criterion in equation (6).

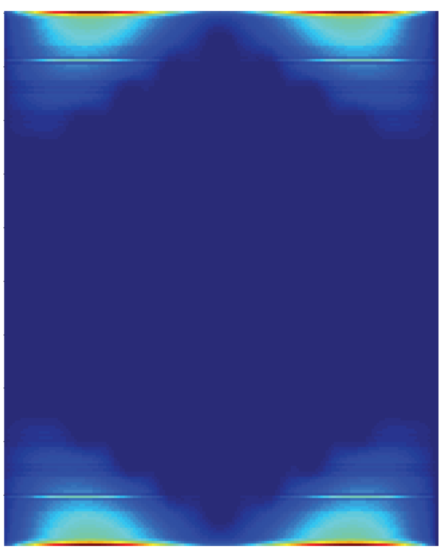

Fig. 5. Magnitude of electrical field of one of the undesired modes: Wave guiding within the PML.

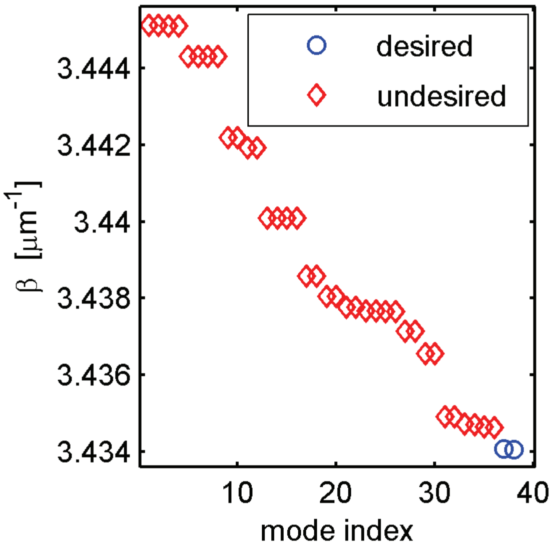

Fig. 6. Propagation constants β of the PCF. The modes with indices 37 and 38 (o) are the desired ones, which are guided by the core.

V. COMPARISON OF JD SOLVERS

The unmodified Jacobi-Davidson solver as well as weighted JD solver are used to compute the first two guided modes of the PCF from the previous section. For all eigensolver computations, the system matrix is preconditioned through a shift of the spectrum before the solver starts, which significantly improves the condition of the eigenvalue problem. The target is chosen to be the smallest real part. The initial subspace is generated randomly and is fed in each of both solvers in order to have equal starting conditions. The correction equation within the JD algorithm is solved by a direct solver in both solvers. This is time-consumptive, but we can expect at least a second order convergence. For the ordinary JD solver the dimension of the search subspace is kept between 7 and 12, while for the weighted JD solver no reduction of the search subspace is done. The eigenvalues are accepted when the residual is below 1e-13.

Table 1: Results of the standard JD and the weighted JD.

Version	Modes	Time	Iterations
standard	38	2678 s	108
weighted	2	165 s	46

The results are given in Table 1. We look for two core guided modes, which are found by both solvers. The weighted JD outperforms the standard JD by a factor of 15 in time. The number of iterations, which are needed to gradually refine the subspace, is reduced by a factor larger than two.

The reason for the disagreement of these two factors can be seen in the convergence history in Fig. 7 and Fig. 8. A lot of iterations are needed at the beginning of both algorithms, in order to improve the quality of the subspace. Once refined, the subspace allows the quick computation of the consecutive eigenvalues.

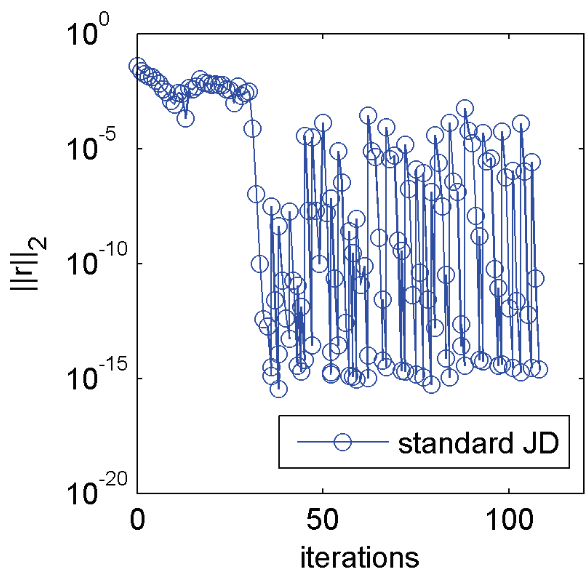

Fig. 7. Convergence history of the standard JD.

VI. SOLVER TUNING

In further investigations we consider the choice of the initial subspace, the correction equation and the maximum dimension of the search subspace. Details to the selection process of the prospective eigenvectors are given.

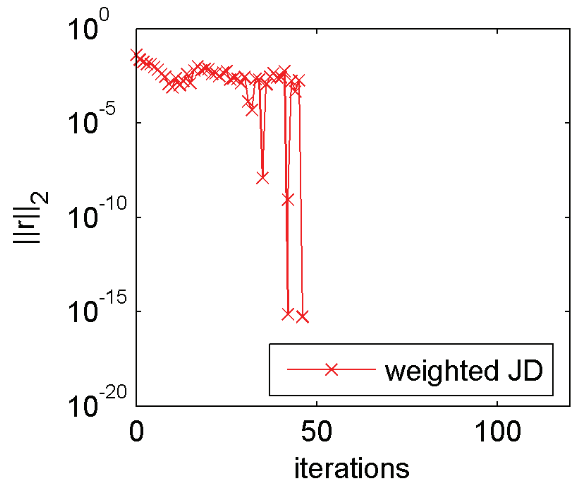

Fig. 8. Convergence history of the weighted-JD.

A. Initial Subspace

Since we are interested in modes, which have a similar spatial field distribution like the weighting function from (6) we use weighting function itself as the start vector for the Jacobi-Davidson process. Fig. 9 shows the convergence history. The number of iterations needed to find both of the desired modes is reduced to 15. This is less than one third of the 46 iterations the weighted JD algorithm without special initial vector treatment needed.

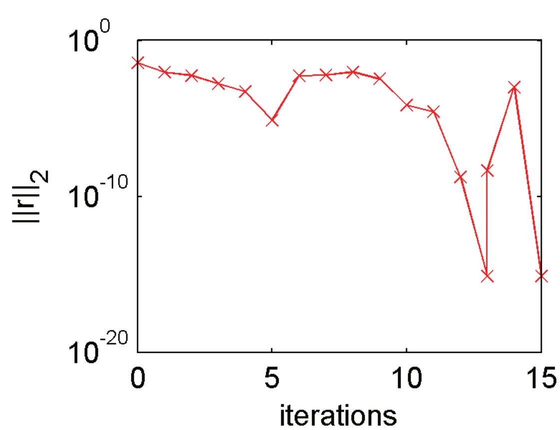

Fig. 9. Convergence history of the weighted-JD with the weighting function applied as start vector.

B. Correction Equation

The correction equation of the Jacobi-Davidson process is used to generate the subsequent extensions for the search subspace. For this, a linear system of equations has to be solved. In the preceding sections the correction equation has been solved directly, which turns out to be computationally quite expensive. Alternatives are iterative solvers which all need preconditioners in order to perform well. The JD process is supposed to converge even with an inexactly solved correction equation.

We choose exemplarily the bicgstab solver [12] which is included in the jdqr-package from [3]. As a preconditioner we take the LU factorization of $\mathbf{A}-\lambda_{approx}\mathbf{I}$, where λ_{approx} is an approximation of the eigenvalue with the smallest real part. We choose arbitrarily $\lambda_{approx} = 3.624e13$, which is not inside the spectrum as the comparison with Fig. 6 shows. As initial subspace we use again the random subspace from section V.

Table 2: Results of the weighted JD solver for different residuals in the solution of the correction equation.

bicgstab Tol	5e-1	1e-1	1e-2
bicgstab MaxIt	200	200	400
JD Iterations	100	48	42
Time / sec	679	773	1566

In Table 2 some results are given and it turns out that indeed the correction equation may be solved with a certain amount of error and the JD process finds the 2 guided modes anyway. Not always is the desired accuracy reached by the bicgstab and the maximum number of iterations aborts the iteration. The number of JD iterations needed is around the same as the result of Table 1. The reason for the increased time, although the number of JD iterations is comparable, is the well-parallel performing direct solver while the iterative bicgstab is more or less single-threaded. An interesting case occurs in the last column where the number of JD iterations is less than in the case where the correction equation is solved exactly. The only reason for that is the rather good preconditioner which is a complete LU factorization at an eigenvalue estimation.

C. Search Subspace Dimension

The reduction of the search subspace after it has reached a specific dimension, limits the maximal dimension of the low-dimensional eigenvalue problem to be solved. We make a study in which we vary the maximum search space dimension. The correction equation is solved exactly. The minimum dimension should not be too small, otherwise it may happen that none of the eigenvector approximations fulfills the weighting criterion.

Table 3: Results of the weighted JD solver for different residuals in the solution of the correction equation.

$\dim_{\min}$	7	7	13
$\dim_{\max}$	12	21	21
JD Iterations	81	59	82

In Table 3 there are the results for different maximum dimensions of the search subspace. It turns out that there is a choice of the maximum dimension, which leads to accelerated convergence.

D. Selection Process

In our first implementation of this algorithm, the eigenvalues of the low-dimensional problem are simply sorted according to their distance to the target. In the second step, only those eigenvalues are retained, whose full-dimension eigenvectors fulfill the weighting criterion (6) with $\psi > 1$. It is important to note, that these approximate eigenpairs do not fulfill the eigenvalue problem very well. That means that the residual

$$\|\mathbf{r}\|_2 = \|\mathbf{A}\mathbf{u}_i - \theta_i\mathbf{u}_i\|_2 \tag{8}$$

for a specific approximate eigenpair (θ_i, u_i) is not negligible small in general. Especially in the case when the selection process leads to an oscillation between two eigenvalues during the iteration, one of them could be fixed for some iterations, in order to get a better residual and decide afterwards, whether it fulfills the weighting criterion or not. If high-accuracy eigenvectors occur within the process, which do not fulfill the weighting criterion, they can be added to the subspace to prevent the process to regenerate them again.

These circumstances could be considered in an improved implementation.

VII. CONCLUSION AND OUTLOOK

We have shown that a simple extension of the selection process of the approximate eigenpairs within a Jacobi-Davidson algorithm leads to a superior convergence behavior for waveguide models which are surrounded by a PML boundary condition. The number of eigenvalues which have to be computed until we arrive at the desired ones is drastically reduced. The occurrence of degenerated (or nearly degenerated) modes are not unusual in unbounded waveguides. They have also shown up in our examples, and the modified solver obviously has no problems with them. The weighting function should be chosen carefully enough that criterion (6) yields $\psi < 1$ for the external mode (guided within the PML) and $\psi > 1$ for the core guided mode. Then the undesired mode is eliminated by the selection process.

Of course, there are a couple of possible improvements concerning the performance, the computational efficiency, and the range of application of the modified eigensolver:

At first, other weighting functions may be used, e.g. it should be possible to find only modes with a specific polarization, modes with energy transport in specific regions of the cross section, etc. In the current implementation only the values of the electrical grid voltage are taken into account by the weighting function. However, it may also be applied to Poynting's vector or other secondary quantities. Furthermore, the fact that we identify an undesired eigenvector without doing anything against its reoccurrence is not yet satisfactory. Since we also know the corresponding eigenvalue, it should be possible to apply some kind of filter, which is able to suppress the undesired modes. Another idea would be to implement the weighting into other eigensolvers such as the implicitly restarted Arnoldi algorithm, where it should also be possible to eliminate the undesired eigenvectors from the approximate subspace.

Finally, this kind of solver can also be applied to other types of waveguides such as microstrip lines or even three dimensional structures.

REFERENCES

[1] J.-P. Berenger, “Application of the CFS PML to the absorption of evanescent waves in waveguides”, Microwave and Wireless Components Letters, IEEE, vol. 12, no. 6, pp. 218-220, Jun 2002.

[2] G. L. G. Sleijpen and H. A. Van der Vorst, “A Jacobi-Davidson iteration method for linear eigenvalue problems”, SIAM J. Matrix Anal. Appl., vol. 17, no. 2, pp. 401-425, 1996.

[3] M. Hochstenbach, “Jacobi-Davidson gateway”, *http://www.win.tue.nl/casa/research /topics/jd/*.

[4] G. Hebermehl, F.-K. Hübner, R. Schlundt, T. Tischler, H. Zscheile and W. Heinrich, “Eigen mode computation of microwave and laser structures including PML”, in Scientific Computing in Electrical Engineering, ser. Mathematics in Industry, W. H. A. Schilders, E. J. W. ter Maten, and S. H. M. J. Houben, Eds., vol. 4. Springer Verlag, pp. 196-205, 2004.

[5] G. Hebermehl, F.-K. Hübner, R. Schlundt, T. Tischler, H. Zscheile and W. Heinrich, “Perfectly matched layers in transmission lines”, in Numerical Mathematics and Advanced Applications, ser. ENUMATH 2001, F. Brezzi, A. Buffa, S. Corsaro, and A. Murli, Eds. Springer Italia, pp. 281-290, 2001.

[6] G. Hebermehl, J. Schefter, R. Schlundt, T. Tischler, H. Zscheile, and W. Heinrich, “Simulation of microwave and semiconductor laser structures including PML: Computation of the eigenmode problem, the boundary value problem, and the scattering matrix”, in Proc. 5th International Workshop Scientific Computing in Electrical Engineering (SCEE), Capo D'Orlando, Italy, September 5-9, 2004, ser. Scientific Computing in Electrical Engineering, G. M. A. Anile, G. Ali, Ed. Springer Verlag, pp. 203-214, 2006.

[7] T. Weiland, “Eine Methode zur Lösung der Maxwellschen Gleichungen für sechskomponentige Felder auf diskreter Basis“, Archiv für Elektronik und Übertragungstechnik, vol. 31, pp. 116-120, 1977.

[8] T. Weiland, “Time Domain Electromagnetic Field Computation with Finite Difference Methods”, International Journal of Numerical Modelling, vol. 9, no. 4, pp. 295-319, 1996.

[9] R. Schuhmann and T. Weiland, “Conservation of discrete energy and related laws in the finite integration technique”, in Geometric Methods for Computational Electromagnetics, ser. Electromagnetic Waves: Progress in Electromagnetics Research (PIER), F. L. Teixeira, Ed. Cambridge, MA: EMW Publishing, vol. 32, pp. 301-316, 2001.
[10] P. S. Russell, “Photonic-crystal fibers”, J. Lightwave Technol., vol. 24, no. 12, pp. 4729-4749, 2006.
[11] Computer Simulation Technology AG (CST), “CST Studio Suite 2008”, *http://www.cst.com*.
[12] G. L. G. Sleijpen and D. R. Fokkema, “BiCGstab(l) for linear equations involving unsymmetric matrices with complex spectrum”, Electron. Trans. Numer. Anal., vol. 1, No. Sept., pp. 11-32 (electronic only), 1993.

Bastian Bandlow was born in Frankfurt am Main, Germany. He received the Dipl.-Ing. degree in electrical engineering from the Technische Universität Darmstadt, Germany, in 2005, and is currently working toward the Ph.D. degree at the Universität Paderborn, Germany.

Since 2006, he has been with the group of Theoretische Elektrotechnik, Universität Paderborn.

His research is focused on simulation techniques for periodic structures such as metamaterials and photonic crystals at microwave and optical frequencies.

Rolf Schuhmann was born in Osterburken, Germany. He received the Dipl.-Ing. degree and Dr.-Ing. degree in electrical engineering from the Technische Universität Darmstadt, Germany, in 1994 and 1999, respectively.

Since 2005, he has been a Full Professor of Theoretische Elektrotechnik with the Universität Paderborn, Germany. His research interests concern computational electromagnetics with grid-based methods such as finite integration, finite elements, and finite differences. Applications include all types of components in microwave technology and optics and novel material concepts, as well as the characterization of metamaterials.

Multi-Fidelity Optimization of Microwave Structures Using Response Surface Approximation and Space Mapping

Slawomir Koziel

Engineering Optimization and Modeling Center, School of Science and Engineering, Reykjavik University, IS-103 Reykjavik, Iceland

koziel@ru.is

Abstract **—** A computationally efficient method for design optimization of CPU-intensive microwave structures is discussed. The presented technique exploits a response surface approximation surrogate model set up using data from the coarse-mesh EM-based model being a relaxed-accuracy representation of the microwave structure in question. The surrogate model is further subjected to the classical space mapping optimization. It is demonstrated that the new technique is able to provide a satisfactory design with a few electromagnetic simulations of the original structure. Because of using functional approximation, no circuit equivalent coarse model is necessary, which makes the presented approach particularly suitable for structures for which the development of the reliable coarse model is problematic (e.g., antennas).

Index Terms **—** Computer-aided design (CAD), multi-fidelity optimization, response surface approximation, space mapping, electromagnetic simulation, engineering design optimization.

I. INTRODUCTION

Due to the increasing complexity of contemporary microwave devices and structures as well as the demand for higher accuracy of electromagnetic simulation, the evaluation of microwave structures is becoming more and more time-consuming. Therefore, computer-aided design optimization—a critical part of modern microwave design process—faces fundamental difficulties. Direct optimization involving numerous evaluations of EM-simulation-based objective functions is typically impractical because of its high computational cost, and, in many cases, because of its infeasibility which is due to poor analytical properties of EM-based objective functions as well as the lack of sensitivity data or sensitivity being too expensive to evaluate. This means, in particular, that the traditional, gradient-based techniques become obsolete. On the other hand, certain modern techniques such as evolutionary algorithms [1] or particle swarm optimizers [2] permit to handle some issues that are problematic for the classical optimization (e.g., objective function discontinuity, lack of derivative information, multiple local optima). However, these methods are even more CPU-intensive because they typically require a huge number of objective function evaluations.

One of the possible approaches to alleviate this problem is decomposition, i.e., breaking down an EM model into smaller parts and combine them in a circuit simulator to reduce the CPU-intensity of the design process [3]-[7]. This is only a partial solution though, because the EM-embedded co-simulation model is still subjected to direct optimization.

Space mapping (SM) is a technique that has been successfully applied to microwave engineering design problems as well as in other engineering fields [8]-[13] and seems to be one of the most efficient approaches to date. SM allows efficient optimization of expensive or "fine" models—usually implemented with a CPU-intensive EM simulator—by means of the iterative optimization and updating of the so-called "coarse" models, less accurate but cheaper to evaluate. The coarse model is supposed to be a physically-based representation of the fine model. In order to take advantage of the space mapping principle, the coarse model should be computationally much cheaper than the fine model. Therefore, equivalent-circuit models or models exploiting analytical formulas are preferred [8]. Reliable equivalent-circuit models, however, may be difficult to develop for certain types of microwave devices (e.g., antennas, waveguide structures). Moreover, an extra simulator must be involved in the optimization process.

In this paper, another method is proposed that is a combination of a response surface approximation (RSA) approach [14] and space mapping, and does not require a circuit-based coarse model. Therefore, it can be implemented using a single EM-simulator, here, FEKO. The presented method uses a space-mapped RSA-based surrogate established with the coarse-mesh EM-based model and a generic surrogate-based optimization principle [15]. Design optimization examples are provided to demonstrate the robustness of the proposed approach.

II. OPTIMIZATION APPROACH

A. Design Optimization Problem Formulation

The goal is to solve the following problem

$$\boldsymbol{x}_f^* \in \arg\min_{\boldsymbol{x}} U\left(\boldsymbol{R}_f(\boldsymbol{x})\right) \tag{1}$$

where $R_f \in R^m$ denotes the response vector of a fine model of the device of interest, e.g., the modulus of the reflection coefficient $|S_{21}|$ evaluated at m different frequencies. U is a given scalar merit function, e.g., a minimax function with upper and lower specifications. Vector x_f^* is the optimal design to be determined. As mentioned in the introduction, R_f is assumed to be computationally expensive so that the direct optimization is usually prohibitive. In this paper, R_f is evaluated using FEKO.

B. Initial Surrogate Model

A basis of the proposed approach is a computationally cheap surrogate model. We assume that the surrogate model is a response surface approximation (RSA) model. Here, we exploit a radial basis function (RBF) interpolation [16]; the surrogate will be denoted as R_{RBF}. Normally, RSA model would be set up using a sampled fine model data. However, in order to reduce the computational overhead, the surrogate is constructed using a simplified representation R_c of the fine model. R_c is evaluated in the same EM simulator as the fine model, however, with much coarser mesh. This not only results in a much shorter evaluation time, but also introduces some inaccuracy, which will be dealt with in Section II.*C*.

Let $X_B = \{x^1, x^2, \ldots, x^N\}$ denote a base set, such that the responses $R_c(x^j)$ are known for $j = 1, 2, \ldots, N$. Here, the base set is selected using a modified Latin hypercube sampling algorithm [17] that gives a quite uniform distribution of samples in the design space. Figure 1 shows an example allocation of 50 base points in the unity interval $[0,1] \times [0,1]$.

We shall adopt the notation $\boldsymbol{R}_c(x) = [\boldsymbol{R}_{c.1}(x) \ldots \boldsymbol{R}_{c.m}(x)]^T$, where $\boldsymbol{R}_{c.k}(x)$ is the kth component of the response vector $\boldsymbol{R}_c(x)$. The radial basis function model R_{RBF} is defined as

$$\boldsymbol{R}_{RBF}(\boldsymbol{x}) = \begin{bmatrix} \sum_{j=1}^{N} \lambda_{1.j}\phi(\|\boldsymbol{x}-\boldsymbol{x}^j\|/\gamma) \\ \ldots \\ \sum_{j=1}^{N} \lambda_{m.j}\phi(\|\boldsymbol{x}-\boldsymbol{x}^j\|/\gamma) \end{bmatrix} \tag{2}$$

where $\|.\|$ denotes the Euclidean norm. The parameters $\lambda_{k.j}$ are calculated so that they satisfy

$$\Phi\boldsymbol{\lambda}_k = \boldsymbol{F}_k, \qquad k = 1, 2, \ldots, m \tag{3}$$

where $\boldsymbol{\lambda}_k = [\lambda_{k.1}\ \ \lambda_{k.2}\ \ \ldots\ \ \lambda_{k.N}]^T$,

$$\boldsymbol{F}_k = \left[R_{c.k}(\boldsymbol{x}^1)\ \ \ldots\ \ R_{c.k}(\boldsymbol{x}^N)\right]^T \tag{4}$$

and Φ is an $N\times N$ matrix with elements

$$\Phi_{ij} = \phi(\|\boldsymbol{x}^i - \boldsymbol{x}^j\|/\gamma) \tag{5}$$

where $\gamma = (2/(nN^{1/n}))\sum_{l=1}^{n}\max\{j,k=1,\ldots,N : \|\boldsymbol{x}^j - \boldsymbol{x}^k\|_l\}$ is a normalization factor representing an average distance between base points (n is the number of design variables).

In this paper we use a Gaussian basis function defined as

$$\phi(r) = e^{-cr^2}, \quad r \geq 0, \quad c > 0 \tag{6}$$

Parameter c is adjusted to minimize the generalization error calculated using cross-validation [15]. Figure 2 shows the example of the scalar $\boldsymbol{R}_{RBF}$ model surface. Note that the RBF model has an interpolation property (guaranteed by the condition (3)), i.e., the response surface fits exactly the $\boldsymbol{R}_c$ model at all base designs.

C. Space Mapping Correction of the Response Surface Approximation Model

The surrogate model $\boldsymbol{R}_{RBF}$ is computationally cheap but it is not as accurate representation of the microwave structure in question as the fine model $\boldsymbol{R}_f$. This is not only because $\boldsymbol{R}_{RBF}$ is set up using a limited number of base points, but, most importantly, because it is constructed using the data from the coarse-mesh model $\boldsymbol{R}_c$ instead of the original fine model $\boldsymbol{R}_f$. Therefore, before optimization, the model $\boldsymbol{R}_{RBF}$ has to be corrected to improve its (local) accuracy with respect to the fine model.

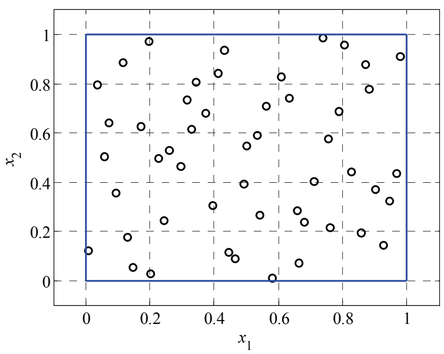

Fig. 1. Example of the base set for the RBF surrogate model $\boldsymbol{R}_{RBF}$: 50 base points allocated in the unity interval $[0,1] \times [0,1]$ using the modified Latin hypercube sampling [17].

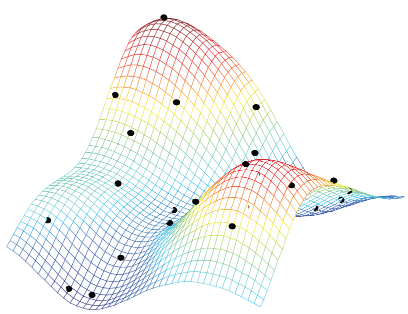

Fig. 2. Example of the (scalar) $\boldsymbol{R}_{RBF}$ model. Base points denoted using black circles.

In this paper the surrogate model is corrected using a classical space mapping (SM) approach [13]. The corrected surrogate model $\boldsymbol{R}_{SM}$ is defined as follows

$$\boldsymbol{R}_{SM}(\boldsymbol{x}) = P_L(\boldsymbol{R}_{RBF}(P_R(\boldsymbol{x}, \boldsymbol{p}_R)), \boldsymbol{p}_L) \tag{7}$$

where SM parameters are obtained using a parameter extraction (PE) process

$$(\boldsymbol{p}_L, \boldsymbol{p}_R) = \arg\min_{\boldsymbol{y},\boldsymbol{z}} \sum_{\boldsymbol{x} \in X_{PE}} \| \boldsymbol{R}_f(\boldsymbol{x}) - P_L(\boldsymbol{R}_{RBF}(P_R(\boldsymbol{x}, \boldsymbol{y})), \boldsymbol{z}) \tag{8}$$

Here, P_L is an output-SM-like mapping (e.g., $P_L(R,p_L) = P_L(R,A,d) = A \cdot R + d$) [13], P_R is an input-SM-like mapping (e.g., $P_R(x,p_R) = P_R(x,B,c) = B \cdot x + c$) [8], whereas X_{PE} is the set of points (designs) used in PE.

D. Optimization Procedure [18]

The proposed optimization procedure establishes an RSA model R_{RBF} using sampled data from the coarse-mesh model R_c. The space-mapping-corrected RSA model, R_{SM}, is then created using (7), (8) with the parameter extraction based on a current design at which the fine model response is known. Subsequently, a new design is found by means of optimizing the R_{SM} model. The surrogate models are set up in a restricted domain, being the neighbourhood of a current design. More specifically, the neighbourhood is defined by a small deviation δ from the current design; the value of δ is updated after each iteration of the optimization algorithm.

The optimization procedure can be formalized as follows [18]:

Step 0 Set $i = 0$; Initialize control parameters: $\delta \in (0,1)$ and N (positive integer); optimize the model R_c to find an initial design $x^{(0)} = \arg\min\{x : U(R_c(x))\}$;

Step 1 Assign lower bounds $x_{\min}$ and upper bounds $x_{\max}$ for the design variables: $x_{\min} = (1-\delta)\cdot x^{(i)}$ and $x_{\max} = (1+\delta)\cdot x^{(i)}$;

Step 2 Select the base set $X_B = \{x^1,\ldots,x^N\}$ # so that $x_{\min} \le x^j \le x_{\max}$ (component-wise), $j = 1, \ldots, N$; evaluate R_c at all designs from X_B;

Step 3 Establish the surrogate model R_{RBF} according to (2)-(6);

Step 4 Establish the corrected surrogate model R_{SM} according to (7) and (8) using $X_{PE} = \{x^{(i)}\}$;

Step 5 Find a new design $x^{(i+1)}$ by optimizing R_{SM}: $x^{(i+1)} = \arg\min\{x_{\min} \le x \le x_{\max} : U(R_{SM}(x))\}$;

Step 6 Update δ: $\delta = \max\{j = 1, ..., N : |x_j^{(i+1)} - x_j^{(i)}|/|x_j^{(i+1)}|\}$ $; Set $i = i + 1$;

Step 7 If the termination condition is not satisfied, go to 1; else END;

The base set is selected using a modified Latin hypercube sampling [17].

$ $x_j^{(i)}$ and $x_j^{(i+1)}$ are the jth components of $x^{(i)}$ and $x^{(i+1)}$, respectively; the updating procedure assumes positive values for all design variables.

Note that the updating rule for δ ensures that the new surrogate model domain is not larger than the previous one. The algorithm is terminated after user-defined maximum number of iterations or if the value of δ becomes sufficiently small.

Computational cost of the optimization process is determined by the evaluation time t_c of the coarse-mesh model R_c and the evaluation time t_f of the fine model R_f (other factors such as the cost of setting up R_{RBF} and R_{SM} models can be neglected). The total optimization time can be calculated as

$$t_{opt} = t_c \sum_{i=0}^{n_{iter}} N_i + (n_{iter} + 1)t_f \qquad (9)$$

where n_{iter} is the number of iterations of the optimization algorithm, N_0 is the number of evaluations of R_c necessary to find $x^{(0)}$ (cf. *Step* 0), and N_i, $i > 0$, is the number of new base points at iteration i (may be smaller than N because some base points from previous iterations are reused).

To measure the computational efficiency of the proposed algorithm a relative time t_{rel} is used that is the number of fine model evaluations required to complete the optimization procedure:

$$t_{rel} = n_{iter} + 1 + (t_c / t_f) \sum_{i=0}^{n_{iter}} N_i \qquad (10)$$

It should be noted that it is possible to use the coarse-mesh model $\boldsymbol{R}_c$ directly as a coarse model in the SM optimization algorithm. However, the computational cost of such a process is expected to be much higher than for the technique proposed here because of the larger total number of evaluations of $\boldsymbol{R}_c$ (both parameter extraction and surrogate model optimization would be performed directly on $\boldsymbol{R}_c$). Also, analytical properties of the coarse-mesh EM model may be poor (the model may be non-differentiable or even discontinuous) in contract to the RSA-based model which is always smooth.

III. EXAMPLES

A. 2nd-Order Tapped-Line Microstrip Filter [19]

Consider a second-order tapped-line microstrip filter [19] shown in Fig. 3. The design parameters are $\boldsymbol{x} = [L_1 \;\; g]^T$. The fine model $\boldsymbol{R}_f$ is simulated in FEKO [20]. The number of meshes for the fine model is 360. Simulation time for the fine model is 204 s. The design specifications are $|S_{21}| \geq -3$ dB for 4.75 GHz $\leq \omega \leq$ 5.25 GHz, and $|S_{21}| \leq -20$ dB for 3.0 GHz $\leq \omega \leq$ 4.0 GHz, and 6.0 GHz $\leq \omega \leq$ 7.0 GHz.

The coarse-mesh $\boldsymbol{R}_c$ is the structure in Fig. 3 also simulated in FEKO, however, the number of meshes is only 48. The number of meshes for $\boldsymbol{R}_f$ and $\boldsymbol{R}_c$ correspond to $\boldsymbol{x}_c = [6.0 \;\; 0.1]^T$ mm. The simulation time for $\boldsymbol{R}_{f\text{-}c}$ is about 8 s. Initial design $\boldsymbol{x}^{(0)} = [3.83 \; 0.103]^T$ mm is found by optimizing $\boldsymbol{R}_c$ and requires 34 model evaluations using $\boldsymbol{x}_c$ as a starting point (small number of evaluations is due to using relaxed tolerance requirements). The number of base points to set up model $\boldsymbol{R}_{RBF}$ is N = 25. Initial value of δ is 0.3. The space-mapping-corrected model $\boldsymbol{R}_{SM}$ uses only output SM of the form: $\boldsymbol{R}_{SM}(\boldsymbol{x}) = \boldsymbol{A}\cdot\boldsymbol{R}_{RBF}(\boldsymbol{x})$ with $\boldsymbol{A} = \mathrm{diag}\{a_1, a_2, \ldots, a_m\}$ (i.e., $P_L(\boldsymbol{R}) = \boldsymbol{A}\cdot\boldsymbol{R}$, and $P_R(\boldsymbol{x}) = \boldsymbol{x}$). This choice comes from the fact that a relatively small surrogate model domain allows us to assume that the misalignment between the surrogate model and the fine model has similar character throughout the domain.

We performed three iterations of the optimization algorithm. Figure 4 shows the responses of models $\boldsymbol{R}_f$ and $\boldsymbol{R}_c$ at the initial design (fine model specification error +0.9 dB), the $\boldsymbol{R}_f$ response at $\boldsymbol{x}_c$ (specification error +1.0 dB), as well as response of $\boldsymbol{R}_f$ at the final design $\boldsymbol{x}^{(3)}$ = $[3.92 \;\; 0.145]^T$ mm (specification error –0.7 dB). Figure 3 shows the surrogate model domains, base sets, and the evolution of the design for all three iterations. The total number of evaluations of model $\boldsymbol{R}_c$ is 59 and it is smaller than $3N$ = 75, which is because some of the base points were reused as indicated in Fig. 5. Table 1 indicates that the total optimization time corresponds to only 7.6 evaluations of the fine model.

For the sake of comparison, an SM optimization of the filter was also performed using directly $\boldsymbol{R}_c$ as a coarse model and the same output SM surrogate. The optimization time was 48 minutes, almost twice as much as for the proposed technique (with the total evaluation time of $\boldsymbol{R}_c$ being almost three times larger), even though the SM matrix $\boldsymbol{A}$ can be, in this case, obtained analytically without performing the parameter extraction process (8). In case of using any kind of input SM [8], the optimization cost would be much higher.

The first example is provided mostly to illustrate the operation of the proposed optimization algorithm (cf. Fig. 5). Other design problems are provided in the next sub-sections.

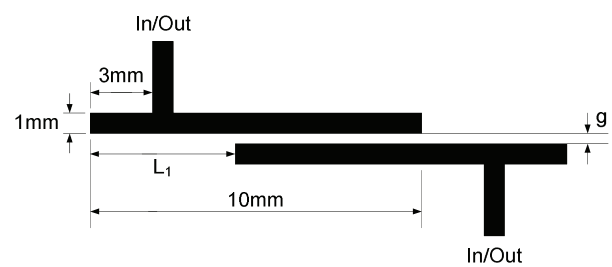

Fig. 3. Geometry of the second-order tapped-line microstrip filter [19].

Table 1: 2^{nd}-order tapped line filter: optimization cost

Algorithm Component	Model Involved	Number of Model Evaluations	CPU Cost t_{opt} [min]	CPU Cost t_{rel}
Optimization of $\boldsymbol{R}_c$	$\boldsymbol{R}_c$	34	4.5	1.3
Setting up base sets for $\boldsymbol{R}_{RBF}$	$\boldsymbol{R}_c$	59	7.9	2.3
Evaluation of $\boldsymbol{R}_f$	$\boldsymbol{R}_f$	4	13.6	4.0
Total optimization time	N/A	N/A	26.0	7.6

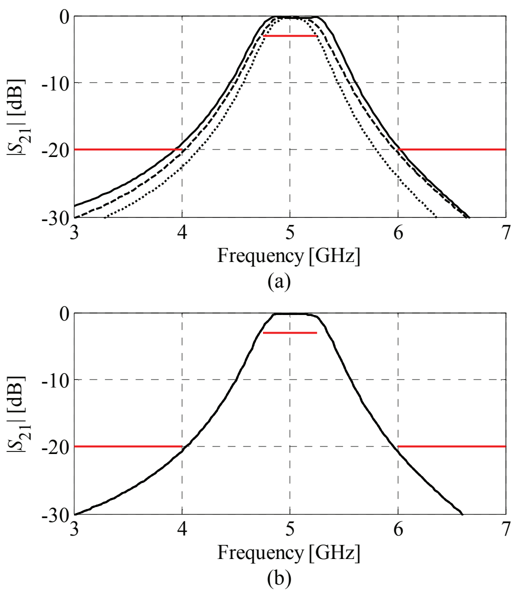

Fig. 4. Second-order tapped-line filter: (a) responses of $\boldsymbol{R}_f$ (solid line) and $\boldsymbol{R}_c$ (dashed line) at initial design $\boldsymbol{x}^{(0)}$ and response of $\boldsymbol{R}_f$ at $\boldsymbol{x}_c$ (dotted line); (b) response of $\boldsymbol{R}_f$ at the final design.

B. Patch Antenna [21]

Consider the patch antenna [21] shown in Fig. 6. This antenna is printed on a substrate with relative dielectric constant $\varepsilon_r = 2.32$ and height $h = 1.59$ mm. The design parameters are the patch length and width, i.e., $\boldsymbol{x} = [L\ W]^T$. The objective is to obtain 50 Ω input impedance at 2 GHz. The fine model $\boldsymbol{R}_f$ is simulated in FEKO [20]. The number of meshes for the fine model is 1024, which ensures mesh convergence for the structure. Simulation time for the fine model is 41s.

The coarse-mesh model $\boldsymbol{R}_c$ is the structure in Fig. 6 also simulated in FEKO, however, the number of meshes is only 100. Simulation time for model $\boldsymbol{R}_c$ is 0.6s. The number of meshes for $\boldsymbol{R}_f$ and $\boldsymbol{R}_c$ correspond to $\boldsymbol{x}_c = [50\ 100]^T$ mm.

Initial design $\boldsymbol{x}^{(0)} = [50.85\ 101.86]^T$ mm is found by optimizing $\boldsymbol{R}_c$ and requires 39 model evaluations. The number of base points to set up model $\boldsymbol{R}_{RBF}$ is $N = 30$. Initial value of δ is 0.01. As before, the space-mapping-corrected model $\boldsymbol{R}_{SM}$ is of the form $\boldsymbol{R}_{SM}(\boldsymbol{x}) = \boldsymbol{A}\cdot\boldsymbol{R}_{RBF}(\boldsymbol{x})$.

The fine model response at the initial design is 38.15 Ω. The response of $\boldsymbol{R}_f$ at the design obtained after four iterations of the proposed optimization procedure, $\boldsymbol{x}^{(4)} = [50.25\ 101.09]^T$ mm, is 49.94 Ω. The total number of evaluations of model $\boldsymbol{R}_c$ is 97. For illustration purposes, Fig. 7 shows the response surface of the fine model, the $\boldsymbol{R}_{RBF}$ model, and the space-mapping-corrected RBF model $\boldsymbol{R}_{SM}$ at the first iteration of the optimization procedure. Table 2 summarizes the computational cost of the optimization: the total optimization time corresponds to only 6.8 evaluations of $\boldsymbol{R}_f$.

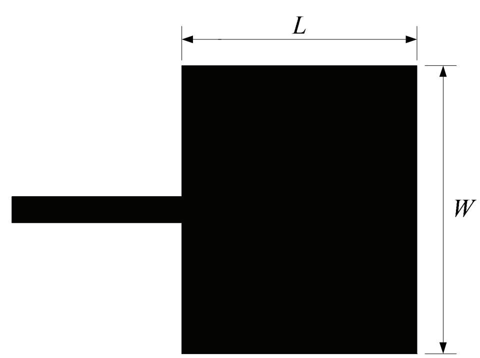

Fig. 6. Geometry of the patch antenna [21].

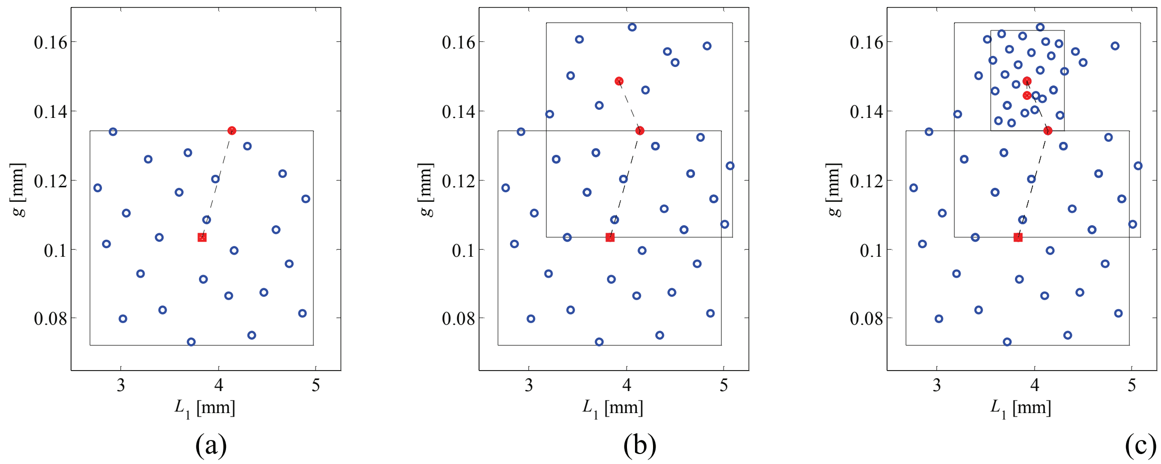

Fig. 5. Surrogate model domains, base sets (circles) and updated designs (filled circles) after: (a) first iteration, (b) second iteration, and (c) third iteration of the optimization procedure. Initial design is marked as a square.

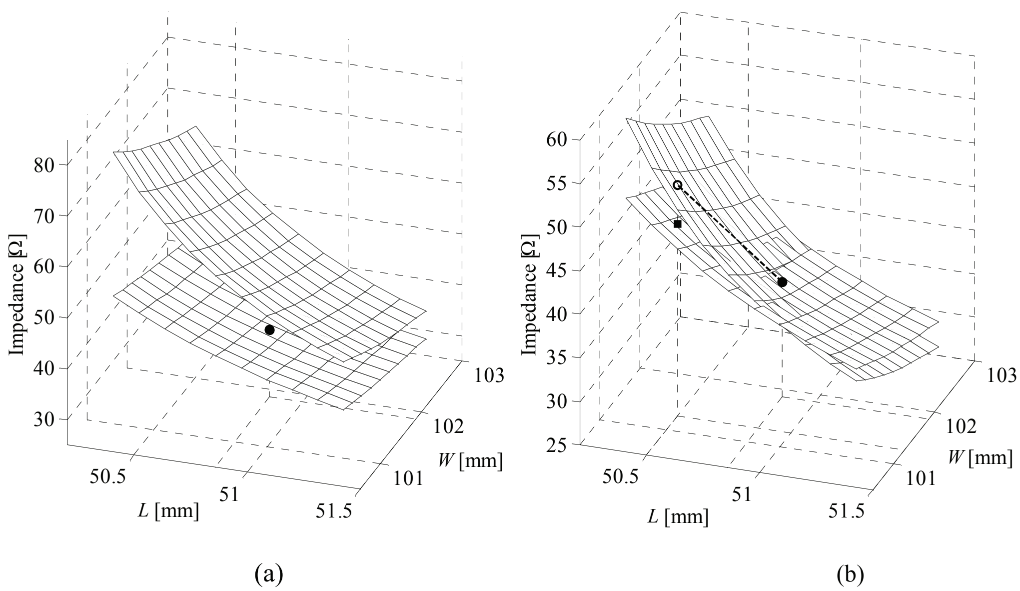

Fig. 7. Patch antenna: (a) fine model response surface (bottom) and the $\boldsymbol{R}_{RBF}$ model response surface (top) at the first iteration of the proposed optimization procedure. Initial fine model response is denoted as the filled circle; (b) fine model response and the SM-corrected RBF model $\boldsymbol{R}_{SM}$ at the first iteration. Initial fine model response, optimal response of the $\boldsymbol{R}_{SM}$ model and the corresponding fine model response denoted as the filled circle, empty circle and the filled rectangle, respectively.

.

The direct optimization of the fine model using Matlab's *fmincon* routine was performed for comparison purposes using $x^{(0)}$ as a starting point. Direct optimization required 54 evaluations of R_f to obtain a comparable design (almost 40 minutes of CPU time compared to less than 5 minutes required by the procedure discussed in this paper).

It should be noted that in case of the patch antenna no circuit equivalent model is available. This is a serious problem for the standard space mapping technique. In [21], the coarse-mesh FEKO model was used as a coarse model for space mapping algorithm to optimize the same patch antenna. Special meshing techniques had to be used to make the coarse model optimizable, and cost-saving termination conditions were used. Nevertheless, the computational cost of SM optimization was about 50% to over 100% higher than that reported here (depending on the space mapping type used to build the surrogate model).

Table 2: Patch antenna: optimization cost.

Algorithm Component	Model Involved	Number of Model Evaluations	CPU Cost	
			t_{opt} [min]	t_{rel}
Optimization of $\boldsymbol{R}_c$	$\boldsymbol{R}_c$	39	23	0.6
Setting up base sets for $\boldsymbol{R}_{RBF}$	$\boldsymbol{R}_c$	97	57	1.4
Evaluation of $\boldsymbol{R}_f$	$\boldsymbol{R}_f$	5	205	5
Total optimization time	N/A	N/A	285	7

C. 2nd-Order Capacitively-Coupled Dual-Behavior Resonator (CCDBR) Microstrip Filter [19]

Consider a second-order capacitively-coupled dual-behavior resonator (CCDBR) microstrip filter [19] shown in Fig. 8. The design variables are $\boldsymbol{x} = [L_1\ L_2\ L_3]^T$. Parameter S is set to 0.05 mm. The fine model is simulated in FEKO [20]. The number of meshes for the fine model is 1134. Simulation time for the fine model is 37.7 min. The design specifications are $|S_{21}| \geq -3$ dB for 3.8 GHz $\leq \omega \leq$ 4.2 GHz, and $|S_{21}| \leq -20$ dB for 2.0 GHz $\leq \omega \leq$ 3.2 GHz and 4.8 GHz $\leq \omega \leq$ 6.0 GHz.

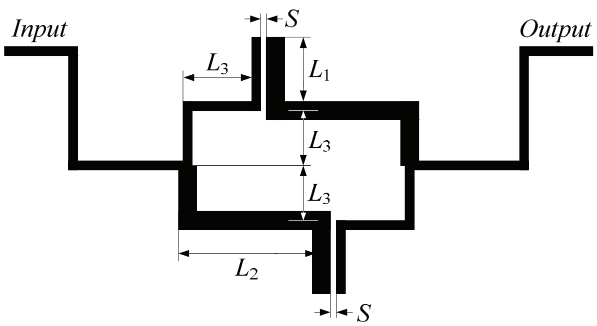

Fig. 8. Geometry of the 2nd -order CCDBR filter [19].

The coarse-mesh model $\boldsymbol{R}_c$ is the structure in Fig. 8 also simulated in FEKO with the number of meshes equal to 130. The number of meshes for $\boldsymbol{R}_f$ and $\boldsymbol{R}_c$ correspond to $\boldsymbol{x}_c = [2.89\ 6.24\ 0.92]^T$ mm (optimal solution of the circuit equivalent ADS model [22]). The simulation time for $\boldsymbol{R}_c$ is 37 s.

Initial design $\boldsymbol{x}^{(0)} = [2.97\ 4.69\ 1.54]^T$ mm is found by optimizing $\boldsymbol{R}_c$ and requires 63 model evaluations (small number of evaluations is due to using relaxed tolerance requirements). The number of base points to set up model $\boldsymbol{R}_{RBF}$ is $N = 50$. Initial value of δ is 0.1. As before, the space-mapping-corrected model $\boldsymbol{R}_{SM}$ is of the form $\boldsymbol{R}_{SM}(\boldsymbol{x}) = \boldsymbol{A}\cdot\boldsymbol{R}_{RBF}(\boldsymbol{x})$.

Figure 9 shows the responses of models $\boldsymbol{R}_f$ and $\boldsymbol{R}_c$ at the initial design (fine model specification error +0.8 dB), the $\boldsymbol{R}_f$ response at $\boldsymbol{x}_c$ (specification error +6.7 dB), as well as the fine model response at the final design, $\boldsymbol{x}^{(3)} = [3.21\ 4.63\ 1.27]^T$ mm, obtained after three iterations (specification error –1.5 dB). The total number of evaluations of model $\boldsymbol{R}_c$ is 112. Table 3 summarizes the computational cost of the optimization: the total optimization time corresponds to only 6.8 evaluations of $\boldsymbol{R}_f$.

For comparison purposes, the direct optimization of the fine model using Matlab's *fminimax* routine was performed using $\boldsymbol{x}^{(0)}$ as a starting point. The design obtained after 100 evaluations of $\boldsymbol{R}_f$ (over 63 hours of CPU time; the algorithm was terminated without convergence) corresponds to the specification error of –0.6 dB.

On the other hand, SM optimization of the filter using directly $\boldsymbol{R}_c$ as a coarse model resulted in the design comparable with the one obtained using the proposed technique, however, the optimization time was 390 minutes, 50% more than for our method (with the total evaluation time of $\boldsymbol{R}_c$ being 120% larger). For this example, the SM parameters can be determined analytically; otherwise (e.g., in case of using input SM [8]), the optimization cost would be substantially higher.

Table 3: CCDBR filter: optimization cost

Algorithm Component	Model Involved	Number of Model Evaluations	CPU Cost	
			t_{opt} [min]	t_{rel}
Optimization of $\boldsymbol{R}_c$	$\boldsymbol{R}_c$	63	39	1.0
Setting up base sets for $\boldsymbol{R}_{RBF}$	$\boldsymbol{R}_c$	112	69	1.8
Evaluation of $\boldsymbol{R}_f$	$\boldsymbol{R}_f$	4	151	4.0
Total optimization time	N/A	N/A	259	6.8

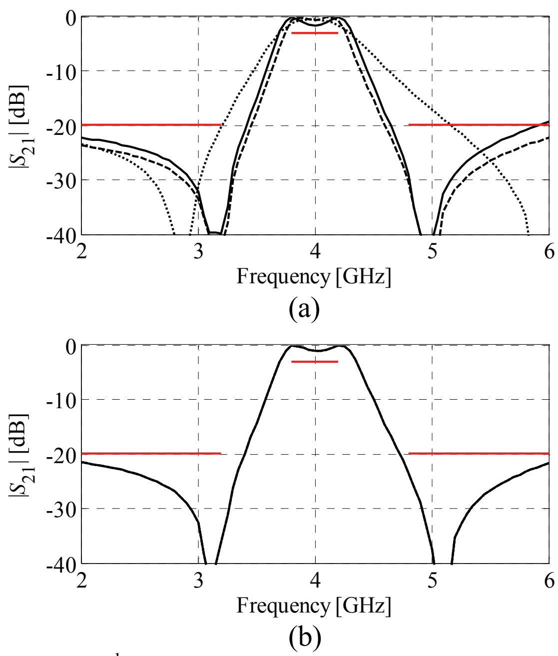

Fig. 9. 2nd-order CCDBR filter: (a) responses of R_f (solid line) and R_c (dashed line) at initial design $x^{(0)}$ and response of R_f at x_c (dotted line); (b) response of R_f at the final design.

IV. CONCLUSION

An efficient algorithm for microwave design optimization is discussed that combines response-surface-approximation-based surrogate modeling, space mapping and multi-fidelity electromagnetic simulations. Unlike classical space mapping, the proposed technique does not require a circuit-equivalent or analytical coarse model, which makes it particularly suitable for problems where finding such a coarse model may be problematic, e.g., antennas. Although our technique is illustrated using microwave structures evaluated with FEKO, it can be used with any other electromagnetic simulator. It is demonstrated that the presented method is able to yield satisfactory design with the optimization time corresponding to a few evaluations of the fine model.

ACKNOWLEDGEMENT

This work was supported in part by the Reykjavik University Development Fund.

REFERENCES

[1] M.-I. Lai and S.-K. Jeng, “Compact microstrip dual-band bandpass filters design using genetic-algorithm techniques,” *IEEE Trans. Microwave Theory Tech.*, vol. 54, no. 1, pp. 160-168, Jan. 2006.

[2] N. Jin, and Y. Rahmat-Samii, “Analysis and particle swarm optimization of correlator antenna arrays for radio astronomy applications,” *IEEE Trans. Antennas and Prop.*, vol. 56, no. 5, pp. 1269-1279, May 2008.

[3] R. V. Snyder, “Practical aspects of microwave filter development,” *IEEE Microwave Magazine*, vol. 8, no.2, pp. 42-54, Apr. 2007.

[4] S. Shin and S. Kanamaluru, “Diplexer design using EM and circuit simulation techniques,” *IEEE Microwave Magazine*, vol.8, no.2, pp.77-82, Apr. 2007.

[5] V. Rizzoli, A. Costanzo, D. Masotti and P. Spadoni, “Circuit-level nonlinear/electromagnetic co-simulation of an entire microwave link,” *IEEE MTT-S Int. Microwave Symp. Dig.*, Long Beach, CA, pp. 813-816, June 2005.

[6] J. Sercu and F. Demuynck, “Electromagnetic/ Circuit co-optimization of lumped component and physical layout parameters using generalized layout components,” *IEEE MTT-S Int. Microwave Symp. Dig.*, Seattle, WA, pp. 2073-2076, June 2002.

[7] A. Bhargava, “Designing circuits using an EM/circuit co-simulation technique,” *RF Design*, p. 76, Jan. 2005.

[8] J. W. Bandler, Q. S. Cheng, S. A. Dakroury, A. S. Mohamed, M. H. Bakr, K. Madsen, and J. Søndergaard, “Space mapping: the state of the art,” *IEEE Trans. Microwave Theory Tech.*, vol. 52, no. 1, pp. 337-361, Jan. 2004.

[9] S. J. Leary, A. Bhaskar, and A. J. Keane, “A constraint mapping approach to the structural optimization of an expensive model using surrogates,” *Optimization Eng.*, vol. 2, no. 4, pp. 385-398, Dec. 2001.

[10] H.-S. Choi, D. H. Kim, I. H. Park, and S. Y. Hahn, “A new design technique of magnetic systems using space mapping algorithm,” *IEEE Trans. Magn.*, vol. 37, no. 5, pp. 3627-3630, Sept. 2001.

[11] M. A. Ismail, D. Smith, A. Panariello, Y. Wang, and M. Yu, “EM-based design of large-scale dielectric-resonator filters and multiplexers by space mapping,” *IEEE Trans. Microwave Theory Tech.,* vol. 52, no. 1, pp. 386-392, Jan. 2004.

[12] D. Echeverria and P. W. Hemker, “Space mapping and defect correction,” *CMAM The International Mathematical Journal Computational Methods in Applied Mathematics,* vol. 5, no. 2, pp. 107-136, 2005.

[13] S. Koziel, J. W. Bandler, and K. Madsen, “A space mapping framework for engineering optimization: theory and implementation,” *IEEE*

Trans. Microwave Theory Tech., vol. 54, no. 10, pp. 3721-3730, Oct. 2006.

[14] R. H. Myers and D.C. Montgomery, “Response surface methodology,” John Wiley & Sons, Inc. 2002.

[15] N. V. Queipo, R. T. Haftka, W. Shyy, T. Goel, R. Vaidynathan, and P.K. Tucker, “Surrogate-based analysis and optimization,” *Progress in Aerospace Sciences*, vol. 41, no. 1, pp. 1-28, Jan. 2005.

[16] T. W. Simpson, J. D. Peplinski, P. N. Koch, and J. K. Allen, “Metamodels for computer-based engineering design: survey and recommendations,” *Engineering with Computers*, vol. 17, no. 2, pp. 129-150, 2001.

[17] B. Beachkofski, R. Grandhi, “Improved distributed hypercube sampling,” *American Institute of Aeronautics and Astronautics*, paper AIAA 2002-1274, 2002.

[18] S. Koziel, “Multi-fidelity optimization of microwave structures with FEKO using response surface approximation and space mapping,” *International Review of Progress in Applied Computational Electromagnetics*, *ACES 2009*, March 8-12, Monterey, CA, pp. 347-352, 2009.

[19] A. Manchec, C. Quendo, J.-F. Favennec, E. Rius, and C. Person, “Synthesis of Capacitive-Coupled Dual-Behavior Resonator (CCDBR) Filters,” *IEEE Trans. Microwave Theory Tech.,* vol. 54, no. 6, pp. 2346-2355, June 2006.

[20] FEKO, Suite 5.4, EM Software & Systems-S.A. (Pty) Ltd, 32 Techno Lane, Technopark, Stellenbosch, 7600, South Africa, 2008.

[21] J. Zhu, J. W. Bandler, N. K. Nikolova and S. Koziel, “Antenna optimization through space mapping,” *IEEE Transactions on Antennas and Propagation*, vol. 55, no. 3, pp. 651-658, March 2007.

[22] S. Koziel and J. W. Bandler, “Space mapping optimization of microwave structures with FEKO,” *International Review of Progress in Applied Computational Electromagnetics*, *ACES 2008*, March 30-April 4, Niagara Falls, Canada, pp. 320-325, 2008.

Slawomir Koziel received the M.Sc. and Ph.D. degrees in electronic engineering from Gdansk University of Technology, Poland, in 1995 and 2000, respectively. He also received the M.Sc. degrees in theoretical physics and in mathematics, in 2000 and 2002, respectively, as well as the PhD in mathematics in 2003, from the University of Gdansk, Poland. He is currently an Associate Professor with the School of Science and Engineering, Reykjavik University, Iceland. His research interests include CAD and modeling of microwave circuits, surrogate-based optimization, space mapping, circuit theory, analog signal processing, evolutionary computation and numerical analysis.

Modeling of UIC Cables in Railway Systems for Their Use as Power Line Communication Channels

S. Barmada[1], A. Gaggelli[2], P. Masini[2], A. Musolino[1], R. Rizzo[1] and M. Tucci[1]

[1] Department of Electrical Systems and Automation
University of Pisa, via Diotisalvi 2, 56126 Pisa, Italy
sami.barmada@dsea.unipi.it,
[2] Trenitalia S.p.A. – Direzione Ingegneria, Sicurezza e Qualità di Sistema
V.le Spartaco Lavagnini, 58, 50129 Firenze, Italy
a.gaggelli@trenitalia.it

Abstract **–** In this paper the authors investigate the possibility of using the preexisting electrical-control grid onboard trains as a wideband communication channel. In particular the attention is focused on a particular class of cables (UIC) present in most trains. A model and a set of simulations are presented in the paper, showing that the PLC technology can be used in this new environment.

Index Terms**:** PLC, channel modeling, railway systems and onboard communications.

I. INTRODUCTION

Signal transmission over power lines (Power Line Communications, PLC) is not a new technology, but it is gaining a growing interest for applications such as Internet or data services. The main reason for this new interest is that the PLC technology's infrastructure is based on the pre-existing electrical grid reaching each user in the locations where such applications are required; this is leading towards cost saving since there is no need for creating a new signal transmission network, and a LAN can be created (for instance in a group of offices, house, industry plant, etc.) by simply equipping the power grid with the proper couplers [1] – [6]. The use of new protocols allows a broadband transmission, hence the same technology is referred to as Broadband Power Line (BPL).

The accurate modeling of the PLC channel is of fundamental importance since the performance of the power grid as a communication channel depend on characteristics such as impulse response, frequency response, and noise.

The calculation of the system's impulse response is fundamental in analyzing the robustness of modulation schemes (usually Orthogonal Frequency Division Modulation (OFDM)) with regard to the channel performance: from the impulse response duration we can obtain the actual "guard interval" to avoid Inter Symbol Interference (ISI), and from the frequency response we can derive the upper and lower bounds for the attenuation of each sub-channel, thus selecting the more stable and better performing sub-channels [7] – [9].

Modern railway systems are provided with an increasing number of electronic equipment to be placed on each hauled stock. We are moving towards more comfortable trains with modern travelers demanding for enhanced services; from this fact comes the need for increasing the trip's quality (onboard entertainment, high speed internet connection, etc.) while travel security (additional information and video vigilance) is becoming relevant.

With the actual trend, this additional setup would require a new set of dedicated cables, which could have a high impact in the global cost of the train.

The use of PLC in vehicles is a new application that looks very promising. First studies regarding BPL in automotive vehicles and aircrafts show potential success of this technique ([10] – [16]) and are mainly dedicated to the analysis of the issues related to this new use of the power grid. Nevertheless PLC technology onboard trains is a new field of study, and the present paper is the first approach to this new application.

The paper is organized as follows: section II is dedicated to the PLC channel selection; section III to the modeling of the selected channel and section IV to the results obtained and to their evaluation.

II. CHANNEL SELECTION

The power grid of a train is a very complex systems, and is composed of several apparatuses and devices onboard the traction-stock and each hauling-stock. They include, besides the traction engines, a lighting system, heating, air conditioning, batteries, converters, and transformers. These devices are present (in different configurations, complexity, and redundancy) in all kind of trains. An additional characteristic of the power grid of trains is that, besides its complexity, it is highly affected by several noise sources, i.e. the electric arcs of the pantograph-catenary system, or disturbances created by motor drives.

In addition, different train types are characterized by a completely different power grid topology and characteristics. This is a very important point, since our main goal is to approach the problem of implementing a PLC system onboard trains in a general way, which means that the system could be setup onboard different kind of trains with little variations, i.e. with little hardware/software changes making it more versatile and practically convenient from an economic point of view.

For this reason the attention of the authors has been focused on the remote control and communication line, described in [17]. The most important characteristic of this line is that it is present in most trains, and the characteristics of the cables are unified by the above mentioned regulation. It is the only set of cables which crosses the whole train (traction-stock and hauling-stocks) and for safety reasons particular care is taken in order to avoid any possible disconnection. At the same time all the connectors (plugs and sockets) are unified according to international regulations, making an exact analysis of the electrical parameters possible.

As described in [17] most modern trains are equipped with UIC cables, being the main core of the remote control and communication line. In particular an 18 conductors flexible shielded cable (terminated by a plug) connects the stocks to one another and it is connected (inside each stock) to a connection box (present at both ends of each vehicle). Inside the vehicle the 18 conductors are split in two different cables: a 16 conductors and a two conductor cables, both shielded. The outline of these connections is reported in Fig. 1 while Fig. 2 shows the section of the 16 conductors cable with the cable numbering as explained in [17].

The 16 conductors have different roles in the train control, and they are divided in functional groups: each single group has one conductor serving as a reference and one or more conductors as signal line. Amongst the available functional groups the authors have chosen the one in charge of the doors opening and closure: it is composed of conductors 9, 10, 11, 12, 14, 15 and 16, with conductor 12 as common return. The reason for this choice is the following: among the different functional groups the ones carrying ac signals (in different frequency bands) have been excluded in order not to interfere with the OFDM signal and vice versa. Among the remaining groups characterized by DC signals, the peculiarity of the above mentioned group is that the signals it is carrying are DC pulses of maximum 2 sec duration.

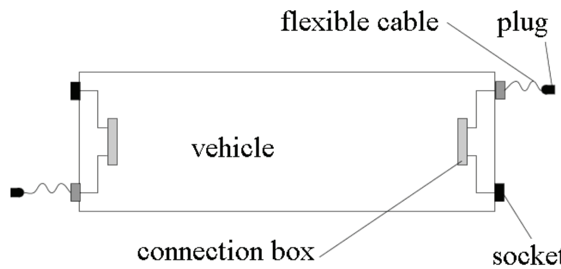

Fig. 1. Outline of the remote control line.

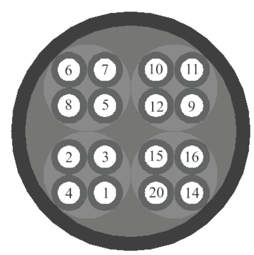

Fig. 2. Section of the 16 conductors cable.

Conductor number 12 will be used as a return and conductors number 10 or number 11 (dedicated to the switching on and off of the light signals “stop” and “go”) will be the one dedicated to the data transmission. The reason for this choice comes from the fact that any possible interference (even if not desired) caused by this additional use seems not to damage the proper operation of the light signals.

Even though a safety assessment is not within the aim of this paper it is worth mentioning that further studies shall be devoted to the verification that OFDM signals will not corrupt the ones which normally flow through selected and nearby conductors.

In the next section we will show the developed channel model together with the results of a preliminary set of measurements on a cable.

It is fundamental to underline that these result show eventual theoretical feasibility of the PLC implementation, but a thorough experimental measurement campaign is needed to assess the simulation results.

Section 4 is dedicated to the development of the channel model and to the analysis of its behaviour with respect to the transmission rate.

III. CHANNEL MODEL

The first step to be performed when modeling a multiconductor transmission line is to obtain its per unit length parameters. In this case a FEM model of the cable section (Fig. 2) has been implemented, obtaining the R, L, C and G matrices. In this case the frequency range typical of the OFDM protocol is between 1 and 30 MHz, for this reason the p.u.l. parameters have been calculated for 3 frequencies in the above mentioned range, and the frequency behavior has been modeled as described in [18]. The values of resistance, capacitance and inductance at a frequency of 15 MHz is here reported.

1.708E-10	-1.19E-11	-5.89E-11	-1.41E-11	-8.67E-12	-2.62E-11
-1.19E-11	1.596E-10	-6.27E-11	-1.81E-11	-4.57E-12	-5.27E-12
-5.89E-11	-6.27E-11	1.97E-10	-4.52E-11	-7.15E-12	-1.31E-11
-1.41E-11	-1.81E-11	-4.52E-11	1.690E-10	-2.39E-11	-6.30E-11
-8.67E-12	-4.57E-12	-7.15E-12	-2.39E-11	1.292E-10	-5.47E-11
-2.62E-11	-5.27E-12	-1.31E-11	-6.30E-11	-5.47E-11	1.701E-10

Capacitance Matrix of the cable (F/m)

0.78955	0.34807	0.4452	0.40162	0.35895	0.42051
0.34807	0.7809	0.43699	0.3835	0.32168	0.3502
0.4452	0.43699	0.89924	0.41954	0. 34653	0.39102
0.40162	0.3835	0.41954	0.98015	0.45056	0.53954
0.35895	0.32168	0.34653	0.45056	0.79845	0.4546
0.42051	0.3502	0.39102	0.53954	0.4546	0.86429

Resistance Matrix of the cable (Ω/m)

3.7412E-7	1.5297E-7	2.1868E-7	1.977E-7	1.7432E-7	2.064E-7
1.5297E-7	3.7545E-7	2.2166E-7	1.9614E-7	1.6279E-7	1.7617E-7
2.1868E-7	2.2166E-7	4.0733E-7	2.5111E-7	2.0524E-7	2.278E-7
1.977E-7	1.9614E-7	2.5111E-7	4.6352E-7	2.5752E-7	3.0605E-7
1.7432E-7	1.6279E-7	2.0524E-7	2.5752E-7	4.5657E-7	2.8878E-7
2.064E-7	1.7617E-7	2.278E-7	3.0605E-7	2.8878E-7	4.9198E-7

Inductance Matrix of the cable (H/m)

The simulated p.u.l. parameters have been compared to the values obtained by measurements operated on a 6m UIC cable provided by Trenitalia S.p.a. In particular the measurements have been performed on a couple of conductors whose distance was the least (i.e. 9-11 or 14-16). The experimental setup is shown in Figure 3, while the p.u.l. behavior in a range [0 30] MHz is shown in Figures 4 – 7, showing good agreement with the parameters obtained by the FEM simulation.

The relative error between measurements and simulations in the frequency range of interest is below 10%. Some small divergences are caused by the measurement system, but the global frequency behavior of the measured p.u.l. parameters is well reproduced by the FEM model. While the p.u.l. L, R and G have been both calculated and measured, the simple FEM model could not allow us to calculate the conductance (mainly because the dispersive properties of the insulating material composing the cable were not known); for this reason the value of G used in the channel simulations is taken directly from the measurements.

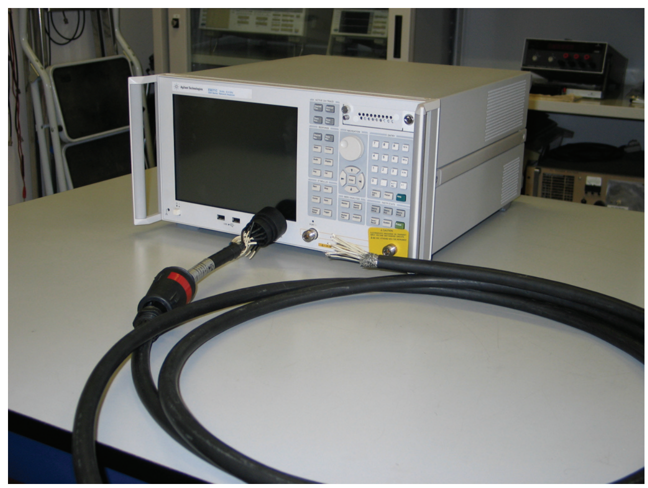

Fig.3. Experimental setup.

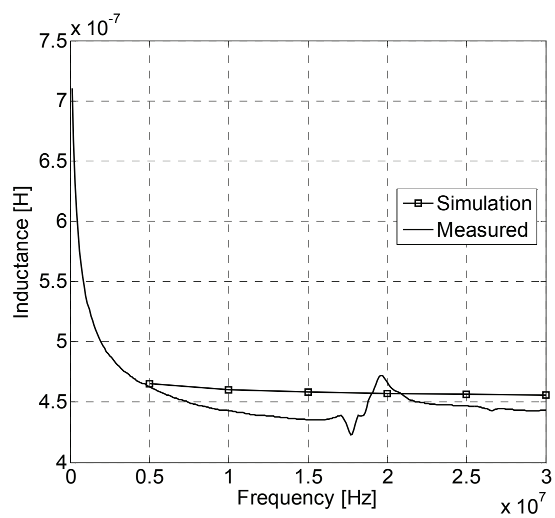

Fig.4. Measured and simulated inductance.

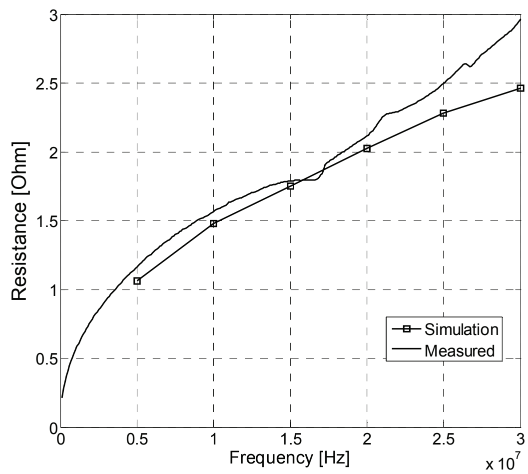

Fig. 5. Measured and simulated resistance.

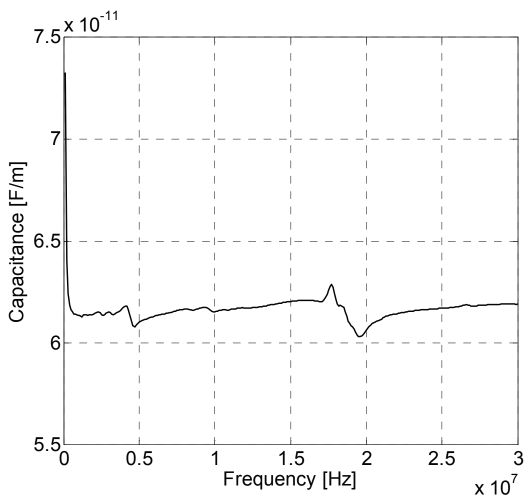

Fig. 6. Measured capacitance.

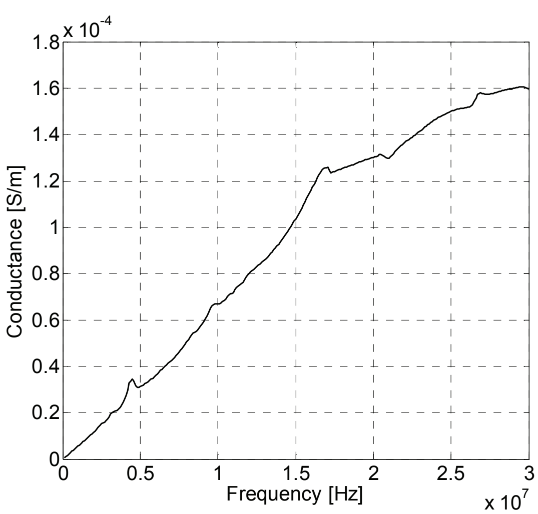

Fig. 7. Measured conductance.

The MTL inside each single stock can be described as in Fig. 7: conductors 9, 10, 11, 14, 15, 16 are carrying the signals (in particular, we are interested in the performances of conductor 10 in carrying the OFDM signals for PLC) while conductor 12 is the reference conductor.

The impedance between conductor 16 and 12 is not specified a priori, thus it is assumed to be comparable with that of relays operating door locks: according to [17] this value must be not lower than 1200 Ω. Although Figure 8 shows such impedances for conductor 16, all the conductors have derivations with the same resistance values. There is not a general topology for these parallel connections, so we have decided to place them at the beginning, at the end, and in the centre of the lines. As a matter of fact, their high value does not practically affect the channel's behavior, as it will be shown afterwards. Further work in this area will be to measure the input impedance of these relays, in order to have a more accurate modeling.

According to [17] conductors 9 to 15 carry pulses of amplitude between 18V and 33V (their nominal value is 24V) with a duration of $t \leq 2$ sec; for this reason the crosstalk between conductors 9 to 15 and conductor 16 is fundamental to verify its use as a PLC channel, since this is a noise which could limit the bandwidth of the OFDM signal, hence the channel's performance.

The lines are modeled according to [18], while in case there is uncertainty in the p.u.l. parameters value the problem can be approached according to [18] and [19].

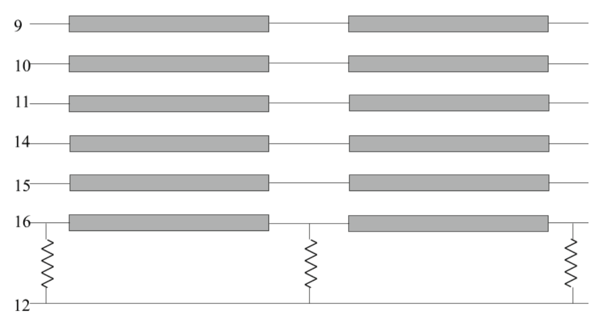

Fig. 8. MTL inside each stock.

The electrical length of the cable inside each stock is of l = 20m, plus 5m can be considered the length of the connection between the two coaches. A model of 6 hauled stocks has been considered (length = 150m) and the voltages have been calculated at the end of the first stock (length = 20 m, referred to as short path) and at the end of the last stock (145m, referred to as long path), respectively being the best and worst case in terms of transmission quality.

The outline of the implemented system is shown in Figure 9.

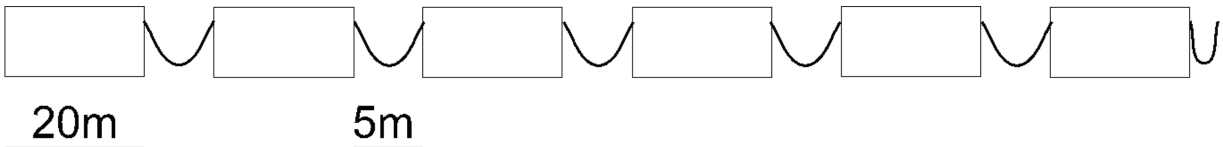

Fig. 9. Outline of the simulation

At the moment, the cable is terminated with an open circuit, but in order to optimize the communication performances a termination of 50 Ω can be set up. In fact both the situations have been simulated. As input signal, an impulse generator has been connected to conductor number 10, while a step input with amplitude of 24 V has been connected to the other conductors.

IV. SIMULATIONS RESULTS

A. Frequency responses of the direct channels

Figures 10 and 11 show the frequency responses of the first channel (short path) when the line at the end of the long path is matched (Fig. 4) and open (Fig. 5). It is evident that in the matched case the frequency response exhibits a flatter behavior, although in both cases strong fading is not present, resulting in a high-quality channel for multicarrier broadband communication in the frequency band 2-30 MHz. It can be assessed, at this point of the analysis, that the termination at the end of the line does not significantly influence the frequency response at intermediate receivers. When we move towards the end of the line, the effect of the unmatched termination increases, reaching a maximum for the last vehicle.

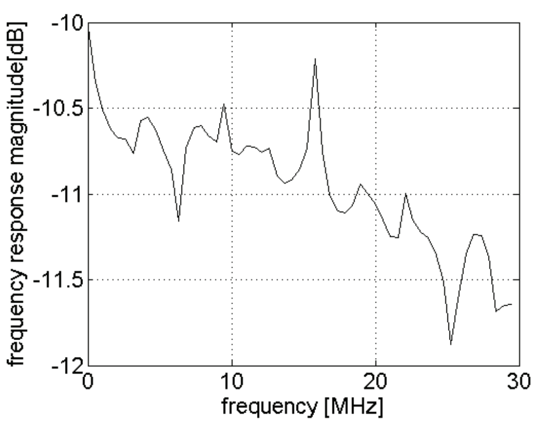

Fig. 10. Frequency response of the short path (matched).

Figures 12 and 13 show the frequency response of the second simulated channel (long path) respectively in the matched and non matched cases.

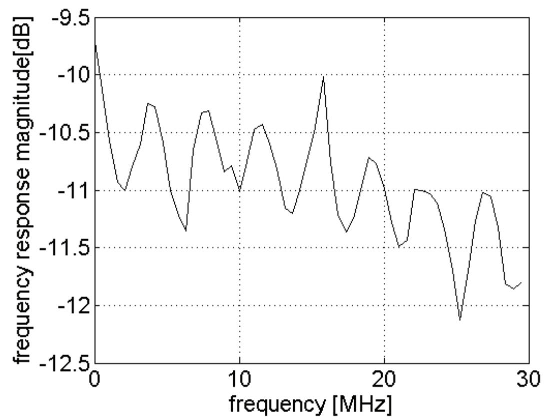

Fig. 11. Frequency response of the short path (non matched).

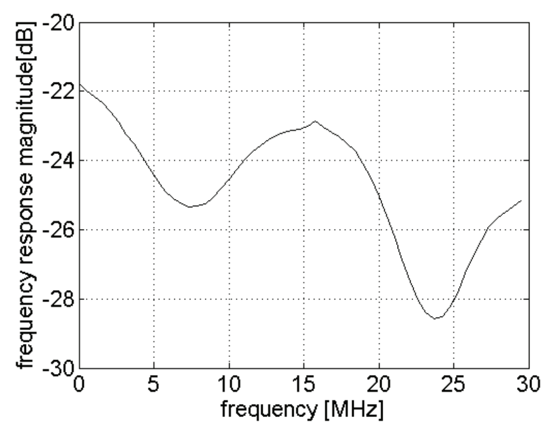

Fig. 12. Frequency response of the long path (matched).

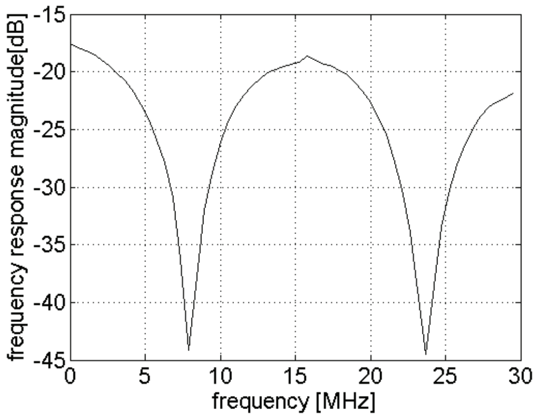

Fig. 13. Frequency response of the long path (non matched).

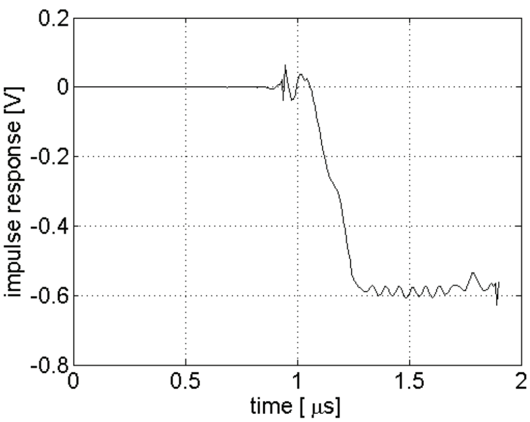

Fig. 14. Time response to the step signal (matched).

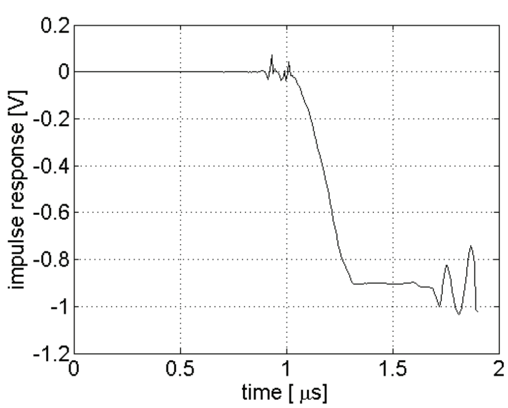

Fig. 15. Time response to the step signal (non matched).

We observe that the two situations are now rather different: the matched case behaves as a smooth channel with amplitudes between -15 and -25 dB, whereas if the line is open, there is more destructive interference which produces strong fading.

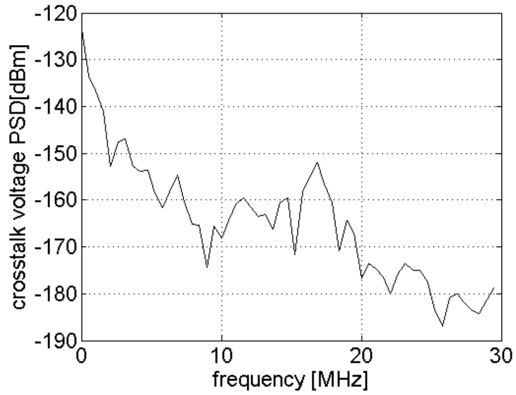

Fig. 16. Crosstalk PSD (matched).

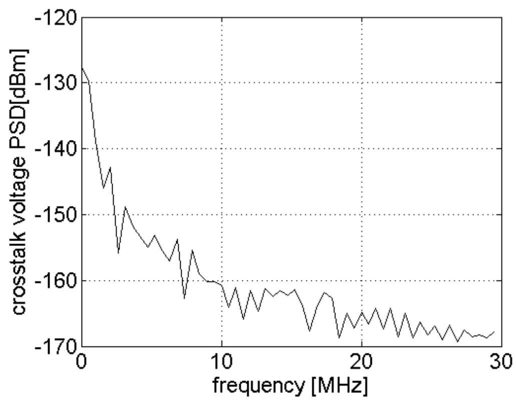

Fig. 17. Crosstalk PSD (non matched).

In particular the frequency response vanishes (values below -30dB) in two frequency ranges: from 7.5 MHz to 9MHz, and from 22MHz to 24.8 MHz. Transmitted data in the carriers inside these frequency intervals are likely to be lost. Hence, for the receiver to better exploit the channel, in the last car a matched line termination is recommended.

B. Crosstalk interference

The next figures are relative to the case of conductor number 11 excited by the 24V step signal, in order to evaluate its effect on the selected PLC channel: the crosstalk in this case is seen as a noise source. Figs. 14 and 15 show the computed crosstalk voltage present at the end of the long path in the cases of matched and open line termination respectively. In both cases there is a steady state produced by the constant voltage in conductor 1. The matched case reaches a steady state with a voltage offset of -0.6 V, while in the open case a steady state of -0.9V is observable. For an OFDM multicarrier communication an instantaneous variation of the DC component does not affect communication, since it is removed from the high pass filter at the receiver. By taking the power spectral density (PSD) of the received crosstalk signals we obtain Figures 16 and 17. The absolute power is expressed in dBm/Hz. In order to understand if this interference PSD can affect the communication we need to estimate the PSD of the received useful signal. Considering a transmitted power P_{TX} of the OFDM useful signal of -50 dBm/Hz equal for all frequencies, the received power $P_{RX}(\omega)$ can be obtained by the link budget equation:

$$P_{RX}(\omega) = P_{TX}(\omega) + W(\omega)$$

where $W(\omega)$ is the channel frequency attenuation expressed in dB, and absolute powers are expressed in dBm/Hz. Considering the frequency response of the matched channel in Figure 13, we take an average value of $W(\omega) \approx -20dB$, obtaining an average received useful power of $P_{RX}(\omega) \approx -70dBm/Hz$. A comparison of the power of the received useful signal with the power of the crosstalk interference signal in 16 and 17, we can conclude that this interference is 70 dB lower and there are not communication drawbacks.

Based on the link-budget equation and the previous result, the OFDM signal have a power of -50 dBm/Hz, that considering an occupied band of 30MHz gives a total transmitted power of 0.3Watt .We consider an OFDM signal with 256 carriers uniformly distributed in the frequency range from 117kHz to 30MHz. Figure 18 shows a $2\mu s$ window of the OFDM signal, which has been used as input voltage to conductor number 10.

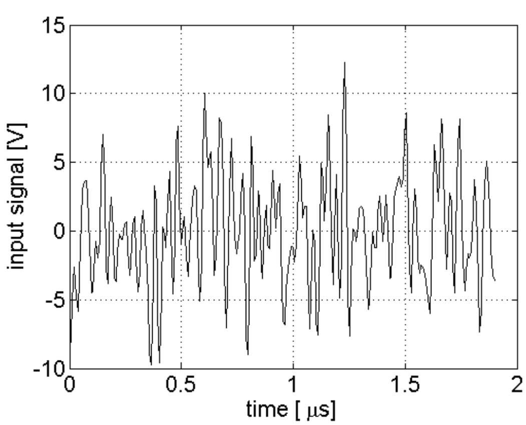

Fig. 18. Input OFDM signal.

Figures 19 and 20 show the crosstalk of the short and long path (only in the matched case), relative to the input shown in Figure 18.

The figures confirm that the effects of the data signal on the other conductors are negligible, practically being a low amplitude noise compared to the low frequency – high amplitude signals characteristics of their use.

Based on this preliminary analysis of the frequency response of the channel and the crosstalk effects the selected channel is found to be an appropriate medium for a digital transmission. To further characterize the transmission channel an analysis of the background noise and impulsive noise is necessary in order to establish the maximum theoretical bitrates attainable.

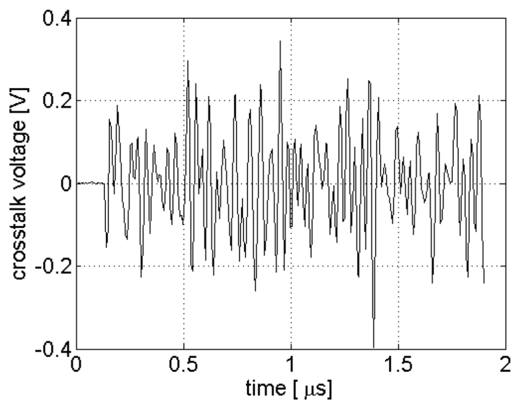

Fig. 19. Short path crosstalk, for OFDM signal.

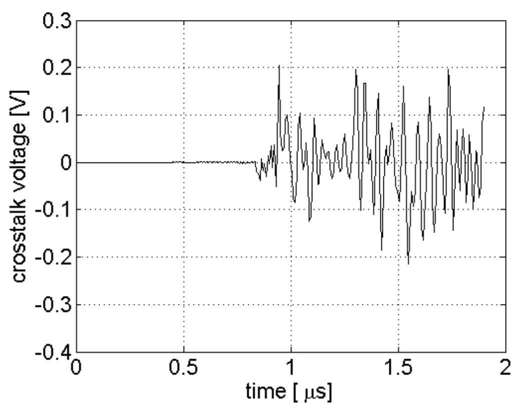

Fig. 20. Long path crosstalk, for OFDM signal.

V. CONCLUSIONS

The present paper shows the feasibility of implementing a PLC communication system onboard trains using part of the pre-existing grid. A PLC channel has been chosen among the different ones (selection based on functional issues) and an accurate model is here presented. The simulation results are encouraging, showing that the selected channel is characterized by good performances. In particular it seems to be appropriate for a high speed data communication system, where transmission rates of several MB/s could be reached.

Further work will be to perform a set of field tests to validate the presented results and to acquire some components characteristics which will lead to a more accurate channel model.

ACKNOWLEDGMENTS

This work was supported by the Italian Ministry of University (MIUR) under a Program for the Development of Research of National Interest (PRIN grant # 2006095890) and the Italian State railway undertaker Trenitalia S.p.A.

REFERENCES

[1] K. Dostert, Powerline Communications, Prentice Hall, 2001.

[2] M. Zimmermann, K. Dostert, “A multipath model for the powerline channel,” IEEE Trans Commun., vol. 50, no. 4, pp. 553 – 559, Apr. 2002.

[3] D. Sabolic, A. Bazant, R. Malaric, "Signal propagation modeling in power-line communication networks," IEEE Trans. on Power Delivery, vol. 20, no. 4, pp. 2429 – 2436, Oct. 2005.

[4] S. Galli and T. Banwell, “A novel approach to the modeling of the indoor power line channel - Part I: Circuit analysis and companion model,” IEEE Trans. Power Delivery, vol. 20, no. 2, pp. 655-663, Apr. 2005.

[5] H. Meng, S. Chen, Y. L. Guan, C. L. Law, P. L. So, E. Gunawan, T. T. Lie, “Modeling of transfer Characteristics for the broadband power line communication channel,” IEEE Trans. on Power Delivery, vol. 19, no. 3, pp. 1057 – 1064, Jul. 2004.

[6] D. Anastasiadou, T. Antonakopoulos, "Multipath characterization of indoor power-line networks," IEEE Transactions on Power Delivery, vol. 20, no. 1, Jan. 2005.

[7] E. Del Re, R. Fantacci, S. Morosi, R. Serravalle “Comparison of CDMA and OFDM techniques for downstream power-line communications on low voltage grid,” IEEE Trans. on Power Delivery, vol. 18, no. 4, pp. 1104 – 1109, Oct. 2003.

[8] C Luo; S. Cheng; L. Xiong; J. Nguimbis; Y. Zhang; J. Ma, “A nonlinear equalization method based on multilayer perceptron for OFDM power-line communication,” IEEE Trans. on Power Delivery, vol. 20, no. 4, pp. 2437 – 2442, Oct. 2005.

[9] Y. H. Ma, P.L. So, E. Gunawan, “Performance analysis of OFDM systems for broadband power line communications under impulsive noise and multipath effects,” IEEE Trans. on Power Delivery, vol. 20, no. 2, part I, pp. 674 – 682, Apr. 2005.

[10] P. A. J. van Rensburg, H. C. Ferreira,A. J. Snyders, "An experimental setup for in-circuit optimization of broadband automotive power-line communications", ISPLC 2005, pp. 322 – 325, 6-8 Apr. 2005.

[11] T. Huck, J. Schirmer, T. Hogenm, K. Dostert, "Tutorial about the implementation of a vehicular high speed communication system" ISPLC 2005, pp. 162 – 166, 6-8 Apr. 2005.

[12] C. H. Jones, "Communication over aircraft power lines" ISPLC 2006, pp. 149 – 154, 26 - 29 Mar. 2006.

[13] V. Degardin, P. Laly, M. Lienard, P. Degauque, "Impulsive noise on in-vehicle power lines: characterization and impact on communication performance", ISPLC 2006, pp. 222 – 226, 26 - 29 Mar. 2006.

[14] V. Degardin, P. Laly, M. Lienard, P. Degauque, “Performances of the HomePlug PHY Layer in the Context of in-vehicle Powerline Communications", ISPLC 2007, Pisa, Italy pp. 93 – 98, 26 -28 Mar. 2007.

[15] E. Liu, Y. Gao, G. Samdani, O. Mukhtar, T. Korhonen, “Powerline Communication over Special Systems", ISPLC 2005, Vancouver, Canada pp. 167 – 171, 6 -8 Apr. 2005.

[16] S. Tsuzuki et. al. “Characteristics of Power-Line Channels in Cargo Ships", ISPLC 2007, Pisa, Italy pp. 324 – 32, 26 -28 Mar. 2007.

[17] UIC 558, “Ligne de telecommande et d’information. Caracteristiquest techniques unifiees por l’equipment des voitures RIC”, Union Internationale des Chemins de fer.

[18] C. R. Paul “Analysis of Multiconductor Transmission Lines”, Wiley, 1994.

[19] S. Barmada, M. Raugi, A. Musolino “Innovative Model for Time-Varying Power Line Communication Channel Response Evaluation”, IEEE Journal on Selected Areas in Communications, vol. 24 no. 7, pp. 1317 - 1326, Jul. 2006.

[20] S. Barmada, M. Raugi, A. Musolino, M. Tucci “Analysis of Power Lines Uncertain Parameter Influence on Power Line Communications”, IEEE Transactions on Power Delivery, vol. 22 no. 4, pp. 2163 - 2171, Oct. 2007.

Sami Barmada was born in Livorno, Italy, in 1970. He received the Master and Ph.D. degrees in electrical engineering from the University of Pisa, Italy, in 1995 and 2001, respectively.

From 1995 to 1997, he was with ABB Teknologi, Oslo, Norway, where he was involved with distribution network analysis and optimization. He is currently an Associate Professor with the Department of Electrical System and Automation,

University of Pisa, where he is involved with numerical computation of electromagnetic fields, particularly on the modeling of multiconductor transmission lines and to the application of wavelet expansion to computational electromagnetics.

Prof. Barmada was the technical chairman of the Progress In Electromagnetic Research Symposium (PIERS), Pisa, Italy, 2004 and the general chairman of the ACES 2007 conference in Verona, Italy. He was the recipient of the 2003 J F Alcock Memorial Prize, presented by The Institution of Mechanical Engineering, Railway Division, for the best paper in technical innovation

Alessio Gaggelli was born in Vinci, Italy, in 1969. He received the Laurea degree in electronic engineering (cum laude) from the University of Florence, Italy, in 1996 and the Ph.D. degree in electrical sciences from the University of Bologna, Italy, in 2000. In 1998, he joined Trenitalia S.p.A., where he was involved in testing of rolling stock and high speed lines. From 2005 to 2007 he spent his efforts in the start up of high speed commercial service in Italy within the high speed division. Now, he attend to electrical tests for rolling stock and subsystem homologation. He has been co-chairman of the “EMC of railways systems, session I & II” at the 2004 International Symposium on Electromagnetic Compatibility held in Sendai (Japan) and of the “Workshop on Transportation EMC” at the EMC-Zurich in Singapore 2006 held in Singapore.

Paolo Masini was born in Montevarchi, Italy, in 1963. He received the Laurea degree in electronic engineering from the University of Florence, Italy, in 1990. In 1993, he joined Trenitalia S.p.A., where he was involved in testing of rolling stock and high speed lines, becoming in 2002 manager of electrical branch of rolling stock test department. From 2006 he has the responsibility of the whole Trenitalia’s test laboratory. He has published and presented several articles on rolling stock tests and EMC aspects related to railway.

Antonino Musolino was born in Reggio Calabria on January the 7th 1964. He received the Master degree in Electronic Engineering and the Ph. D degree in Electrical Engineering from the University of Pisa in 1990 and 1995 respectively. He is currently an Associate Professor of electrical engineering with the Department of Electrical Systems and Automation, University of Pisa. His main research activities are the numerical methods for the analysis of electromagnetic fields in linear and nonlinear media, the design of special electrical machines and the application of the WE to computational electromagnetics.

Rocco Rizzo is Assistant Professor of Electrical Engineering at the University of Pisa. He graduated at the University of Pisa and received his Ph.D. degree in Electrical Engineering from the Department of Electrical Systems And Automation in 2002. His primary area of research is focused on the development of analytical and numerical methods for the analysis of electromagnetic fields in linear and non-linear media. Main applications have been devoted to Magnetic Levitation, Electromagnetic Launchers, synthesis of Electromagnetic devices for special purposes. He has published more than 40 papers in international journals and refereed conferences. In April 2004 he has been appointed as a member of Academy of Nonlinear Sciences (ANS) in Russia.

Mauro Tucci received the degree in Automation Engineering from the University of Pisa in 2004 and at present he is a student in the international PhD course “Applied Electromagnetism in electrical and biomedical engineering, electronics, smart sensors, nano-technologies” at the Department of Electrical Systems and Automation of the University of Pisa. His research activity is in machine learning, data analysis, and system identification, with applications in electromagnetism, Non Destructive Testing, and power-lines communications.

Enhancing Microwave Breast Tomography with Microwave-Induced Thermoacoustic Imaging

Guangran Zhu and Milica Popović

Department of Electrical and Computer Engineering
McGill University, 3480 University Street
Montreal, Quebec Canada H3A 2A7
guangran.zhu@mail.mcgill.ca, milica.popovich@mcgill.ca

Abstract – Finite-element based microwave tomographic system can successfully recover dielectric properties of the human breast, aiming to image malignant breast tissues. When compared with microwave radar imaging, microwave tomography requires simpler electronics and antenna design due to its narrowband operation. However, the narrowband feature limits the resolution of the finite-element mesh often used to recover the dielectric properties of the breast, as there is no *a priori* information for mesh refinement in the critical location within the breast. In this paper, we present a two-dimensional model of a microwave imaging system with monopole antennas and pressure sensors placed in an interleaving arrangement around the breast in its pendant position. The proposed system would synergistically function together with the microwave tomographic modality in a fashion that is envisioned as follows: (1) The system uses a monopole antenna to trigger microwave absorption and, consequently, heating and expansion of the tumor. (2) The array of pressure transducers placed around the breast detect the thermally-induced pressure signals. (3) These signals are used to construct a preliminary breast image. (4) The image is used to generate a non-uniform finite-element mesh, with increased refinement around the suspected tumor locations. (5) The refined mesh is fed to an algorithm utilized by the microwave tomographic system to solve the inverse problem, which will now have *a priori* information and will hence have improved resolution in its resulting image.

Keywords – Microwave tomography, thermoacoustic imaging, breast imaging, FDTD.

I. INTRODUCTION

Human breast imaging has attracted much attention due to the high fatality rate caused by breast cancer. Microwave tomography is one of the imaging techniques for detection of breast tumors. The objective of microwave tomography is to reconstruct the dielectric properties of a body section illuminated with microwaves from a measurement of the scattered field and it can be mathematically described in terms of a non-linear inverse scattering problem [1]. This technique has been applied to image human breasts, most noticeably by Meaney *et al.* [2–5]. The tomographic algorithm developed with these systems belongs to the class of iterative algebraic reconstruction algorithms [6]. The tomographic algorithm assumes that the cross section consists of an array of unknowns in terms of the measured data. The unknowns are initialized with some estimates and the forward problem is solved. Although numerous numerical methods can be used for getting the forward solution, in our work, we focus on the microwave tomographic systems that employ the finite-element formulation. The calculated data are compared with the measurement, yielding some error to assist in updating the unknowns. This iteration continues until the unknowns converge to values that meet a previously defined acceptable threshold. Since knowledge of the breast profile is rarely known *a priori*, the finite-element mesh for the forward problem is uniform. This seriously limits the image resolution and renders the technique not as a screening tool for discovering new lesions.

Thermoacoustic breast imaging is a technique that exploits the heating differential between cancerous tumor and healthy tissue. Depending on the frequency of the electromagnetic wave used to trigger the thermally induced acoustic effect, literature to date reports on optoacoustic (photoacoustic) methods, where the heating is caused by laser illumination [7] and on microwave-induced thermoacoustic methods. Among microwave-induced thermoacoustic imaging systems, Kruger *et al.* reported a design involving 8 waveguides and 128 transducers residing below a pendant breast, showing success in obtaining tomographic images of the breast [8]. Xu and Wang reported a system using unfocused transducers with enhancement in the imaging reconstruction algorithm [9–12]. Recently, Jin and Wang pro-

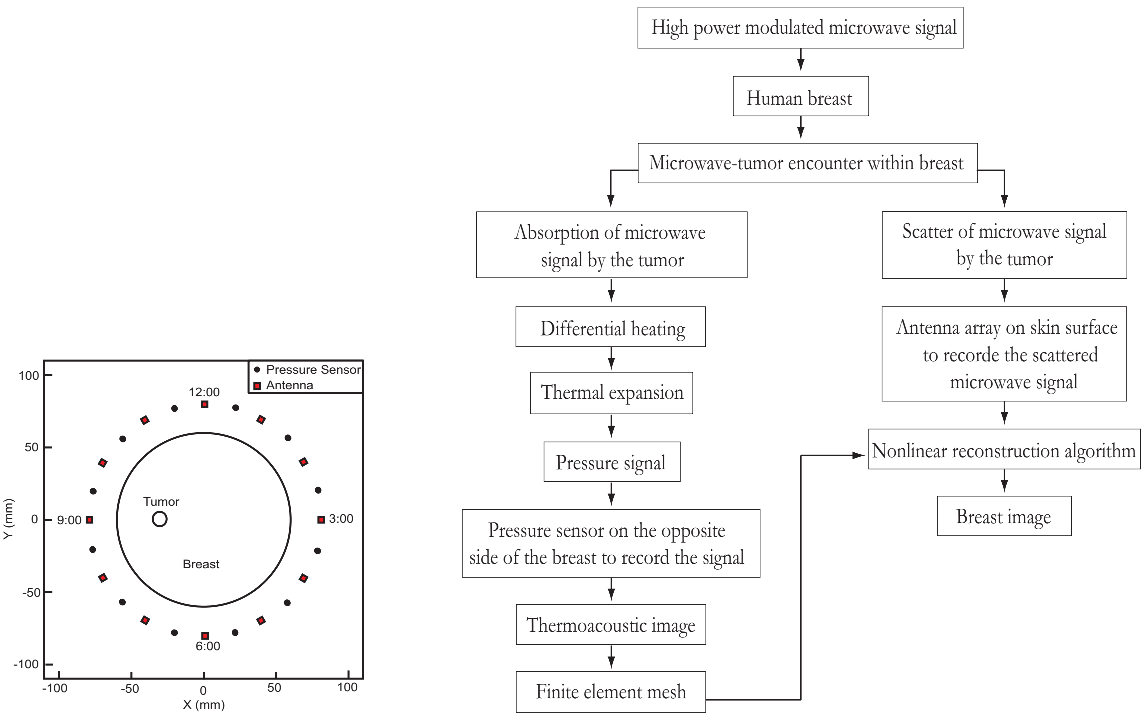

(a) (b)

Figure 1: (a) Two-dimensional model of a microwave-based imaging system with monopole antennas and acoustic pressure sensors placed in an interleaving arrangement around the breast in its pendant position. (b) Microwave-induced processes: the flowchart illustrating the thermoacoustic process, resulting from the microwave absorption, and the scattering process.

posed a multi-modality approach, using a pair of ultrasonic transducers to obtain a map of acoustic speed across a breast phantom [13]. Their image reconstruction algorithm, based on the obtained speed map, achieves a signal-to-noise ratio higher than the previous algorithms that assume homogeneity in the acoustic properties of the breast tissue. These studies suggest that microwave-induced thermoacoustic technique may have the capacity to detect early, millimeter-size tumors. Finally, Xu and Wang offered a comprehensive review of the current development in both photoacoustic and microwave-induced thermoacoustic imaging systems [14].

In this work, we present a preliminary study of a system that integrates microwave-induced thermoacoustic imaging with microwave tomography. The system is illustrated in Figure 1 (a). It consists of interleaving monopole antennas and pressure sensors. The system illuminates the pendant breast with a pulse-modulated microwave signal from one antenna. When the pulse encounters a tumor, two processes of interest to our proposed technique happen: (1) Thermoacoustic process is a consequence of microwave absorption as it propagates through the lossy tissues. As the tumor is characterized by a higher electrical conductivity at microwave frequencies, it absorbs more microwave energy and is heated to a higher temperature than the surrounding fatty tissue. The tumor expands thermally and this expansion generates an acoustic (pressure) signal. The pressure signal propagates through the breast and can be detected with the pressure sensors placed around the breast. (2) The scattering process is caused by the dielectric contrast (relative permittivity) between the tumor and healthy breast tissue . The scattered microwave signal can be sensed and collected by the antennas placed around the breast. The location of the microwave transmitter is changed by sequentially using each of the antennas as the source, while other antennas act as passive scatter-collectors, thereby providing several sets of signals. Here, we propose the usage of the signals resulting from the above-mentioned processes in the following manner: the pressure signals can be utilized to construct a preliminary thermoacoustic image and transform the image to a non-uniform, finite-element mesh, which will then resolve the anticipated tumor locations with more elements. This mesh and the scattered microwave signal are then subjected to the non-linear reconstruction algorithm commonly used in microwave tomographic systems to generate a breast image. The proposed method is illustrated by a flowchart in Figure 1 (b). Unlike a related work that used the ultrasound modality to obtain the preliminary image [15], the here proposed method eliminates the need to have a separate ultrasound source.

An important point on the dielectric data of breast tissue must be addressed here prior to further description of our methodology. A thorough and extremely valuable study on breast tissue parameters was recently reported by Lazebnik *et al.* [16, 17]. Their measurements of samples from normal tissue demonstrate that different composition of the adipose, fibroconnective, and glandular tissue in the sample, inhomogeneous by nature, cause large variations in the dielectric properties, while the previously noted high-permittivity and high-conductivity cancer tissue values at microwave frequencies are consistent with this recent study. This implies that the contrast between the tumor and the glandular tissue surrounding it is not necessarily as pronounced as those assumed in simulation and phantom-based studies to date [18–22]. Nonetheless, these investigations provide valuable insight in the overall underlying principle of microwave breast cancer detection. Similarly, although our work assumes fat-like healthy breast tissue, well contrasted by the tumor in terms of their electrical properties, its main goal is to provide the multi-physics framework for a system that incorporates microwave tomography with microwave-induced thermoacoustic imaging. We also note that the thermoacoustic profile does not provide a detailed image, but rather informs the finite-element mesh generator about the suspect locations where the mesh should resolve the image intended for the microwave tomographic process more finely then elsewhere. For the future model modified according to the newly published data of [16, 17], the higher-conductivity fibroconnective and glandular tissue would also yield finely-meshed suspect locations in the simulation geometry; however, we note again that these locations are simply used to locally refine the mesh but do not instruct the finite-element forward-model to treat them, parameter-wise, in the model as tumors.

This paper focuses on a preliminary computational study of the proposed imaging system. In the next section, we present the modeling of the microwave-induced thermoacoustic process. Section III includes the methodology on the electromagnetic simulation, the artifact removal algorithm, and the algorithm for constructing the preliminary thermoacoustic image. The Specific Absorption Rate (SAR), the computed pressure signals, the thermoacoustic image of the breast, and the non-uniform finite-element mesh are presented in Section IV. In section V, we summarize our findings and offer directions for future work.

II. MICROWAVE-INDUCED THERMOACOUSTIC PROCESS

The thermoacoustic process occurs when the tissue is exposed to electromagnetic radiation. Since there exists a significant contrast in conductivity between normal tissue and breast tumors at certain frequencies, the tumors absorbs more electromagnetic energy. This elevates the tumor temperature and the tumor expands. The mechanical expansion generates pressure signals that propagate to the breast surface, which can be collected by pressure sensors and processed to construct a breast image.

The Pennes' bioheat transfer equation is commonly used to model the heat transfer in perfused tissue, e.g. human breasts,

$$\rho c \frac{\partial T}{\partial t} = \nabla \cdot (k \nabla T) + \rho Q + \rho S - D(T - T_b) \ , \quad (1)$$

where ρ is the tissue density in kgm^{-3}, c is the specific heat capacity in $\mathrm{Jkg}^{-1}\mathrm{K}^{-1}$, T is the local tissue temperature in K, k is the thermal conductivity in $\mathrm{Wm}^{-1}\mathrm{K}^{-1}$, Q is the metabolic heat generation rate in Wkg^{-1}, S is the SAR in Wkg^{-1}, T_b is the temperature of the arterial blood in K, and D is the heat transfer rate that models the heat removal due to blood circulation in $\mathrm{Jm}^{-3}\mathrm{K}^{-1}\mathrm{s}^{-1}$. If the duration of the microwave pulse is short, on the scale of a few micro seconds, the thermal diffusion can be neglected and the Pennes' equation reduces to

$$\rho c \frac{\partial T}{\partial t} = H(\mathbf{r}, t) \ , \quad (2)$$

where H represents the heat deposited into the tissue in $\mathrm{Js}^{-1}\mathrm{m}^{-3}$. In the theory of acoustics, the equation of continuity of mass can be expressed as

$$\frac{1}{B}\frac{\partial p}{\partial t} - \beta \frac{\partial T}{\partial t} = -\nabla \cdot \vec{u} \ , \quad (3)$$

where B is the bulk modulus in Pa, p is the acoustic pressure in Pa, β is the isobaric temperature coefficient of volume expansion in K^{-1}, and $\vec{u}$ is velocity of the differential volume within the mass matter in ms^{-1}. The simple force equation represents the acceleration and deceleration of fluid elements, and it is given by

$$\rho_o \frac{\partial \vec{u}}{\partial t} = -\nabla p \ . \quad (4)$$

Combining (2), (3) and (4) gives the thermoacoustic wave equation

$$\nabla^2 p - \frac{\rho_o}{B}\frac{\partial^2 p}{\partial t^2} = -\frac{\beta}{c}\frac{\partial H}{\partial t} \ . \tag{5}$$

The analytical solution to (5) in 2D, is expressed in terms of the Green's function, which is

$$\begin{aligned} p(\boldsymbol{\rho}, t) &= \int_S g_{2D}(\boldsymbol{\rho}, \boldsymbol{\rho'}, t) \otimes f(\boldsymbol{\rho'}, t)\mathrm{d}S \\ &= \int_S \frac{1}{2\pi}\frac{u(t - |\boldsymbol{\rho} - \boldsymbol{\rho'}|/c_a)}{\sqrt{t^2 - (|\boldsymbol{\rho} - \boldsymbol{\rho'}|/c_a)^2}} \\ &\quad \otimes \left(-\frac{\beta}{c}\frac{\partial H(\boldsymbol{\rho'}, t)}{\partial t}\right)\mathrm{d}S \ , \end{aligned} \tag{6}$$

where $\otimes$ denotes convolution in time, $u(\cdot)$ is the unit step function, and c_a is the acoustic propagation speed in ms^{-1}.

The microwave excitation is a pulse-modulated sinusoidal wave. The heat function can be expressed as

$$H(\boldsymbol{\rho}, t) = \rho S(\boldsymbol{\rho}) I(t) \ , \tag{7}$$

where the temporal illumination $I(t)$ denotes a normalized Gaussian pulse. The SAR, in Wkg^{-1}, is calculated from

$$S(\boldsymbol{\rho}) = \frac{\sigma_e}{2\rho}|\boldsymbol{E}|^2 \ , \tag{8}$$

where σ_e is the electric conductivity in Sm^{-1} and $\boldsymbol{E}$ denotes the electric field in Vm^{-1}.

III. METHODOLOGY

A. Electromagnetic Modeling

We have developed at 2-D TM_z finite-difference time-domain model to simulate the microwave-tissue interaction. The electromagnetic model, shown in Figure 1 (a)), consists of one 120-mm diameter cylinder to mimic the breast cross-section and one 6-mm diameter cylinder to mimic the tumor cross-section. We use deionized (DI) water as the matching medium. The monopole antennas are modeled as infinite-line sources. The computation domain is 200 mm×200 mm, with a uniform grid size of 0.3 mm×0.3 mm and it is truncated with a Perfectly Matched Layer. The single-pole Debye dispersion model is commonly used to approximate the dispersive characteristics of tissue materials. Its expression is

$$\epsilon_r - j\frac{\sigma}{\omega\epsilon_o} = \epsilon_\infty + \frac{\epsilon_s - \epsilon_\infty}{1 + j\omega\tau} - j\frac{\sigma_s}{\omega\epsilon_o} \ , \tag{9}$$

where ϵ_∞ is the relative permittivity at infinite frequency, ϵ_s is the static relative permittivity, σ_s is the static conductivity in Sm^{-1}, and τ is the relaxation time constant in s. We use the Debye parameters of tumor, breast tissue, and deionized water from [22] to calculate their dielectric constants, which are listed in Table 1. Figure 2 shows the dielectric constants over the microwave range. These constants are assigned to the electromagnetic model and we allow a 10% variation in the dielectric constants of the breast tissue over the region to mimic the heterogeneity. For comparison, we show the dielectric constant values both at 6 GHz, frequency used in our previous related work [23] and at 434 MHz, the operating frequency in this paper and in [8].

Table 1: Debye parameters from [22] and the dielectric constants at 434 MHz and 6 GHz [24].

Parameter	Tumor	Tissue	DI Water
ϵ_∞	3.99	6.57	4.55
ϵ_s	54	16.29	77.11
σ_s	0.7	0.23	0.0002
τ (ps)	7	7	7.37
ϵ_r at 434 MHz	53.9818	16.2865	77.0807
σ at 434 MHz	0.7230	0.2345	0.0354
ϵ_r at 6 GHz	50.74	9.8	71.91
σ at 6 GHz	4.82	0.4	6.25

B. Thermoacoustic Modeling

We use the solution expressed in terms of Green's function (6) to numerically compute the pressure signals at particular locations. Table 2 lists the physical properties of the materials recorded in [22, 24]. These parameters are included in (6) to calculate the pressure signals. The normalized Gaussian pulse has a standard deviation of 0.5 µs. Its bandwidth-to-center-frequency ratio is approximately 1/434. Therefore, the distortion in the recorded field magnitude and phase, which will be used in the tomographic system, is considered negligible.

Table 2: Material thermal and mechanical properties [22, 24].

Parameter	Tumor	Average	DI Water
c	3049	2279	4186
ρ	1182	1069	1000
β	9.2×10^{-4}	3.5×10^{-4}	2.07×10^{-4}
c_a	1550	1550	1500

C. Artifact Removal Algorithm

Monopole antennas cause non-uniform heating of the tissue. The tissue close to the antennas is responsible for absorbing the initial, unattenuated microwave energy, and it consequently experiences more heating

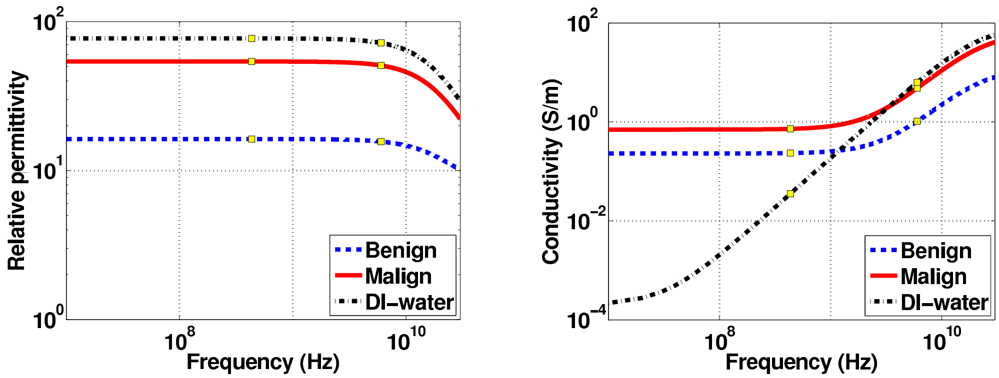

(a) (b)

Figure 2: (a) Relative permittivity and (b) conductivity over the microwave frequency range. [22]

than the rest of the tissue and tumors. The heating-induced artifact is much stronger than the pressure signal due to the heating of tumor and the artifact overshadows the tumor response. We need to eliminate this breast-heating artifact and recover the weak tumor response.

This non-uniform heating happens at all antenna sites and the breast-heating artifacts received on the opposite side of the breast are all similar, but not identical due to the tissue heterogeneity. To remove this artifact, we borrow the skin subtraction method from microwave radar imaging, which removes the reflection of the microwave pulse at the breast-skin interface [25]. This method is based on the assumption that the back-scattered microwave signals from the breast-skin interface contain similar but not identical unwanted artifacts at various antenna sites. The artifact in one signal can be eliminated by a filtered combination of other signals, where the filter weights minimize the mean-squared error between the signal at one antenna and the sum of the filtered signals at all other antenna sites over the portion of the signals dominated by the artifact.

In our scenario, the artifact in the received pressure signal is from the maximally heated tissue, near the transmitting antenna. Assume there are N pressure sensors. Let $p_n(i)$ denote the discrete pressure signal received at the n^{th} pressure sensor at time i. Let $p_1(i)$ be the target signal to be filtered. $\vec{p}_n$ denotes the $(2J+1)\times 1$ vector centered at time i, i.e. $\vec{p}_n(i) = [p_n(i-J)\cdots p_n(i+J)]$. $\vec{w}_n$ denotes the time-independent filter weight applied to $\vec{p}_n(i)$, i.e. $\vec{w}_n = [w_n(-J)\cdots w_n(J)]^T$. Let $\mathbf{p}(\vec{i})) = [\vec{p}_2(i);\cdots\vec{p}_N(i)]$, the concatenated pressure signal from Sensor 2 to Sensor N and $\vec{\mathbf{w}} = [\vec{w}_2;\cdots\vec{w}_N]$, the concatenated filter weights. The optimal weights are calculated from

$$\min_{\vec{\mathbf{w}}} \sum_{i=i_o}^{i_o+M-1} \left|p_1(i) - \vec{\mathbf{w}}^T\vec{\mathbf{p}}(i)\right|^2 \ , \qquad (10)$$

where the time interval i_o to i_o+M-1 denotes the portion of the signal that contains the breast-heating artifact. The solution to this problem is [26]

$$\vec{\mathbf{w}} = \mathbf{R}^{-1}\vec{\mathbf{P}} \ , \qquad (11)$$

where $\mathbf{R}$ is the correlation matrix

$$\mathbf{R} = \frac{1}{m}\sum_{i=i_o}^{i_o+M-1} \vec{\mathbf{p}}(i)\vec{\mathbf{p}}(i)^T \ , \qquad (12)$$

and $\vec{\mathbf{P}}$ is the cross-correlation vector

$$\vec{\mathbf{P}} = \frac{1}{m}\sum_{i=i_o}^{i_o+M-1} p_1(i)\vec{\mathbf{p}}(i) \ . \qquad (13)$$

The filtered signal from the first pressure sensor is $\hat{p}_1(i) = p_1(i) - \vec{\mathbf{w}}^T\vec{\mathbf{p}}(i)$ and this procedure is repeated for the second pressure sensor being the target signal.

D. Image Reconstruction and Mesh Generation

We use the simple delay-sum algorithm to process the collected pressure signals [18]. The intensity of each pixel Z at location $\boldsymbol{\rho}$ is the energy of the sum of N delayed signals, which is expressed as

$$Z(\boldsymbol{\rho}) = \sum_{i=0}^{M}\left[\sum_{n=1}^{N} a_n p_n\left(i + \left\lfloor\frac{|\boldsymbol{\rho}-\boldsymbol{\rho}_n|}{c_a\Delta t}\right\rfloor\right)\right]^2 \ , \qquad (14)$$

where M is the number of discrete time steps, a_n is the weight introduced to compensate for the radial spreading of each cylindrical wave as it propagates outward from the location $\boldsymbol{\rho}$, p_n is the n^{th} pressure signal, Δt is the acoustic time step size, and $\lfloor\cdot\rfloor$ denotes the floor operator.

Given the breast image from the thermoacoustic data, we obtain the contour plot and assign uniform points along each contour to generate the point map. We feed the point map to the DistMesh [27] to acquire the non-uniform, adapted mesh, which can in the next stage of the process be used in the algorithm to solve the inverse problem and generate a more accurate dielectric properties.

IV. RESULTS

Figure 3 (a) shows the SAR over the computation domain under the radiation from the infinite-line source located in the far-right position (3 o'clock). The plot is on the log scale with the peak SAR normalized to 0.4 Wkg^{-1} [28], which is the limit of the ANSI-IEEE Criterion for the average SAR in the whole body. We observe the expected non-uniform heating over the breast area, with pronounced heating in the immediate vicinity of the transmitting antenna. The tumor, due to its high conductivity, also absorbs more microwave energy than its ambient tissue. In two and three dimensions, a cylindrically (spherically) symmetrical source produces one wave that propagates outwardly to the pressure sensor, and at the same time, a second wave that propagates inwardly to the origin. The latter undergoes a reflection at the origin and reappears as an inverted, outwardly propagating wave that eventually reaches the field point. Therefore, the time profile of a photoacoustic wave assumes an N-shape. (In one dimension, the second wave propagates in the opposite direction and will not reach the pressure sensor.) Diebold and Sun presented the solution to the thermoacoustic wave equation (5) of a uniformly-excited homogeneous cylinder under a δ-pulse heating function [29], which is confirmed later by Hoelen and de Mul [30]. This theoretical thermoacoustic signal is shown in Figure 3 (b). Figure 3 (c)-(h) graphs the computed pressure waves at the locations indicated in Figure 3 (a). Our heating-function is a Gaussian pulse with a standard deviation of 0.5 µs, whose spatial span is about 1.5 mm given the constant acoustic speed of 1500 ms^{-1}. This pulse resembles a δ-pulse heating function in comparison to the diameter of the cylinder. Therefore, Figure 3 (c)-(h) all have N-shape traces. The deviation from the theoretical result at different sensor locations is due to the non-uniform heating of the cylinder and heating of the ambient matching background. If the cylinder and the background were uniformly heated, Figure 3 (c)-(h) would assume the theoretic shape regardless of the sensors' locations. The thermoacoustic response of the tumor is also marked in this figure. This tumor response, though, resembles the shape of a differentiated Gaussian pulse since the diameter of the tumor, i.e. 6 mm, is comparable to the spatial span of the heating function.

Due to the high heating of the tissue close to the microwave source, this region generates acoustic waves of high amplitude. The first half of the pressure wave at 2:30 o'clock location in Figure 3 (c) is generated predominantly by the region that is close to the microwave source. As we move the pressure sensor further away from the microwave source, the response generated by the tumor becomes more pronounced with respect to the response of the surrounding tissue, being most noticeable at 10:30 o'clock location in Figure 3 (g), and at 09:30 o'clock location in Figure 3 (h). This suggests that a system based on microwave-induced thermoacoustic imaging may benefit from collecting signals from the pressure sensor placed on the opposite side of the microwave source. In addition, our goal is to apply an algorithm that will remove the artifact of the high-peak pressure signal generated in the immediate vicinity of the transmitting antenna.

In microwave radar imaging, the early breast-skin artifact is separated from the later tumor response in the backscattered microwave signal in time. The time interval parameters i_o and M are carefully chosen to only include the breast-skin artifact. In microwave-induced thermoacoustic imaging, since the pressure wave travels at a significantly lower speed than electromagnetic wave, the breast-heating artifact overlaps with the tumor acoustic response. Therefore, this artifact removal method is applied over the entire range of the pressure signal and the number of consecutive pressure samples weighted before being subtracted from the target signal is bigger than the value used in [25]. In Figure 4, we demonstrate the capability of the artifact removal algorithm when the antenna and the pressure sensor are placed on the opposite sides of the breast. The signals before and after the filtering process are presented. The artifact is clearly removed in all cases, allowing for the tumor response to emerge. We also observe that the filtered signals that contains strong tumor response as in Figure 4 (c) and (d), are less noisier than the signals that contain week tumor response as in Figure 4 (a) and (b).

The delay-sum scheme for image reconstruction has the averaging effect when the noise is added incoherently and the tumor response is added coherently. Therefore, we are still able to recover the tumor in the thermoacoustic image. Finally, Figure 5 shows the thermoacoustic map and the finite-element mesh that contains locally refined elements in the regions that are suspected to contain the tumor. This mesh can now be used in conjunction with the scattered

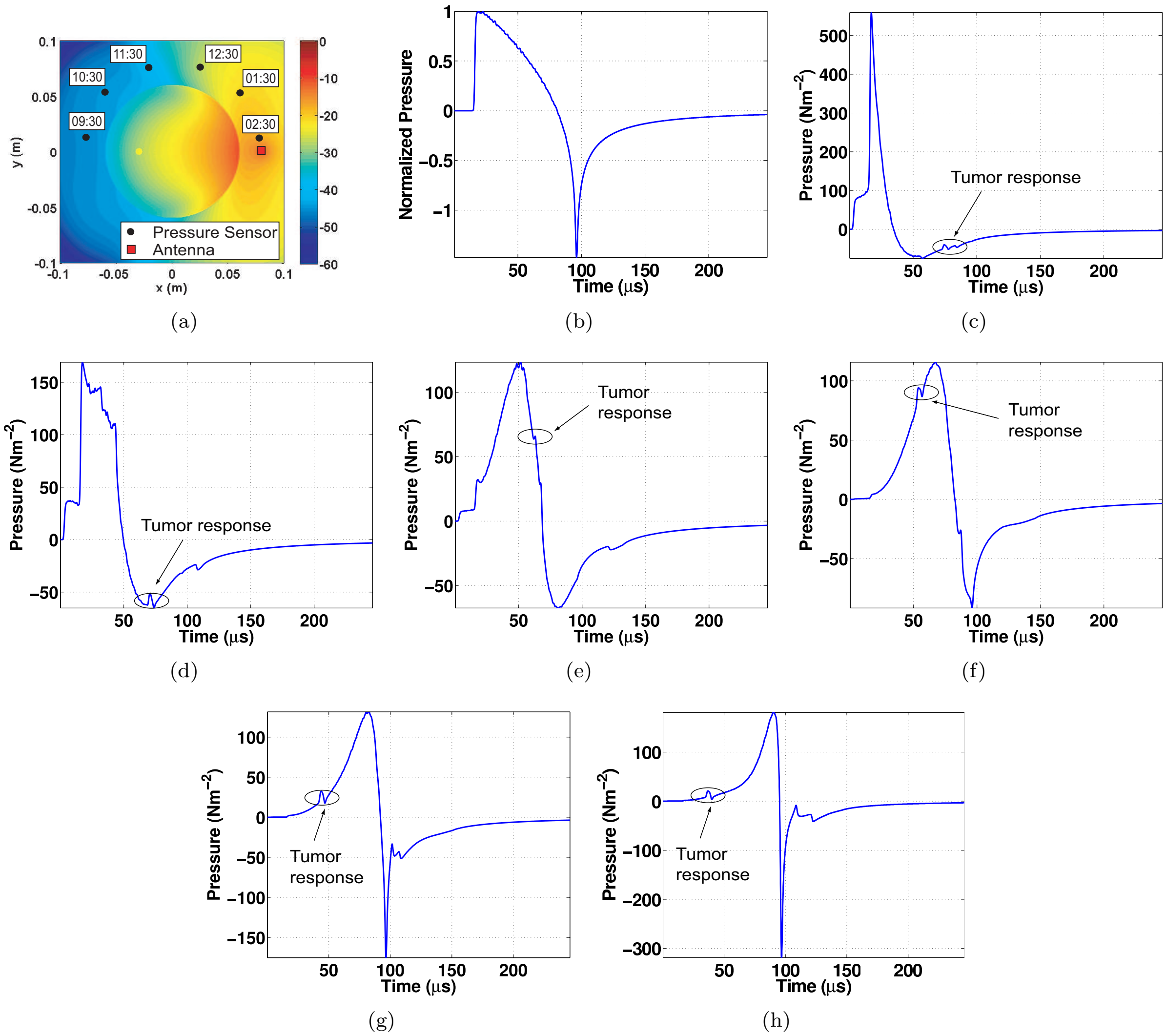

Figure 3: (a) SAR at 434 MHz on a dB scale normalized to 0.4 Wkg^{-1}, with the locations of the antenna (square symbol, at the 3 o'clock location) and pressure sensors indicated by the black dots. (b) Theoretical thermoacoustic signal generated by a uniformly-excited homogeneous cylinder. The trace shows the signal for a δ-pulse heating function. The following graphs show the calculated pressure signals at the sensor locations at the following approximate clock-handle positions: (c) 02:30, (d) 01:30, (e) 12:30, (f) 11:30, (g) 10:30, (h) 9:30.

microwave signals for an improved microwave tomographic image of the breast.

V. CONCLUSIONS AND FUTURE WORK

In this paper, we presented a preliminary study of a breast imaging system that uses microwave-induced thermoacoustic imaging to enhance microwave tomography. Monopole antennas and pressure sensors are interleaved and surround a pendant breast. Monopole antennas are sequentially excited to induce the thermoacoustic process in the breast. The pressure sensors collect signals, which form a thermoacoustic image of the breast. The aim of our paper was to show how an image formed in this fashion can guide the construction of the finite-element mesh which is locally refined to resolve, with more elements, the suspect locations that are likely to contain a tumor. At the same time, the scattered microwave energy is recored at other antennas in terms of magnitude and phase. Therefore, in a complete system, the obtained non-uniform finite-element mesh and the field quantities can be used to recover the

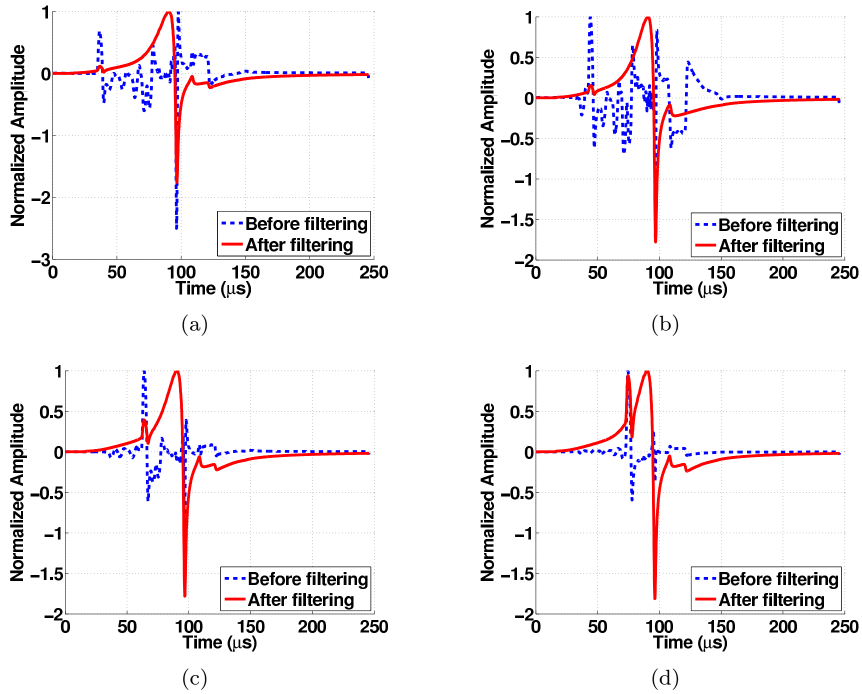

Figure 4: Pressure signals at the side of the breast opposite to the antennas, before and after the removal of breast-heating artifact. Antennas are located at (a) 3:00, (b) 1:00, (c) 11:00, and (d) 9:00 o'clock positions.

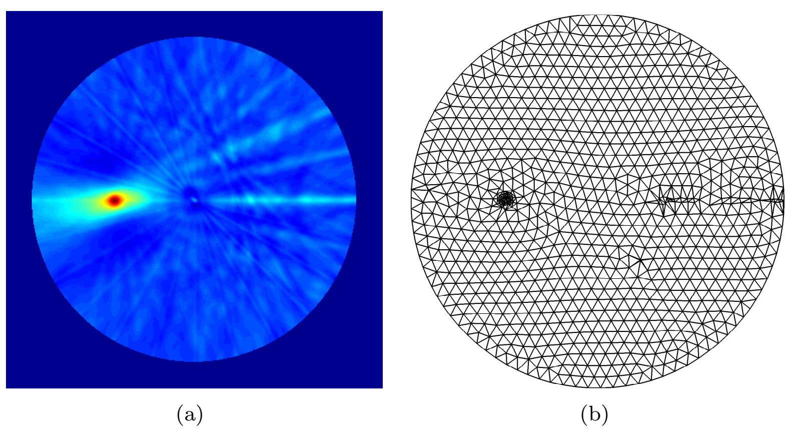

Figure 5: (a) Thermoacoustic map constructed from the pressure signals. (b) Finite-element mesh with local refinement in the region suspected to contain a tumor, to be used for enhancement in the microwave tomographic process.

dielectric properties of the breast. Such a system would overcome the low resolution of microwave tomographic system by providing a finite-element mesh that contains *a priori* information about the potential tumor location. In our preliminary study, we simulated the thermoacoustic process, constructed the thermoacoustic image, and have shown the locally refined finite-element mesh. In the on-going and immediate future work, the more anatomically realistic geometry and tissue parameters as in [16, 17] will be incorporated in the breast model. Further, we are presently implementing an iterative tomographic algorithm to recover the dielectric properties over the non-uniform mesh.

VI. ACKNOWLEDGMENTS

This work was funded by Natural Science and Engineering Research Council (NSERC) of Canada Discovery Grant and by the Le Fonds Québécois de la Recherché sur la Nature et les Technologies (FQRNT) Nouveaux Chercheurs grant.

REFERENCES

[1] A. Broquetas, J. Romeu, J. Rius, A. Elias-Fuste, A. Cardama, and L. Jofre, "Cylindrical geometry: a further step in active microwave tomography," *IEEE Trans. Microw. Theory Tech.*, vol. 39, no. 5, pp. 836–844, 1991.

[2] P. M. Meaney, M. W. Fanning, D. Li, S. P. Poplack, and K. D. Paulsen, "A clinical prototype for active microwave imaging of the breast," *IEEE Trans. Microw. Theory Tech.*, vol. 48, no. 11, pp. 1841–1853, 2000.

[3] P. M. Meaney, K. D. Paulsen, B. W. Pogue, and M. I. Miga, "Microwave image reconstruction utilizing log-magnitude and unwrapped phase to improve high-contrast object recovery," *IEEE Trans. Med. Imag.*, vol. 20, no. 2, pp. 104–116, 2001.

[4] P. M. Meaney, S. A. Pendergrass, M. W. Fanning, D. Li, and K. D. Paulsen, "Importance of using a reduced contrast coupling medium in 2d microwave breast imaging," *Journal of Electromagnetic Waves and Applications*, vol. 17, no. 2, pp. 333–355, 2003.

[5] T. Rubæk, P. M. Meaney, P. Meincke, and K. D. Paulsen, "Nonlinear microwave imaging for breast-cancer screening using gauss-newton's method and the cgls inversion algorithm," *IEEE Trans. Antennas Propag.*, vol. 55, no. 8, pp. 2320–2331, 2007.

[6] A. C. Kak and M. Slaney, *Principles of Computerized Tomographic Imaging.* IEEE Press, 1987.

[7] A. A. Oraevsky and A. A. Karabutov, *Optoacoustic Tomography.* Boca Raton, FL: CRC Press, 2003.

[8] R. A. Kruger, K. Stantz, and W. L. Kiser, Jr., "Thermoacoustic CT of the breast," in *Proc. of SPIE*, L. E. Antonuk and M. J. Yaffe, Eds., vol. 4682. SPIE, pp. 521–525, 2002.

[9] Y. Xu, D. Feng, and L. V. Wang, "Exact frequency-domain reconstruction for thermoacoustic tomography. i. planar geometry," *IEEE Trans. Med. Imag.*, vol. 21, no. 7, pp. 823–828, Jul. 2002.

[10] Y. Xu, M. Xu, and L. V. Wang, "Exact frequency-domain reconstruction for thermoacoustic tomography. II. cylindrical geometry," *IEEE Trans. Med. Imag.*, vol. 21, no. 7, pp. 829–833, Jul. 2002.

[11] M. Xu and L. V. Wang, "Time-domain reconstruction for thermoacoustic tomography in a spherical geometry," *IEEE Trans. Med. Imag.*, vol. 21, no. 7, pp. 814–822, 2002.

[12] ——, "Analytic explanation of spatial resolution related to bandwidth and detector aperture size in thermoacoustic or photoacoustic reconstruction," *Physical Review*, vol. 67, no. 5, p. 056605, May 2003.

[13] X. Jin and L. V. Wang, "Thermoacoustic tomography with correction for acoustic speed variations," *Physics in Medicine and Biology*, vol. 51, no. 24, pp. 6437–6448, 2006.

[14] M. Xu and L. V. Wang, "Photoacoustic imaging in biomedicine," *Review of Scientific Instruments*, vol. 77, no. 4, pp. 1–22, 2006.

[15] H. Jiang, C. Li, D. Pearlstone, and L. L. Fajardo, "Ultrasound-guided microwave imaging of breast cancer: Tissue phantom and pilot clinical experiments," *Medical Physics*, vol. 32, no. 8, pp. 2528–2535, 2005.

[16] M. Lazebnik, L. McCartney, D. Popovic, C. B. Watkins, M. J. Lindstrom, J. Harter, S. Sewall, A. Magliocco, J. H. Booske, M. Okoniewski, and S. C. Hagness, "A large-scale study of the ultrawideband microwave dielectric properties of normal breast tissue obtained from reduction surgeries," *Physics in Medicine and Biology*, vol. 52, no. 10, pp. 2637–2656, 2007.

[17] M. Lazebnik, D. Popovic, L. McCartney, C. B. Watkins, M. J. Lindstrom, J. Harter, S. Sewall, T. Ogilvie, A. Magliocco, T. M. Breslin, W. Temple, D. Mew, J. H. Booske, M. Okoniewski, and S. C. Hagness, "A large-scale study of the ultrawideband microwave dielectric properties of normal, benign and malignant breast tissues obtained from cancer surgeries," *Physics in Medicine and Biology*, vol. 52, no. 20, pp. 6093 – 6115, 2007.

[18] X. Li and S. C. Hagness, "A confocal microwave imaging algorithm for breast cancer detection," *IEEE Microw. Wireless Compon. Lett.*, vol. 11, no. 3, pp. 130–132, 2001.

[19] E. C. Fear, X. Li, S. Hagness, and M. A. Stuchly, "Confocal microwave imaging for breast cancer detection: localization of tumors in three dimensions," *IEEE Trans. Biomed. Eng.*, vol. 49, no. 8, pp. 812–822, 2002.

[20] J. M. Sill and E. C. Fear, "Tissue sensing adaptive radar for breast cancer detection - experimental investigation of simple tumor models," *IEEE Trans. Microw. Theory Tech.*, vol. 53, no. 11, pp. 3312–3319, 2005.

[21] P. Kosmas and C. Rappaport, "Fdtd-based time reversal for microwave breast cancer detection-localization in three dimensions," *IEEE Trans. Microw. Theory Tech.*, vol. 54, no. 4, pp. 1921–1927, 2006.

[22] M. Converse, E. J. Bond, B. D. van Veen, and S. C. Hagness, "A computational study of ultra-wideband versus narrowband microwave hyperthermia for breast cancer treatment," *IEEE Trans. Microw. Theory Tech.*, vol. 54, no. 5, pp. 2169–2180, 2006.

[23] G. Zhu and M. Popović, "2-d computational study of the microwave-induced thermoacoustic effect on human breast with tumor," in *Proc. Annual Review of Progress in Applied Computational Electromagnetics (ACES'07)*, Verona, Italy, Mar. 2007.

[24] F. A. Duck, *Physical properties of tissue: A comprehensive reference book.* San Diego, CA: Academic Press, 1990.

[25] E. J. Bond, X. Li, S. C. Hagness, and B. D. van Veen, "Microwave imaging via space-time beamforming for early detection of breast cancer," *IEEE Trans. Antennas Propag.*, vol. 51, pp. 1690–1705, 2003.

[26] S. Haykin, *Adaptive Filter Theory*, 4th ed. Upper Saddle River, NJ: Prentice-Hall, 2002.

[27] P. olof Persson and G. Strang, "A simple mesh generator in MATLAB," *SIAM Review*, vol. 46, no. 2, pp. 329–345, 2004.

[28] "IEEE standard for safety levels with respect to human exposure to radio frequency electromagnetic fields, 3 khz to 300 ghz," IEEE, Piscataway, NJ, 2006.

[29] G. J. Diebold and T. Sun, "Properties of photoacoustic waves in one, two, and three dimensions," *Acustica*, vol. 80, no. 4, pp. 339–351, 1994.

[30] C. Hoelen and F. de Mul, "A new theoretical approach to photoacoustic signal generation," *Journal of the Acoustical Society of America*, vol. 106, no. 2, pp. 695 – 706, 1999.

Guangran Zhu received the B.Sc. degree in computer engineering and M.Sc. degree in electrical engineering both from University of New Brunswick, Fredericton, Canada in 2003 and 2005. He is currently working towards the Ph.D. degree in the department of electrical and computer engineering at McGill University, Montreal. His research interests include computational electromagnetics, particularly finite-difference time-domain method, microwave-tissue interaction, and related signal processing problems. Mr. Zhu was a recipient of the Graduate Fellowship from IEEE Antenna and Propagation Society in 2007.

Milica Popović received her B.Sc. (1994) from University of Colorado (Boulder, Colorado, USA) and M.Sc. (1997) and Ph.D. (2001) degrees from Northwestern University (Evanston, Illinois, USA), all in electrical engineering. She is currently an associate professor with the Department of Electrical and Computer Engineering at McGill University in Montreal, Canada. Her research interests focus on numerical methods in computational electromagnetics for bio-medical applications, in particular: breast cancer screening with microwaves, wireless implants for physiological research and light interaction with retinal photoreceptor cells. On the teaching side, her efforts include improvement methods for instruction of introductory electromagnetics courses.

Electrodynamics of Dipolar Beads in an Electrophoretic Spherical Cavity

M.H. Lean and A.R. Völkel
Palo Alto Research Center, Palo Alto, CA 94304, US
meng.lean@parc.com , armin.volkel@parc.com

Abstract – This paper describes an algorithm to simulate transient behavior of a dipolar bead in an electrophoretic spherical cavity. The model includes consideration of form drag and viscous damping, both corrected for wall effects. In particular, the bead rotation as a function of monopole and dipole charge, and the impact of gravity on the bead dynamics is investigated. Several levels of approximation are implemented to expedite the overall computation. A consistent set of results is presented to describe the accuracy of the simulation.

I. INTRODUCTION

The transient dynamics of dipolar beads in an electrophoretic spherical cavity presents an interesting phenomenon, because it captures the interplay of electrophoretics, particle dynamics, and tribology. The problem geometry is described by a dipolar bead immersed in a polarized fluid within the cavity. Switching bias voltages are applied to induce both translational and rotational motion of the bead. This paper details a model of coupled phenomena which employs ODE's to describe the bead dynamics, integral equations for the field solution, and particle simulation for the bipolar migrations. Special focus is given to the impact of confinement and gravitational force on the bead dynamics.

II. PROBLEM FORMULATION

We assume a dipolar bead with radius r_b and mass m in a spherical cavity of radius r_c. The bead is divided into two distinct hemispheres with different net charges q_b and q_w. For low counter ion concentrations, we can approximate the charge distribution on the bead by the first two terms of a multipole expansion, i.e. by the monopole charge $q_m = q_b + q_w$ and the dipole moment $\mathbf{p} = q_d d_p$, where $q_d = |q_b - q_w|/2$ is the dipole charge and d_p is the distance between the hemispherical charges q_w and q_b. This dipole length d_p depends on the actual distribution of charge on each hemisphere, and is given by $2r_b$, r_b, and $3r_b/4$ for uniform polar, surface, and volume distributions in each hemisphere, respectively.

External electrodes are placed above and below the cavity. Fig. 1 shows a schematic 2D cross section of the computational cell. The cavity is centered between the top and bottom electrode, and all linear dimensions (width W, length L, and height H) are identical for the uniform cube. The whole system is filled with a liquid that exhibits a low, but finite conductivity σ (e.g. we can think of the sheet material as a gel that has been swollen with an oil). Fig. 2 shows a snapshot of the animated dipolar bead dynamics within a spherical cavity.

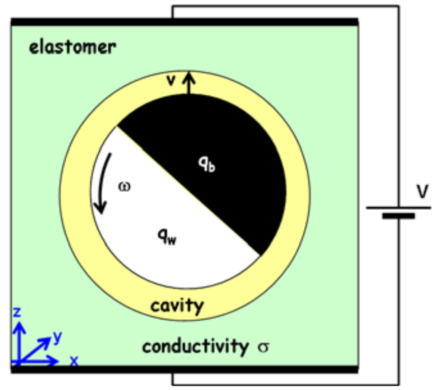

Fig. 1: *Cross-section of unit cell with one dipolar bead inside the cavity. Shown dimensions are not to scale. For the present discussion we assume a cavity radius that is 25% larger than the bead radius.*

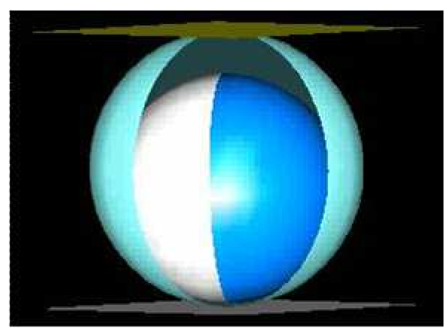

Fig. 2: *3D snapshot of animation of dipolar bead inside the cavity. One quadrant of the cavity wall has been removed for clarity. The graphic is rendered using the commercial software package AVS.*

A. Translational Motion

The translational motion is governed by Newton's equation

$$m\ddot{\mathbf{R}} = q_m\mathbf{E} + (\mathbf{p}\cdot\nabla)\mathbf{E} - \Gamma_t f_t(\mathbf{R})\dot{\mathbf{R}} - m_b g\mathbf{e_z}, \qquad (1)$$

where Γ_t is the translational drag coefficient, m_b is the buoyant mass of the bead, and g is the gravitational accel-

1054-4887 © 2009 ACES

eration. For beads with a radius of $r_b \approx 50\mu m$ the gravitational force becomes relevant for the bead dynamics, if the bead and solvent densities are not well matched (i.e. $m_b \neq 0$). The parameter $f_t(\mathbf{R})$ is a position-dependent drag correction due to the cavity walls, and has been chosen as [1]

$$f_t(\mathbf{R}) = 1 + \frac{2\epsilon}{\epsilon^2 - \xi^2}, \tag{2}$$

where $\xi = |\mathbf{R} - \mathbf{r}_c|/r_b$ is the scaled actual distance of the bead center from the cavity center $\mathbf{r}_c$, while $\epsilon = (r_c - r_b)/r_b$ is the maximal possible distance of the bead center from the cavity center.

The first term on the right-hand-side of Eqn. 1 is the Coulomb force due to the electrostatic field. The second term is a dipole force, which includes both the Clausius-Mossotti contribution and a "hard" dipole due to the assigned hemispherical charges. The third term is the form drag, which is dependent on the shape of the bead and its location relative to the cavity walls. For spherical particles at low speed this term reduces to the Stokes drag $\Gamma_t = 6\pi\eta r_b$ modified by the wall correction factor (Eqn. 2) (η is the viscosity of the fluid inside the cavity). From Eqn. 2 we see that drag increases significantly when the bead is in close proximity to the wall.

B. Rotational Motion

Bead rotation is governed by the torque equation

$$I\dot{\Omega} = \mathbf{p} \times \mathbf{E} - k\Gamma_r f_r(\mathbf{R})\Omega, \tag{3}$$

where Ω is the angular velocity, I is the moment of inertia of the bead, and Γ_r is the rotational drag coefficient. The position dependent parameter f_r describes the wall corrections to the rotational drag and has been chosen as [2]

$$f_r(\mathbf{R}) = 1 + \frac{1}{\epsilon_1} \ln\left(\frac{2\epsilon_1}{\epsilon - \xi}\right), \tag{4}$$

where $\epsilon_1 = \epsilon/(1+\epsilon)$. The parameter k depends on material and operational properties, and can be chosen to control the oscillation of the bead about its equilibrium position. An estimate for k is given by the particular solution

$$k = \frac{2\sqrt{pEI}}{\Gamma_r} \tag{5}$$

to Eqn. 3, which results in critically damped oscillations of the electrical dipole of the bead around the direction of the applied electric field.

C. Field Solution

Several levels of approximations are implemented to expedite computations. The most accurate version solves for the electrostatic field using a boundary integral equation method [3] that takes into account contributions from the diverse collection of free charge, interfacial bound charge, volume space charge, and assigned bead charge. Lower order versions may be invoked through combinations of image symmetries, analytic representations, particle-particle particle-mesh (PPPM) scheme [4], and "super-ion" or particle clumbing [5] schemes.

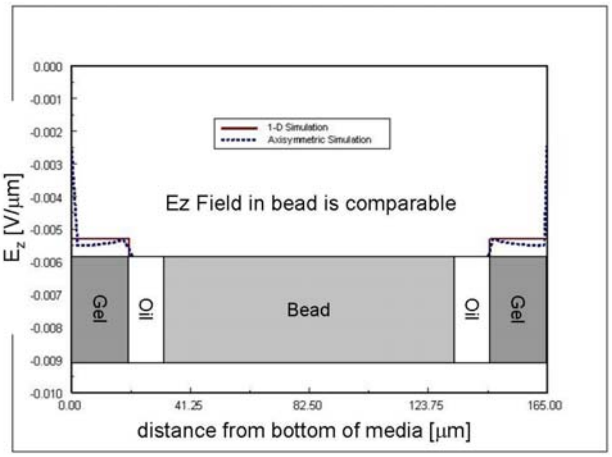

Fig. 3: *Explicit electric field calculation along a straight line through the center of a bead in the model system. Since the dielectric constants of the different materials are very similar, the electric field changes only very slightly within the sheet.*

Fig. 3 shows the electric field due to an applied bias voltage calculated along a line through the center of the bead using a 1D and a cylindrical symmetric model. Both models give very similar results, with the axisymmetric model exhibiting departure from 1D fields near the polar regions of the bead and the cavity due to the finite curvature of the interface regions.

D. Time Integration Algorithm

Difference formulas are used for time integration of the second order differential equations. The central difference approximation

$$\ddot{\mathbf{R}} = \frac{[\mathbf{R}(t+\Delta t) - 2\mathbf{R}(t) + \mathbf{R}(t-\Delta t)]}{\Delta t^2} \tag{6}$$

may be rearranged to result in

$$\begin{aligned}
\mathbf{R}(t_+) &= 2\mathbf{R}(t) - \mathbf{R}(t_-) + \frac{\mathbf{F}(t) - \mathbf{F}_{drag}}{m\Delta t^2} && \text{(7a)}\\
\Theta(t_+) &= 2\Theta(t) - \Theta(t_-) + \frac{\mathbf{T}_\Theta(t) - \mathbf{T}_{\Theta,drag}}{I\Delta t^2}, && \text{(7b)}\\
\Psi(t_+) &= 2\Psi(t) - \Psi(t_-) + \frac{\mathbf{T}_\Psi(t) - \mathbf{T}_{\Psi,drag}}{I\Delta t^2}, && \text{(7c)}
\end{aligned}$$

where Eqn. 7a represents the three cartesian coordinates of the bead position, Eqns. 7b and 7c represent the corresponding torque equations resolved in the two independent spherical angles, and $t_\pm = t \pm \Delta t$.

E. Boundary Conditions

Since charge-charge interactions are long-range, we have to choose proper boundary conditions to avoid nonphysical behavior in our finite-size computational cell.

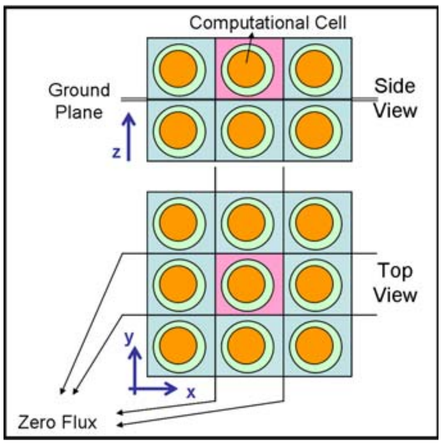

Fig. 4: *Schematic drawing of image cells used to implement the different boundary conditions.*

In order to satisfy the ground plane boundary condition at the bottom of the sheet ($z = 0$), a mirror image with opposite charge for each ion has to be considered (Fig. 4, top).

For zero-flux boundary condition we have to satisfy the condition $\mathbf{E}_n = 0$ on each of the vertical sidewalls, where $\mathbf{E}_n$ is the normal component of the electric field on the boundary. This can be approximated by placing mirror-symmetric nearest neighbor image cells in the xy plane (Fig. 4, bottom). More accurate approximations would include more terms (mirror image cells) in this series expansion.

If we want to allow ions to move in and out of the computational cell, one can impose periodic boundary conditions on the vertical sidewalls, where ions moving out of one side wall re-enter from the opposite sidewall. These can be achieved by placing nearest neighbor image cells with the identical ion distribution as in the computational cell in the xy plane.

III. RESULTS AND DISCUSSION

Both, Eqn. 1 and Eqn. 3, can be made dimensionless by introducing proper length and time scales. In the case of bead translation it is convenient to introduce as length scale the bead radius r_b and as time scale $\tau_t = m/\Gamma_t$, which leads to the dimensionless equation of motion

$$\ddot{\xi} = \tau b - f_t(\xi)\dot{\xi} \tag{8}$$

with

$$b = \frac{q_m E - m_b g}{\Gamma_t r_b}. \tag{9}$$

Note that the time scale here measures the time over which inertial effects dominate over drag effects. At times $t \gg \tau_t$ we can ignore the inertial term. In this case Eqn. 8 has the analytic solution

$$bt = \xi + \xi_0 + 2[\mathrm{arctgh}(\xi/\epsilon) + \mathrm{arctgh}(\xi_0/\epsilon)], \tag{10}$$

where t is the real system time (i.e. we now have the drag dominated time scale $\tau = 1/|b|$), and ξ_0 is the position of the bead at $t = 0$. Because the drag correction diverges as the distance of the bead from the cavity wall goes to zero, it also takes a very long time for the bead to touch the cavity wall. In computer simulations we therefore limit the bead translation such that each bead always keeps a minimum distance from the cavity wall to prevent numerical divergences. The additional rationale is that surface roughness would result in this order of magnitude spacing between the bead and cavity surfaces.

The sign of the parameter b determines whether the bead moves up ($b > 0$) or down ($b < 0$). The gravitational force breaks the symmetry between up and down translation times for a fixed applied voltage. In particular, the bead can travel upward only, if the electric field is strong enough to overcome gravity, i.e.

$$q_m E > m_b g. \tag{11}$$

Fig. 5 shows the minimal monopole charge q_m required for a given bead size and applied voltage. For a bead with $r_b = 45\mu m$, $q_m = 8fC$, and $m_b = 0.29 * m_{bead}$, a field of at least $E \geq 0.16V/\mu m$ is required before it moves against gravity.

The bead rotation is characterized by the time scale $\tau_r = \sqrt{I/pE}$ and the dimensionless version of Eqn. 7b becomes

$$\ddot{\Theta} = \sin\Theta - 2f_r(\xi)\dot{\Theta}. \tag{12}$$

In the case where the inertial term can be neglected in the equation of motion for the bead rotation the dipole orientation angle is given by the closed form

$$\Theta(\hat{t}) = 2\,\mathrm{arctg}\left\{\exp\left[\int \frac{d\hat{t}}{2f_r(\xi(\hat{t}))}\right]\right\}, \tag{13}$$

where $\hat{t} = t/\tau_r$ is the dimensionless time parameter.

Without the wall correction to the rotational drag ($f_r = 1$) the bead rotation is completely specified by its size and shape (which determine the moment of inertia I), its dipole moment p, and the applied electric

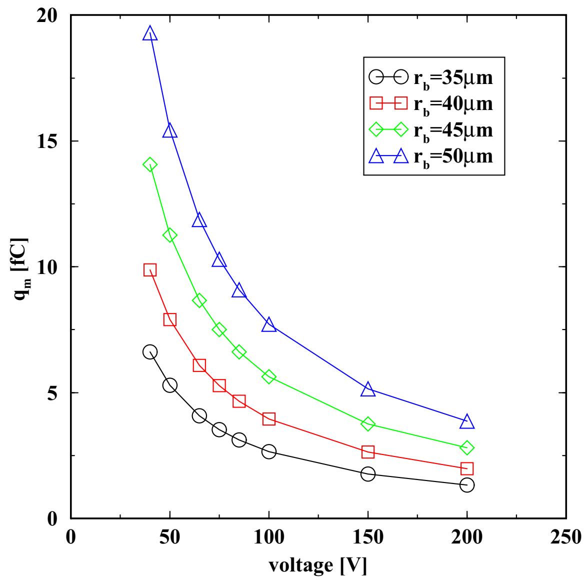

Fig. 5: *Minimal monopole charge required to levitate a bead of radius r_b for a given applied voltage assuming a sheet thickness $H = 450\mu m$.*

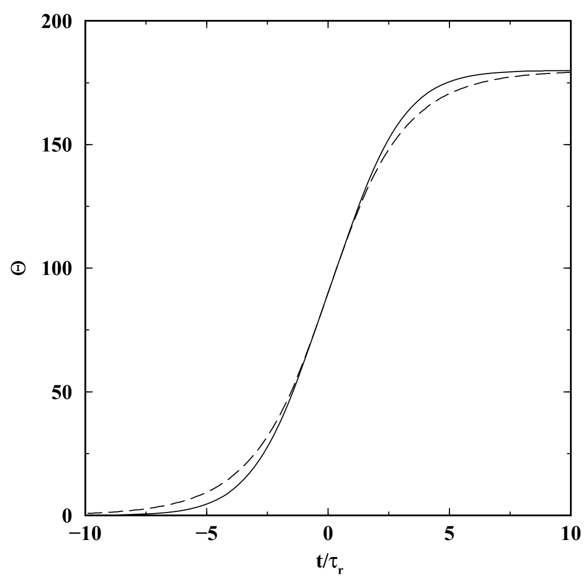

Fig. 6: *Bead orientation as function of scaled time for a system without wall drag corrections. (solid): complete solution of Eqn. 12; (dashed): solution of Eqn. 12 without the inertial term $\ddot{\Theta}$.*

field. Fig. 6 shows the bead orientation as a function of dimensionless time for this case. The inertial term of Eqn. 12 has the most effect when the bead dipole is closely aligned with the electric field, where it slows down the bead rotation visibly. Without the inertial term, the bead rotation is described by the function

$$\Theta(\hat{t}) = 2\,\mathrm{arctg}\left\{\exp\left[\frac{\hat{t}-\hat{t}_0}{2}\right]\right\}, \qquad (14)$$

where $\hat{t}_0$ is the time at which $\Theta = \pi/2$.

With the wall drag fully included the translational and rotational equation of motion become coupled and a numerical approach is needed to solve for the bead dynamics.

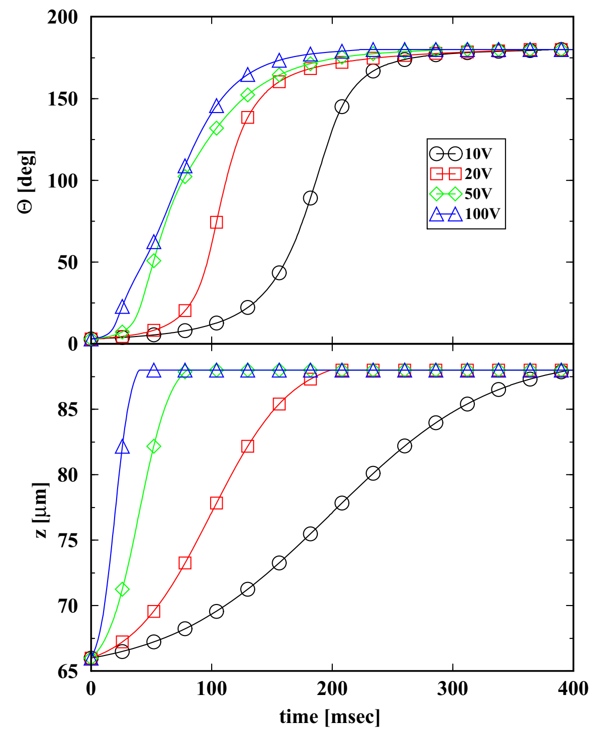

Fig. 7: *Bead orientation angle and position as function of time for different applied voltages and zero buoyant mass ($m_b = 0$).*

Fig. 7 shows typical orientation and position curves as function of time for a bead moving inside the cavity. In the case when the density of the bead material is matched by the density of the solvent, the buoyant mass m_b is zero and the response of the bead becomes independent on the direction of the applied field. However, because of the coupling between the translational and translational dynamics through the drag coefficients, we observe quite different rotation speeds as function of applied field: For free rotation, we would expect a rotation time scale that is inversely proportional to the square root of the applied field. With the impact of the walls on the drag, we observe instead a slowing down of the bead rotation times at increased applied voltage (50V and 100V in Fig. 7). This is due to the fact that at these voltages the bead moves through the cavity before it has a chance to rotate, so most of its orientation change happens near the cavity wall where the drag is highest.

When the buoyant mass of the bead is not zero, the bead is also influenced by gravity, and its response to an applied electric field depends on the orientation of this field to the gravitational field. Fig. 8 shows bead

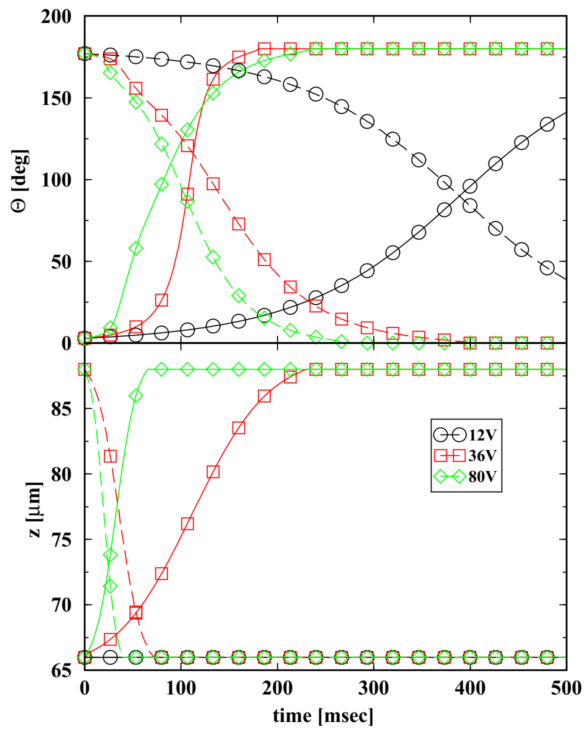

Fig. 8: *Bead orientation angle and position as function of time for different applied voltages and buoyant mass $m_b = 0.29 m_{bead}$. (solid line): upward motion; (dashed line): downward motion.*

orientation and position as function of time for a bead with buoyant mass $m_b = 0.29 * m_{bead}$ for different applied fields that are either parallel or anti-parallel to gravity, causing the bead to either move up or down. Again, we see that the biggest impact on the rotation time scale of the bead is its location relative to the cavity wall. In particular, we observe, that for the case when the field is parallel to gravity (bead moves down) the translational motion is much faster than the rotational motion, and the bead always changes its orientation close to the bottom of the cavity. Also, because of its finite buoyant mass the bead does not move upward for low applied voltages (10V case in Fig. 8).

In order to discuss the rotation times for beads with different monopole and dipole charges and buoyant masses, we fitted the time-dependent orientation change to a standard step function. In particular, we fitted the expression

$$F(t) = \sin^2\left(\frac{\Theta(t)}{2}\right) \quad (15)$$

to the "Fermi-like" function

$$R_{fit}(t) = \frac{1}{1 + \exp((t - t_0)/\tau_r)}, \quad (16)$$

with the two fit parameters τ_r, which represents the time scale of rotation, and t_0, which denotes the time when the bead rotates through $\Theta = 90^o$. The expression $F(t)$ corresponds to the projection of the visible part of one hemisphere onto a plane perpendicular to the applied field. The fit function Eqn. 16 is motivated by the solution to the freely rotating sphere without wall drag correction (Eqn. 14). Though this function is expected to represent

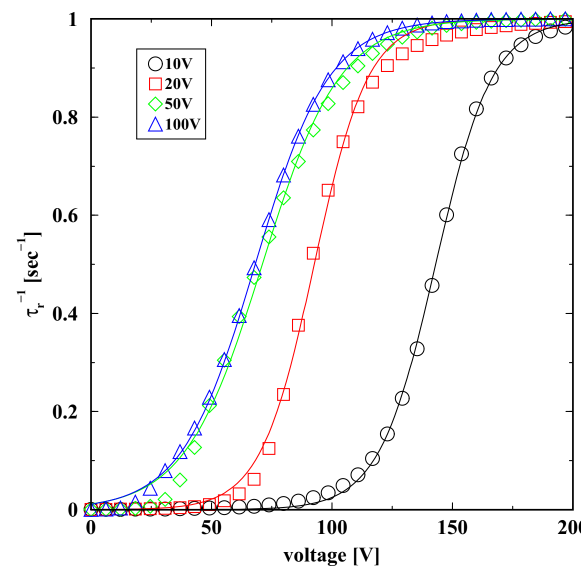

Fig. 9: *Fits of time-dependence of bead orientation to Eqn. 8.*

a good description of the bead rotation only, when the bead rotates without changing position within the cavity, we observe that it captures the main orientation change very well in all situations encountered by our simulations, as is demonstrated in Fig. 9. In all cases shown, the function fits the steepest part of the rotation curve very well, while it may deviate from the observed data at small and large orientation angles.

Figs. 10, 11, and 12 show fitted rotation times as function of applied voltage for beads with different buoyant mass, monopole charge, and dipole charge, respectively.

At zero buoyant mass the bead translation and rotation times are independent of the applied field, but are shortest for the applied voltage where the rotation takes place while the bead moves through the center of the cavity (at about 20V for the situation shown in Fig. 10). For smaller or larger voltages, the bead rotates closer to the cavity wall and the rotation times are substantially longer. For high applied voltages the bead moves across the cavity before it has a chance to rotate, and the observed inverse rotation times again decrease with voltage as we expect for the case where the bead rotates

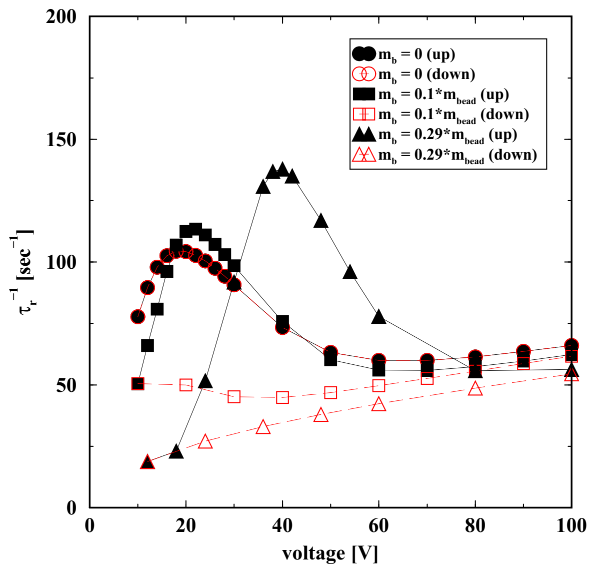

Fig. 10: *Inverse bead orientation times as function of applied voltage for different buoyant masses m_b. (solid line): upward motion; (dashed line): downward motion.*

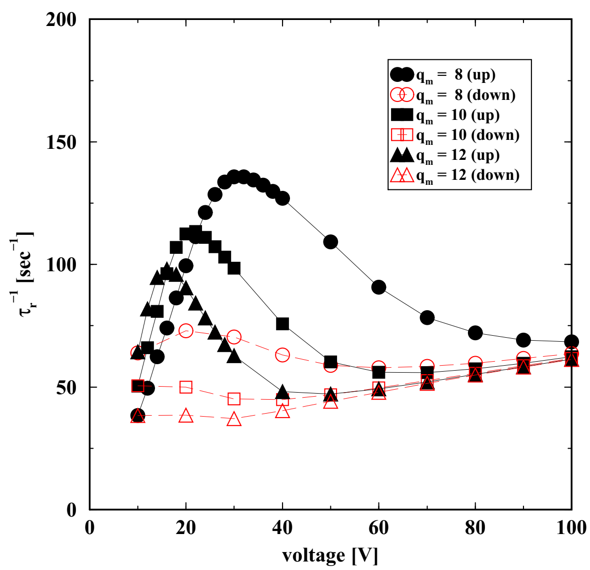

Fig. 11: *Inverse bead orientation times as function of applied voltage for different bead monopole charge q_m [in fC], but constant dipole charge $q_d = 4fC$. (solid line): upward motion; (dashed line): downward motion.*

at a fixed location within the cavity. For beads with a finite buoyant mass, gravity either speeds up or slows down the translational motion, and the rotation times become dependent on the direction of the applied field. In particular, for the case where the field moves the bead downward, translational motion becomes even for small buoyant mass much faster than rotational motion and the bead almost always rotates near the bottom of the

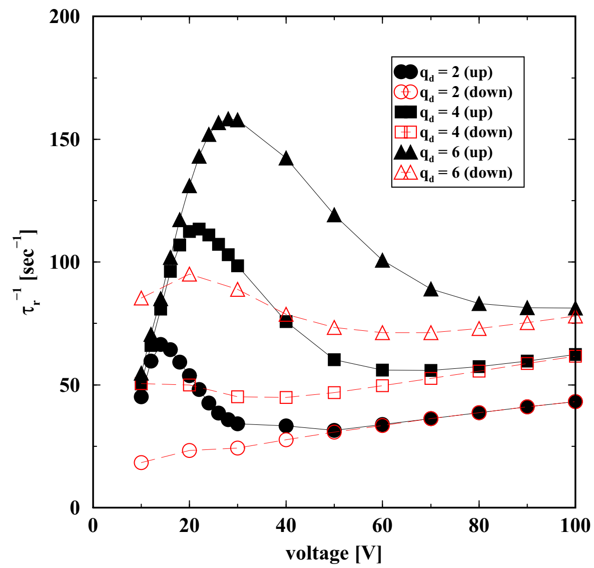

Fig. 12: *Inverse bead orientation times as function of applied voltage for different bead monopole charge q_d [in fC], but constant monopole charge $q_m = 10fC$. (solid line): upward motion; (dashed line): downward motion.*

cavity.

A change in monopole charge of the bead has the biggest impact on the translational speed of the bead. However, with the coupling of the bead location into the rotational drag, we observe also an impact of varying q_m on the rotational motion, especially at applied voltages where the bead rotation happens near the cavity center (Fig. 11). In particular, we see shorter rotation times for beads with smaller q_m at lower applied voltages when moving downward, and at higher voltages when the bead moves upward.

A change in dipolar charge has a direct impact on the rotational speed. In the case where the bead moves downward and rotation happens mainly near the cavity bottom the change in rotation speed is directly related to the dipole moment and we see a linear increase in the inverse rotation time with dipole moment (Fig. 12). For the upward motion we see a shift (increase) in the voltage for which the rotation time is minimal with increasing dipole moment, reflecting the fact that at a higher dipole moment the faster bead rotation requires a slightly faster translational motion to make the bead rotate near the center of the cavity.

An application may be flexible displays, where these dipolar beads are dispersed in an elastomer sheet. Array addressable electrodes on either side of the sheet will allow for controlled switching of the beads to display images.

Fig. 13 shows a comparison of our model to experimental data. Dipolar beads of size $r_b \approx 50\mu m$ have been densely packed into a thin gel matrix that has been swollen with a silicone oil (see e.g. Sheridon et al. [6]

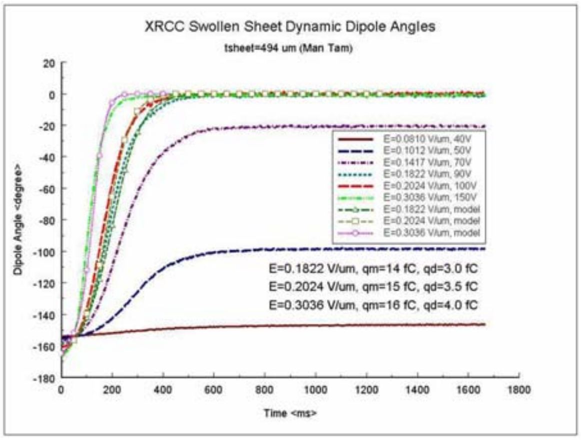

Fig. 13: *Comparison of model predictions with experimental data: Charge parameters q_b, q_m, q_d, and q_w that fit the experimental data best as function of applied field.*

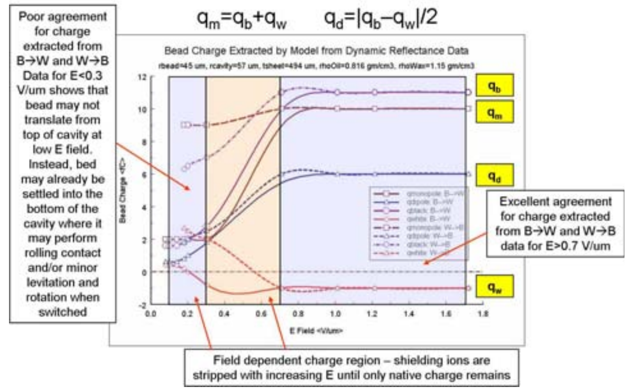

Fig. 14: *Comparison of model predictions with experimental data: Charge parameters q_b, q_m, q_d, and q_w that fit the experimental data best as function of applied field.*

for more details). The dipolar character of the bead is introduced by selecting different materials for each of the two hemispheres, e.g. a black-colored and a white-colored wax. The oil causes a homogeneous swelling of the gel, resulting in cavities around the beads that are about 25% larger in diameter, while maintaining a very low conductivity throughout the gel ($\sigma \approx 10^{-12} S/m$). By applying a slowly alternating voltage pulses on a horizontally aligned gel sheet the beads are switched from top to bottom and vice versa. The dynamics of this switching is captured by measuring the dynamic reflectivity of the sheet, which is directly proportional to the white area of the beads exposed to the observer, as a function of time. This experiment is repeated for different values of the applied voltage. We then use our mathematical model (Eqn. 1 and 3) to obtain monopole and dipole charges of the bead (or, correspondingly the charge on each of the hemispheres can be obtained from the relations $q_m = q_b + q_w$ and $q_d = 0.5 * |q_b - q_w|$) that best fit the experimentally obtained reflectance data for each applied voltage. For the three highest field values shown in Fig. 13 the fit is clearly good and shows only a slight monotonic increase in charge magnitude. The remaining three curves for lower fields are for incomplete rotation. Since these fields are not able to levitate the bead, the switch from black-to-white happens near the cavity floor rather than originate from the roof of the cavity. This short period of time would be insufficient for the bead to complete rotation. When the bead settles or makes contact with the cavity floor, friction would stop the rotation leading to partial switching as shown by the asymptote to smaller changes in dipole angles.

If the model is a good representation of the experiment, the fitted charge values for the bottom-to-top switching cycle should be the same as that for the top-to-bottom switching cycle. Fig. 14 shows the monopole and dipole charge that best fits the experimental data at each applied voltage. At the higher voltage we extract consistent values for the bead charges for bottom-up and top-down bead dynamics, while at the lower voltages this is no longer the case. The major reason is that we assume the bead to be located at the top plate as initial condition for the top-to-down switching cycle, which is not physically possible at low fields that are insufficient to levitate the beads.

In addition to the choice of initial condition, other dynamic processes that are dependent on the applied field become relevant, e.g. field-dependent stripping of counterions from the bead's surface/Debye layer, or counterion migration, may introduce additional time scales to the bead dynamics that are not covered by the model we discussed here. Additional mobile charges can have dif-

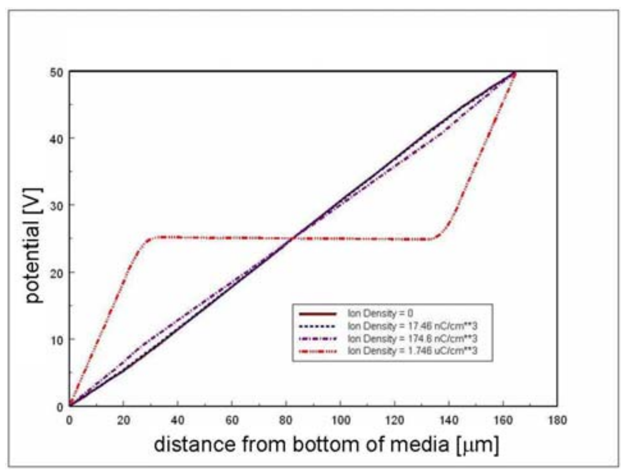

Fig. 15: *Calculated electric field along a straight line through the model system for different ionic concentrations.*

ferent impact on the bead dynamics, depending on their concentration and mobility. If the additional charges are substantially faster than the bead (what one typically would expect for small counter charges in a low-viscosity medium such as the solvent), then their main contribution on the bead dynamics will consist of the shielding of the electric field that the bead sees. In particular, if the concentration of the these ions is large enough, the electric field at the bead position can become completely shielded (see Fig. 15).

However, if the concentration of the additional charges is small enough to not incur complete shielding of the applied field, the bead will still respond to the external field. Moreover, if the mobility of these charges is reduced, e.g. when moving through the elastomer layer outside of the cavity, the time for those charges to move a distance comparable to the bead size may become of the order of the bead translation and rotation times, leading to competing effects on the bead dynamics. A detailed study of such scenarios will be presented elsewhere.

IV. SUMMARY

This paper described an effective algorithm to simulate the dynamics of a dipolar bead inside a spherical cavity under the influence of an electrostatic field and gravity, subject to wall effects on drag and viscous damping. Using this model we have shown that the wall effects on the drag effectively couple the translational and rotational motion of the bead, leading to a rather rich response behavior of the bead as a function of applied field, bead monopole and bead dipole charge. In addition, if the bead density is not matched exactly by the solvent density, gravity breaks the symmetry between upward and downward motion, which can lead to substantially lower switching times for upward motion due to different locations at which the bead rotates. Several levels of approximation have been implemented to expedite computations, and the accuracy of the model has been verified by analytic solutions. Comparison of our model to dynamic reflectivity measurements on dipolar beads packed into a swollen, low-conductivity, gel matrix show very good agreement at higher applied fields, where the dynamic effects of other mobile charges (e.g. counterions) becomes negligible.

REFERENCES

[1] H. Brenner, "The slow motion of a sphere through a viscous fluid towards a plane surface", Chemical Engineering Science, vol. 16, pp. 242-251, 1961.

[2] M. Cooley, "The slow rotation in a viscous fluid of a sphere close to another fixed sphere about a diameter perpendicular to the line of centers", Q. J. Mechanics Appl. Math., vol. 24, pp. 237-250, 1971.

[3] M. H. Lean, "Application of boundary integral equation methods to electromagnetics", IEEE Trans. Mag., vol. 21, pp. 1823-1828, 1985.

[4] M. H. Lean, "Particle simulations of ion cloud in a magnetic field", IEEE Trans. Mag., vol. 34, pp. 3122-3125, 1998.

[5] M. H. Lean, J. F. O Brien, K. Pietrowski, H. Okuda, "Microscopic particle simulation of air ionization", Proc. NIP-15, pp. 513-516, 1999.

[6] N. K. Sheridon, M. A. Berkovitz, "The Gyricon - a twisting ball display", Proc. S.I.D., vol. 18, pp. 289-293, 1977.

Meng H. Lean has 25 years of R&D experience developing multiphysics models from first principles and building hardware prototypes for xerographic and digital imaging applications. He extended the use of boundary element methods in electromagnetics to transient and nonlinear couple thermal and fluid dynamic problems. As an adjunct professor at Cornell (1988-1992), he led the implementation of a computational platform for hierarchical simulation of a xerographic color print engine. He has extensive experience in high performance computing in collaboration with researchers at LANL and PPPL. His recent work is in the simulation and development of Bio MEMS devices for bio defense and bio medical applications. Some examples include high-speed high resolution protein separation, bio concentration and enrichment cells, and portable non-contacting surface spore collectors.

Armin R. Völkel received his diploma and Ph.D., both in physics, from the University of Bayreuth, Germany, in 1989 and 1992, respectively. During his graduate studies he was also a Research Assistant at the Los Alamos National Laboratory from 1989 to 1990. He was a postdoc for 6 months at the University of Florence before joining Xerox in 1993, where he worked both at the Xerox Research Center in Canada and, since 2000, at the Palo Alto Research Center. His research interests are in modeling and simulation of complex physical systems including the dynamics of charged particles and polymers in free flow and restricted media under the influence of external electric fields, protein stability, and micro electromechanical systems.

2009 INSTITUTIONAL MEMBERS

AUSTRALIAN DEFENCE LIBRARY
Northcott Drive
Canberra, A.C.T. 2600 Australia

BAE SYSTEMS
W423A Warton Aerodome
Preston, Lancashire
United Kingdom PR4 1AX

DARTMOUTH COLLEGE
6193 Murdough Center
Hanover, NH 03755-3560

DSTO-DSTORL EDINBURGH
Jets AU/33851-99, PO Box 562
Milsons Point, NSW
Australia 1565

DTIC-OCP/LIBRARY
8725 John J. Kingman Rd. Ste 0944
Ft. Belvoir, VA 22060-6218

ELLEDIEMME
Libri Dal Mondo
PO Box 69/Poste S. Silvestro
Rome, Italy 00187

ELSEVIER
Bibliographic Databases
PO Box 2227
Amsterdam, Netherlands 1000 CE

ENGINEERING INFORMATION, INC
PO Box 543
Amsterdam, Netherlands 1000 Am

ETSE TELECOMUNICACION
Biblioteca, Campus Lagoas
Vigo, 36200 Spain

FGAN-FHR
Neuenahrerstrasse 20
Wachtberg, Germany 53343

FLORIDA INTERNATIONAL UNIV
10555 W. Flagler Street
Miami, FL 33174

GEORGIA TECH LIBRARY
225 North Avenue, NW
Atlanta, GA 30332-0001

HANYANG UNIVERSITY
Paiknam Academic Info. Ctr Library
17 Haengdang-Dong
Seongdong-Ku
Seoul, South Korea 133-791

HRL LABS, RESEARCH LIBRARY
3011 Malibu Canyon
Malibu, CA 90265

IEE INSPEC/Acquisitions Section
Michael Faraday House
6 Hills Way
Stevenage, Herts UK SG1 2AY

IND CANTABRIA
PO Box 830470
Birmingham, AL 35283

INSTITUTE FOR SCIENTIFIC INFO.
Publication Processing Dept.
3501 Market St.
Philadelphia, PA 19104-3302

L-3 IS
1133 Wood Valley Drive
Woodway, TX 76712

LIBRARY – DRDC OTTAWA
3701 Carling Avenue
Ottawa, Ontario, Canada K1A OZ4

LIBRARY of CONGRESS
Reg. Of Copyrights
Attn: 40T Deposits
Washington DC, 20559

LINDA HALL LIBRARY
5109 Cherry Street
Kansas City, MO 64110-2498

LULEA UNIV. OF TECHNOLOGY
Porson
Lulea, Sweden 97187

MISSISSIPPI STATE UNIV LIBRARY
PO Box 9570
Mississippi State, MS 39762

MISSOURI S&T
400 W 14^{th} Street
Rolla, MO 56409

MIT LINCOLN LABORATORY
Periodicals Library
244 Wood Street
Lexington, MA 02420

NATIONAL DEFENSE ACADEMY
1-10-20 Hashirimizu
Yokosuka, Kanagawa
239-8686 Japan

NAVAL POSTGRADUATE SCHOOL
Attn:J. Rozdal/411 Dyer Rd./ Rm 111
Monterey, CA 93943-5101

NDL KAGAKU
C/0 KWE-ACCESS
PO Box 300613 (JFK A/P)
Jamaica, NY 11430-0613

OHIO STATE UNIVERSITY
1320 Kinnear Road
Columbus, OH 43212

OVIEDO LIBRARY
PO BOX 830679
Birmingham, AL 35283

PENN STATE UNIVERSITY
126 Paterno Library
University Park, PA 16802-1808

DAVID J. PINION
1122 E PIKE STREET #1217
SEATTLE, WA 98122

SOUTHWEST RESEARCH
INSTITUTE
6220 Culebra Road
San Antonio, TX 78238

SWETS INFORMATION SERVICES
160 Ninth Avenue, Suite A
Runnemede, NJ 08078

TELSTRA
13/242 Exhibition Street
Melbourne, Victoria
3000 Australia

TIB & UNIV. BIB. HANNOVER
DE/5100/G1/0001
Welfengarten 1B
Hannover, Germany 30167

TU DARMSTADT
Schlossgartenstrasse 8
Darmstadt, Hessen
Germany D-64289

UNIV OF CENTRAL FLORIDA LIB.
4000 Central Florida Boulevard
Orlando, FL 32816-8005

UNIVERSITY OF KANSAS –
WATSON
1425 Jayhawk Blvd 210S
Lawrence, KS 66045-7594

UNIVERSITY OF MISSISSIPPI
JD Williams Library
University, MS 38677-1848

UNIVERSITY OF PALERMO
PO Box 69- Poste S. Silvestr
Rome, 00187, Italy

VIRTUAL EM INC.
2019 Georgetown Blvd.
Ann Arbor, MI 48105

ACES COPYRIGHT FORM

This form is intended for original, previously unpublished manuscripts submitted to ACES periodicals and conference publications. The signed form, appropriately completed, MUST ACCOMPANY any paper in order to be published by ACES. PLEASE READ REVERSE SIDE OF THIS FORM FOR FURTHER DETAILS.

TITLE OF PAPER:

AUTHORS(S)

PUBLICATION TITLE/DATE:

RETURN FORM TO:

Dr. Atef Z. Elsherbeni
University of Mississippi
Dept. of Electrical Engineering
Anderson Hall Box 13
University, MS 38677 USA

PART A - COPYRIGHT TRANSFER FORM

(NOTE: Company or other forms may not be substituted for this form. U.S. Government employees whose work is not subject to copyright may so certify by signing Part B below. Authors whose work is subject to Crown Copyright may sign Part C overleaf).

The undersigned, desiring to publish the above paper in a publication of ACES, hereby transfer their copyrights in the above paper to The Applied Computational Electromagnetics Society (ACES). The undersigned hereby represents and warrants that the paper is original and that he/she is the author of the paper or otherwise has the power and authority to make and execute this assignment.

Returned Rights: In return for these rights, ACES hereby grants to the above authors, and the employers for whom the work was performed, royalty-free permission to:

1. Retain all proprietary rights other than copyright, such as patent rights.
2. Reuse all or portions of the above paper in other works.
3. Reproduce, or have reproduced, the above paper for the author's personal use or for internal company use provided that (a) the source and ACES copyright are indicated, (b) the copies are not used in a way that implies ACES endorsement of a product or service of an employer, and (c) the copies per se are not offered for sale.
4. Make limited distribution of all or portions of the above paper prior to publication.
5. In the case of work performed under U.S. Government contract, ACES grants the U.S. Government royalty-free permission to reproduce all or portions of the above paper, and to authorize others to do so, for U.S. Government purposes only.

ACES Obligations: In exercising its rights under copyright, ACES will make all reasonable efforts to act in the interests of the authors and employers as well as in its own interest. In particular, ACES REQUIRES that:

1. The consent of the first-named author be sought as a condition in granting re-publication permission to others.
2. The consent of the undersigned employer be obtained as a condition in granting permission to others to reuse all or portions of the paper for promotion or marketing purposes.

In the event the above paper is not accepted and published by ACES or is withdrawn by the author(s) before acceptance by ACES, this agreement becomes null and void.

AUTHORIZED SIGNATURE | TITLE (IF NOT AUTHOR)

EMPLOYER FOR WHOM WORK WAS PERFORMED | DATE FORM SIGNED

Part B - U.S. GOVERNMENT EMPLOYEE CERTIFICATION

(NOTE: if your work was performed under Government contract but you are not a Government employee, sign transfer form above and see item 5 under Returned Rights).

This certifies that all authors of the above paper are employees of the U.S. Government and performed this work as part of their employment and that the paper is therefor not subject to U.S. copyright protection.

AUTHORIZED SIGNATURE | TITLE (IF NOT AUTHOR)

NAME OF GOVERNMENT ORGANIZATION | DATE FORM SIGNED

PART C - CROWN COPYRIGHT

(NOTE: ACES recognizes and will honor Crown Copyright as it does U.S. Copyright. It is understood that, in asserting Crown Copyright, ACES in no way diminishes its rights as publisher. Sign only if *ALL* authors are subject to Crown Copyright).

This certifies that all authors of the above Paper are subject to Crown Copyright. (Appropriate documentation and instructions regarding form of Crown Copyright notice may be attached).

AUTHORIZED SIGNATURE TITLE OF SIGNEE

NAME OF GOVERNMENT BRANCH DATE FORM SIGNED

Information to Authors

ACES POLICY

ACES distributes its technical publications throughout the world, and it may be necessary to translate and abstract its publications, and articles contained therein, for inclusion in various compendiums and similar publications, etc. When an article is submitted for publication by ACES, acceptance of the article implies that ACES has the rights to do all of the things it normally does with such an article.

In connection with its publishing activities, it is the policy of ACES to own the copyrights in its technical publications, and to the contributions contained therein, in order to protect the interests of ACES, its authors and their employers, and at the same time to facilitate the appropriate re-use of this material by others.

The new United States copyright law requires that the transfer of copyrights in each contribution from the author to ACES be confirmed in writing. It is therefore necessary that you execute either Part A-Copyright Transfer Form or Part B-U.S. Government Employee Certification or Part C-Crown Copyright on this sheet and return it to the Managing Editor (or person who supplied this sheet) as promptly as possible.

CLEARANCE OF PAPERS

ACES must of necessity assume that materials presented at its meetings or submitted to its publications is properly available for general dissemination to the audiences these activities are organized to serve. It is the responsibility of the authors, not ACES, to determine whether disclosure of their material requires the prior consent of other parties and if so, to obtain it. Furthermore, ACES must assume that, if an author uses within his/her article previously published and/or copyrighted material that permission has been obtained for such use and that any required credit lines, copyright notices, etc. are duly noted.

AUTHOR/COMPANY RIGHTS

If you are employed and you prepared your paper as a part of your job, the rights to your paper initially rest with your employer. In that case, when you sign the copyright form, we assume you are authorized to do so by your employer and that your employer has consented to all of the terms and conditions of this form. If not, it should be signed by someone so authorized.

NOTE RE RETURNED RIGHTS: Just as ACES now requires a signed copyright transfer form in order to do “business as usual”, it is the intent of this form to return rights to the author and employer so that they too may do “business as usual”. If further clarification is required, please contact: The Managing Editor, R. W. Adler, Naval Postgraduate School, Code EC/AB, Monterey, CA, 93943, USA (408)656-2352.

Please note that, although authors are permitted to re-use all or portions of their ACES copyrighted material in other works, this does not include granting third party requests for reprinting, republishing, or other types of re-use.

JOINT AUTHORSHIP

For jointly authored papers, only one signature is required, but we assume all authors have been advised and have consented to the terms of this form.

U.S. GOVERNMENT EMPLOYEES

Authors who are U.S. Government employees are not required to sign the Copyright Transfer Form (Part A), but any co-authors outside the Government are.

Part B of the form is to be used instead of Part A only if all authors are U.S. Government employees and prepared the paper as part of their job.

NOTE RE GOVERNMENT CONTRACT WORK: Authors whose work was performed under a U.S. Government contract but who are not Government employees are required so sign Part A-Copyright Transfer Form. However, item 5 of the form returns reproduction rights to the U. S. Government when required, even though ACES copyright policy is in effect with respect to the reuse of material by the general public.

January 2002

APPLIED COMPUTATIONAL ELECTROMAGNETICS SOCIETY JOURNAL

http://aces.ee.olemiss.edu

INFORMATION FOR AUTHORS

PUBLICATION CRITERIA

Each paper is required to manifest some relation to applied computational electromagnetics. **Papers may address general issues in applied computational electromagnetics, or they may focus on specific applications, techniques, codes, or computational issues.** While the following list is not exhaustive, each paper will generally relate to at least one of these areas:

1. **Code validation.** This is done using internal checks or experimental, analytical or other computational data. Measured data of potential utility to code validation efforts will also be considered for publication.

2. **Code performance analysis.** This usually involves identification of numerical accuracy or other limitations, solution convergence, numerical and physical modeling error, and parameter tradeoffs. However, it is also permissible to address issues such as ease-of-use, set-up time, run time, special outputs, or other special features.

3. **Computational studies of basic physics.** This involves using a code, algorithm, or computational technique to simulate reality in such a way that better, or new physical insight or understanding, is achieved.

4. **New computational techniques** or new applications for existing computational techniques or codes.

5. **"Tricks of the trade"** in selecting and applying codes and techniques.

6. **New codes, algorithms, code enhancement, and code fixes.** This category is self-explanatory, but includes significant changes to existing codes, such as applicability extensions, algorithm optimization, problem correction, limitation removal, or other performance improvement. **Note: Code (or algorithm) capability descriptions are not acceptable, unless they contain sufficient technical material to justify consideration.**

7. **Code input/output issues.** This normally involves innovations in input (such as input geometry standardization, automatic mesh generation, or computer-aided design) or in output (whether it be tabular, graphical, statistical, Fourier-transformed, or otherwise signal-processed). Material dealing with input/output database management, output interpretation, or other input/output issues will also be considered for publication.

8. **Computer hardware issues.** This is the category for analysis of hardware capabilities and limitations of various types of electromagnetics computational requirements. Vector and parallel computational techniques and implementation are of particular interest.

Applications of interest include, but are not limited to, antennas (and their electromagnetic environments), networks, static fields, radar cross section, inverse scattering, shielding, radiation hazards, biological effects, biomedical applications, electromagnetic pulse (EMP), electromagnetic interference (EMI), electromagnetic compatibility (EMC), power transmission, charge transport, dielectric, magnetic and nonlinear materials, microwave components, MEMS, RFID, and MMIC technologies, remote sensing and geometrical and physical optics, radar and communications systems, sensors, fiber optics, plasmas, particle accelerators, generators and motors, electromagnetic wave propagation, non-destructive evaluation, eddy currents, and inverse scattering.

Techniques of interest include but not limited to frequency-domain and time-domain techniques, integral equation and differential equation techniques, diffraction theories, physical and geometrical optics, method of moments, finite differences and finite element techniques, transmission line method, modal expansions, perturbation methods, and hybrid methods.

Where possible and appropriate, authors are required to provide statements of quantitative accuracy for measured and/or computed data. This issue is discussed in "Accuracy & Publication: Requiring, quantitative accuracy statements to accompany data," by E. K. Miller, *ACES Newsletter,* Vol. 9, No. 3, pp. 23-29, 1994, ISBN 1056-9170.

SUBMITTAL PROCEDURE

All submissions should be uploaded to ACES server through ACES web site (http://aces.ee.olemiss.edu) by using the upload button, journal section. Only pdf files are accepted for submission. The file size should not be larger than 5MB, otherwise permission from the Editor-in-Chief should be obtained first. Automated acknowledgment of the electronic submission, after the upload process is successfully completed, will be sent to the corresponding author only. It is the responsibility of the corresponding author to keep the remaining authors, if applicable, informed. Email submission is not accepted and will not be processed.

PAPER FORMAT (INITIAL SUBMISSION)

The preferred format for initial submission manuscripts is 12 point Times Roman font, single line spacing and single column format, with 1 inch for top, bottom, left, and right margins. Manuscripts should be prepared for standard 8.5x11 inch paper.

EDITORIAL REVIEW

In order to ensure an appropriate level of quality control, papers are peer reviewed. They are reviewed both for technical correctness and for adherence to the listed guidelines regarding information content and format.

PAPER FORMAT (FINAL SUBMISSION)

Only camera-ready electronic files are accepted for publication. The term **"camera-ready" means that the material is neat, legible, reproducible, and in accordance with the final version format listed below.**

The following requirements are in effect for the final version of an ACES Journal paper:

1. The paper title should not be placed on a separate page. The title, author(s), abstract, and (space permitting) beginning of the paper itself should all be on the first page. The title, author(s), and author affiliations should be centered (center-justified) on the first page. The title should be of font size 16 and bolded, the author names should be of font size 12 and bolded, and the author affiliation should be of font size 12 (regular font, neither italic nor bolded).

2. An abstract is required. The abstract should be a brief summary of the work described in the paper. It should state the computer codes, computational techniques, and applications discussed in the paper (as applicable) and should otherwise be usable by technical abstracting and indexing services. The word "Abstract" has to be placed at the left margin of the paper, and should be bolded and italic. It also should be followed by a hyphen (—) with the main text of the abstract starting on the same line.

3. All section titles have to be centered and all the title letters should be written in caps. The section titles need to be numbered using roman numbering (I. II. ….)

4. Either British English or American English spellings may be used, provided that each word is spelled consistently throughout the paper.

5. Internal consistency of references format should be maintained. As a guideline for authors, we recommend that references be given using numerical numbering in the body of the paper (with numerical listing of all references at the end of the paper). The first letter of the authors' first name should be listed followed by a period, which in turn, followed by the authors' complete last name. Use a coma (,) to separate between the authors' names. Titles of papers or articles should be in quotation marks (" "), followed by the title of journal, which should be in italic font. The journal volume (vol.), issue number (no.), page numbering (pp.), month and year of publication should come after the journal title in the sequence listed here.

6. Internal consistency shall also be maintained for other elements of style, such as equation numbering. As a guideline for authors who have no other preference, we suggest that equation numbers be placed in parentheses at the right column margin.

7. The intent and meaning of all text must be clear. For authors who are not masters of the English language, the ACES Editorial Staff will provide assistance with grammar (subject to clarity of intent and meaning). However, this may delay the scheduled publication date.

8. Unused space should be minimized. Sections and subsections should not normally begin on a new page.

ACES reserves the right to edit any uploaded material, however, this is not generally done. It is the author(s) responsibility to provide acceptable camera-ready pdf files. Incompatible or incomplete pdf files will not be processed for publication, and authors will be requested to re-upload a revised acceptable version.

COPYRIGHTS AND RELEASES

Each primary author must sign a copyright form and obtain a release from his/her organization vesting the copyright with ACES. Copyright forms are available at ACES, web site (http://aces.ee.olemiss.edu). To shorten the review process time, the executed copyright form should be forwarded to the Editor-in-Chief immediately after the completion of the upload (electronic submission) process. Both the author and his/her organization are allowed to use the copyrighted material freely for their own private purposes.

Permission is granted to quote short passages and reproduce figures and tables from and ACES Journal issue provided the source is cited. Copies of ACES Journal articles may be made in accordance with usage permitted by Sections 107 or 108 of the U.S. Copyright Law. This consent does not extend to other kinds of copying, such as for general distribution, for advertising or promotional purposes, for creating new collective works, or for resale. The reproduction of multiple copies and the use of articles or extracts for commercial purposes require the consent of the author and specific permission from ACES. Institutional members are allowed to copy any ACES Journal issue for their internal distribution only.

PUBLICATION CHARGES

All authors are allowed for 8 printed pages per paper without charge. Mandatory page charges of $75 a page apply to all pages in excess of 8 printed pages. Authors are entitled to one, free of charge, copy of the journal issue in which their paper was published. Additional reprints are available for a nominal fee by submitting a request to the managing editor or ACES Secretary.

Authors are subject to fill out a one page over-page charge form and submit it online along with the copyright form before publication of their manuscript.

ACES Journal is abstracted in INSPEC, in Engineering Index, DTIC, Science Citation Index Expanded, the Research Alert, and to Current Contents/Engineering, Computing & Technology.